

# **Operator description of the dynamics of optical modes**

## **PROEFSCHRIFT**

ter verkrijging van  
de graad van Doctor aan de Universiteit Leiden,  
op gezag van de Rector Magnificus Dr. D. D. Breimer,  
hoogleraar in de faculteit der Wiskunde en  
Natuurwetenschappen en die der Geneeskunde,  
volgens besluit van het College voor Promoties  
te verdedigen op donderdag 29 september 2005  
klokke 14.15 uur

door

**Jorrit Visser**

geboren te Haarlem  
op 15 juni 1976

**Promotiecommissie:**

Promotor: Prof. dr. G. Nienhuis  
Referent: Prof. dr. D. Lenstra (Vrije Universiteit Amsterdam)  
Leden: Prof. dr. J. P. Woerdman  
Prof. dr. C. W. J. Beenakker  
Dr. E. R. Eliel  
Dr. M. P. van Exter  
Prof. dr. P. H. Kes

The work reported in this thesis is part of a research programme of 'Stichting voor Fundamenteel Onderzoek der Materie' (FOM) and was supported by the EU programme ATESIT.

---

## Contents

---

<b>1</b>	<b>Introduction</b>	<b>1</b>
<b>2</b>	<b>Wave description of geometric modes of a resonator</b>	<b>5</b>
2.1	Introduction . . . . .	6
2.2	Operator description for optical systems . . . . .	6
2.3	Propagation of Gaussian beams . . . . .	9
2.4	The modes of an optical resonator . . . . .	11
2.4.1	Resonance condition . . . . .	11
2.4.2	Degeneracy . . . . .	13
2.5	Geometric modes . . . . .	14
2.5.1	Geometric picture . . . . .	14
2.5.2	Displaced state . . . . .	15
2.5.3	Electric field of geometric modes . . . . .	15
2.6	Special limiting cases . . . . .	16
2.7	Conclusions . . . . .	18
<b>3</b>	<b>The spectrum of a resonator with spherical aberration</b>	<b>19</b>
3.1	Introduction . . . . .	20
3.2	Operator description for Gaussian wave optics . . . . .	20
3.3	Matrix representation and ray optics . . . . .	22
3.4	Iwasawa decomposition . . . . .	23
3.5	Spectrum of a resonator without aberrations . . . . .	24
3.5.1	Lens guide . . . . .	24
3.5.2	Hamiltonian for half a round trip . . . . .	25
3.5.3	Spectrum and degeneracy . . . . .	27
3.6	Spectrum in the presence of aberrations . . . . .	28
3.6.1	Spherical aberration . . . . .	28

Contents

3.6.2	Perturbation Hamiltonian due to aberrations . . . . .	28
3.6.3	Spectrum in the presence of spherical aberration . . . . .	30
3.7	Conclusions . . . . .	31
<b>4</b>	<b>Orbital angular momentum of general astigmatic modes</b>	<b>33</b>
4.1	Introduction . . . . .	34
4.2	The fundamental mode . . . . .	35
4.2.1	Gaussian beam . . . . .	35
4.2.2	Propagation . . . . .	36
4.2.3	Gouy phase . . . . .	38
4.2.4	Orbital angular momentum . . . . .	38
4.3	Operator method . . . . .	40
4.3.1	Coordinate picture . . . . .	40
4.3.2	Momentum picture . . . . .	41
4.4	Properties of modes . . . . .	42
4.4.1	Propagation of the fundamental mode . . . . .	42
4.4.2	Higher-order modes in one transverse plane . . . . .	44
4.4.3	Propagation of the higher-order modes . . . . .	49
4.5	Orbital angular momentum of the higher-order modes . . . . .	51
4.5.1	Orbital angular momentum of astigmatic modes . . . . .	51
4.5.2	Simple expression for the orbital angular momentum . . . . .	52
4.5.3	Significance of the contributions to the orbital angular momentum . . . . .	54
4.6	Conclusions and discussion . . . . .	55
<b>5</b>	<b>Vortices in Gaussian light beams</b>	<b>57</b>
5.1	Introduction . . . . .	58
5.2	Vortices in general astigmatic beams . . . . .	58
5.2.1	Beam profile . . . . .	58
5.2.2	Position of the vortices . . . . .	61
5.2.3	Charge and morphology . . . . .	61
5.3	Vortices imposed on Gaussian beams . . . . .	62
5.3.1	Position of the vortex . . . . .	62
5.3.2	Change of the vortex charge . . . . .	64
5.3.3	Interaction between vortices . . . . .	64
5.4	Dark rays . . . . .	66
5.4.1	Propagation through lens guide . . . . .	66
5.4.2	Change in the propagation direction of the vortex . . . . .	67
5.4.3	Vortex modes of a resonator at degeneracy . . . . .	68
5.5	Conclusions . . . . .	70
<b>6</b>	<b>Using paraxial quantum operators</b>	<b>71</b>
6.1	Introduction . . . . .	72
6.2	Paraxial operators . . . . .	73
6.2.1	Electric-field operator . . . . .	73
6.2.2	Interpretation of the paraxial creation operator . . . . .	75

6.3	Spontaneous parametric down-conversion . . . . .	76
6.3.1	Two-photon state . . . . .	76
6.3.2	Coincidence detection rate . . . . .	78
6.4	Quantum erasing . . . . .	79
6.4.1	Scheme . . . . .	79
6.4.2	Transfer functions . . . . .	80
6.4.3	The two cases . . . . .	81
6.5	Conclusions . . . . .	82
<b>7</b>	<b>Interference between entangled photon states in space and time</b>	<b>85</b>
7.1	Introduction . . . . .	86
7.2	Two-photon state . . . . .	87
7.3	Spatial entanglement . . . . .	89
7.3.1	Spatial interferometer . . . . .	89
7.3.2	The coincidence detection rate . . . . .	89
7.4	Temporal entanglement . . . . .	94
7.5	Conclusions . . . . .	98
<b>8</b>	<b>Polarisation entanglement in a crystal with three-fold symmetry</b>	<b>99</b>
8.1	Introduction . . . . .	100
8.2	Representation of the two-photon polarisation state on the Poincaré sphere . . . . .	100
8.2.1	Single-photon polarisation states . . . . .	100
8.2.2	Two-photon polarisation states . . . . .	101
8.2.3	Intrinsic angular momentum associated with polarisation . . . . .	102
8.3	Symmetry properties of the susceptibility tensor . . . . .	103
8.3.1	Invariances of the susceptibility . . . . .	103
8.3.2	Rotations and spherical basis . . . . .	104
8.3.3	Non-vanishing spherical components of $\chi^{(2)}$ . . . . .	105
8.3.4	Transverse part of $\chi^{(2)}$ . . . . .	106
8.4	SPDC in a crystal with $C_{3v}$ symmetry . . . . .	106
8.4.1	Hamiltonian . . . . .	106
8.4.2	Representation on the Poincaré sphere . . . . .	107
8.4.3	Intrinsic angular momentum . . . . .	110
8.5	Conclusions . . . . .	110
8.A	Interchangeability of detected and projected states . . . . .	111
<b>9</b>	<b>Quantum-trajectory description of laser noise with pump depletion</b>	<b>113</b>
9.1	Introduction . . . . .	114
9.2	Optical Bloch equations . . . . .	115
9.2.1	Laser model . . . . .	115
9.2.2	The fraction of atoms needed for lasing . . . . .	116
9.2.3	Spectrum of intensity fluctuations . . . . .	117
9.3	Quantum trajectories . . . . .	117
9.3.1	Model description . . . . .	117
9.3.2	Statistics of cycle trajectories . . . . .	118

Contents

9.3.3	Cycle time of the gain trajectory . . . . .	120
9.3.4	Dynamics of a laser . . . . .	122
9.3.5	Intensity fluctuations . . . . .	122
9.4	Semi-classical rate equations . . . . .	124
9.4.1	Steady state . . . . .	124
9.4.2	Intensity fluctuations . . . . .	126
9.5	Conclusions . . . . .	129
9.A	Mandel Q parameter . . . . .	129
	<b>Bibliography</b>	<b>131</b>
	<b>Samenvatting</b>	<b>137</b>
	<b>List of publications</b>	<b>145</b>
	<b>Curriculum vitae</b>	<b>147</b>
	<b>Nawoord</b>	<b>149</b>

# CHAPTER 1

---

## Introduction

---

Before the derivation of the Maxwell equations light was already well-understood. According to Huygens' principle (1678), every point of a wave front of light can be considered as a point source, from which spherical waves emanate. The envelope of all these spherical waves is then the wave front at a later instant. In this way reflection and refraction can be understood. Fresnel postulated that the spherical waves from these point sources interfere. This construction, which is now known as the Huygens-Fresnel principle, explains diffraction and interference very well.

For a monochromatic light beam propagating in the positive  $z$  direction, the field in the transverse plane  $z = z'$  is described by the profile function  $u(x', y', z')$ . According to the Huygens-Fresnel principle, each point in this plane can be considered as a point source, of which the strength and phase is described by  $u(x', y', z')$ . The light field at the position  $\vec{r} = (x, y, z)$  is then given by

$$u(x, y, z) \propto \int dx' \int dy' \frac{\exp(ik \|\vec{r} - \vec{r}'\|)}{\|\vec{r} - \vec{r}'\|} u(x', y', z'), \quad (1.1)$$

where  $\vec{r}' = (x', y', z')$  and where  $k$  is the wavenumber. The flaw in the Huygens-Fresnel principle is that the spherical waves emanating from the point sources have no preferred direction, so that the light beam described by  $u(x, y, z)$  has no well-defined direction. This problem is solved by the inclination factor in the Fresnel-Kirchhoff diffraction theory, which appears inside the integrals in Eq. (1.1) and favours those parts of the spherical waves that propagate in the forward direction [1].

It follows from the Maxwell equations that the electric field in vacuum satisfies the wave equation. For light beams the propagation direction is well-defined and it is allowed to apply the paraxial approximation, which gives rise to the paraxial wave equation for the profile  $u(x, y, z)$  of a monochromatic light beam. When the light beam propagates in the positive  $z$

## 1. Introduction

direction the paraxial wave equation is given by

$$\left( \frac{\partial^2}{\partial x^2} + \frac{\partial^2}{\partial y^2} + 2ik \frac{\partial}{\partial z} \right) u(x, y, z) = 0. \quad (1.2)$$

When the profile of the light beam in the plane  $z = z'$  is given by  $u(x', y', z')$ , the profile at the position  $\vec{r} = (x, y, z)$  is given by

$$u(x, y, z) = \frac{2\pi k}{i(z-z')} \int dx' \int dy' \exp \left\{ \frac{ik}{2(z-z')} [(x-x')^2 + (y-y')^2] \right\} u(x', y', z'). \quad (1.3)$$

It can be checked that this is a solution by inserting the expression for  $u(x, y, z)$  into the paraxial wave equation in Eq. (1.2).

In a paraxial description of the spherical waves that emanate from the point sources in the Huygens-Fresnel picture, only those parts of the spherical waves are taken into account that propagate almost parallel to the light beam, in the positive  $z$  direction. This means that in Eq. (1.1) only the values  $z > z'$  are used and that the following approximation is valid:

$$\|\vec{r} - \vec{r}'\| = \sqrt{(x-x')^2 + (y-y')^2 + (z-z')^2} \approx (z-z') + \frac{(x-x')^2 + (y-y')^2}{2(z-z')}. \quad (1.4)$$

This approximation is used for the term  $\|\vec{r} - \vec{r}'\|$  that appears in the rapidly-oscillating exponential term in Eq. (1.1), while  $\|\vec{r} - \vec{r}'\|$  is replaced by  $(z-z')$  in the numerator. Then the integral solution of the paraxial wave equation (1.3) is recovered. Besides this relation with the Huygens-Fresnel principle, the paraxial wave equation is also identical in form to the Schrödinger equation for a free particle in two spatial dimensions. This demonstrates the strong analogy between optics and quantum mechanics.

The paraxial wave equation is central in most of this thesis. The paraxial wave equation is considered from a quantum-mechanical perspective, where the propagation of a light beam is described by applying an operator to the "state" of the light beam. Still, the description of the light beam is completely classical. The advantage of this operator description of light beams becomes evident in the following Chapters:

- In Chapter 2 an operator description is developed for the propagation of a light beam through a Gaussian optical system. By defining ladder operators a basis of eigenstates of the optical system is obtained. The result is applied to describe geometric modes in degenerate resonators.
- In Chapter 3 the spectrum of a two-mirror resonator is obtained in the presence of the spherical aberration of the mirrors. The spherical aberration is treated by using perturbation theory as in quantum mechanics.
- In Chapter 4 the operator description is used to obtain basis sets of modes of free space, where astigmatic beams are included. The orbital angular momentum of the modes, which arises due to the astigmatism of the beam and due to the presence of phase singularities, is calculated.

- In Chapter 5 the vortices, or phase singularities, which appear naturally in the modes of free space derived in Chapter 4 are studied. By imposing vortices on Gaussian beams, the propagation of and interaction between vortices is studied.

The paraxial wave equation also plays an important role in the description of experiments with twin photons, since in these experiments twins are selected of which the photons have well-defined directions of propagation. Because these experiments are in the single-photon regime, a description is required that is both quantum mechanical and paraxial. In the following Chapters we obtain such a description and apply it to study twin photons:

- In Chapter 6 we define paraxial creation and annihilation operators of photons in paraxial modes. The electric-field operator is written in terms of these operators and the paraxial approximation is applied. It is shown how to use the results in a description of twin-photon experiments.
- In Chapter 7 the similarity between the temporal and spatial entanglement of the photons of a twin is discussed using the paraxial creation and annihilation operators.
- In Chapter 8 the polarisation entanglement of twin photons is studied, where the symmetry of the non-linear crystal in which the twins are created is important.

Finally, in the last Chapter an operator method is employed to describe the dynamics of a laser system:

- In Chapter 9 a quantum-trajectory description is used to understand the dynamics of a single atom in the gain medium of a laser. The intensity fluctuations of the laser are studied in the depleted-pump regime.

With the exception of Chapter 5, all the Chapters are independent and can be read separately. As a consequence, there is some overlap between Chapters. Although within a Chapter each physical quantity has a unique symbol, some symbols are used for different physical quantities in different Chapters.

1. Introduction

## CHAPTER 2

---

### Wave description of geometric modes of a resonator

---

*By using both an operator and a geometric argument we obtain a wave description of geometric modes of a degenerate optical resonator. This is done by considering the propagation of a displaced Gaussian beam inside the resonator. The round-trip Gouy phase, which is independent of the wavelength of the light, determines the properties of the Gaussian eigenmode. The extra freedom in the case of degeneracy allows for the existence of geometric modes.*

*J. Visser, N. J. Zelders, and G. Nienhuis, accepted for publication in J. Opt. Soc. Am. A..*

## 2.1 Introduction

The propagation of light waves is described by the wave equation, which can be derived from the Maxwell equations. If the propagation direction of a light wave is well determined, which is the case for light beams, the paraxial approximation can be applied, giving rise to the paraxial wave equation [2], which is similar in form to the Schrödinger equation for a free particle in two dimensions. This suggests that an operator method can be used to describe the propagation of a light beam and obtain the modes of free space [3] (see also Chapter 4). Also, the propagation through other Gaussian optical elements, such as a lens, can be incorporated into the operator description [4–6].

By unfolding a stable resonator into a lens guide, the operator formalism can also be used to study the eigenmodes of a resonator. It is well-known that the eigenvalues of the round-trip ABCD matrix of the resonator, which describes the change in the position and slope of a ray after a round trip, determine the round-trip Gouy phase of the Gaussian eigenmode of the resonator [7]. When the Gouy phase is  $2\pi K/N$ , where  $K$  and  $N$  are integers with no common divisor, the resonator is  $N$ -fold degenerate, and any ray retraces itself after  $N$  round trips. This defines a geometric mode [8]. Also, any Gaussian beam transforms into itself after  $N$  round trips, which follows from the ABCD law [9]. This indicates that a displaced Gaussian beam transforms into itself after  $N$  round trips, where the centre of the Gaussian beam follows the trajectory of a ray. By using both an operator and a geometric argument, we obtain a wave description of geometric modes by considering the propagation of a displaced Gaussian beam inside an  $N$ -fold degenerate resonator. The advantage of our description is that there is a clear physical picture, which is lacking in the description of geometric modes by Chen *et al.*, who use an analogy with spin-coherent states [10].

In Section 2.2 we develop the operator method for the description of light beams propagating inside an optical system. We introduce the displacement operator, which shifts and tilts a beam, and show that the centre of the displaced beam follows the trajectory of a ray. In Section 2.3 we define ladder operators that generate the fundamental and higher-order Gaussian eigenmodes of the optical system. The evolution of these ladder operators is also governed by the ABCD matrix of the optical system, from which the ABCD law follows immediately. In Section 2.4 we apply the operator method to obtain the eigenmodes of a two-mirror resonator and consider the case of degeneracy. In Section 2.5 we obtain a wave description of geometric modes by using a simple geometric argument. In Section 2.6 we briefly discuss some peculiar resonator configurations, such as the symmetric confocal resonator.

## 2.2 Operator description for optical systems

The real electric field of a monochromatic light beam that propagates in the positive  $z$  direction is taken as  $\text{Re}[\vec{\epsilon} E(R, z, t)]$ , where  $R = (x, y)$  is the transverse coordinate vector. In this expression  $\vec{\epsilon}$  is the normalised polarisation vector, and  $E$  the complex electric field, which is related to the normalised beam profile  $u(R, z)$  by

$$E(R, z, t) = E_0 u(R, z) \exp(ikz - i\omega t), \quad (2.1)$$

where  $E_0$  is the complex amplitude of the field. The polarisation will be assumed uniform throughout this Chapter, and polarisation effects are not considered. Equation (2.1) is inserted into the scalar wave equation, and it is assumed that  $|\partial u/\partial z| \ll ku$ , which means that the profile  $u(R, z)$  varies only slowly with  $z$ . Then the profile  $u(R, z)$  satisfies the paraxial wave equation [2]:

$$\left( \frac{\partial^2}{\partial R^2} + 2ik \frac{\partial}{\partial z} \right) u(R, z) = 0, \quad (2.2)$$

where  $\partial^2/\partial R^2 = \partial^2/\partial x^2 + \partial^2/\partial y^2$ . The paraxial wave equation is identical in form to the Schrödinger equation for a free particle in two dimensions, where time plays the role of the longitudinal coordinate  $z$ . This similarity is the starting point for an operator description of the propagation of a monochromatic light beam through an optical system containing Gaussian optical elements that are lossless and non-astigmatic [4–6]. Examples of optical elements are the propagation through vacuum, lenses and mirrors.

The transverse profile  $u(R, z) = \langle R|u(z)\rangle$  of the light beam corresponds to the time-dependent wave function in quantum mechanics, and  $|u(z)\rangle$  is the "state" of the light beam in the transverse plane  $z$ . The propagation through vacuum is described by

$$|u(z)\rangle = \hat{U}_f(z)|u(0)\rangle, \quad \hat{U}_f(z) = \exp\left(-\frac{iz}{2k}\hat{P}^2\right), \quad (2.3)$$

where  $\hat{P}^2 = \hat{p}_x^2 + \hat{p}_y^2$ . The transverse-momentum operator  $\hat{P}$  takes the form  $-i\partial/\partial R$  in the coordinate representation. When passing through a parabolic lens, the transverse profile of the light beam acquires a phase shift that depends quadratically on the transverse coordinate. It is assumed that the lens is thin, so that the transverse beam profile is constant inside the lens. Then the effect of the lens is described by multiplying the transverse beam profile by a parabolic phase factor. We consider only cases where the optical axis of the lens coincides with the  $z$  axis. When the lens is located in the transverse plane  $z$ , the state of the light beam  $|u(z_+)\rangle$  after the lens is expressed in terms of the state  $|u(z_-)\rangle$  before the lens by

$$|u(z_+)\rangle = \hat{U}_l(f)|u(z_-)\rangle, \quad \hat{U}_l(f) = \exp\left(-\frac{ik}{2f}\hat{R}^2\right), \quad (2.4)$$

where  $f$  is the focal distance of the lens. We mention that Eq. (2.4) also holds for spherical lenses as long as the approximation of the spherical shape by a parabola is accurate enough within the spot size of the light beam on the lens (which is usually the case for thin lenses). Under this condition the spherical lens can be considered a Gaussian optical element. Now the change of the state of the light beam when going from the input plane to the output plane of the optical system is described by the unitary operator  $\hat{U}$ , which is a product of multiples of  $\hat{U}_f$  and  $\hat{U}_l$  in the proper order, according to the arrangement of the lenses in the optical system. For instance, the optical system in Fig. 2.1, which begins at  $z = 0$  and ends at  $z = 2L$ , has a lens with focal distance  $f_1$  at  $z = 0$  and a lens with focal distance  $f_2$  at  $z = L$ . The evolution operator  $\hat{U}$  for this optical system is equal to

$$\hat{U} = \hat{U}_f(L)\hat{U}_l(f_2)\hat{U}_f(L)\hat{U}_l(f_1). \quad (2.5)$$

We define the displacement operator by

$$\hat{D}(a, q) = \exp\left(iq^T\hat{R} - ia^T\hat{P}\right), \quad (2.6)$$

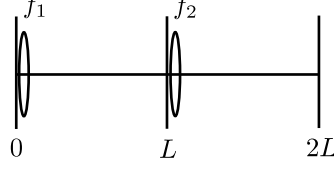


**Figure 2.1:** Optical system stretching from  $z = 0$  to  $z = 2L$ . The lenses have focal distances  $f_1$  and  $f_2$  and are located in the planes  $z = 0$  and  $z = L$ , respectively.

where  $a$  is a position vector in the transverse plane,  $q$  is a transverse momentum vector, and  $q^\top \hat{R}$  indicates the inner product of  $q$  with the transverse coordinate operator  $\hat{R} = (\hat{x}, \hat{y})$ . The significance of the displacement operator becomes clear from its properties:

$$\hat{D}^\dagger(a, q) \hat{R} \hat{D}(a, q) = \hat{R} + a, \quad \hat{D}^\dagger(a, q) \hat{P} \hat{D}(a, q) = \hat{P} + q. \quad (2.7)$$

It follows that when the displacement operator is applied to an arbitrary state  $|u\rangle$ , it displaces the average transverse position (or, in quantum-mechanical language, the expectation value of the transverse coordinate operator) by the vector  $a$  and the average transverse momentum (or the expectation value of the transverse momentum operator) by the vector  $q$ . We require that upon propagation through an optical system the displacement operator evolves in such a way that in the input plane  $z_0$  and output plane  $z_1$  of the optical system we have

$$|v(z_0)\rangle = \hat{D}(a(z_0), q(z_0)) |u(z_0)\rangle, \quad |v(z_1)\rangle = \hat{D}(a(z_1), q(z_1)) |u(z_1)\rangle, \quad (2.8)$$

where  $|v\rangle$  is the displaced state obtained when  $\hat{D}$  is applied to  $|u\rangle$ . Since

$$|v(z_1)\rangle = \hat{U} |v(z_0)\rangle, \quad |u(z_1)\rangle = \hat{U} |u(z_0)\rangle, \quad (2.9)$$

it follows that the displacement operators in the input and output planes are related by

$$\hat{D}(a(z_1), q(z_1)) = \hat{U} \hat{D}(a(z_0), q(z_0)) \hat{U}^\dagger. \quad (2.10)$$

Since the optical elements are Gaussian, the displacement operator at the output plane of the optical system still has the general form (2.6), with different coefficients  $a$  and  $q$ . In order to determine how  $a$  and  $q$  change when going from the input to the output plane of the optical system, we use the following properties:

$$\hat{U}_f(L) \hat{R} \hat{U}_f^\dagger(L) = \hat{R} - \frac{L}{k} \hat{P}, \quad \hat{U}_l(f) \hat{P} \hat{U}_l^\dagger(f) = \hat{P} + \frac{k}{f} \hat{R}, \quad (2.11)$$

where  $\hat{U}_f$  and  $\hat{U}_l$  are given in Eqs. (2.3) and (2.4), respectively. The values of  $a$  and  $q$  after propagation over a distance  $L$  in vacuum, for which we write  $a(L)$  and  $q(L)$ , are expressed in terms of their initial values  $a(0)$  and  $q(0)$  by

$$\begin{pmatrix} a(L) \\ q(L)/k \end{pmatrix} = \begin{pmatrix} 1 & L \\ 0 & 1 \end{pmatrix} \begin{pmatrix} a(0) \\ q(0)/k \end{pmatrix}. \quad (2.12)$$

For passage through a lens in the transverse plane  $z$ , the values of  $a(z_+)$  and  $q(z_+)$  immediately after the lens are expressed in terms of their incoming values  $a(z_-)$  and  $q(z_-)$  by

$$\begin{pmatrix} a(z_+) \\ q(z_+)/k \end{pmatrix} = \begin{pmatrix} 1 & 0 \\ -1/f & 1 \end{pmatrix} \begin{pmatrix} a(z_-) \\ q(z_-)/k \end{pmatrix}. \quad (2.13)$$

We see that these matrices correspond to the ABCD matrices for the description of the change in position and slope of a light ray propagating over a distance  $L$  and passing through a lens with focal distance  $f$ , as discussed by Siegman [7]. In the paraxial approximation the value  $q/k$ , which is the transverse momentum divided by the total momentum, can indeed be interpreted as a slope. It follows that, upon propagation through the optical system,  $a$  and  $q/k$  transform in the same way as the position and slope of a light ray, respectively. For a general Gaussian optical system, the ABCD matrix is a  $4 \times 4$  matrix, but since the optical systems that we consider are cylindrical, it is sufficient to use  $2 \times 2$  matrices, since for the two components of the transverse vectors  $a$  and  $q$  the transformation is identical. For a Gaussian optical system, the ABCD matrix, which describes the propagation from the input plane  $z_0$  to the output plane  $z_1$ , completely determines the corresponding evolution operator  $\hat{U}$  within a phase factor, and vice versa. In general we have

$$\begin{pmatrix} a(z_1) \\ q(z_1)/k \end{pmatrix} = \begin{pmatrix} A & B \\ C & D \end{pmatrix} \begin{pmatrix} a(z_0) \\ q(z_0)/k \end{pmatrix}. \quad (2.14)$$

As a consequence, complete knowledge of a Gaussian optical system can be obtained by probing it with two light rays, for which either the position or the slope is zero in the input plane. Then the matrix elements of the ABCD matrix are determined by the positions and slopes of the two rays at the output plane of the optical system.

### 2.3 Propagation of Gaussian beams

Well-known solutions of the paraxial wave equation are the Hermite-Gaussian (HG) beams, which are also eigenmodes of a two-mirror resonator. They resemble the eigenfunctions of the two-dimensional quantum harmonic oscillator [11], which can be explained by using an operator method involving ladder operators, as we will briefly discuss. We saw that upon propagation through a Gaussian optical system, the displacement operator retains the form (2.6), where the propagation is contained in the variation of the coefficients  $a$  and  $q$ . The transformation rules (2.11) show that linear combinations of  $\hat{R}$  and  $\hat{P}$  remain linear combinations upon propagation through an optical system. The propagation is contained in coefficients  $\kappa$  and  $\beta$ , which behave in a similar fashion as  $q$  and  $a$ . These coefficients define a vector  $\hat{A}$  of two lowering operators  $\hat{a}_x$  and  $\hat{a}_y$  in an arbitrary transverse plane by

$$\hat{A} = \frac{1}{\sqrt{2}} (\kappa \hat{R} + i\beta \hat{P}), \quad (2.15)$$

where the coefficients  $\kappa$  and  $\beta$  are complex numbers. The corresponding vector  $\hat{A}^\dagger$  of raising operators  $\hat{a}_x^\dagger$  and  $\hat{a}_y^\dagger$  is given by

$$\hat{A}^\dagger = \frac{1}{\sqrt{2}} (\kappa^* \hat{R} - i\beta^* \hat{P}). \quad (2.16)$$

The ladder operators must satisfy the usual bosonic commutation rules:

$$[\hat{a}_x, \hat{a}_x^\dagger] = [\hat{a}_y, \hat{a}_y^\dagger] = 1, \quad [\hat{a}_x, \hat{a}_y] = [\hat{a}_x, \hat{a}_y^\dagger] = 0. \quad (2.17)$$

These commutation rules are satisfied when

$$\text{Re}(\kappa\beta^*) = 1. \quad (2.18)$$

We require that the ladder operators transform solutions of the paraxial wave equation into other solutions. When the state  $|u(z_0)\rangle$  in the input plane gives the state  $|u(z_1)\rangle$  in the output plane of the optical system, this implies that an input state  $\hat{A}(z_0)|u(z_0)\rangle$  leads to the output state  $\hat{A}(z_1)|u(z_1)\rangle$ . This gives

$$\hat{A}(z_1) = \hat{U}\hat{A}(z_0)\hat{U}^\dagger, \quad (2.19)$$

which is identical to the transformation property of the displacement operator in Eq. (2.10). It follows that the coefficients  $\beta$  and  $i\kappa/k$  transform in the same way as  $a$  and  $q/k$  in Eq. (2.14), so that

$$\begin{pmatrix} \beta(z_1) \\ i\kappa(z_1)/k \end{pmatrix} = \begin{pmatrix} A & B \\ C & D \end{pmatrix} \begin{pmatrix} \beta(z_0) \\ i\kappa(z_0)/k \end{pmatrix}. \quad (2.20)$$

By using the ladder operators, we obtain a complete set of Gaussian beam profiles. In an arbitrary transverse plane, the lowest-order Gaussian beam profile  $u_{00}(R) = \langle R|u_{00}\rangle$  is defined by

$$\hat{A}|u_{00}\rangle = 0. \quad (2.21)$$

It follows that

$$u_{00}(R) = \frac{1}{\beta\sqrt{\pi}} \exp\left(-\frac{\kappa}{2\beta}R^2\right), \quad (2.22)$$

which is normalised to unity, as can be checked by using Eq. (2.18). Because of the propagation property of  $\hat{A}$  in Eq. (2.19), this expression is valid in both the input and output planes of the optical system, as long as the values for  $\kappa$  and  $\beta$  that they acquire in the plane under consideration are taken.

We verify that in a region of free propagation, with the proper values of  $\kappa$  and  $\beta$ , Eq. (2.22) satisfies the paraxial wave equation (2.2). From the ABCD matrix for free propagation, as specified in Eq. (2.12), it follows with Eq. (2.20) that  $\kappa$  is independent of  $z$  and that  $d\beta/dz = i\kappa/k$ . This shows that the lowest-order Gaussian beam  $u_{00}(R, z)$  indeed satisfies the paraxial wave equation. It is customary to introduce for each transverse plane the complex parameter  $Q$ , defined by [7, 9]

$$\frac{1}{Q} = \frac{i\kappa}{k\beta} = \frac{1}{S} + i\frac{1}{k\gamma^2}, \quad (2.23)$$

where  $S$  is the radius of curvature of the wavefront and  $\gamma$  is the spot size. It follows from Eq. (2.20) that the evolution of  $Q$  from the input plane  $z_0$  to the output plane  $z_1$  of the optical system is simply expressed by

$$Q(z_1) = \frac{AQ(z_0) + B}{CQ(z_0) + D}, \quad (2.24)$$

which is known as the ABCD law [9]. Using Eq. (2.18), we find that  $\gamma = |\beta|$ . Moreover, Eq. (2.23) demonstrates that the exponential in the fundamental mode profile (2.22) separates into a curvature factor  $\exp(ikR^2/2S)$  and a real Gaussian  $\exp(-R^2/2\gamma^2) = \exp(-R^2/2|\beta|^2)$ .

We now wish to apply the raising operators to obtain the higher-order Gaussian beam profiles. We use the following property:

$$\exp\left(\frac{ik}{2S}\hat{R}^2\right)\hat{P}\exp\left(-\frac{ik}{2S}\hat{R}^2\right) = \hat{P} - \frac{k}{S}\hat{R}, \quad (2.25)$$

where  $S$  is the radius of curvature defined in Eq. (2.23). With this property the vector of raising operators in Eq. (2.16) can be written as

$$\hat{A}^\dagger = \sqrt{\frac{\beta^*}{\beta}} \exp\left(\frac{ik}{2S}\hat{R}^2\right) \hat{B}^\dagger \exp\left(-\frac{ik}{2S}\hat{R}^2\right), \quad (2.26)$$

where  $\hat{B}^\dagger$  is a vector of real raising operators, defined by

$$\hat{B}^\dagger = \frac{1}{\sqrt{2}} \left( \frac{1}{|\beta|} \hat{R} - i|\beta| \hat{P} \right). \quad (2.27)$$

This can be checked by using Eq. (2.23) and the relation  $\gamma = |\beta|$ . The higher-order Gaussian beam profiles are obtained in the standard way by repeated application of the raising operators expressed as in Eq. (2.26). We have

$$|u_{nm}\rangle = \frac{1}{\sqrt{n!m!}} (\hat{a}_x^\dagger)^n (\hat{a}_y^\dagger)^m |u_{00}\rangle, \quad n, m = 0, 1, 2, \dots \quad (2.28)$$

The operator  $\hat{B}^\dagger$  in (2.27) has the form that is familiar from the quantum-mechanical description of the 2D harmonic oscillator, and it produces the higher-order eigenfunctions when acting on the real Gaussian ground state  $\propto \exp(-R^2/2|\beta|^2)$ . The higher-order Gaussian beam profiles  $u_{nm}(R) = \langle R | u_{nm} \rangle$  are the familiar HG beam profiles

$$u_{nm}(R) = \frac{1}{|\beta| \sqrt{n!m! 2^{n+m} \pi}} \left( \frac{\beta^*}{\beta} \right)^{\frac{1}{2}(n+m+1)} H_n\left(\frac{x}{|\beta|}\right) H_m\left(\frac{y}{|\beta|}\right) \exp\left(-\frac{\kappa}{2\beta} R^2\right), \quad (2.29)$$

where

$$H_n(\xi) = \exp(\xi^2/2) \left( \xi - \frac{\partial}{\partial \xi} \right)^n \exp(-\xi^2/2), \quad n = 0, 1, 2, \dots, \quad (2.30)$$

are the Hermite polynomials. Again, the propagation property of  $\hat{A}$  in Eq. (2.19) guarantees that, with the appropriate values of  $\kappa$  and  $\beta$ , this expression is valid in both the input and output planes of the optical system.

## 2.4 The modes of an optical resonator

### 2.4.1 Resonance condition

As we will demonstrate in this Section, by using the operator method developed in Section 2.3 we can obtain the frequency spectrum and the eigenmodes of a cylindrical optical resonator.

We consider an optical resonator of length  $L$ , with end mirrors with focal distances  $f_1$  and  $f_2$ , located at  $z = 0$  and  $z = L$ . When we unfold the resonator into an equivalent lens guide, we obtain the system displayed in Fig. 2.1, with length  $2L$ . The corresponding evolution operator (2.5) represents the round-trip operator of the resonator, with the input plane of mirror 1 as reference plane. An eigenmode of the resonator must reproduce itself after a round trip, which implies that the corresponding field in the input plane of the lens guide is an eigenstate of the operator (2.5). When the transverse profile of the field propagating to the right in the lens guide is described by the function  $u(R, z)$ , with  $0 \leq z \leq 2L$ , then the complex electric field in the resonator is

$$E(R, z, t) = E_0 \{ u(R, z) \exp(ikz) - u(R, 2L - z) \exp[ik(2L - z)] \} \exp(-i\omega t), \quad (2.31)$$

for  $0 \leq z \leq L$ . The real electric field vanishes on the end mirrors at  $z = 0$  and  $z = L$ .

The eigenstates of the operator (2.5) can be found from the ABCD matrix  $M$  for the lens guide, which is identical to the ABCD matrix for the round trip in the resonator, starting in the input plane of mirror 1. A resonator is stable when the eigenvalues of  $M$  have unit absolute values [7]. Since  $M$  is a real matrix with unit determinant, one of the eigenvalues is then the complex conjugate of the other and one eigenvector is the complex conjugate of the other. The special case where the eigenvalues are identical, and therefore real, will be considered in Section 2.6. For complex eigenvectors of  $M$  there exists no ray that transforms into itself after one round trip, since rays are described by the real position and slope. We saw in Section 2.3 that the evolution of the parameters  $\kappa$  and  $\beta$ , which determine the ladder operators, is also governed by  $M$ , as expressed by Eq. (2.20). It is possible to find values  $\kappa_0$  and  $\beta_0$  for which

$$M \begin{pmatrix} \beta_0 \\ i\kappa_0/k \end{pmatrix} = \exp(i\chi) \begin{pmatrix} \beta_0 \\ i\kappa_0/k \end{pmatrix}, \quad (2.32)$$

where  $\exp(i\chi)$  is one of the eigenvalues of  $M$  and where  $\kappa_0$  and  $\beta_0$  satisfy Eq. (2.18). Apart from a phase factor this defines in a unique way the lowering operator  $\hat{A}_0$ , which transforms into itself after a round trip [12]. By introducing

$$\hat{A}_0 = \frac{1}{\sqrt{2}} (\kappa_0 \hat{R} + i\beta_0 \hat{P}), \quad (2.33)$$

we find from Eq. (2.20) that

$$\hat{U} \hat{A}_0 \hat{U}^\dagger = \exp(i\chi) \hat{A}_0, \quad (2.34)$$

where  $\hat{U}$  is the evolution operator for the round trip. The corresponding raising operator  $\hat{A}_0^\dagger$  is determined by the other eigenvector of  $M$ . The Hermitian conjugate of (2.34) expresses the round-trip evolution of  $\hat{A}_0^\dagger$ . We see that although the round-trip matrix  $M$  has two eigenvectors, there is only one Gaussian fundamental mode, since only one of the eigenvectors can correspond to a lowering operator.

With the values  $\kappa_0$  and  $\beta_0$ , the HG profiles in (2.29), which we will designate by  $u_{nm}(R; \kappa_0, \beta_0)$ , transform into themselves after a round trip up to a phase factor. It follows that  $u_{nm}(R; \kappa_0, \beta_0)$  are the transverse profiles  $u(R)$  of the eigenmodes of the resonator in the input plane of mirror 1. To find the profiles in a different transverse plane we must obtain the ABCD matrix for the propagation in the allowed direction to this plane. Then the values that

$\kappa$  and  $\beta$  acquire in that plane are obtained from Eq. (2.20), and the mode profiles are found by using Eq. (2.29).

After a round trip  $\beta_0$  picks up a phase factor  $\exp(i\chi)$ . We see then from Eq. (2.22) that after a round trip the fundamental mode profile acquires a phase factor  $\exp(-i\chi)$ , which is the round-trip Gouy phase. This Gouy phase is completely determined by the characteristics of the resonator, since it is an eigenvalue of the round-trip ABCD matrix. It follows from Eq. (2.29) that

$$\hat{U}|u_{nm}(\kappa_0, \beta_0)\rangle = \exp[-i(n+m+1)\chi]|u_{nm}(\kappa_0, \beta_0)\rangle. \quad (2.35)$$

Without loss of generality we have left out the overall phase of  $\hat{U}$  in this expression. Taking into account the phase due to the plane-wave part of the electric field in Eq. (2.1), we obtain the well-known resonance condition [7]:

$$2kL = (n+m+1)\chi + 2\pi l, \quad (2.36)$$

where  $l$  is an integer and  $2L$  is the length of the lens guide. The integer  $l$  has the significance of the longitudinal mode number, which determines the number  $l+1$  of transverse nodal planes.

## 2.4.2 Degeneracy

It is clear from Eq. (2.36) that the eigenmodes with mode numbers  $n$  and  $m$  for which  $n+m$  attains the same value are degenerate. Any linear combination of eigenmodes with the same value of  $n+m$  is also an eigenmode of the resonator. These can be Laguerre-Gaussian (LG) modes or modes that are between LG and HG modes [13–16].

When the Gouy phase takes the value

$$N\chi = 2\pi K, \quad (2.37)$$

where  $N$  and  $K$  are integers, it follows from Eq. (2.36) that eigenmodes with mode numbers  $n$  and  $m$  for which  $n+m$  differs by a multiple of  $N$  are degenerate. When  $n+m$  is increased by  $N$  and  $l$  is decreased by  $K$ , the resonance condition is satisfied for the same wavenumber  $k$ . Without loss of generality we can assume that  $N$  and  $K$  have no common divisor. In that case there are no other modes with the same wavenumber. When the condition of degeneracy (2.37) is satisfied, we have  $M^N = 1$  and, equivalently,  $\hat{U}^N = 1$ , where a possible overall phase of  $\hat{U}$  is left out for simplicity. Then the eigenvalues of the unitary operator  $\hat{U}$  belong to the finite set of  $N$  values  $\exp(-2\pi is/N)$ , with  $s = 0, 1, \dots, N-1$ .

It is illuminating to identify  $N$  projection operators  $\hat{V}_s$  on the subspaces of transverse eigenmodes with eigenvalue  $\exp(-2\pi is/N)$ . These operators can be expressed as

$$\hat{V}_s = \frac{1}{N} \sum_{r=0}^{N-1} \exp\left(\frac{2\pi irs}{N}\right) \hat{U}^r, \quad s = 0, 1, \dots, N-1. \quad (2.38)$$

From direct substitution it follows that

$$\hat{U}\hat{V}_s = \exp\left(-\frac{2\pi is}{N}\right) \hat{V}_s, \quad (2.39)$$

which shows that for an arbitrary state  $|u\rangle$  the state  $\hat{V}_s|u\rangle$  is an eigenstate of the round-trip operator  $\hat{U}$ , with eigenvalue  $\exp(-2\pi is/N)$ . Moreover, the set of operators  $\hat{V}_s$  with  $s = 0, 1, \dots, N-1$  is complete, in the sense that the operators add up to the unit operator. From Eqs. (2.35) and (2.37) one checks that  $\hat{V}_s|u_{nm}(\kappa_0, \beta_0)\rangle = |u_{nm}(\kappa_0, \beta_0)\rangle$ , provided that  $\exp[-2\pi i(n+m+1)K/N] = \exp(-2\pi is/N)$ . This implies that

$$K(n+m+1) = pN + s, \quad (2.40)$$

with  $p$  an integer. The corresponding values of  $n+m$  differ by a multiple of  $N$  and define modes with wavenumbers specified by the resonance condition

$$2kL = 2\pi l' + 2\pi s/N, \quad (2.41)$$

with  $l' = l + p$ . The resonant wavenumbers (2.41) form an equidistant mesh with separation determined by  $L\Delta k = \pi/N$ , which is  $1/N$  times the free spectral range of the resonator with length  $L$ .

## 2.5 Geometric modes

### 2.5.1 Geometric picture

The structure of the projection operators (2.38) can be understood directly from a geometric picture of modes in the resonator. We consider the lens guide in Fig. 2.2, which consists of a sequence of  $N$  times the unfolded resonator of Fig. 2.1 and thus stretches from  $z = 0$  to  $z = 2NL$ . In the case of degeneracy the round-trip ABCD matrix for the resonator satisfies  $M^N = 1$ . It follows that for the  $N$ -fold lens guide the ABCD matrix is the unit matrix and also that the unitary operator that describes the propagation from the plane  $z = 0$  to the plane  $z = 2NL$  is the unit operator. Therefore any transverse beam profile  $u(R, 0)$  at the plane  $z = 0$  transforms into itself after propagation to the plane  $z = 2NL$ . We write  $u(R, z)$  for the  $z$ -dependent profile, where  $0 \leq z \leq 2NL$ . It follows that  $u(R, 2NL) = u(R, 0)$ . The same periodicity holds for the traveling wave  $\exp(ikz)u(R, z)$ , provided that the wavenumber  $k$  obeys the requirement

$$2kNL = 2\pi s', \quad (2.42)$$

with  $s'$  an integer. When this resonance condition holds, the  $N$ -fold lens guide can be folded into the resonator of length  $L$ , with the complex electric field

$$\begin{aligned} E(R, z, t) = & E_0 \sum_{p=0}^{N-1} u(R, 2pL + z) \exp[ik(2pL + z)] \exp(-i\omega t) \\ & - E_0 \sum_{p=0}^{N-1} u(R, 2(p+1)L - z) \exp[ik(2(p+1)L - z)] \exp(-i\omega t), \end{aligned} \quad (2.43)$$

where now  $0 \leq z \leq L$ . The terms on the first and second line describe the field propagating to the right and the left, respectively. When we compare the requirement (2.42) with the resonance condition for degeneracy in Eq. (2.41), we see that  $s' = s + Nl'$ . When a value

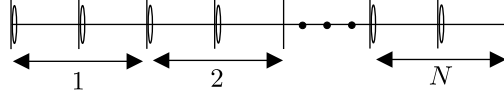


**Figure 2.2:** Lens guide that is a sequence of  $N$  times the unfolded resonator.

of  $s'$  is chosen, the value of  $s$ , which determines the round-trip Gouy phase by Eq. (2.39), is given by  $s' \bmod N$ . Note that the transverse profile  $u(R, 0)$  in the input plane of the lens guide can be freely chosen, within the validity range of the paraxial approximation. The field in the reference plane of the resonator, *i.e.*, the input plane of mirror 1, is specified by the second line in Eq. (2.43), with  $z = 0$ . The resulting expression is equivalent to the action of the projection operator  $\hat{V}_s$ , as defined by Eq. (2.38), on the input field. This proves that the total field in the reference plane of the resonator is an eigenstate of the round-trip operator  $\hat{U}$ , with eigenvalue  $\exp(-2\pi i s/N)$ .

### 2.5.2 Displaced state

We consider the evolution of the displacement operator in the  $N$ -fold lens guide in Fig. 2.2. As discussed in Section 2.2, the displacement operator, as defined in Eq. (2.6), shifts the average transverse position and momentum by  $a$  and  $q$ , respectively. During propagation through the lens guide,  $a$  and  $q/k$  transform in the same way as the position and slope of a ray. We write  $a(z)$  and  $q(z)$  for their values in the plane  $z$ . If for an arbitrary state  $|v(z)\rangle$  the average position and momentum vanish in a plane  $z_0$ , that is, if  $\langle v(z_0)|\hat{R}|v(z_0)\rangle = 0$  and  $\langle v(z_0)|\hat{P}|v(z_0)\rangle = 0$ , then the average transverse position and momentum vanish in any other transverse plane as well. This is because the transformation rules (2.11) of  $\hat{R}$  and  $\hat{P}$  are linear and homogeneous. It follows that the centre of the beam described by the state

$$|u(z)\rangle = \hat{D}(a(z), q(z))|v(z)\rangle, \quad (2.44)$$

follows the trajectory of a ray inside the  $N$ -fold lens guide. In the case of  $N$ -fold degeneracy, we have  $|v(2NL)\rangle = |v(0)\rangle$ ,  $a(2NL) = a(0)$  and  $q(2NL) = q(0)$ . We fold the  $N$ -fold lens guide into a resonator. Then the electric field inside the resonator is described by Eq. (2.43). The electric field is a linear combination of  $2N$  displaced beams, of which  $N$  propagate to the right and  $N$  to the left. When following one of the displaced beams during  $N$  round trips, the displaced beam transforms into another displaced beam after each round trip, finally to transform into itself after  $N$  round trips. The centre of the displaced beam follows a closed trajectory, which means that the mode is a geometric mode.

### 2.5.3 Electric field of geometric modes

In order to find an expression for the electric field of a geometric mode, it is necessary to obtain an expression for the transverse profile of a displaced state. In an arbitrary plane the displaced state  $|u\rangle$  is defined in terms of the arbitrary state  $|v\rangle$  by

$$|u\rangle = \hat{D}(a, q)|v\rangle. \quad (2.45)$$

In the case in which the commutator of two operators  $\hat{A}$  and  $\hat{B}$  commutes with both  $\hat{A}$  and  $\hat{B}$ , the following relation holds:

$$\exp(\hat{A} + \hat{B}) = \exp\left(-\frac{1}{2}[\hat{A}, \hat{B}]\right) \exp(\hat{A}) \exp(\hat{B}) . \quad (2.46)$$

We use this to express the displacement operator in Eq. (2.6) as

$$\hat{D}(a, q) = \exp(-iq^T a/2) \exp(iq^T \hat{R}) \exp(-ia^T \hat{P}) . \quad (2.47)$$

Using this expression, we find that

$$\langle R | \hat{D} | R' \rangle = \exp(-iq^T a/2) \exp(iq^T R) \delta(R - R' - a) . \quad (2.48)$$

It follows that

$$u(R) = \exp(-iq^T a/2) \exp(iq^T R) v(R - a) . \quad (2.49)$$

Equation (2.49) expresses the transverse profile  $u(R)$  of the displaced state  $|u\rangle$  in terms of the profile  $v(R)$  of the state  $|v\rangle$ .

As an example we consider geometric modes consisting of displaced beams that are obtained by displacing the Gaussian fundamental mode of the resonator  $u_{00}(R; \kappa_0, \beta_0)$ . Then the displaced beams all have the waist in the middle of the resonator. The energy density of a mode is calculated by averaging the square of the real part of the complex electric field over time and over a range of  $z$  of several times the wavelength that is still small enough for the beam profile to be considered constant. Then the energy density is simply the sum of the squared absolute values of the right- and left-propagating parts of the beam profile. It follows that only beams that propagate in the same direction can give rise to interference fringes in the energy density profile. The energy density profiles of two geometric modes are depicted in Fig. 2.3 for three-fold degeneracy. The focal distances of the mirrors are equal to the length of the resonator. The values  $kf_1 = kf_2 = kL = 3\pi \times 10^4$  are used, which correspond to a zero round-trip Gouy phase, as follows from Eq. (2.42) and the discussion below. In the vertical, or transverse, direction, the pictures are magnified by a factor of 4 compared to the horizontal direction, which is parallel to the optical axis. Interference fringes occur at the crossings of beams that propagate in the same direction.

Our expressions for the displaced beams differ from those used by Chen *et al.* [10]. Inspired by the expressions for spin-coherent states, these authors use a finite expansion of HG modes with indices that differ by multiples of the degeneracy number. The weights are binomial and contain arbitrarily chosen parameters. We find expressions for the eigenmodes in which the significance of the parameters is fully specified by the requirement that the beams be displaced Gaussian fundamental modes.

## 2.6 Special limiting cases

In this Section we consider resonators for which the eigenvalues of the round-trip ABCD matrix  $M$  are  $\pm 1$ , so that the Gouy phase  $\chi$  is a multiple of  $\pi$ . Since  $M$  has unit determinant, the eigenvalues must be identical. In order to find the ladder operators that determine the

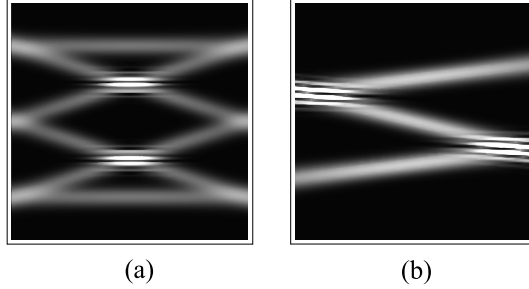


**Figure 2.3:** Energy density profiles of two geometric modes for three-fold degeneracy. The focal distances of both mirrors are equal to the resonator length. In both pictures the transverse or vertical direction is magnified by a factor of 4 compared with the horizontal direction, which is parallel to the optical axis of the resonator. In (a) the geometric mode contains a horizontal beam, while in (b) the beam retraces itself.

eigenmodes of the resonator, we must find the values of  $\kappa_0$  and  $\beta_0$  that satisfy Eq. (2.32). When  $M$  is  $\pm 1$  times the unit matrix, Eq. (2.32) is satisfied for all values of  $\kappa_0$  and  $\beta_0$ . Still, not all values are allowed, since the requirement in Eq. (2.18) must be fulfilled, which follows from the commutation rules for the ladder operators. When  $M$  is not  $\pm 1$  times the unit matrix, it has only one eigenvector. Since  $M$  is a real matrix, this eigenvector must be real. For the eigenvector in Eq. (2.32) to be real,  $\kappa_0$  must be purely imaginary and  $\beta_0$  must be real. It follows that no ladder operators can be defined, since the requirement  $\text{Re}(\kappa_0\beta_0^*) = 1$  in Eq. (2.18) cannot be satisfied. Therefore, when  $M$  has real eigenvalues and is not equal to  $\pm 1$  times the unit matrix, the resonator has no Gaussian eigenmodes. Also, there exists no value of  $N$  for which  $M^N = 1$ . Still, the resonator has one eigenray.

These cases can be illustrated for a symmetric resonator. Then it is sufficient to consider the ABCD matrix for only half the round trip, which corresponds to propagation from the plane  $z = 0$  to the plane  $z = L$  in the lens guide of Fig. 2.1. We write  $f$  for the focal distance of both mirrors. The ABCD matrix  $M_h$  for half the round trip is found by multiplying the lens matrix in Eq. (2.13) on the left by the matrix for free propagation in Eq. (2.12). We find that

$$M_h(g) = \begin{pmatrix} 2g-1 & L \\ -2(1-g)/L & 1 \end{pmatrix}, \quad (2.50)$$

where  $g = 1 - L/2f$  is the  $g$  parameter of the resonator [7]. For stable resonators the eigenvalues  $g \pm i\sqrt{1-g^2}$  of  $M_h(g)$  must have unit absolute values, which means that  $-1 \leq g \leq 1$ . The eigenvalues of the full round-trip ABCD matrix  $M = M_h^2(g)$  are real when  $g$  takes the values 1,  $-1$ , and 0.

When  $g = 1$ , both mirrors of the resonator are flat and the full round-trip ABCD matrix  $M = M_h^2(1)$  is given by

$$M = \begin{pmatrix} 1 & 2L \\ 0 & 1 \end{pmatrix}. \quad (2.51)$$

The real vector  $(1, 0)$  is the only eigenvector of this matrix, with eigenvalue 1, and evidently corresponds to the only eigenray of this resonator, which is a horizontal ray with no slope. As

discussed above in the first paragraph of this Section, this resonator does not sustain Gaussian modes, since the eigenvector is real. It follows then that there are also no geometric modes possible. For the round-trip ABCD matrix  $M$  in Eq. (2.51), there is indeed no value of  $N > 0$  for which  $M^N = 1$ .

In a concentric resonator, for which  $g = -1$ , the surfaces of the spherical mirrors lie on the surface of a sphere. The full round-trip ABCD matrix  $M = M_h^2(-1)$  is given by

$$M = \begin{pmatrix} 5 & -2L \\ 8/L & -3 \end{pmatrix}, \quad (2.52)$$

for which  $(L/2, 1)$  is the only eigenvector, with eigenvalue 1. The corresponding eigenray originates from the centre of the sphere on which the mirror surfaces lie. Again, no appropriate values of  $\kappa_0$  and  $\beta_0$  exist, so that a concentric resonator also does not have Gaussian eigenmodes and hence has no geometric modes.

In a symmetric confocal resonator, for which  $g = 0$ , the focal points of the mirror coincide, and the full round-trip ABCD matrix is  $M = M_h^2(0) = -1$ . Every ray is then an eigenray for a single round trip, with eigenvalue  $-1$ . Also, all values of  $\kappa_0$  and  $\beta_0$  satisfying (2.18) can be used to define ladder operators. As a consequence, every Gaussian beam is an eigenmode of the symmetric confocal resonator. This means that the focal planes of the right- and left-propagating beams do not have to coincide and that, when they do, the waist does not have to be in the middle of the resonator [17]. Because of the two-fold degeneracy, every transverse profile transforms into itself after two round trips, which means that the symmetric confocal resonator does have geometric modes. It follows from Eq. (2.35) that the two eigenspaces of the round-trip evolution operator for eigenvalues  $\pm 1$  are spanned by the HG eigenstates for which  $n + m + 1$  is even and odd, respectively [12].

## 2.7 Conclusions

We used an operator method to study the modes of a resonator. The Gaussian eigenmodes of the resonator were generated by introducing ladder operators. The round-trip Gouy phase of the resonator, which is completely determined by the geometry of the resonator, and therefore independent of the wavelength of the light, determines the properties of the Gaussian eigenmode. The displacement operator was used to create displaced beams, with a centre that follows the trajectory of a ray. For the case of  $N$ -fold degeneracy,  $N$  projection operators were defined that project onto modes of the resonator, each with a different Gouy phase. The geometric argument to obtain modes of the resonator in the case of degeneracy consists of folding a light beam propagating through a sequence of  $N$  times the lens guide of the unfolded resonator back into a resonator. This geometric argument was shown to be equivalent to the operation of one of the projection operators. The beam parameters, such as shape and size of spot and curvature, can be freely chosen in one transverse plane. In the case of degeneracy, when a displaced beam in the sequence of lens guides is folded into a resonator, it gives rise to a geometric mode, which consists of beams that follow a closed trajectory.

## CHAPTER 3

---

### The spectrum of a resonator with spherical aberration

---

*By using an operator description we derive the spectrum of a symmetric two-mirror resonator in the presence of spherical aberration.*

*J. Visser and G. Nienhuis, accepted for publication in J. Opt. Soc. Am. A.*

### 3.1 Introduction

As we saw in Chapter 2, it is convenient to use an operator description to obtain the spectrum of a resonator. It is then necessary that the optical elements in the lens guide of the unfolded resonator are Gaussian. The surface of a mirror in the resonator is then described by a parabola. Due to the production process the surface of the mirrors is usually not parabolic, and there are aberrations. As a consequence, the spectrum of a resonator with aberrated mirrors does not have the full degeneracy that is expected with aberration-free mirrors [7]. The lifting of the degeneracy due to astigmatism is simple to derive, since the astigmatic aberration is Gaussian as well. On the other hand, the spherical aberration does not have a Gaussian nature, and therefore it seems that the operator method cannot be used to derive the spectrum in the presence of spherical aberration. In this Chapter we show that the spherical aberration can still be treated with the operator description by using degenerate perturbation theory as it is used in quantum mechanics [18].

In Section 3.2 we introduce the operator description of a light field inside a lens guide. The propagation through free space and the passage through a lens is described by a Gaussian operator acting on the state of the light beam. In Section 3.3 we discuss the ABCD-matrix representation of these Gaussian operators. When a Gaussian beam propagates through a lens guide, its spot size, radius of curvature of the wavefronts, and Gouy phase change. As discussed in Section 3.4, the Iwasawa decomposition expresses this behaviour in an elegant operator form, with parameters expressed in terms of the matrix elements of the ABCD matrix of the lens guide. The Iwasawa decomposition is used in Section 3.5 to derive the Hamiltonian for half a round trip in an aberration-free two-mirror resonator, which determines the spectrum. In Section 3.6 spherical aberration is introduced. By using degenerate perturbation theory, we obtain the spectrum of the resonator in the presence of spherical aberration.

The standard theory of aberrations of optical systems considers its effect on the imaging properties [1, 19], but does not typically consider resonators. Laabs and Friberg studied the effect of non-paraxial propagation on the spectrum and eigenmodes of a resonator numerically [20]. The change of the spectrum of a resonator due to aberrations was studied experimentally by Klaassen *et al.* [21].

### 3.2 Operator description for Gaussian wave optics

The electric field of a monochromatic light beam with frequency  $\omega$  that propagates in the positive  $z$  direction, is taken as  $\text{Re}[\vec{\epsilon} E(x, y, z, t)]$ , where  $x$  and  $y$  are the transverse coordinates. In this expression  $\vec{\epsilon}$  is the normalised polarisation vector, and  $E$  the complex electric field, which is related to the normalised beam profile  $u(x, y, z)$  by

$$E(x, y, z, t) = E_0 u(x, y, z) \exp(ikz - i\omega t), \quad (3.1)$$

with  $E_0$  the complex amplitude of the field. The polarisation will be assumed uniform throughout this Chapter, and polarisation effects are not considered. Equation (3.1) is inserted into the scalar wave equation, and it is assumed that  $|\partial u / \partial z| \ll ku$ , which means that the profile  $u(x, y, z)$  varies only slowly with  $z$ . Then the profile  $u(x, y, z)$  satisfies the paraxial

wave equation [2]:

$$\left(\frac{\partial^2}{\partial x^2} + \frac{\partial^2}{\partial y^2} + 2ik\frac{\partial}{\partial z}\right)u(x,y,z) = 0. \quad (3.2)$$

The paraxial wave equation is identical in form to the Schrödinger equation for a free particle in two dimensions, where the time plays the role of the longitudinal coordinate  $z$ . This similarity is the starting point for an operator description of the propagation of a monochromatic light beam inside a lens guide [4–6].

To simplify the notation we first consider only one transverse dimension. The transverse profile  $u(x,z) = \langle x|u(z)\rangle$  of the light beam corresponds to the time-dependent wave function in quantum mechanics, and  $|u(z)\rangle$  is the "state" of the light beam in the transverse plane  $z$ . The propagation through vacuum is described by

$$|u(z)\rangle = \hat{U}_f(z)|u(0)\rangle, \quad \hat{U}_f(z) = \exp\left(-\frac{iz}{2k}\hat{p}_x^2\right). \quad (3.3)$$

In the coordinate representation the transverse-momentum operator  $\hat{p}_x$  takes the form  $-i\partial/\partial x$ . When passing through a lens the transverse profile of the light beam acquires a phase shift which depends on the optical thickness of the lens, which varies over the lens. For a lens without aberrations the phase shift depends quadratically on the transverse coordinate. It is assumed that the lens is thin, so that the transverse beam profile is constant inside the lens. Then the effect of the lens is described by multiplying the transverse beam profile by a parabolic phase factor. We consider only cases where the optical axes of the lenses coincide with the  $z$  axis, and where the lenses are non-astigmatic. When the lens is located in the transverse plane  $z$ , the state of the light beam  $|u(z_+)\rangle$  after the lens is expressed in terms of the state  $|u(z_-)\rangle$  before the lens, by

$$|u(z_+)\rangle = \hat{U}_l(f)|u(z_-)\rangle, \quad \hat{U}_l(f) = \exp\left(-\frac{ik}{2f}\hat{x}^2\right), \quad (3.4)$$

where  $f$  is the focal distance of the lens. Now the change of the state of the light beam when going from the input plane to the output plane of a lens guide, is described by the unitary operator  $\hat{U}$ , which is a repeated product of  $\hat{U}_f$  and  $\hat{U}_l$  in the proper order, according to the arrangement of the lenses in the lens guide.

The operators  $\hat{U}_f$  and  $\hat{U}_l$  are Gaussian operators, that is, exponential functions quadratic in  $\hat{x}$  and  $\hat{p}_x$ . An operator that is quadratic in  $\hat{x}$  and  $\hat{p}_x$  can be written as a linear combination of the Hermitian operators  $\hat{T}_m$ , which are defined by

$$\hat{T}_1 = \frac{1}{4}(\hat{x}\hat{p}_x + \hat{p}_x\hat{x}), \quad \hat{T}_2 = \frac{1}{4}\left(\frac{1}{\gamma^2}\hat{x}^2 - \gamma^2\hat{p}_x^2\right), \quad \hat{T}_3 = \frac{1}{4}\left(\frac{1}{\gamma^2}\hat{x}^2 + \gamma^2\hat{p}_x^2\right), \quad (3.5)$$

where  $\gamma$  is a free scaling parameter [22]. The commutators between the quadratic operators  $\hat{T}_m$  are again quadratic, which follows from the commutation rule  $[\hat{x}, \hat{p}_x] = i$ . Therefore, the operators  $\hat{T}_m$  are closed under taking the commutator. They satisfy commutation rules that are similar to the commutation rules for the components of the angular-momentum operator, the difference being that one sign is different [23]. We have

$$[\hat{T}_1, \hat{T}_2] = -i\hat{T}_3, \quad [\hat{T}_2, \hat{T}_3] = i\hat{T}_1, \quad [\hat{T}_3, \hat{T}_1] = i\hat{T}_2. \quad (3.6)$$

Since the unitary operator  $\hat{U}$  is a product of Gaussian operators, it can in general be written as

$$\hat{U} = \exp \left[ -i (\beta_1 \hat{T}_1 + \beta_2 \hat{T}_2 + \beta_3 \hat{T}_3) \right], \quad (3.7)$$

where the real coefficients  $\beta_m$  are determined by the order of the Gaussian operators and their parameters.

### 3.3 Matrix representation and ray optics

In order to obtain the coefficients  $\beta_m$  in Eq. (3.7), it is necessary to write the evolution operator  $\hat{U}$  of the lens guide, which is a product of Gaussian operators, as a single exponential operator. It is then convenient to make use of a matrix representation of the Gaussian operators. For free space propagation over distance  $z$  we have

$$\hat{U}_f^\dagger(z) \begin{pmatrix} \hat{x} \\ \hat{p}_x/k \end{pmatrix} \hat{U}_f(z) = M_f(z) \begin{pmatrix} \hat{x} \\ \hat{p}_x/k \end{pmatrix}, \quad M_f(z) = \begin{pmatrix} 1 & z \\ 0 & 1 \end{pmatrix}, \quad (3.8)$$

while for passage through a lens we have

$$\hat{U}_l^\dagger(f) \begin{pmatrix} \hat{x} \\ \hat{p}_x/k \end{pmatrix} \hat{U}_l(f) = M_l(f) \begin{pmatrix} \hat{x} \\ \hat{p}_x/k \end{pmatrix}, \quad M_l(f) = \begin{pmatrix} 1 & 0 \\ -1/f & 1 \end{pmatrix}, \quad (3.9)$$

which follows from the commutation rule  $[\hat{x}, \hat{p}_x] = i$ . We see that  $M_f(z)$  and  $M_l(f)$  are simply the ABCD matrices for free space propagation and passage through a lens, respectively, describing the change in position and slope of a ray. Notice that the existence of this matrix representation relies on the fact that the operators are Gaussian, that is, exponential functions quadratic in  $\hat{x}$  and  $\hat{p}_x$ . As a consequence, linear combinations of  $\hat{x}$  and  $\hat{p}_x$  remain linear combinations, and the transformation can be described by multiplication of the vector with the components  $\hat{x}$  and  $\hat{p}_x/k$  by a matrix. It follows that the evolution operator  $\hat{U}$  of the lens guide is represented by the ABCD matrix of the lens guide  $M$ , which is a repeated product in the right order of the ABCD matrices for free space propagation and lenses. This leads to the general result for a lens guide,

$$\hat{U}^\dagger \begin{pmatrix} \hat{x} \\ \hat{p}_x/k \end{pmatrix} \hat{U} = M \begin{pmatrix} \hat{x} \\ \hat{p}_x/k \end{pmatrix}. \quad (3.10)$$

An explicit form of the ABCD matrix  $M$  corresponding to the operator (3.7), is also obtained from the matrix representation of the operators  $\hat{T}_m$  in Eq. (3.5). We introduce the matrices  $J_m$ , so that

$$\left[ \hat{T}_m, \begin{pmatrix} \hat{x} \\ \hat{p}_x/k \end{pmatrix} \right] = -J_m \begin{pmatrix} \hat{x} \\ \hat{p}_x/k \end{pmatrix}, \quad m = 1, 2, 3, \quad (3.11)$$

with

$$J_1 = \frac{i}{2} \begin{pmatrix} 1 & 0 \\ 0 & -1 \end{pmatrix}, \quad J_2 = -\frac{i}{2} \begin{pmatrix} 0 & b \\ 1/b & 0 \end{pmatrix}, \quad J_3 = \frac{i}{2} \begin{pmatrix} 0 & b \\ -1/b & 0 \end{pmatrix}, \quad (3.12)$$

where  $b = k\gamma^2$ . For a Gaussian beam with waist  $\gamma$ , the length  $b$  is the Rayleigh range. The matrices  $J_m$  satisfy the same commutation rules as the operators  $\hat{T}_m$ , for which the commutation rules are given in Eq. (3.6). Thus the operators  $\hat{T}_m$  are represented by the corresponding matrices in Eq. (3.12). By replacing the operator  $\hat{U}$  by the ABCD matrix  $M$  of the lens guide, and the  $\hat{T}_m$  operators by the corresponding  $J_m$  matrices, Eq. (3.7) gives the matrix equality

$$M = \exp[-i(\beta_1 J_1 + \beta_2 J_2 + \beta_3 J_3)]. \quad (3.13)$$

This equality relates the coefficients  $\beta_m$  to the matrix elements of the ABCD matrix of the lens guide  $M$ . In general it is difficult to evaluate the matrix on the right-hand side of (3.13), since it is an exponential function of a matrix. For some matrices, though, it is simple to obtain the exponential function of the matrix, as is used in the Iwasawa decomposition.

### 3.4 Iwasawa decomposition

It is well-known that when a Gaussian beam propagates through a lens guide, the spot size and the curvature of the wavefronts of the Gaussian beam change, and the beam picks up a phase factor, the Gouy phase. This behaviour is described in an elegant way by an operator identity: the Iwasawa decomposition [22]. The Iwasawa decomposition expresses the unitary operator  $\hat{U}$  of the lens guide as a product of three unitary operators, in the form

$$\hat{U} = \exp[-i\alpha(\hat{T}_2 + \hat{T}_3)] \exp(-i\xi\hat{T}_1) \exp(-i\theta\hat{T}_3). \quad (3.14)$$

The operators  $\hat{T}_m$  are given in Eq. (3.5), and the parameters  $\theta$ ,  $\xi$  and  $\alpha$  are to be determined.

For an arbitrary lens guide, the parameters  $\theta$ ,  $\xi$  and  $\alpha$  in the Iwasawa decomposition (3.14) are obtained by using the matrix representation of the unitary operators appearing in the decomposition. The unitary operator  $\hat{U}$  of the lens guide corresponds to the ABCD matrix of the lens guide  $M$ . This matrix is also obtained when the operators  $\hat{T}_m$  on the right-hand side of (3.14) are replaced by their corresponding matrices  $J_m$  given in Eq. (3.12). We find that

$$M \equiv \begin{pmatrix} A & B \\ C & D \end{pmatrix} = \exp[-i\alpha(J_2 + J_3)] \exp(-i\xi J_1) \exp(-i\theta J_3). \quad (3.15)$$

This matrix equality gives rise to relations between the parameters  $\theta$ ,  $\xi$  and  $\alpha$ , and the elements of the ABCD matrix of the lens guide. The exponential functions of the matrices on the right-hand side can simply be evaluated. Expressing the parameters  $\theta$ ,  $\xi$  and  $\alpha$  in terms of the elements of the ABCD matrix gives the explicit expressions

$$\begin{aligned} \cos\left(\frac{\theta}{2}\right) &= \frac{bA}{\sqrt{b^2 A^2 + B^2}}, \\ \exp(\xi) &= A^2 + \frac{B^2}{b^2}, \\ \alpha &= -b \frac{b^2 AC + BD}{b^2 A^2 + B^2}. \end{aligned} \quad (3.16)$$

Since  $\det(M) = AD - BC = 1$ , the matrix elements  $A$  and  $B$  can not vanish both. Therefore, the numerators in these expression are always non-zero, and the parameters are well-defined.

### 3. The spectrum of a resonator with spherical aberration

As a check of consistency we consider the Iwasawa decomposition for the unitary operator that describes the passage through a lens in Eq. (3.4). In the ABCD matrix in (3.9) we have  $A = D = 1$ ,  $B = 0$  and  $C = -1/f$ . Using (3.16) we find that  $\theta = \xi = 0$  and  $\alpha = b/f$ . Inserting these values in (3.14), and using (3.5), we find agreement with (3.4).

The Iwasawa decomposition for free space propagation over a distance  $z$  is obtained by inserting the values  $A = D = 1$ ,  $B = z$  and  $C = 0$ , as given by (3.8). We find that

$$\tan \left[ \frac{\theta(z)}{2} \right] = \frac{z}{b}, \quad \exp[\xi(z)] = 1 + \frac{z^2}{b^2}, \quad \alpha(z) = -\frac{bz}{b^2 + z^2}. \quad (3.17)$$

When the Iwasawa decomposition of  $\hat{U}$  is applied to the state of a Gaussian beam at the waist, where  $b$  is the Rayleigh range, there is a clear physical interpretation of these parameters. The last unitary operator on the right-hand side of Eq. (3.14) contains the operator  $\hat{T}_3$ , which has the shape of the harmonic oscillator Hamiltonian, where the free parameter  $\gamma$  determines the scale of the oscillator. This term operates on the harmonic oscillator ground state and is responsible for the Gouy phase  $\theta(z)/2$  of the beam. The unitary operator containing  $\hat{T}_1$  is a squeezing operator, which follows from the property

$$\exp(i\xi\hat{T}_1)\hat{x}\exp(-i\xi\hat{T}_1) = \exp(\xi/2)\hat{x}. \quad (3.18)$$

It describes the spot size of the beam, which is given by  $\gamma\exp[\xi(z)/2]$ . The first unitary operator on the right-hand side of Eq. (3.14), which can be written as  $\exp(-i\alpha\hat{x}^2/2\gamma^2)$ , is responsible for the curvature of the wavefronts of the light beam, and the radius of curvature is  $-b/\alpha(z)$ .

The Iwasawa decomposition for free space propagation can also be obtained by using the method of invariants of Lewis and Riesenfeld [24]. A method for checking the Iwasawa decomposition for free space propagation, different from a matrix representation, is a brute-force method for combining exponential operators [25].

## 3.5 Spectrum of a resonator without aberrations

### 3.5.1 Lens guide

We determine the spectrum of a symmetric two-mirror resonator, as depicted in Fig. 3.1(a), by using an operator method. The radius of curvature of the spherical mirrors is  $R$  and the distance between the mirrors is  $L$ . When a light beam is reflected by a mirror, the transverse profile acquires a phase shift that depends on the transverse coordinate, which is due to the curvature of the mirror. For a concave spherical mirror with radius of curvature  $R$  located in the plane  $z_1$ , the mirror surface is described by  $z = z_1 + \sqrt{R^2 - x^2 - y^2} - R$ . The optical path length for reflection by the mirror is then given by

$$d(x, y) = 2k \left( \sqrt{R^2 - x^2 - y^2} - R \right), \quad (3.19)$$

where the on-axis optical path length is set to vanish. When the size of the beam is small compared to the radius of curvature of the mirror, it is justified to make a Taylor expansion of

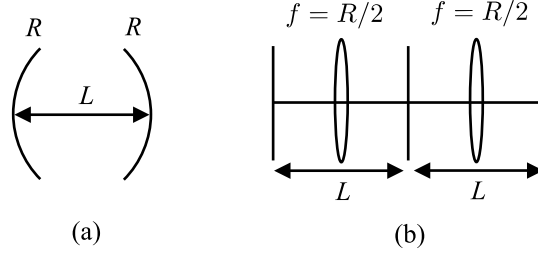


**Figure 3.1:** Symmetric two-mirror resonator for which the distance between the mirrors is  $L$  and the radius of curvature of the spherical mirrors is  $R$ . In (a) the resonator configuration is depicted, and in (b) the corresponding lens guide, which is obtained by unfolding the resonator. The input plane of the lens guide is the plane in the middle of the resonator.

$d(x,y)$  in  $x^2 + y^2$  and retain only the lowest-order term  $-k(x^2 + y^2)/R$ , which approximates the spherical surface of the mirror by a parabola. The unitary operator for the reflection by a mirror is then given by the unitary operator for a lens in Eq. (3.4), with a focal distance  $f = R/2$ .

The resonator is unfolded into a lens guide, where the plane in the middle of the resonator is the input plane of the lens guide. The mirrors with radius of curvature  $R$  are replaced by lenses with focal distance  $f = R/2$ . The lens guide is depicted in Fig. 3.1(b). Because the resonator is symmetric, the lens guide consists of two identical parts, both corresponding to half a round trip in the resonator. The unitary operator  $\hat{U}$  that describes the evolution of a light beam inside the resonator during half a round trip, is expressed in terms of the unitary operators for free space propagation and passage through a lens in Eqs. (3.3) and (3.4), respectively, by

$$\hat{U} = \hat{U}_f(L/2)\hat{U}_l(R/2)\hat{U}_f(L/2). \quad (3.20)$$

### 3.5.2 Hamiltonian for half a round trip

In order to determine the eigenmodes and spectrum of the resonator, the exponential operators in the expression for  $\hat{U}$  in Eq. (3.20) are combined into a single exponential operator, for which we write

$$\hat{U} = \exp(-i\hat{H}), \quad (3.21)$$

where  $\hat{H}$  is a Hermitian operator, which can be interpreted as the Hamiltonian for half a round trip in the resonator. The eigenfunctions of  $\hat{H}$  are then the eigenmodes of the resonator and the corresponding eigenvalues determine the spectrum of the resonator. The operator  $\hat{H}$  is obtained by using the Iwasawa decomposition for  $\hat{U}$ , which is found by calculating the ABCD matrix  $M$  for half a round trip. The parameters  $\theta$ ,  $\xi$  and  $\alpha$  of the Iwasawa decomposition in Eq. (3.14) are related to the elements of  $M$  by Eq. (3.16). For the symmetric two-mirror resonator in Fig. 3.1(a) the waist of the Gaussian eigenmode lies in general in the plane in the middle of the resonator, which corresponds both to the input and output plane of the lens guide for half a round trip. Then the unitary operator  $\hat{U}$  describes the propagation of the beam

### 3. The spectrum of a resonator with spherical aberration

over half a round trip from waist to waist. At the waist of the beam the wavefronts are flat. Therefore, the wavefronts must be flat again after half a round trip, so that the parameter  $\alpha$  in the Iwasawa decomposition (3.14), which determines the curvature of the wavefronts, must vanish. This requirement is satisfied when the parameter  $b = k\gamma^2$  in Eq. (3.16), which is the Rayleigh range of the Gaussian beam, satisfies

$$b^2 = -\frac{BD}{AC}, \quad (3.22)$$

which fixes the spot size  $\gamma$  of the Gaussian beam at the waist. In Eq. (3.22) we assume that all the matrix elements of  $M$  are non-zero and that the right-hand side is positive.

With this value of  $b$  it follows that

$$\cos\left(\frac{\theta}{2}\right) = \text{sign}(A)\sqrt{AD}, \quad \exp(\xi) = \frac{A}{D}, \quad (3.23)$$

where we used that  $\det(M) = AD - BC = 1$ . The ABCD matrix for half a round trip is given by

$$M = M_f(L/2)M_l(R/2)M_f(L/2) = \begin{pmatrix} g & \frac{L}{2}(1+g) \\ -\frac{2}{L}(1-g) & g \end{pmatrix}, \quad (3.24)$$

where  $g = 1 - L/R$  is the  $g$  parameter of the resonator. For a stable resonator  $0 \leq g^2 < 1$  [7]. When  $g = 0$  and  $g = \pm 1$ , Eq. (3.22) does not apply, since then not all the matrix elements of  $M$  are non-zero. For a confocal resonator we have  $g = 0$ , which means that  $A = D = 0$ . It follows from (3.16) that  $\alpha = 0$  for all values of  $b$ . This means that the waists of the beams propagating to the right and the left inside the resonator do not coincide (see Section 2.6). For  $g = \pm 1$  there is no positive value of  $b$  for which  $\alpha = 0$ .

By using Eqs. (3.22) and (3.24) it follows that the Rayleigh range of the Gaussian eigenmode is given by

$$b = k\gamma^2 = \frac{L}{2} \sqrt{\frac{1+g}{1-g}}, \quad (3.25)$$

which is in agreement with the result by Siegman [7]. By using (3.23) we find that for the parameters of the Iwasawa decomposition we have  $\xi = \alpha = 0$  and  $\cos(\theta/2) = g$ . It follows that, by using the Iwasawa decomposition (3.14), the unitary operator  $\hat{U}$  can be written as a single exponential operator, which is written as in Eq. (3.21). Taking into account both transverse dimensions again, the Hamiltonian for half a round trip  $\hat{H}$  is given by

$$\hat{H} = \frac{1}{2} \arccos(g) \left[ \gamma^2 (\hat{p}_x^2 + \hat{p}_y^2) + \frac{1}{\gamma^2} (\hat{x}^2 + \hat{y}^2) \right], \quad (3.26)$$

which is the Hamiltonian of the two-dimensional isotropic quantum harmonic oscillator. When applied to the state of the Gaussian beam with Rayleigh range  $b$  at the waist, the only effect of  $\hat{U}$  is a phase factor, which is the Gouy phase for half a round trip.

### 3.5.3 Spectrum and degeneracy

When considering the quantum harmonic oscillator, it is customary to introduce the ladder operators

$$\begin{aligned} \hat{a}_x &= \frac{1}{\sqrt{2}} \left( \frac{\hat{x}}{\gamma} + i\gamma\hat{p}_x \right), & \hat{a}_x^\dagger &= \frac{1}{\sqrt{2}} \left( \frac{\hat{x}}{\gamma} - i\gamma\hat{p}_x \right), \\ \hat{a}_y &= \frac{1}{\sqrt{2}} \left( \frac{\hat{y}}{\gamma} + i\gamma\hat{p}_y \right), & \hat{a}_y^\dagger &= \frac{1}{\sqrt{2}} \left( \frac{\hat{y}}{\gamma} - i\gamma\hat{p}_y \right), \end{aligned} \quad (3.27)$$

which satisfy the boson commutation rules. In terms of these ladder operators Eq. (3.26) is given by

$$\hat{H} = \arccos(g) (\hat{n}_x + \hat{n}_y + 1), \quad (3.28)$$

where  $\hat{n}_x = \hat{a}_x^\dagger \hat{a}_x$  and  $\hat{n}_y = \hat{a}_y^\dagger \hat{a}_y$ . The eigenstates of  $\hat{H}$  are the Hermite-Gaussian (HG) states  $|u_{nm}\rangle$ . We have

$$\hat{H}|u_{nm}\rangle = \arccos(g) (n + m + 1) |u_{nm}\rangle. \quad (3.29)$$

In order for a light beam to be an eigenmode of a resonator it is necessary that the electric field (3.1) of the light beam transforms into  $\pm$  itself after half a round trip. Besides the Gouy phase, the electric field acquires a phase  $kL$  after half a round trip due to the plane-wave part of the field. These phases must add up to a multiple of  $\pi$ , which defines the resonance condition:

$$kL = \arccos(g) (n + m + 1) + \pi q, \quad (3.30)$$

where  $n$  and  $m$  are the mode numbers of the HG eigenmodes, and  $q$  is the longitudinal mode number. From this resonance condition the spectrum of allowed frequencies  $\omega = ck$  of the light beam follows [7].

The  $z$  component of the angular-momentum operator, defined by

$$\hat{l}_z = \hat{x}\hat{p}_y - \hat{y}\hat{p}_x, \quad (3.31)$$

commutes with  $\hat{H}$ . It follows that there is a basis of eigenstates of  $\hat{H}$ , in which  $\hat{l}_z$  is diagonal as well. This basis is generated by the circular ladder operators [18]

$$\hat{a}_\pm = \frac{1}{\sqrt{2}} (\hat{a}_x \mp i\hat{a}_y), \quad \hat{a}_\pm^\dagger = \frac{1}{\sqrt{2}} (\hat{a}_x^\dagger \pm i\hat{a}_y^\dagger). \quad (3.32)$$

In terms of these circular ladder operators

$$\hat{H} = \arccos(g) (\hat{n}_+ + \hat{n}_- + 1), \quad \hat{l}_z = \hat{n}_+ - \hat{n}_-, \quad (3.33)$$

where  $\hat{n}_+ = \hat{a}_+^\dagger \hat{a}_+$  and  $\hat{n}_- = \hat{a}_-^\dagger \hat{a}_-$ . Eigenstates of both  $\hat{H}$  and  $\hat{l}_z$  are the Laguerre-Gaussian (LG) states  $|u_{n_+n_-}\rangle$ , where  $n_+$  and  $n_-$  are the mode numbers. The more familiar mode numbers  $l$  and  $p$  are expressed in terms of  $n_+$  and  $n_-$  by  $l = n_+ - n_-$  and  $p = \min(n_+, n_-)$  [26]. In terms of the mode numbers of the LG eigenstates the spectrum is given by Eq. (3.30), where  $n + m$  is replaced by  $n_+ + n_-$ . The HG states with different mode numbers with a fixed sum  $n + m = N$  are degenerate. These modes form an  $N + 1$ -dimensional degenerate subspace. This space is also spanned by the LG states with  $n_+ + n_- = N$ , or eigenbases intermediate between the HG and LG bases [13].

## 3.6 Spectrum in the presence of aberrations

### 3.6.1 Spherical aberration

We determine the spectrum of the resonator in Fig. 3.1 in the presence of spherical aberration by using perturbation theory as it is known in quantum mechanics. In the expression for the optical path length in Eq. (3.19) the surface of the mirror was approximated by a parabola. We take into account the next term in the expansion. We write

$$d(x,y) = -\frac{k(x^2+y^2)}{R} - \frac{k(x^2+y^2)^2}{4R^3} + \dots \quad (3.34)$$

In terms of the  $g$  parameter of the resonator and the spot size  $\gamma$  of the Gaussian eigenmode of the resonator in Eq. (3.25), this is written as

$$d(x,y) = -\frac{1}{2}\sqrt{1-g^2}\left(\frac{x^2+y^2}{\gamma^2}\right) - \frac{\varepsilon}{16}(1-g^2)\left(\frac{x^2+y^2}{\gamma^2}\right)^2 + \mathcal{O}(\varepsilon^2), \quad (3.35)$$

where  $\varepsilon = 1/kR$  is a small number for optical wavelengths and typical mirror radii. It is allowed to neglect terms of order  $\varepsilon^2$  as long as  $x^2+y^2 \ll R^2$ .

By using that  $\hat{U}_1^2(R) = \hat{U}_1(R/2)$ , the unitary operator for a mirror with radius of curvature  $R$  with aberrations, can in general be written in a symmetric form as

$$\hat{U}_1(R) \exp[-i\varepsilon V(\hat{x}, \hat{y})] \hat{U}_1(R), \quad (3.36)$$

where  $V(x,y)$  describes the aberrations of the mirror, which in our case is spherical aberration, for which from Eq. (3.35) we have

$$V(x,y) = \frac{1}{16}(1-g^2)\left(\frac{x^2+y^2}{\gamma^2}\right)^2. \quad (3.37)$$

In this way the mirror with aberrations is represented in the lens guide by two lenses with focal distance  $R$ , in between which there is a phase plate that introduces a small phase  $\varepsilon V(x,y)$ , all of which lie in the plane of the mirror. In Fig. 3.2 the lens guide for half a round trip is given for the case of a mirror with aberrations. For the unitary operator for half a round trip we write

$$\hat{U} = \hat{U}_2 \exp[-i\varepsilon V(\hat{x}, \hat{y})] \hat{U}_1, \quad (3.38)$$

where

$$\hat{U}_1 = \hat{U}_1(R) \hat{U}_f(L/2), \quad \hat{U}_2 = \hat{U}_f(L/2) \hat{U}_1(R). \quad (3.39)$$

### 3.6.2 Perturbation Hamiltonian due to aberrations

In order to determine the spectrum in the presence of aberrations, we write the expression for the unitary operator for half a round trip in Eq. (3.38) in terms of a single exponential operator. For the unitary operator  $\hat{U}_f(L/2)$  that appears in the expression for  $\hat{U}_1$  in Eq. (3.39), we use the Iwasawa decomposition for free space propagation in Eq. (3.17) with  $z = L/2$ ,

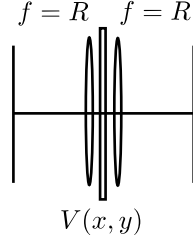


**Figure 3.2:** When a mirror with radius of curvature  $R$  has aberrations, it can be represented in the lens guide by two lenses with focal distance  $R$  in between which there is a phase plate that introduces the aberrations  $\varepsilon V(x, y)$  of the mirror. Both lenses and the phase plate lie in the plane of the mirror.

where  $\gamma$  is determined by Eq. (3.25). Then the term in the Iwasawa decomposition that introduces the curvature of the wavefronts exactly cancels the lens term  $\hat{U}_l(R)$ , since the mirror surface matches the wavefronts when the Rayleigh range satisfies (3.25). We have

$$\hat{U}_1 = \exp[-i\xi(L/2)\hat{T}_1] \exp[-i\theta(L/2)\hat{T}_3]. \quad (3.40)$$

For  $\hat{U}_2$  we use that  $\hat{U}_f(z) = \hat{U}_f^\dagger(-z)$ , so that the exponential operators in the Iwasawa decomposition (3.14) are reversed in order. We use that  $\theta(z)$  and  $\alpha(z)$  are odd, and  $\xi(z)$  is even in  $z$ , which follows from Eq. (3.17). Then we find that, as for  $\hat{U}_1$ , the term that introduces the curvature of the wavefronts cancels the lens term  $\hat{U}_l(R)$ , and that

$$\hat{U}_2 = \exp[-i\theta(L/2)\hat{T}_3] \exp[i\xi(L/2)\hat{T}_1]. \quad (3.41)$$

When the expressions for  $\hat{U}_1$  and  $\hat{U}_2$  in Eq. (3.40) and (3.41), respectively, are inserted in the expression for  $\hat{U}$  in Eq. (3.38) we see that the exponential operator that contains the aberration, is sandwiched between the squeeze operators that introduces the scaling of the beam in the Iwasawa decomposition. It follows from Eqs. (3.18) and (3.25) that

$$\exp[i\xi(L/2)\hat{T}_1] \hat{x} \exp[-i\xi(L/2)\hat{T}_1] = \sqrt{\frac{2}{1+g}} \hat{x}. \quad (3.42)$$

All the results above hold also for the  $y$  transverse coordinate. Taking into account both transverse dimensions again, we conclude that the unitary operator for half a round trip in the presence of aberrations in Eq. (3.38) can be written as

$$\hat{U} = \exp\left(-\frac{i}{2}\hat{H}\right) \exp(-i\varepsilon\hat{V}) \exp\left(-\frac{i}{2}\hat{H}\right), \quad (3.43)$$

with  $\hat{H}$  given by (3.26), and

$$\hat{V} = V\left(\sqrt{\frac{2}{1+g}}\hat{x}, \sqrt{\frac{2}{1+g}}\hat{y}\right) = \frac{1-g}{4(1+g)} \left(\frac{\hat{x}^2 + \hat{y}^2}{\gamma^2}\right)^2. \quad (3.44)$$

### 3. The spectrum of a resonator with spherical aberration

We see that in the absence of aberrations, in which case  $\varepsilon = 0$ , Eq. (3.21) is recovered. For combining the exponential operators we use the Campbell-Baker-Hausdorff formula, which is given by

$$\exp(\hat{A})\exp(\hat{B}) = \exp\left(\hat{A} + \hat{B} + \frac{1}{2}[\hat{A}, \hat{B}] + \frac{1}{12}[\hat{A}, [\hat{A}, \hat{B}]] + \frac{1}{12}[\hat{B}, [\hat{B}, \hat{A}]] + \dots\right). \quad (3.45)$$

We find that

$$\hat{U} = \exp[-i\hat{H} - i\varepsilon\Delta\hat{H} + \mathcal{O}(\varepsilon^2)], \quad (3.46)$$

with

$$\Delta\hat{H} = \hat{V} - \frac{1}{6}[\hat{H}, [\hat{H}, \hat{V}]] + \dots, \quad (3.47)$$

where the dots refer to terms consisting of nested commutators of  $\hat{H}$  with  $\hat{V}$ , with  $\hat{V}$  appearing only once. We see that the aberrations of the mirror introduce the perturbation term  $\Delta\hat{H}$  to the unperturbed Hamiltonian  $\hat{H}$ .

### 3.6.3 Spectrum in the presence of spherical aberration

The perturbation  $\Delta\hat{H}$  to the unperturbed Hamiltonian  $\hat{H}$  can be treated by degenerate quantum-mechanical perturbation theory. The perturbation matrix is obtained by determining the matrix elements of  $\Delta\hat{H}$  between the degenerate eigenstates of  $\hat{H}$ . In the matrix elements, all the commutators of  $\hat{H}$  with  $\hat{V}$  in (3.47) vanish, because the operator  $\hat{H}$  can be replaced by its eigenvalue, since it operates immediately on an eigenstate. Notice that it is essential for this argument that  $\hat{V}$  appears only once in all these nested commutators. In the terms of order  $\varepsilon^2$  the operator  $\hat{V}$  appears twice and can prevent  $\hat{H}$  from operating on an eigenstate immediately.

It is convenient to use a basis for the degenerate space in which the perturbation Hamiltonian is as diagonal as possible within the degenerate subspace. We know that a spherical mirror has cylindrical symmetry about the optical axis. Therefore it is convenient to use as a basis the eigenbasis of the angular-momentum operator  $\hat{l}_z$  in (3.31), which commutes with  $\hat{V}$  in Eq. (3.44), and also with all the other corrections to the parabolic approximation to the spherical surface of the mirror. The eigenbasis of  $\hat{l}_z$  consists of the LG eigenstates  $|u_{n_+n_-}\rangle$ . In terms of the circular ladder operators, defined in Eq. (3.32), we have

$$\frac{\hat{x}^2 + \hat{y}^2}{\gamma^2} = \hat{n}_+ + \hat{n}_- + 1 + \hat{a}_+\hat{a}_- + \hat{a}_+^\dagger\hat{a}_-^\dagger. \quad (3.48)$$

In this expression we see that the terms on the right-hand side that change  $n_+$  and  $n_-$ , do not conserve the sum  $n_+ + n_-$ . For  $\hat{V}$ , which is proportional to the square of (3.48), the same holds. Therefore, in the basis of the LG eigenstates of the resonator the perturbation matrix of the operator  $\hat{V}$  is diagonal. The diagonal elements are given by

$$\begin{aligned} \Delta H(n_+, n_-) &= \langle u_{n_+n_-} | \hat{V} | u_{n_+n_-} \rangle \\ &= \frac{1-g}{4(1+g)} [(n_+ + n_- + 2)(n_+ + n_- + 1) + 2n_+n_-]. \end{aligned} \quad (3.49)$$

When the  $g$  parameter of the resonator approaches  $-1$ , the diagonal elements  $\Delta H(n_+, n_-)$  become large. The case  $g = -1$  corresponds to a concentric resonator configuration, and when this configuration is approached, the Gaussian eigenmode tends to fill the mirror and feels a lot of the spherical aberration, giving rise to a large  $\Delta H(n_+, n_-)$ . When  $g = -1$  is approached, the spot size at the waist of the Gaussian eigenmode vanishes, as follows from Eq. (3.25), and the propagation is not paraxial anymore. Laabs and Friberg studied the effect of non-paraxial propagation on the spectra and eigenmodes of stable resonators close to the concentric configuration [20]. When approaching  $g = 1$  ( $R \rightarrow \infty$ ),  $\Delta H(n_+, n_-)$  vanishes, since  $g = 1$  corresponds to a plano-plano configuration, which has no spherical aberration.

The spectrum of the resonator with spherical aberration is then determined by the resonance condition

$$kL = \arccos(g)(n_+ + n_- + 1) + \varepsilon \Delta H(n_+, n_-) + \pi q, \quad (3.50)$$

where  $\varepsilon = 1/kR$  is a small number. The LG eigenstates for which  $n_+ + n_- = N$ , are degenerate in the absence of aberrations. Since  $\Delta H(n_+, n_-)$  is not a function of  $n_+ + n_-$  it follows that the degeneracy is lifted partially. Only a two-fold degeneracy remains between states with  $n_+$  and  $n_-$  interchanged. A reflection in a plane that contains the optical axis, leaves the aberration function  $V(x, y)$  in (3.37) invariant, and interchanges  $n_+$  and  $n_-$ . Due to the aberration, for even  $N$ , the manifolds of  $N + 1$  degenerate states split up in  $N/2$  two-fold degenerate states and a single non-degenerate eigenstate with mode numbers  $n_+ = n_- = N/2$ . For odd  $N$ , there are  $(N + 1)/2$  two-fold degenerate states. The mirror surface is invariant under the reflection in a plane containing the optical axis, and therefore the remaining two-fold degeneracy is not lifted when higher-order terms in the expression for  $d(x, y)$  in Eq. (3.34) are taken into account. The degeneracy is completely lifted only when the reflection symmetry is broken, which occurs for astigmatic aberration.

As discussed below Eq. (3.35), the higher-order corrections to the spectrum can be neglected when  $x^2 + y^2 \ll R^2$ . This means that the spot size of the mode on the mirror must be much smaller than the radius of the mirror. It follows from Eq. (3.48) that for the LG modes with mode numbers  $n_+$  and  $n_-$  the expectation value of  $\hat{x}^2 + \hat{y}^2$  on the mirror is  $2\gamma^2(n_+ + n_- + 1)/(1 + g)$ , where it is used that  $\gamma\sqrt{2/(1 + g)}$  is the spot size of the Gaussian eigenmode on the mirror, which is expressed by Eq. (3.42). The requirement  $x^2 + y^2 \ll R^2$  is then satisfied when

$$\sqrt{\frac{1-g}{1+g}}(n_+ + n_- + 1) \ll kR. \quad (3.51)$$

Thus the higher-order corrections to the spectrum cannot be neglected only for very large mode numbers and when the concentric resonator configuration ( $g = -1$ ), as discussed below Eq. (3.49), is approached.

### 3.7 Conclusions

We used an operator description to obtain the spectrum and the modes of a symmetric two-mirror resonator. First we considered the case where the mirrors have no aberrations. The Hamiltonian for half a round trip was shown to have the form of the two-dimensional quantum

### 3. The spectrum of a resonator with spherical aberration

harmonic oscillator. We obtained the spectrum of the resonator from the eigenvalues of the Hamiltonian. The HG eigenfunctions of the Hamiltonian are the eigenmodes of the resonator. The HG modes with mode numbers with a fixed sum  $n+m=N$  are degenerate. An alternative basis for this degenerate subspace is formed by the LG modes having mode numbers  $n_+ + n_- = N$ .

The spherical aberration of the mirrors gives rise to a perturbation term in the Hamiltonian for half a round trip. By using degenerate perturbation theory we obtained the first-order correction to the unperturbed eigenvalues due to the spherical aberration. The spectrum in the presence of spherical aberration is given by Eq. (3.50). The  $N+1$ -fold degeneracy is almost completely lifted. There is only a two-fold degeneracy left of LG modes which have mode numbers  $n_+$  and  $n_-$  that are interchanged. This operation corresponds to the reflection in a plane through the optical axis of the resonator. When this reflection symmetry is broken, which occurs for astigmatic aberration, the degeneracy is completely lifted. The higher-order corrections to the spectrum can be neglected when the requirement (3.51) is satisfied.

## CHAPTER 4

---

### Orbital angular momentum of general astigmatic modes

---

*We present an operator method to obtain complete sets of astigmatic Gaussian solutions of the paraxial wave equation. In case of general astigmatism, the astigmatic intensity and phase distributions of the fundamental mode differ in orientation. As a consequence, the fundamental mode has a non-zero orbital angular momentum, which is not due to phase singularities. Analogous to the operator method for the quantum harmonic oscillator, the corresponding astigmatic higher-order modes are obtained by repeated application of raising operators on the fundamental mode. The nature of the higher-order modes is characterised by a point on a sphere, in analogy with the representation of polarisation on the Poincaré sphere. The north and south poles represent astigmatic Laguerre-Gaussian modes, similar to circular polarisation on the Poincaré sphere, while astigmatic Hermite-Gaussian modes are associated with points on the equator, analogous to linear polarisation. We discuss the propagation properties of the modes and their orbital angular momentum, which depends on the degree of astigmatism and on the location of the point on the sphere.*

*J. Visser and G. Nienhuis, Phys. Rev. A **70**, 013809 (2004).*

## 4.1 Introduction

Optical vortices play an important role in the field of quantum information because they can be used to create higher-dimensional entangled states [27]. The advantage of higher-dimensional entanglement is that more information can be stored and that there is less sensitivity to decoherence [28]. A light beam containing optical vortices can be used to create twin photons in a non-linear crystal. By changing the distribution of the vortices in the pump beam, the entangled state of the twin photons can be manipulated, such that it can be used for quantum communication protocols in higher dimensions [29]. Optical vortices in light beams can be created by using holograms [30], or spiral phase plates [31]. Upon propagation in free space, the vortices in a light beam display interesting behaviour [32]. Vortices can be created and annihilated in pairs of opposite topological charge, and isolated vortices have a certain stability under propagation [33]. An important feature of an optical vortex is that it carries a density of orbital angular momentum (OAM). An example is the central vortex in a Laguerre-Gaussian (LG) mode. The value of the OAM per photon is  $l\hbar$ , with  $l$  the topological charge of the vortex [34]. The value of the OAM of a light beam can be modified when the beam is passed through astigmatic lenses [35]. An example of a beam without vortices that carries OAM, is an astigmatic Gaussian beam, where the orientations of the astigmatic intensity and phase distributions are different [36]. This is called general astigmatism [37]. The OAM of astigmatic LG beams has also been discussed in simple cases [38, 39].

The paraxial wave equation, which describes the propagation of light beams, is identical in form to the two-dimensional Schrödinger equation for a free particle. It is therefore convenient to use the operator language for the description of the propagation of a light beam. The "state" of the light beam in an arbitrary transverse plane  $z$  can then be obtained by applying the propagation operator to the state in the plane  $z = 0$ , like it is done for the Schrödinger evolution. In a Heisenberg-like picture, a linear combination of the coordinate operator  $\hat{R}$  and the momentum operator  $\hat{P}$  will remain a linear combination of  $\hat{R}$  and  $\hat{P}$ , since the propagation operator is Gaussian in the momentum operator  $\hat{P}$ . Also the propagation through optical elements, like thin lenses, can be described in terms of Gaussian operators in  $\hat{R}$  and  $\hat{P}$ . This forms the basis of the operator method for the description of optical systems [4–6, 35]. Nienhuis and Allen [3] define ladder operators that are linear combinations of  $\hat{R}$  and  $\hat{P}$ , where the coefficients depend on the transverse plane  $z$ . Complete sets of solutions of the paraxial wave equation are obtained by repeated action of raising operators on the fundamental mode, in analogy to the operator method for the eigenstates of the quantum harmonic oscillator. This similarity is the reason that the familiar Hermite-Gaussian (HG) solutions of the paraxial wave equation are analogous to the eigenfunctions of the harmonic oscillator [11]. A similar operator method is discussed by Wünsche [40].

In this paper we generalise the operator method of Nienhuis and Allen [3] to include astigmatism. We derive complete sets of solutions of the paraxial wave equation that have OAM, both due to the presence of phase singularities, and due to the difference in the orientations of the astigmatic intensity and phase distributions. In Section 4.2 we discuss the properties of an astigmatic Gaussian beam. We distinguish between simple astigmatism and general astigmatism. For simple astigmatism, both the intensity and phase distributions are astigmatic, but with the same orientation, while for general astigmatism the orientations are different. Simple astigmatism also covers the case for which either the intensity or the phase

distribution is astigmatic. In the case of general astigmatism the Gaussian beam has OAM. In Section 4.3 we obtain complete sets of higher-order modes by operating on the state of the Gaussian beam. In Section 4.4 we discuss some properties of the modes, and characterise the nature of the basis sets of the modes by a point on a sphere, in analogy to the Poincaré-sphere representation of polarisation. This gives a natural way to describe modes that are intermediate between LG and HG modes. In Section 4.5 we evaluate the OAM of the modes. The OAM is composed of three contributions, each with a distinct physical significance.

## 4.2 The fundamental mode

### 4.2.1 Gaussian beam

We consider a Gaussian beam that propagates in the positive  $z$  direction. When the Gaussian beam has circular symmetry its transverse profile can be described completely by a complex number  $\alpha$ , which depends on  $z$ . The real part of  $\alpha$  determines the width of the mode, while the radius of curvature of its wavefronts is determined by the imaginary part. When there is no circular symmetry the Gaussian beam is astigmatic. In its simplest form an astigmatic Gaussian beam is described by two complex numbers, one for each transverse dimension, and an angle which determines the orientation of the astigmatism. The real parts of these complex numbers determine the shape of the intensity distribution of the beam, while their imaginary parts determine the shape of the curves of constant phase. The two complex numbers evolve independently upon propagation, so that the orientation of the astigmatism does not vary with  $z$ . For astigmatism in its most general form the orientations of the intensity and the phase distributions of the beam differ. Upon propagation the orientations of both the phase and the intensity distributions change and the beam tumbles [36, 39].

In general, the Gaussian beam is determined by a complex symmetric  $2 \times 2$  matrix  $\alpha$ . We use Greek letters for  $2 \times 2$  matrices, unless stated otherwise. We write  $\alpha = \alpha_0 - i\alpha_1$ , where  $\alpha_0$  and  $\alpha_1$  are real and symmetric matrices. The normalised mode profile of the Gaussian beam in the transverse plane  $z = 0$  is written as

$$u_{00}(R, 0) = \frac{1}{\sqrt{\pi}} [\det \alpha_0]^{1/4} \exp(-R\alpha R/2), \quad (4.1)$$

where  $R$  is the two-dimensional transverse coordinate vector. For notational convenience we write  $R\alpha R \equiv R^T \cdot \alpha \cdot R$ , where the dot is a matrix multiplication. For Gaussian beams with circular symmetry,  $\alpha$  is a complex number times the unit matrix. When considering astigmatism in its simplest form, where the astigmatic intensity and phase distributions of the beam have the same orientation, the matrices  $\alpha_0$  and  $\alpha_1$  commute. For general astigmatism  $\alpha_0$  and  $\alpha_1$  do not commute.

The matrix  $\alpha_0$  determines the intensity distribution of the beam. The eigenvalues of  $\alpha_0$  are positive, so that the intensity distribution can be normalised. As a consequence, curves of constant intensity have an elliptic shape. The ellipticity or degree of astigmatism is determined by the ratio of the eigenvalues of  $\alpha_0$ . On the other hand, there is no constraint on the determinant of the matrix  $\alpha_1$ , which determines the phase distribution of the beam. For a positive determinant, curves of constant phase have an elliptic shape, while for a negative

determinant, these curves are hyperbolas. The degree of astigmatism for the phase is determined by the ratio of the eigenvalues of  $\alpha_1$ . For non-astigmatic Gaussian beams,  $\alpha_1$  vanishes in the focal plane. In the case of an astigmatic phase distribution the eigenvalues of  $\alpha_1$  are different and there are two focal planes. In a focal plane, one of the eigenvalues vanishes and the curves of constant phase are parallel lines.

## 4.2.2 Propagation

The electric field of a monochromatic light beam with frequency  $\omega$  that propagates in the positive  $z$  direction is written as

$$E(\vec{r}, t) = E_0 \operatorname{Re} [u(R, z) \exp(ikz - i\omega t)] , \quad (4.2)$$

where  $\vec{r} = (R, z)$  is the position vector in three dimensions and  $u(R, z)$  is the normalised transverse profile of the beam. When  $|\partial u / \partial z| \ll ku$ , the transverse profile varies only slowly with  $z$ , and the propagation of the light beam is well described by the paraxial wave equation

$$\left( \frac{\partial^2}{\partial R^2} + 2ik \frac{\partial}{\partial z} \right) u(R, z) = 0 , \quad (4.3)$$

where  $\partial^2 / \partial R^2 = \partial^2 / \partial x^2 + \partial^2 / \partial y^2$ . Well-known solutions of the paraxial wave equation are the HG modes, which form a complete set of solutions. The lowest-order of the HG modes is a Gaussian beam with circular symmetry. The HG modes resemble the eigenfunctions of the two-dimensional harmonic oscillator. As discussed in standard quantum mechanics textbooks, the excited eigenstates of the harmonic oscillator can be found by the repeated application of the raising operator on the ground state [18]. Nienhuis and Allen [3] derived complete sets of solutions of the paraxial wave equation by a similar method. We generalise this operator method by including astigmatism. For the two-dimensional harmonic oscillator a lowering and a raising operator is obtained for each dimension. These operators satisfy the boson commutation rules. The general form of the mode profile  $u_{00}(R, 0)$  of a Gaussian beam in Eq. (4.1) corresponds to the ground-state wave function of the harmonic oscillator. Operating on this function with each of the lowering operators  $\hat{a}_1$  and  $\hat{a}_2$  separately must give zero. We write  $\hat{a}_1$  and  $\hat{a}_2$  in the form of the two-dimensional vector  $\hat{A}$  and find from Eq. (4.1) that  $\hat{A}u_{00}(R, 0) = 0$  is satisfied when

$$\hat{A} = \frac{1}{\sqrt{2}} \beta (\alpha \hat{R} + i\hat{P}) , \quad (4.4)$$

where  $\beta$  is a proportionality matrix and  $\hat{P}$  is the momentum operator, which takes the form  $\hat{P} = -i\partial / \partial R$  in the coordinate representation. The corresponding vector of raising operators  $\hat{a}_1^\dagger$  and  $\hat{a}_2^\dagger$  is

$$\hat{A}^\dagger = \frac{1}{\sqrt{2}} \beta^* (\alpha^* \hat{R} - i\hat{P}) . \quad (4.5)$$

The complex  $2 \times 2$  matrix  $\beta$  must be chosen so that the lowering and raising operators satisfy the boson commutation rules. This will be discussed in Section 4.3.1.

The paraxial wave equation is identical in form to the two-dimensional Schrödinger equation for a free particle where the coordinate  $z$  replaces time. This suggests that the Dirac notation is convenient to use. For a general beam profile in the plane  $z$  we write  $u(R, z) = \langle R | u(z) \rangle$ , which is the mode function in the coordinate representation of the state of the beam  $|u(z)\rangle$  in the plane  $z$ . In operator form the paraxial wave equation is given by

$$\left( \hat{P}^2 - 2ik \frac{\partial}{\partial z} \right) |u(z)\rangle = 0, \quad (4.6)$$

where  $\hat{P}^2 = \hat{p}_x^2 + \hat{p}_y^2$ . Similar to the solution of the Schrödinger equation for a free particle we have

$$|u(z)\rangle = \hat{U}(z) |u(0)\rangle, \quad (4.7)$$

with

$$\hat{U}(z) = \exp\left(-\frac{iz}{2k} \hat{P}^2\right). \quad (4.8)$$

For the lowering operator at  $z = 0$  we write  $\hat{A}(0)$ , and the Gaussian fundamental mode profile in the plane  $z = 0$  is determined by

$$\hat{A}(0) |u_{00}(0)\rangle = 0. \quad (4.9)$$

For arbitrary plane  $z$ , the fundamental mode profile obeys

$$\hat{A}(z) |u_{00}(z)\rangle = 0. \quad (4.10)$$

It follows that the lowering operator in a plane with arbitrary  $z$  is related to the lowering operator in the plane  $z = 0$  by

$$\hat{A}(z) = \hat{U}(z) \hat{A}(0) \hat{U}(z)^\dagger. \quad (4.11)$$

We use the operator identity

$$\hat{U}(z) \hat{R} \hat{U}^\dagger(z) = \hat{R} - \frac{z}{k} \hat{P}, \quad (4.12)$$

and write  $\hat{A}(0)$  as in Eq. (4.4). We find that the  $z$ -dependent lowering operator has the form

$$\hat{A}(z) = \frac{1}{\sqrt{2}} \beta(z) (\alpha(z) \hat{R} + i \hat{P}), \quad (4.13)$$

with  $z$ -dependent matrices  $\alpha$  and  $\beta$ ,

$$\alpha(z) = \left(1 + \frac{iz}{k} \alpha(0)\right)^{-1} \alpha(0), \quad \beta(z) = \beta(0) \left(1 + \frac{iz}{k} \alpha(0)\right). \quad (4.14)$$

The solution of (4.10) is a Gaussian determined by  $\alpha(z)$ . By taking the real and imaginary parts of  $\alpha(z)$  we find the expressions for  $\alpha_0(z)$  and  $\alpha_1(z)$ , which determine how the intensity and phase distributions of the beam profile change upon propagation.

### 4.2.3 Gouy phase

The  $z$ -dependent lowering operator  $\hat{A}(z)$  determines the expression for the fundamental mode profile in different planes within a phase factor  $\exp(-i\chi(z))$ . This factor  $\chi(z)$  is a generalised form of the Gouy phase. The condition (4.10) does not determine the  $z$ -dependent phase  $\chi(z)$ . However, one may check that the solution of the paraxial wave equation (4.3), with the boundary condition (4.1), is

$$u_{00}(R, z) = \frac{1}{\sqrt{\pi}} [\det \alpha_0(0)]^{1/4} \sqrt{\frac{\det \alpha(z)}{\det \alpha(0)}} \exp \left[ -\frac{1}{2} R \alpha(z) R \right]. \quad (4.15)$$

Here  $\alpha(z) = \alpha_0(z) - i\alpha_1(z)$  is given in Eq. (4.14). This check requires the differentiation of  $\det \alpha(z)$  with respect to  $z$ . For this we use the identity for a matrix  $M$  that depends on the parameter  $z$ :

$$\frac{1}{\det M(z)} \frac{d}{dz} \det M(z) = \text{Tr} \frac{1}{M(z)} \frac{dM}{dz}. \quad (4.16)$$

This follows after taking the determinant of  $M(z+dz) = M(z)[1 + dz(1/M(z))(dM/dz)]$ , and linearising in  $dz$ . From the expression for  $\alpha(z)$  in Eq. (4.14) we find  $d\alpha(z)/dz = \alpha^2(z)/ik$ , so that

$$\frac{d}{dz} \det \alpha(z) = \frac{1}{ik} \det \alpha(z) \text{Tr} [\alpha(z)]. \quad (4.17)$$

Using this, it is straightforward to check that Eq. (4.15) is indeed a solution of the paraxial wave equation. The phase  $\chi(z)$ , which is an astigmatic generalisation of the Gouy phase, is then given by

$$\chi(z) = -\arg \left( \sqrt{\frac{\det \alpha(z)}{\det \alpha(0)}} \right) = \frac{1}{2} \arg \left[ \det \left( 1 + \frac{iz}{k} \alpha(0) \right) \right]. \quad (4.18)$$

Just as in the non-astigmatic case,  $\chi$  increases by  $\pi$  between  $z = -\infty$  and  $z = \infty$ .

### 4.2.4 Orbital angular momentum

When both the intensity and phase distributions of a Gaussian beam are astigmatic with different orientations, the beam carries OAM [36, 39]. The beam tumbles upon propagation, and with this tumbling OAM is associated. The origin of the tumbling of the beam can be understood when the transverse-momentum density is considered. For a normalised beam profile  $u(R)$  the transverse-momentum density per photon is given by [34]

$$P(R) = \frac{\hbar}{2i} \left( u^*(R) \frac{\partial}{\partial R} u(R) - u(R) \frac{\partial}{\partial R} u^*(R) \right), \quad (4.19)$$

which is in the direction of the transverse gradient of the phase of the beam. The OAM per photon in the propagation direction is then given by

$$L = \int dR \|R \times P(R)\|. \quad (4.20)$$

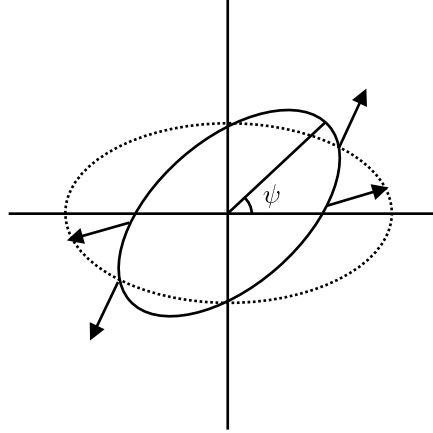


**Figure 4.1:** Two ellipses of constant intensity and phase of a Gaussian mode with general astigmatism. On the solid ellipse the intensity is constant; on the dashed ellipse the phase is constant. The ellipse of constant intensity is rotated over an angle  $\psi$  with respect to the ellipse of constant phase. On four points on the ellipse of constant intensity the direction of the transverse-momentum density is represented by arrows. These arrows point in the direction of the gradient of the phase, which is chosen outwards in this case. They represent the direction in which the intensity will move. Because the ellipses of constant intensity and phase are oriented differently, it can be seen from the arrows that upon propagation the beam will tumble, giving rise to orbital angular momentum.

In Fig. 4.1 two ellipses of constant intensity and phase of a Gaussian mode with general astigmatism are depicted. On four points the direction of the transverse-momentum density is represented by arrows. That the beam has OAM can be understood from the expression for the OAM in Eq. (4.20) and the fact that the arrows have arms. In Fig. 4.1 the direction of the gradient of the phase is chosen to be outwards, corresponding to a situation where the beam has passed the two focal planes. We see that upon propagation the intensity ellipse will try to disalign with the phase ellipse. In case that the gradient of the phase is directed inwards, corresponding to a situation before the focal planes, the intensity ellipse tries to align with the phase ellipse.

By inserting the general expression for the fundamental mode in Eq. (4.15) in Eq. (4.20) we obtain the OAM of the fundamental mode. We find that

$$L_{00} = \frac{\hbar}{4}(\alpha_{1s} - \alpha_{1l}) \left( \frac{1}{\alpha_{0l}} - \frac{1}{\alpha_{0s}} \right) \sin(2\psi), \quad (4.21)$$

where  $\alpha_{0l}$  and  $\alpha_{0s}$  are the eigenvalues of  $\alpha_0$ , and where  $\alpha_{1l}$  and  $\alpha_{1s}$  are the eigenvalues of  $\alpha_1$ . The angle  $\psi$  (this Greek letter is not a matrix) is the difference in orientation of the astigmatic phase and intensity distributions. For non-zero OAM it is necessary that indeed both the intensity and the phase distributions are astigmatic, since the eigenvalues of both  $\alpha_0$  and  $\alpha_1$  must be different. Furthermore, it is also necessary that the astigmatic intensity and phase distributions differ in orientation, because the angle  $\psi$  must be different from 0 or  $\pi/2$ .

This corresponds to the case of general astigmatism, for which  $\alpha_0$  and  $\alpha_1$  do not commute. In Section 4.5 we derive the following matrix expression for the OAM of the fundamental mode:

$$L_{00} = \frac{\hbar}{2} \text{Tr}(\varepsilon \alpha_1 \alpha_0^{-1}) , \quad (4.22)$$

where

$$\varepsilon = \begin{pmatrix} 0 & +1 \\ -1 & 0 \end{pmatrix} \quad (4.23)$$

is the two-dimensional anti-symmetric tensor. This expression is equivalent to (4.21). We will also see that the OAM is conserved indeed, which is not evident from Eq. (4.21), since  $\alpha$  is  $z$  dependent.

## 4.3 Operator method

### 4.3.1 Coordinate picture

Recall that the excited states of the quantum harmonic oscillator are obtained by the repeated application of the raising operator on the ground state. In a similar fashion, we obtain astigmatic higher-order modes by operating on the state  $|u_{00}\rangle$  of the astigmatic fundamental mode. This generalises the operator method of Nienhuis and Allen [3]. In an arbitrary transverse plane  $z$  we define ladder operators that are linear combinations of the coordinate operator  $\hat{R} = (\hat{x}, \hat{y})$  and the momentum operator  $\hat{P} = (\hat{p}_x, \hat{p}_y)$ . In Eqs. (4.4) and (4.5), the vector  $\hat{A}(z)$  of lowering operators  $\hat{a}_1(z)$  and  $\hat{a}_2(z)$ , and the corresponding vector  $\hat{A}^\dagger(z)$  of raising operators, are given, where the  $z$ -dependent matrices  $\alpha(z)$  and  $\beta(z)$  are given in Eq. (4.14). It follows from Eq. (4.11), that, when  $\hat{a}_1(z)$ ,  $\hat{a}_2(z)$ ,  $\hat{a}_1^\dagger(z)$  or  $\hat{a}_2^\dagger(z)$  is applied to a solution  $|u(z)\rangle$  of the paraxial wave equation, another solution is obtained. The ladder operators must satisfy the boson commutation rules

$$[\hat{a}_1(z), \hat{a}_1^\dagger(z)] = [\hat{a}_2(z), \hat{a}_2^\dagger(z)] = 1 , \quad [\hat{a}_1(z), \hat{a}_2(z)] = [\hat{a}_1(z), \hat{a}_2^\dagger(z)] = 0 . \quad (4.24)$$

The higher-order modes are obtained by operating with the raising operators  $\hat{a}_1^\dagger(z)$  and  $\hat{a}_2^\dagger(z)$  on the state of the fundamental mode  $|u_{00}(z)\rangle$ . We have

$$|u_{nm}(z)\rangle = \frac{1}{\sqrt{n!m!}} (\hat{a}_1^\dagger(z))^n (\hat{a}_2^\dagger(z))^m |u_{00}(z)\rangle , \quad (4.25)$$

where  $|u_{nm}(z)\rangle$  is the state of the higher-order mode with mode numbers  $n, m = 0, 1, 2, \dots$ . The normalised profile of a higher-order mode is given by the wave function in the coordinate representation of its state  $\langle R | u_{nm}(z) \rangle$ . It follows from the commutation rules (4.24) and from Eq. (4.11), that the higher-order modes together with the fundamental mode constitute a complete set of solutions of the paraxial wave equation.

The commutation rules (4.24) are satisfied for all values of  $z$  as soon as they are satisfied for a single value of  $z$ , as follows from Eq. (4.11). From the commutation rules  $[\hat{x}, \hat{p}_x] = [\hat{y}, \hat{p}_y] = i$  for  $\hat{R}$  and  $\hat{P}$ , one finds that the commutation rules (4.24) require that

$$\beta \alpha_0 \beta^\dagger = 1 . \quad (4.26)$$

It follows, for all values of  $z$ , that  $\beta^\dagger \beta = \alpha_0^{-1}$ , and that  $\beta$  is invertible. Since  $\alpha_0$  is real, symmetric and positive definite, it uniquely defines a real, symmetric and positive-definite matrix  $\gamma$ , so that

$$\gamma^2 = \alpha_0^{-1} = \beta^\dagger \beta . \quad (4.27)$$

The real eigenvalues of  $\gamma$  are the two widths of the elliptic spot size of the intensity distribution of the fundamental mode profile  $u_{00}(R)$ . The requirement (4.27) is satisfied by writing

$$\beta = \sigma \gamma , \quad (4.28)$$

where  $\sigma$  is a unitary matrix. The  $z$  dependence of the matrices  $\gamma$ ,  $\alpha_1$  and  $\sigma$  can be obtained by using Eq. (4.14). The fundamental mode is determined by choosing  $\alpha$ , or, equivalently,  $\gamma$  and  $\alpha_1$ , in one transverse plane. Higher-order modes are determined by the additional choice of the unitary matrix  $\sigma$  for one plane  $z$ .

### 4.3.2 Momentum picture

The ladder operators are linear combinations of the coordinate operator  $\hat{R}$  and the momentum operator  $\hat{P}$ , which play a similar role. In the coordinate picture we focus on solutions  $u(R, z)$  of the paraxial wave equation. The momentum picture of the solution is given by  $\tilde{u}(P, z)$ , which is the Fourier transform of  $u(R, z)$ . The vector (4.4) of lowering operators is rewritten as

$$\hat{A} = \frac{1}{\sqrt{2}} \kappa (\hat{R} + i\mu \hat{P}) , \quad (4.29)$$

and we see that

$$\kappa = \beta \alpha , \quad \mu = \alpha^{-1} . \quad (4.30)$$

We write  $\mu = \mu_0 + i\mu_1$ , where  $\mu_0$  and  $\mu_1$  are real and symmetric matrices. Moreover,  $\mu_0$  is positive definite. The commutation rules for the ladder operators are satisfied when  $\kappa \mu_0 \kappa^\dagger = 1$ , from which it follows that  $\kappa^\dagger \kappa = \mu_0^{-1}$ , so that  $\kappa$  is invertible. In full analogy to the decomposition (4.28) of  $\beta$  in a unitary and a real symmetric matrix, we write

$$\kappa = \tau \delta , \quad (4.31)$$

with  $\tau$  unitary, and  $\delta$  real, symmetric and positive definite, so that  $\delta^2 = \mu_0^{-1}$ . The real eigenvalues of the matrix  $\delta$  are the two widths of the elliptic momentum distribution. In the momentum picture the fundamental mode is determined by  $\mu$ , or, equivalently, by  $\delta$  and  $\mu_1$ , while the higher-order modes also require  $\tau$ .

For later use we want to express the matrices  $\gamma$ ,  $\alpha_1$  and  $\sigma$  of the coordinate picture in their momentum-picture analogues  $\delta$ ,  $\mu_1$  and  $\tau$ . The two pictures are related by Eq. (4.30), from which it follows that

$$\beta = \kappa \mu , \quad (4.32)$$

and

$$\alpha_1 \mu_0 = \alpha_0 \mu_1 , \quad \mu_0 \alpha_1 = \mu_1 \alpha_0 . \quad (4.33)$$

Because  $\gamma^2 = \alpha_0^{-1}$  and  $\delta^2 = \mu_0^{-1}$ , we find from (4.33) that

$$\gamma^2 \alpha_1 = \mu_1 \delta^2 . \quad (4.34)$$

We use Eqs. (4.27), (4.32) and (4.31), to find that

$$\gamma^2 = \mu^\dagger \delta^2 \mu . \quad (4.35)$$

From Eqs. (4.28), (4.32) and (4.31), we find that

$$\sigma = \tau \delta \mu \gamma^{-1} . \quad (4.36)$$

## 4.4 Properties of modes

### 4.4.1 Propagation of the fundamental mode

In the coordinate picture it is convenient to write the fundamental mode profile as

$$u_{00}(R, z) = \frac{1}{\sqrt{\pi \det \beta}} \exp\left(-\frac{1}{2} R \alpha R\right) . \quad (4.37)$$

From Eqs. (4.14) and (4.28), we see that this expression differs from Eq. (4.15) only by a constant phase factor  $\sqrt{\det \sigma(0)}$ . The fundamental mode profile in the momentum picture is the Fourier transform of (4.37)

$$\tilde{u}_{00}(P, z) = \frac{1}{\sqrt{\pi \det \kappa}} \exp\left(-\frac{1}{2} P \mu P\right) . \quad (4.38)$$

From the relation between the coordinate and the momentum picture in Eq. (4.30), together with (4.14), the  $z$  dependence of  $\mu$  is found as

$$\mu(z) = \mu(0) + \frac{iz}{k} , \quad (4.39)$$

or, equivalently,

$$\delta(z) = \delta(0) , \quad \mu_1(z) = \mu_1(0) + \frac{z}{k} . \quad (4.40)$$

The fundamental mode is characterised by selecting  $\delta$  and  $\mu_1$  in one transverse plane. Now we use Eqs. (4.35) and (4.34) to express  $\gamma(z)$  and  $\alpha_1(z)$  in terms of  $\delta(0)$  and  $\mu_1(0)$ . We find that

$$\gamma^2(z) = \delta^{-2} + \left(\mu_1(0) + \frac{z}{k}\right) \delta^2 \left(\mu_1(0) + \frac{z}{k}\right) , \quad (4.41)$$

$$\gamma^2(z) \alpha_1(z) = \left(\mu_1(0) + \frac{z}{k}\right) \delta^2 , \quad (4.42)$$

where we write  $\delta$  for  $\delta(0)$  since  $\delta$  is independent of  $z$ . In each transverse plane the matrix  $\gamma$  determines the intensity distribution, while  $\alpha_1$  determines the phase distribution of the fundamental mode. In the limit of large  $z$  we find that

$$\gamma^2(z) \rightarrow \frac{z^2}{k^2} \delta^2 , \quad \alpha_1(z) \rightarrow \frac{k}{z} . \quad (4.43)$$

The first identity is a generalisation of the Fourier relation between the near field and the far field. The phase distribution, as determined by  $\alpha_1$ , becomes circular for large  $z$ . This is understandable, because in the far field the beam profile in the focal region can be considered a point source, which produces circular phase fronts.

The propagation properties of the fundamental mode in the coordinate picture are determined by  $\gamma(z)$  and  $\alpha_1(z)$ . In general, the fundamental mode has two focal planes, which are defined by the requirement that the determinant of  $\alpha_1$  vanishes. Then the curvature of the phase fronts vanishes in one transverse direction, and the curves of constant phase are parallel lines. When the determinant of  $\alpha_1$  vanishes, so does the determinant of  $\mu_1$ , which follows from Eq. (4.33). It follows from Eq. (4.40), that  $\det \mu_1(z) = 0$  for the two values of  $z$  that coincide with an eigenvalue of  $\mu_1(0)$  times  $-k$ . We consider the evolution of ellipses of constant intensity during propagation. The ellipses are the curves of constant  $R\alpha_0R$ . Since  $\alpha_0 = \gamma^{-2}$ , the orientation and ellipticity of the ellipses are determined by the eigenvectors and eigenvalues of  $\gamma^2$ . We take the  $x$  and  $y$  axis to coincide with the eigenvectors of  $\mu_1$ , and redefine  $z$  such that the plane  $z = 0$  is exactly in between the two focal planes. Then

$$\mu_1(0) = \begin{pmatrix} m_1 & 0 \\ 0 & -m_1 \end{pmatrix}, \quad (4.44)$$

with  $m_1$  real. The focal planes are then the planes  $z = \pm km_1$ .

In the case of simple astigmatism,  $\delta$  commutes with  $\mu_1(0)$ , so that it is diagonal. The matrix  $\gamma^2(z)$  in Eq. (4.41) is then diagonal for all  $z$ , and the diagonal elements have a hyperbolic dependence on  $z$ . In a focal plane, one of the hyperbolas attains its minimum value. When the diagonal elements of  $\delta$  are different, the slopes of the asymptotes of the hyperbolas differ, so that for two values of  $z$  the intensity distribution is circular. Equation (4.43) shows that the ellipses of constant intensity at  $z \rightarrow \pm\infty$  are identical. When  $m_1$  vanishes, there is only one focal plane, and we see from Eq. (4.41) that  $\gamma^2(z) = \gamma^2(-z)$ . This symmetry is not present when  $m_1 \neq 0$ .

For general astigmatism  $\delta$  is not diagonal. By using that  $\alpha_0^{-1} = \gamma^2$  and  $\mu_0^{-1} = \delta^2$  it follows from (4.33) that  $[\gamma^2, \alpha_1] = [\mu_1, \delta^2]$ . From Eq. (4.40) it follows that when  $\delta^2$  and  $\mu_1$  do not commute in one transverse plane, then they do not commute in any other plane. This proves that for general astigmatism the curves of constant intensity are never circular. When propagating from the plane  $z = -\infty$  to  $z = \infty$ , the long axis of the ellipse rotates over  $180^\circ$ , and from Eq. (4.43) it follows that the ellipticity in the limits  $z \rightarrow \pm\infty$  is identical. As an example, we assume that the basis in which  $\delta$  is diagonal, is rotated over  $45^\circ$  with respect to the  $x$  and  $y$  direction, so that the orientations of  $\delta$  and  $\mu_1$  are maximally different. Then also the general astigmatism is maximal. We parametrise without loss of generality,

$$\delta = \frac{1}{2} \begin{pmatrix} d_+ + d_- & d_+ - d_- \\ d_+ - d_- & d_+ + d_- \end{pmatrix}, \quad (4.45)$$

where  $d_+ > d_- > 0$  are the eigenvalues of  $\delta$ . For the case  $d_+ = \sqrt{3}d_-$  an ellipse of constant intensity is shown in Fig. 4.2 for different transverse planes. When propagating from  $z = -\infty$  to  $z = 0$ , the long axis of the ellipse rotates over  $90^\circ$ , and the ellipticity in the plane  $z = 0$  is the same as for  $z \rightarrow \pm\infty$ . This is confirmed by substituting (4.44) and (4.45) in Eq. (4.41), from which we find after explicit calculation that

$$\gamma^2(0) = \delta^{-2} + \mu_1(0)\delta^2\mu_1(0) = (1 + s^2)\delta^{-2}, \quad s = m_1d_+d_-. \quad (4.46)$$

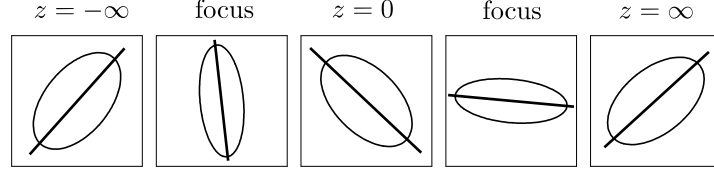


**Figure 4.2:** Ellipse of constant intensity of the fundamental mode in different planes  $z$  for the case that the general astigmatism is maximal. The ellipses in different planes are not to scale.

From Eq. (4.43) it then follows that  $\gamma^2(\pm\infty) \propto \gamma^{-2}(0)$ . The inversion of  $\gamma$  corresponds to a rotation of the ellipse over  $90^\circ$ , where the ellipticity remains the same. We can see from Eqs. (4.41), (4.44) and (4.45) that replacing  $z$  by  $-z$  is identical to interchanging the diagonal elements of  $\gamma^2$ . As a consequence, the ellipse in an arbitrary plane  $z$  is the image of the ellipse in the plane  $-z$  as obtained by a reflection in the line  $x = y$ .

The curves of constant phase are defined by  $R\alpha_1 R$  constant. In a focal plane one of the eigenvalues of  $\alpha_1$  is zero, and the curves of constant phase are lines parallel to the corresponding eigenvector. In the first and the second focal plane  $\mu_1$  takes the form

$$\mu_1 = \begin{pmatrix} 0 & 0 \\ 0 & -2m_1 \end{pmatrix}, \quad \mu_1 = \begin{pmatrix} 2m_1 & 0 \\ 0 & 0 \end{pmatrix}, \quad (4.47)$$

respectively. Writing  $\vec{e}_x$  and  $\vec{e}_y$  for the  $x$  and  $y$  direction, respectively, it follows from Eq. (4.33) that in the first focal plane  $\alpha_1 \mu_0 \vec{e}_x = 0$ , while in the second focal plane  $\alpha_1 \mu_0 \vec{e}_y = 0$ . Therefore,  $\mu_0 \vec{e}_x$  and  $\mu_0 \vec{e}_y$  determine the direction of the parallel lines of constant phase in the first and the second focal plane, respectively. For simple astigmatism  $\delta^2 = \mu_0^{-1}$  is diagonal, so that the angle between the column vectors is  $90^\circ$ . Then the parallel lines of constant phase in one focal plane are orthogonal to the parallel lines in the other focal plane. When  $\delta$  is given by Eq. (4.45) we find that the angle  $\psi_0$  between the lines in the two focal planes is given by

$$\cos \psi_0 = \frac{d_+^4 - d_-^4}{d_+^4 + d_-^4}, \quad (4.48)$$

and we see that for maximal astigmatism the lines in the two focal planes are not orthogonal. In the plane  $z = 0$ , we can calculate  $\alpha_1(0)$  by using (4.42) and (4.46), with the result

$$\alpha_1(0) = \frac{d_+^2 d_-^2}{1 + s^2} \mu_1(0). \quad (4.49)$$

In this plane, the lines of constant phase are hyperbolas, with orthogonal asymptotes.

#### 4.4.2 Higher-order modes in one transverse plane

The higher-order modes are obtained by operating with the raising operator on the fundamental mode. The lowering operator in Eq. (4.4) is written in a more transparent way by using

the operator identity

$$\exp\left(\frac{i}{2}\hat{R}\alpha_1\hat{R}\right)\hat{P}\exp\left(-\frac{i}{2}\hat{R}\alpha_1\hat{R}\right)=\hat{P}-\alpha_1\hat{R}. \quad (4.50)$$

In the coordinate picture we write

$$\hat{A}=\exp\left(\frac{i}{2}\hat{R}\alpha_1\hat{R}\right)\sigma\hat{B}\exp\left(-\frac{i}{2}\hat{R}\alpha_1\hat{R}\right), \quad (4.51)$$

where the real operators  $\hat{b}_x$  and  $\hat{b}_y$  that compose the vector

$$\hat{B}=\frac{1}{\sqrt{2}}\left(\frac{1}{\gamma}\hat{R}+i\gamma\hat{P}\right) \quad (4.52)$$

have the familiar form of the lowering operator of a quantum-mechanical harmonic oscillator. The corresponding expression for the raising operator is

$$\hat{A}^\dagger=\exp\left(\frac{i}{2}\hat{R}\alpha_1\hat{R}\right)\sigma^*\hat{B}^\dagger\exp\left(-\frac{i}{2}\hat{R}\alpha_1\hat{R}\right). \quad (4.53)$$

We consider the operation of the raising operator on the fundamental mode in the coordinate representation in an arbitrary transverse plane. We see that first the phase distribution  $\exp(iR\alpha_1R/2)$  in the expression for the fundamental mode in Eq. (4.1) is removed, so that the real operator  $\hat{B}^\dagger$  operates on a real function. Finally the same phase factor  $\exp(iR\alpha_1R/2)$  is reinserted again, so that all the modes have this phase factor in common.

The unitary matrix  $\sigma$  expresses the freedom in the choice of the ladder operators. For non-astigmatic modes,  $\sigma$  determines whether the higher-order modes are HG or LG, or intermediate modes. In characterising  $\sigma$  we point out an analogy with polarisation. It is intuitively obvious that the HG and LG modes are analogous to linear and circular polarisation, respectively, while the intermediate modes are analogous to elliptic polarisation. It is customary to represent a normalised polarisation vector  $\vec{e}$  in the  $xy$  plane by a point on the unit sphere, which specifies a real unit vector,

$$\vec{u}=(\cos\phi\sin\theta,\sin\phi\sin\theta,\cos\theta)\equiv(u_1,u_2,u_3), \quad (4.54)$$

where  $\theta$  and  $\phi$  are the spherical angles of the point on the sphere (thus the Greek letters  $\theta$  and  $\phi$  are not used for matrices). The vector  $\vec{u}$  is the normalised Stokes vector [1], with components

$$u_1=e_x^*e_x-e_y^*e_y, \quad u_2=e_x^*e_y+e_xe_y^*, \quad u_3=-ie_x^*e_y+ie_xe_y^*. \quad (4.55)$$

The first two components are the degrees of linear polarisation parallel to the  $x$  and the  $y$  axis, and under  $45^\circ$ , and  $u_3$  is the degree of circular polarisation. Each point on the sphere uniquely represents a polarisation apart from its overall phase. The sphere is called the Poincaré sphere. A point on the equator of the sphere ( $\theta=\pi/2$ ) represents linear polarisation, which is oriented in a direction that makes an angle  $\phi/2$  with the  $x$  axis. The poles of the sphere ( $\theta=0$ ,

4. *Orbital angular momentum of general astigmatic modes*

and  $\theta = \pi$ ) represent circular polarisation  $\vec{e} = \vec{e}_{\pm} = (\vec{e}_x \pm i\vec{e}_y)\sqrt{2}$ . For arbitrary values of the angles  $\theta$  and  $\phi$ , the point on the sphere represents the elliptic polarisation,

$$\vec{e}_1(\theta, \phi) = v\vec{e}_+ + w\vec{e}_-, \quad (4.56)$$

with  $v = \cos(\theta/2)\exp(-i\phi/2)$  and  $w = \sin(\theta/2)\exp(i\phi/2)$ . The polarisation

$$\vec{e}_2(\theta, \phi) = -w^*\vec{e}_+ + v^*\vec{e}_-, \quad (4.57)$$

which is orthogonal to  $\vec{e}_1$ , corresponds to the antipodal position on the Poincaré sphere.

In a similar way we can characterise the possible choices of a basis of transverse modes as a point on the sphere, which we will call the Hermite-Laguerre sphere. For this we have to specify the matrix  $\sigma$  for each value of  $\theta$  and  $\phi$ . Equation (4.53) gives the two raising operators  $\hat{a}_1^\dagger$  and  $\hat{a}_2^\dagger$  as linear combinations of the operators  $\hat{b}_x^\dagger$  and  $\hat{b}_y^\dagger$ , when we write the real operator (4.52) in terms of its components as  $\hat{B} = (\hat{b}_x, \hat{b}_y)$ . When we likewise decompose  $\sigma\hat{B}$  as  $(\hat{b}_1, \hat{b}_2)$ , we simply require that the raising operators  $\hat{b}_1^\dagger$  and  $\hat{b}_2^\dagger$  are related to  $\hat{b}_x^\dagger$  and  $\hat{b}_y^\dagger$  by the same linear transformation that relates  $\vec{e}_1$  and  $\vec{e}_2$  to  $\vec{e}_x$  and  $\vec{e}_y$ , apart from an overall phase factor. Because  $\sigma$  is unitary, it is sufficient to specify only the first row of  $\sigma$ , which defines  $\hat{a}_1$  as

$$\hat{a}_1 = \exp\left(\frac{i}{2}\hat{R}\alpha_1\hat{R}\right) (\sigma_{1x}\hat{b}_x + \sigma_{1y}\hat{b}_y) \exp\left(-\frac{i}{2}\hat{R}\alpha_1\hat{R}\right). \quad (4.58)$$

In analogy to Eq. (4.56), this corresponds to the point on the Hermite-Laguerre sphere specified by

$$\begin{aligned} \cos\phi \sin\theta &= \sigma_{1x}\sigma_{1x}^* - \sigma_{1y}\sigma_{1y}^*, \\ \sin\phi \sin\theta &= \sigma_{1x}\sigma_{1y}^* + \sigma_{1y}\sigma_{1x}^*, \\ \cos\theta &= -i\sigma_{1x}\sigma_{1y}^* + i\sigma_{1y}\sigma_{1x}^*. \end{aligned} \quad (4.59)$$

Then the operator  $\hat{a}_2$  corresponds automatically to the antipodal point on the sphere. Hence, strictly speaking, it is sufficient to consider only the matrices  $\sigma$  that correspond to points on the northern hemisphere. Since the phase constants of the modes are unimportant, the phases of the rows of  $\sigma$  are not relevant.

Choices of  $\sigma$  corresponding to a point on the equator of the Hermite-Laguerre sphere, give rise to HG-like modes, while the poles correspond to LG-like modes. For simplicity we take the  $x$  and  $y$  direction along the eigenvectors of  $\gamma$ . The diagonal elements of  $\gamma$  are  $\gamma_x$  and  $\gamma_y$ . For  $\sigma$  we take the unit matrix, for which  $\theta = \pi/2$  and  $\phi = 0$ , which is on the equator. This means that the excitation directions of the higher-order HG modes have the same orientation as the elliptic intensity distribution determined by  $\gamma$ . By using Eqs. (4.25) and (4.1) we find that the normalised higher-order mode functions  $\langle R|u_{nm}\rangle$  are given by

$$\langle R|u_{nm}\rangle = \frac{1}{\sqrt{n!m!\pi 2^{n+m}\gamma_x\gamma_y}} H_n\left(\frac{x}{\gamma_x}\right) H_m\left(\frac{y}{\gamma_y}\right) \exp\left(-\frac{1}{2}R\alpha R\right), \quad (4.60)$$

where  $R = (x, y)$  and

$$H_n(\xi) = \exp(\xi^2/2) \left(\xi - \frac{\partial}{\partial \xi}\right)^n \exp(-\xi^2/2), \quad n = 0, 1, 2, \dots, \quad (4.61)$$

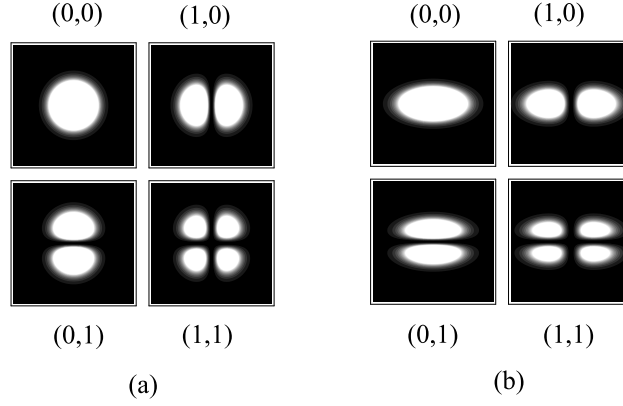


**Figure 4.3:** Intensity profiles of Hermite-Gaussian modes with mode numbers  $(n,m)$ . In (a) the modes are non-astigmatic ( $\gamma_x = \gamma_y$ ), while in (b) the modes are astigmatic with  $\gamma_x/\gamma_y = \sqrt{3}$ .

are the Hermite polynomials. In Fig. 4.3(a) the intensity profiles of the lowest-order modes are given in the non-astigmatic case, for which  $\gamma_x = \gamma_y$ . These are the familiar HG modes. In the astigmatic case  $\gamma_x \neq \gamma_y$ , and the  $x$  and  $y$  direction are scaled differently compared with the non-astigmatic modes, as can be seen in Fig. 4.3(b).

Now we assume that  $\sigma$  corresponds to the point on the equator with  $\phi = \pi/2$ . Then the orientation of the excitation directions of the higher-order HG modes differs from the orientation of the elliptic intensity distribution by an angle of  $\pi/4$ . In Fig. 4.4(a) the intensity profiles of the modes are given for the non-astigmatic case. We see that the modes can be obtained from Fig. 4.3(a) by a rotation over an angle of  $\pi/4$ . The astigmatic case is given in Fig. 4.4(b). We see that again the  $x$  and the  $y$  direction are scaled differently, but compared with Fig. 4.3(b), the orientation of astigmatism is different from the orientation of the excitation directions of the modes.

Now we consider the north pole ( $\theta = 0$ ), which gives rise to LG-like modes. When we compare the non-astigmatic case in Fig. 4.5(a) with the astigmatic case in Fig. 4.5(b), we see that the  $x$  and the  $y$  direction are scaled differently. The non-astigmatic LG modes have circular symmetry, so that their orientation before rescaling is immaterial.

As an example of modes that are intermediate between the HG and LG modes we consider the modes where the point on the Hermite-Laguerre sphere is between the equator and the pole at azimuthal angle  $\phi = 0$ . For simplicity we only consider the non-astigmatic case, for which  $\gamma$  is isotropic. The mode profiles of the modes contain phase singularities for each point between the pole and the equator, except at the equator itself. When the pole is approached, the phase singularities combine at the origin and give rise to the familiar azimuthal angle dependence  $\exp[i(n-m)\phi]$  in the mode profiles of the LG modes, which are OAM eigenfunctions with eigenvalues  $\hbar(n-m)$ . Starting from a HG mode with  $n \neq m$  at  $\theta = \pi/2$ , the intensity distribution becomes less anisotropic until at the north pole it is a LG mode, with circular symmetry. In Fig. 4.6 the intensity profiles of four modes are

4. Orbital angular momentum of general astigmatic modes

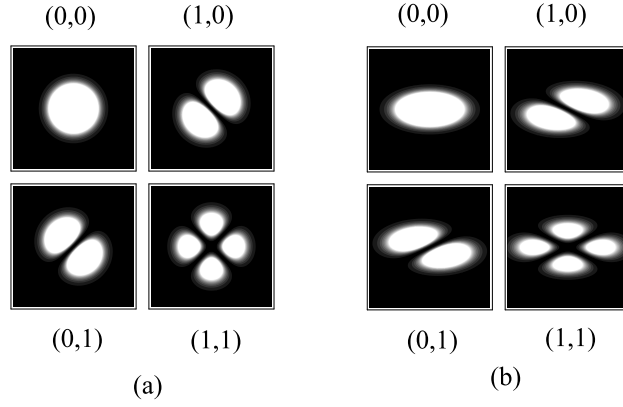


**Figure 4.4:** Intensity profiles of Hermite-Gaussian modes with mode numbers  $(n, m)$ . In (a) the modes are non-astigmatic, while in (b) the modes are astigmatic, where the orientation of astigmatism differs from the orientation of the excitation directions by an angle of  $\pi/4$ . In (b) we have  $\gamma_x/\gamma_y = \sqrt{3}$ .

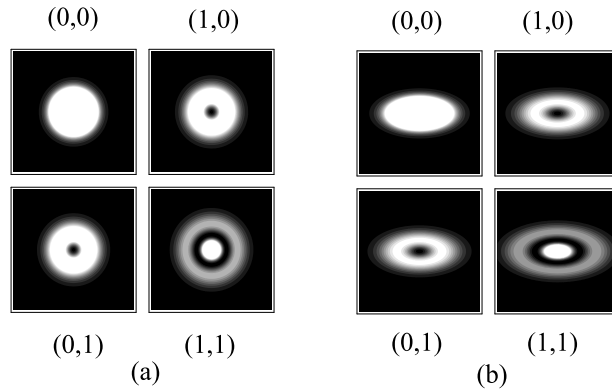


**Figure 4.5:** Intensity profiles of Laguerre-Gaussian modes with mode numbers  $(n, m)$ . In (a) the modes are non-astigmatic, while in (b) the modes are astigmatic with  $\gamma_x/\gamma_y = \sqrt{3}$ .

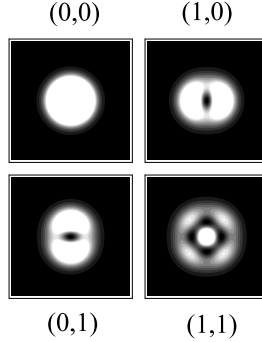


**Figure 4.6:** Intensity profiles of non-astigmatic modes with mode numbers  $n$  and  $m$ , and which are represented by the point between the equator and the north pole with  $\theta = \pi/6$  and  $\phi = 0$ .

given at the polar angle  $\theta = \pi/6$ . We see that indeed the modes in Fig. 4.6 are intermediate between the HG and LG modes in Figs. 4.3(a) and 4.5(a), respectively. The profiles of the  $(1,0)$  and  $(0,1)$  mode contain a phase singularity at the origin, while the  $(1,1)$  mode has four phase singularities, which are located in the holes of the intensity distribution. Modes that are intermediate between HG and LG modes have also been discussed elsewhere [14, 15].

#### 4.4.3 Propagation of the higher-order modes

The  $z$  dependence of the higher-order modes is determined by the matrix  $\sigma(z)$ , in addition to the matrices  $\gamma(z)$  and  $\alpha_1(z)$  discussed in Section 4.4.1. In Section 4.4.2 we demonstrated that the matrix  $\sigma$  can be represented by two opposite points on the Hermite-Laguerre sphere. A description of the propagation of the higher-order modes requires the specification of these points on the sphere as a function of  $z$ . We obtain the  $z$  dependence of  $\sigma$  by using Eqs. (4.36) and (4.40). From Eqs. (4.30) and (4.14), it follows that  $\kappa$  is independent of  $z$ . Then it follows from Eqs. (4.31) and (4.40), that the matrix  $\tau$ , which determines the nature of the higher-order modes in the momentum picture, is independent of  $z$ . We find that the  $z$  dependence of  $\sigma$  is given by

$$\sigma(z) = \tau \delta \left( \delta^{-2} + i\mu_1(0) + \frac{iz}{k} \right) \gamma^{-1}(z). \quad (4.62)$$

We see that upon propagation the nature of the higher-order modes changes. From Eq. (4.43) it follows that for  $z \rightarrow \pm\infty$  we have  $\sigma(z) \rightarrow \pm i\tau$ . The factor  $i$  represents the far-field Gouy phase. The representation of  $\sigma(z)$  on the Hermite-Laguerre sphere is a trajectory  $\vec{u}(z)$  of unit vectors. The limits  $\vec{u}(\pm\infty)$  correspond to the Hermite-Laguerre representation of the unitary matrix  $\tau$ . The choice of  $\tau$  determines the nature of the higher-order modes in the far field.

Alternatively, we may choose  $\sigma$  for a single value of  $z$ . We specify  $\sigma$  by the angles  $\theta = \pi/2$  and  $\phi = 0$ , at the plane  $z = 0$ , which is halfway between the focal planes. Then  $\sigma$  is basically the unit matrix in this plane. We consider the evolution of  $\sigma$  in the case that the angle of orientation between  $\delta$  and  $\mu_1(0)$  is maximally different, and write  $\mu_1(0)$  and  $\delta$  as

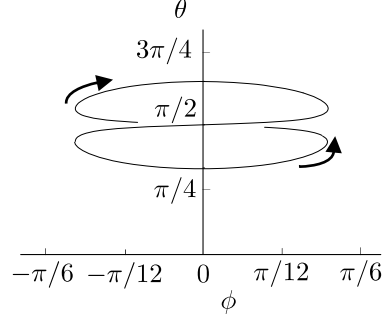


**Figure 4.7:** The trajectory of the point on the Hermite-Laguerre sphere that represents the matrix  $\sigma$ . Between the focal planes at  $z = 0$ , and at  $z = \pm\infty$ , the point is located at  $\theta = \pi/2$  and  $\phi = 0$ .

in Eqs. (4.44) and (4.45), respectively. In Fig. 4.7 the trajectory of the point on the sphere is given for the case that  $s = m_1 d_+ d_- = 4\sqrt{3}$  and  $d_+ = \sqrt{3}d_-$ . For  $z = 0$  the point is on the equator, while for negative and positive values of  $z$  the point is on the southern and northern hemisphere, respectively. For  $z \rightarrow \pm\infty$  the point approaches the equator. This implies that, except for  $z = 0$  and  $z = \pm\infty$ , the modes contain phase singularities, as we discussed in Section 4.4.2.

Now we express the point on the Hermite-Laguerre sphere describing  $\sigma$  at  $z = \pm\infty$  in terms of the point representing  $\sigma$  at  $z = 0$ , for the case that the angles of orientation of  $\mu_1(0)$  and  $\delta$  are maximally different. Using (4.46) and the expressions for  $\mu_1(0)$  and  $\delta$  in Eqs. (4.44) and (4.45), respectively, we find that

$$\sigma(0) = \frac{\tau}{\sqrt{1+s^2}} \begin{pmatrix} 1+is & 0 \\ 0 & 1-is \end{pmatrix}, \quad (4.63)$$

where  $s = m_1 d_+ d_-$ . Since  $\sigma(\pm\infty) = \pm i\tau$ , this equation gives a relation between  $\sigma(0)$  and  $\sigma(\pm\infty)$ . The point on the sphere can be given in terms of its Cartesian components as  $\vec{u} = (u_1, u_2, u_3)$ , as in Eq. (4.54). Writing  $\vec{u}(0)$  and  $\vec{u}(\infty)$  for the coordinates of the point on the sphere at  $z = 0$  and  $z = \pm\infty$ , respectively, we find that

$$\begin{aligned} u_1(\infty) &= u_1(0), \\ u_2(\infty) &= \frac{1-s^2}{1+s^2}u_2(0) + \frac{2s}{1+s^2}u_3(0), \\ u_3(\infty) &= \frac{1-s^2}{1+s^2}u_3(0) - \frac{2s}{1+s^2}u_2(0). \end{aligned} \quad (4.64)$$

The point at  $z = \pm\infty$  is obtained from the point at  $z = 0$  by a rotation about the 1 axis over an angle  $2\arctan(s)$ . We see that only when  $\theta(0) = \pi/2$  and  $\phi(0) = 0$ , as in Fig. 4.7, the location of the point on the sphere is the same for  $z = 0$  as for  $z = \pm\infty$ .

When, for  $s = 1$ , the point is on the north pole at  $z = 0$ , it approaches the equator at  $\phi = \pi/2$  for  $z \rightarrow \pm\infty$ . In the present case, when the point is on the equator with  $\phi = 0$ , the

excitation directions of the higher-order modes have the same orientation as the elliptic phase distribution determined by  $\mu_1$ , while for  $\phi = \pi/2$  the angles of orientation differ by  $\pi/4$ . The angles of orientation of the elliptic momentum and phase distribution, as determined by  $\delta$  and  $\mu_1$ , respectively, differ also by  $\pi/4$  in the present case. Therefore, the orientation associated with  $\sigma(\pm\infty)$  is the same as the orientation of  $\delta$ , and also of  $\gamma(0)$ , which follows from Eq. (4.46). This means that at  $z = 0$  the modes are like the astigmatic LG modes in Fig. 4.5(b), while for  $z \rightarrow \pm\infty$  they become like the astigmatic HG modes in Fig. 4.3(b).

## 4.5 Orbital angular momentum of the higher-order modes

### 4.5.1 Orbital angular momentum of astigmatic modes

We calculate the OAM per photon of a higher-order general astigmatic beam with mode numbers  $(n, m)$ . As indicated in Eqs. (4.19) and (4.20), the OAM is easily expressed by employing the OAM operator, given by

$$\hat{L} = \hbar(\hat{x}\hat{p}_y - \hat{y}\hat{p}_x) = \hbar\hat{R}\varepsilon\hat{P}, \quad (4.65)$$

where the anti-symmetric matrix  $\varepsilon$  is given in Eq. (4.23). We express  $\hat{R}$  and  $\hat{P}$  in terms of  $\hat{A}$  and  $\hat{A}^\dagger$ . We multiply Eq. (4.4) from the left by  $\beta^\dagger$  and Eq. (4.5) by  $\beta^T$ . We add these expressions, and use Eq. (4.27) to find that

$$\hat{R} = \frac{1}{\sqrt{2}}(\beta^\dagger\hat{A} + \beta^T\hat{A}^\dagger). \quad (4.66)$$

Similarly, using Eq. (4.29), we find that

$$\hat{P} = \frac{1}{i\sqrt{2}}(\kappa^\dagger\hat{A} - \kappa^T\hat{A}^\dagger). \quad (4.67)$$

According to Eq. (4.20) the OAM is then found as

$$\begin{aligned} L_{nm} &= \langle u_{nm} | \hat{L} | u_{nm} \rangle \\ &= \frac{\hbar}{4i} [(n+m+2)\text{Tr}(\kappa\varepsilon\beta^\dagger) + (n-m)\text{Tr}(\kappa\varepsilon\beta^\dagger\eta)] \\ &\quad + \frac{\hbar}{4i} [(n+m)\text{Tr}(\beta\varepsilon\kappa^\dagger) + (n-m)\text{Tr}(\beta\varepsilon\kappa^\dagger\eta)], \end{aligned} \quad (4.68)$$

where

$$\eta = \begin{pmatrix} 1 & 0 \\ 0 & -1 \end{pmatrix}. \quad (4.69)$$

We now use the momentum picture, and we express the expectation value in terms of the matrices  $\delta$ ,  $\mu_1$  and  $\tau$ . By using the results in Section 4.3.2, we find

$$\text{Tr}(\kappa\varepsilon\beta^\dagger) = \text{Tr}(\beta\varepsilon\kappa^\dagger) = i\text{Tr}(\varepsilon\delta^2\mu_1), \quad (4.70)$$

and

$$\kappa\varepsilon\beta^\dagger + \beta\varepsilon\kappa^\dagger = \tau(\delta\varepsilon\delta^{-1} + \delta^{-1}\varepsilon\delta)\tau^\dagger + i\tau\delta[\mu_1, \varepsilon]\delta\tau^\dagger. \quad (4.71)$$

By using that  $\delta$  is symmetric, we can show that

$$\delta \varepsilon \delta^{-1} + \delta^{-1} \varepsilon \delta = \varepsilon \text{Tr}(\delta^2) / \det(\delta) \equiv 2r_+ \varepsilon . \quad (4.72)$$

The parameter  $r_+$ , defined in Eq. (4.72), is a measure of the ellipticity of the momentum distribution. For an isotropic distribution corresponding to two equal eigenvalues of  $\delta$ ,  $r_+$  attains the minimum value 1. After substitution of the quantities (4.70)-(4.72) in (4.68), we arrive at the general expression for the OAM

$$\begin{aligned} L_{nm} = & \frac{\hbar}{2}(n+m+1) \text{Tr}(\varepsilon \delta^2 \mu_1) + \frac{\hbar}{2i}(n-m)r_+ \text{Tr}(\tau \varepsilon \tau^\dagger \eta) \\ & + \frac{\hbar}{4}(n-m) \text{Tr}(\tau \delta[\mu_1, \varepsilon] \delta \tau^\dagger \eta) . \end{aligned} \quad (4.73)$$

We see that the OAM in a higher-order astigmatic mode is separated in three contributions. Among the different matrices occurring in Eq. (4.73), only  $\mu_1$  depends on  $z$ , as is expressed by Eq. (4.40). It is easy to verify that this  $z$  dependence does not survive the trace, and we conclude that each of the three terms in (4.73) is invariant under free-space propagation.

The OAM in the mode  $|u_{nm}\rangle$  can also be described in the coordinate picture, in terms of the matrices  $\gamma$ ,  $\alpha_1$  and  $\sigma$ . By using (4.28) and (4.30) to express  $\beta$  and  $\kappa$  in these three matrices, we obtain from Eq. (4.68)

$$\begin{aligned} L_{nm} = & \frac{\hbar}{2}(n+m+1) \text{Tr}(\varepsilon \alpha_1 \gamma^2) + \frac{\hbar}{2i}(n-m)q_+ \text{Tr}(\sigma \varepsilon \sigma^\dagger \eta) \\ & - \frac{\hbar}{4}(n-m) \text{Tr}(\sigma \gamma[\alpha_1, \varepsilon] \gamma \sigma^\dagger \eta) , \end{aligned} \quad (4.74)$$

with  $q_+ = \text{Tr}(\gamma^2)/2\det(\gamma)$ . The expression for the angular momentum operator in (4.65) takes the same form in the momentum and coordinate picture. Therefore, the expressions for the OAM in the momentum and coordinate picture in Eqs. (4.73) and (4.74), respectively, have the same structure, and the qualitative statements about the origin of the OAM are valid in both pictures. The first term on the right-hand side of (4.73) is identical to the one in (4.74), as follows from (4.34), and both terms are independent of  $z$ . However, the last two terms in (4.74) vary with  $z$ , although their sum is constant. Therefore, despite the similarity in form, these last two terms in (4.74) are not identical to the last two terms in (4.73).

By substituting  $n = m = 0$  in (4.74), the expression for  $L_{00}$  in Eq. (4.22) is recovered, as can be checked by recalling that  $\gamma^2 = \alpha_0^{-1}$ . Only when  $\gamma$  and  $\alpha_1$  do not commute, the OAM of the fundamental mode is non-zero. This corresponds indeed to the case of general astigmatism, where the phase and intensity distributions are astigmatic with different orientations. The value of the OAM per photon can be many units of  $\hbar$  [36]. Notice that the OAM of the fundamental mode is independent of  $\sigma$ , as expected.

### 4.5.2 Simple expression for the orbital angular momentum

When the intensity and phase distributions of the fundamental mode in the coordinate picture, as determined by  $\gamma$  and  $\alpha_1$ , respectively, are astigmatic with different orientations this gives rise to a tumbling of the intensity distribution upon propagation. This gives rise to OAM, as

we saw in Section 4.2.4. Also the higher-order modes have an orientation, which is determined by the azimuthal angle of the point on the Hermite-Laguerre sphere representing  $\sigma$ . The interplay of these three orientations gives rise to the complicated structure of the expression for the OAM in the coordinate picture in (4.74). It is then more convenient to use the momentum picture since in this picture these orientations do not change upon propagation.

In order to gain more insight we express the OAM in (4.73) in terms of the matrix elements of the matrices  $\delta$ ,  $\mu_1$  and  $\tau$  of the momentum picture. In the expression for the OAM in Eq. (4.73), the third term on the right-hand side contains the matrix  $\delta$  twice, but  $\mu_1$  only once. Therefore, it is convenient to use a basis for the transverse coordinates in which  $\delta$  is diagonal. We write

$$\delta = \begin{pmatrix} d_+ & 0 \\ 0 & d_- \end{pmatrix}, \quad (4.75)$$

where  $d_+ \geq d_- > 0$ . The angle between the orientations of the astigmatic phase and momentum distributions, as determined by  $\mu_1$  and  $\delta$ , respectively, is  $0 \leq \psi < \pi$ . We take  $z = 0$  as the plane exactly in between the focal planes. The matrix  $\mu_1(0)$  can then be written as

$$\mu_1(0) = m_1 \begin{pmatrix} \cos 2\psi & \sin 2\psi \\ \sin 2\psi & -\cos 2\psi \end{pmatrix}, \quad (4.76)$$

where  $2km_1$  is the distance between the focal planes. For  $\psi = 0$  Eq. (4.44) is recovered. For the matrix  $\tau$  we can write

$$\tau = \begin{pmatrix} \tau_{1x} & \tau_{1y} \\ -\tau_{1y}^* & \tau_{1x}^* \end{pmatrix}, \quad (4.77)$$

with  $\det \tau = |\tau_{1x}|^2 + |\tau_{1y}|^2 = 1$ . The unit determinant can be assumed without loss of generality. The matrix  $\tau$  of the momentum picture can be represented by a point on the Hermite-Laguerre sphere in the same way as the matrix  $\sigma$  of the coordinate picture. Since  $\tau$  is independent of  $z$ , the point on the sphere is fixed. It is convenient to specify the point on the Hermite-Laguerre sphere by the unit vector  $\vec{v} = (v_1, v_2, v_3)$ . The vector  $\vec{v}$  is related to the matrix elements of  $\tau$  by replacing  $\sigma$  by  $\tau$  in Eq. (4.59). The left-hand sides of the three equations in (4.59) correspond to the components  $v_1$ ,  $v_2$  and  $v_3$  in the same order. When the point on the Hermite-Laguerre sphere that represents  $\tau$  is on the equator ( $v_3 = 0$ ), the modes are called momentum HG modes. The modes represented by the poles of the sphere ( $v_3 = \pm 1$ ) are called momentum LG modes. In the absence of astigmatism, the momentum HG and LG modes coincide with the standard definition. In the case of astigmatism, the HG-LG nature of the modes in the coordinate picture varies with  $z$ .

By inserting the expressions (4.75)-(4.77) for the matrices in the expression for the OAM per photon in (4.73), we find that

$$L_{nm} = (n+m+1)L_0 + (n-m)\vec{v} \cdot \vec{L}, \quad (4.78)$$

with

$$L_0 = \hbar s r_- \sin(2\psi) \quad (4.79)$$

the OAM of the fundamental mode and  $\vec{L} = (L_1, L_2, L_3)$  given by

$$L_1 = -\hbar s r_+ \sin(2\psi), \quad L_2 = \hbar s \cos(2\psi), \quad L_3 = \hbar r_+, \quad (4.80)$$

where  $s = m_1 d_+ d_-$  and  $r_{\pm} = (d_{\pm}^2 \pm d_{\mp}^2)/2d_+ d_-$ .

### 4.5.3 Significance of the contributions to the orbital angular momentum

The OAM of the fundamental mode in (4.79) is independent of the position  $\vec{v}$  on the Hermite-Laguerre sphere, as expected. Interestingly, the OAM of the higher-order modes with mode numbers  $n = m$  is also independent of the point on the sphere, as follows from Eq. (4.78). For the higher-order modes with  $n \neq m$  there is a contribution to the OAM that depends on the position  $\vec{v}$  on the Hermite-Laguerre sphere. This contribution is determined by the angle between  $\vec{v}$  and the vector  $\vec{L}$ , and by the length of  $\vec{L}$ , which is determined by the properties of the fundamental mode in Eq. (4.80).

When there is no astigmatism, we have  $s = 0$  and  $r_+ = 1$  ( $r_- = 0$ ). Then the matrix  $\sigma$  of the coordinate picture is represented by the same point on the Hermite-Laguerre sphere as the matrix  $\tau$  of the momentum picture, and therefore the momentum HG and LG modes are identical to the HG and LG modes of the coordinate picture. The only non-vanishing component of  $\vec{L}$  is  $L_3$ , and the OAM is given by

$$L_{nm} = \hbar(n - m) \cos \theta , \quad (4.81)$$

where  $\theta$  is the angle of the vector  $\vec{v}$  with  $\vec{L}$ , which is the polar angle of the point on the sphere in this case. The mode indices  $n$  and  $m$  correspond to opposite points on the sphere, and give an opposite contribution to the OAM. For LG modes we have  $\theta = 0$ , and the well-known expression for the OAM is recovered [34]. When  $\theta > 0$ , the point moves away from the pole of the sphere, and the modes are intermediate between LG and HG modes. The unit of angular momentum is reduced by a factor  $\cos \theta$ . The HG modes are represented by points on the equator, for which  $\vec{v}$  and  $\vec{L}$  are perpendicular, and the OAM vanishes. If  $n - m = \pm 1$ , there is a similarity of OAM with the angular momentum due to the photon polarisation, which is  $\hbar \cos \theta$  per photon, where  $\theta$  is the polar angle of the position on the Poincaré sphere.

For simple astigmatism we distinguish three cases. In the first case  $\mu_1$  is anisotropic, while  $\delta$  is isotropic. In the second case  $\delta$  is anisotropic, while  $\mu_1$  is isotropic. In the third case both  $\mu_1$  and  $\delta$  are anisotropic, but with coinciding axes. In the first case we have  $r_+ = 1$  ( $r_- = 0$ ), while  $s \neq 0$ . The momentum distribution is circular, while the phase distribution, as determined by  $\mu_1$ , is astigmatic. The vector  $\vec{L}$  has a length  $\hbar\sqrt{1+s^2}$ . The OAM is given by

$$L_{nm} = \hbar(n - m) [v_3 + sv_2 \cos(2\psi) - sv_1 \sin(2\psi)] . \quad (4.82)$$

The first term on the right-hand side is the same as in the absence of astigmatism. The angle of orientation  $\psi$  of the phase distribution appears as a double angle, for the same reason why the azimuthal angle on the Poincaré sphere for polarisation is twice the angle of orientation of the polarisation ellipse. For the momentum HG modes ( $v_3 = 0$ ) the OAM is given by  $\hbar(n - m)s \sin(\phi - 2\psi)$ , where  $\phi$  is the azimuthal angle of the point on the equator. The angle with the  $x$  axis of the direction of the excitations of the momentum HG modes with mode numbers  $n > 0$  and  $m = 0$  is then given by  $\phi/2$ . The OAM of the momentum HG modes vanishes when the excitation directions are aligned with the elliptic phase distribution, and is maximal when the difference in angle of orientation is  $\pi/4$ .

In the second case of simple astigmatism we have  $s = 0$ , while  $r_+ > 1$ . In this case it is the momentum distribution that is astigmatic. The expression for the OAM simplifies to

$$L_{nm} = \hbar(n - m)r_+v_3 . \quad (4.83)$$

This expression is similar to the expression (4.81) in the absence of astigmatism, the difference being that due to the elliptic momentum distribution the unit of angular momentum has increased by a factor  $r_+ > 1$ .

In the third case of simple astigmatism we have  $\psi = 0$ , while  $s \neq 0$  and  $r_+ > 1$ . In this case the astigmatic momentum and phase distributions have the same orientations. The component  $L_1$  of the vector  $\vec{L}$  vanishes. The OAM is given by

$$L_{nm} = \hbar(n-m)(sv_2 + r_+v_3). \quad (4.84)$$

The OAM of the momentum HG modes vanishes when their orientation is the same as the orientation of the momentum and phase distributions, since then  $v_1 = 1$ , so that  $\vec{v}$  is perpendicular to the vector  $\vec{L}$ . The OAM of the momentum HG modes is maximal when the orientation of the excitation directions is at an angle of  $\pi/4$  with the orientation of the elliptic momentum and phase distributions, for which  $v_2 = 1$ .

For given values of  $s \neq 0$ ,  $r_+ > 1$  and  $r_- > 0$ , the length of the vector  $\vec{L}$  attains its largest value  $\hbar r_+ \sqrt{1+s^2}$  for maximal astigmatism, for which  $\psi = \pi/4$ . For maximal astigmatism the OAM is given by

$$L_{nm} = \hbar(n+m+1)sr_- + \hbar(n-m)r_+(-sv_1 + v_3). \quad (4.85)$$

For  $s > 0$  and  $n > m$  the OAM takes its maximum value when  $\vec{v}$  is in the same direction as  $\vec{L}$ , which is the case when

$$v_1 = -s/\sqrt{1+s^2}, \quad v_2 = 0, \quad v_3 = 1/\sqrt{1+s^2}. \quad (4.86)$$

For this point on the sphere we determine the spherical angles of the point on the sphere that represents the matrix  $\sigma(0)$  of the coordinate picture. Equation (4.46) still holds, as can be checked by using Eqs. (4.75) and (4.76) with  $\psi = \pi/4$ . The matrix  $\sigma(0)$ , which is found by using (4.62), is then given by

$$\sigma(0) = \frac{\delta}{\sqrt{1+s^2}} \begin{pmatrix} 1 & is \\ is & 1 \end{pmatrix}, \quad (4.87)$$

which differs from (4.63) since we chose a different basis for the transverse coordinates. Equations (4.87) and (4.59) are used to express the spherical angles of the point on the sphere that represents  $\sigma(0)$  in terms of the unit vector in Eq. (4.86) representing  $\tau$ . We find that  $\tan \theta = s$  and  $\phi = 0$ . The maximal astigmatic modes with maximum OAM are in between the LG modes and the HG modes of which the excitation directions have the same orientation as the elliptic intensity distribution, which is determined by  $\gamma$ . When the distance between the focal planes, as determined by  $s$ , is increased, the modes with maximum OAM get more HG nature, since the point on the sphere moves towards the equator.

## 4.6 Conclusions and discussion

We presented an operator method to characterise in a systematic way the possible complete orthonormal sets of astigmatic Gaussian modes. The fundamental mode is specified by a

Gaussian function in terms of a complex symmetric  $2 \times 2$  matrix  $\alpha$ . The real part of the matrix specifies the elliptic intensity distribution, and the imaginary part defines the phase distribution. The behaviour of the mode under propagation, as determined by the paraxial wave equation, is given by Eqs. (4.15) and (4.14), in terms of a simple  $z$  dependence of the matrix.

A general Gaussian function is also characterised by the requirement that it vanishes when a lowering operator is applied. In two dimensions, this defines two independent lowering operators. Higher-order modes can be constructed by repeated application of the corresponding raising operators  $\hat{a}_1^\dagger$  and  $\hat{a}_2^\dagger$ , as expressed in Eq. (4.25). Since there are two independent raising operators, the choice of  $\hat{a}_1^\dagger$  and  $\hat{a}_2^\dagger$  as linear combinations of the basis set is an inherent degree of freedom, which determines the nature of the set of higher-order modes for a given fundamental mode. This freedom is used by selecting the unitary matrix  $\sigma$ , in one transverse plane. When the linear combinations are basically real,  $\sigma$  is equivalent to a rotation in two dimensions, and the set of modes has the nature of HG modes, which is reminiscent of linear polarisation. In general the choice of the higher-order modes for a given fundamental mode can be represented by a point on the unit sphere. This Hermite-Laguerre sphere is analogous to the Poincaré sphere that represents polarisation. The power of this description is that the astigmatism and the Hermite-Laguerre nature of the modes as a function of the transverse plane is automatically accounted for. The  $z$  dependence of the symmetric matrix  $\alpha$  (determining the astigmatism) and the unitary matrix  $\sigma$  (which describes the nature of the modes) are studied in Section 4.4. The OAM of the various sets of modes is analysed in Section 4.5. It can be separated in a term that depends only on the astigmatism and terms that depend also on the selection of the nature of the modes, as determined by the point on the Hermite-Laguerre sphere. In general, astigmatism has a tendency to enhance the OAM.

Simple astigmatism is naturally imposed on a non-astigmatic beam by sending it through an astigmatic lens (or, equivalently, by reflecting it by an astigmatic mirror). Simple astigmatism can be converted into general astigmatism by a second astigmatic lens, with an orientation different from the first. An astigmatic lens can be specified by a two-dimensional real symmetric matrix  $\zeta$ , with eigenvalues  $1/f_1$  and  $1/f_2$  the inverse focal lengths, and with eigenvectors in the corresponding directions in the transverse plane. The effect of the lens is simply a multiplication of the mode by the factor  $\exp(-ikR\zeta R/2)$ . This is equivalent to a change of the matrix  $\alpha$  that determines the astigmatism. The effect of the lens is that  $\alpha$  is replaced by  $\alpha + ik\zeta$  after the lens, which implies that  $\alpha_1$  is replaced by  $\alpha_1 - k\zeta$ . The matrix  $\sigma$  remains unaffected by the lens. Combined with the effect of free propagation, which is expressed in the simplest way by Eq. (4.39), this information is sufficient to evaluate the variation of all sets of modes as they propagate through a given lens system.

The paraxial wave equation is identical in form to the two-dimensional Schrödinger equation for a free particle. As a consequence, the complete sets of solutions that we derived in this paper are also complete sets of solutions of the Schrödinger equation for a free particle. The fundamental mode corresponds to a wave packet that tumbles upon propagation, and therefore has OAM. Also, the wave packet has a minimal size at two instants of time, corresponding to the two focal planes. In general, when the point on the Hermite-Laguerre sphere is not on the equator, the higher-order modes contain vortices, and the corresponding wave packets do as well. The operator method can easily be extended to three dimensions, so that solutions of the three-dimensional Schrödinger equation for a free particle are found.

## CHAPTER 5

---

### Vortices in Gaussian light beams

---

*The dynamics of vortices in light beams is complicated in general. Still, it is possible to derive some general properties of vortices in Gaussian beams. We study the vortices that occur naturally in higher-order astigmatic Gaussian beams, and derive a general expression for the positions of the vortex centres. By imposing mathematical vortices on a Gaussian beam, more general statements about the propagation properties of the vortices are obtained. In non-astigmatic Gaussian beams, the trajectory of a canonical vortex represents a dark ray. In a degenerate resonator a vortex mode is obtained in which a dark ray forms a closed trajectory, similar to a light ray in a geometric mode.*

*Partially based on J. Visser and G. Nienhuis, Proc. of SPIE 5736, 126 (2005) and G. Nienhuis and J. Visser, J. Opt. A: Pure Appl. Opt. 6, S248 (2004).*

## 5.1 Introduction

The dynamics of vortices in light beams attracts a lot of attention. Vortices that occur naturally in Gaussian beams are studied in the literature both experimentally and theoretically. The trajectory of the vortex centre can be very complicated [41], and the sign of the vortex charge can change [32] under free space propagation. By imposing mathematical vortices on Gaussian beams, some general propagation properties of vortices and their interaction can be obtained [33].

In Section 5.2 we study the vortices that occur naturally in light beams that are in higher-order transverse modes. The vortex centres in astigmatic beams follow a complicated trajectory upon propagation. The morphology of a simple vortex can be represented by a point on the morphology sphere [42]. We discuss the relation between the point on the Hermite-Laguerre sphere that characterises the nature of the higher-order modes, and the point on the morphology sphere that represents the morphology of the vortices in the modes.

In Section 5.3 we consider the properties of vortices that are imposed on astigmatic Gaussian beams propagating through free space. We obtain the trajectory of the vortex centre, and show that the charge of a vortex can change sign. We derive conditions under which vortices imposed on a Gaussian beam do not interact.

In Section 5.4 we consider the trajectory of the centre of a canonical vortex imposed on a non-astigmatic Gaussian beam that propagates through a lens guide. In between the lenses the trajectory of the centre of the vortex is a straight line, while at the lenses the direction of propagation changes. Since the intensity of the light beam at the vortex centre vanishes, it represents a dark ray. Inside a degenerate resonator these dark rays form a closed trajectory, in the same way as the light rays of a geometric mode.

## 5.2 Vortices in general astigmatic beams

### 5.2.1 Beam profile

We study the vortices that occur naturally in the (astigmatic) Gaussian beams that were discussed in Chapter 4. In order to obtain the positions and morphologies of the vortices in these beams, an analytical expression for the mode profiles is necessary. When one of the mode numbers is equal to zero, an analytical expression can be obtained and the vortices in these modes can be studied. We consider the beam profiles of the higher-order modes for the case that  $(n, m) = (n, 0)$ . For an arbitrary transverse plane these higher-order modes are obtained by repeated application of the raising operator  $\hat{a}_1^\dagger$  on the fundamental mode profile. From Eq. (4.58) it follows that

$$\hat{a}_1^\dagger = \exp\left(\frac{i}{2}\hat{R}\alpha_1\hat{R}\right) (\sigma_{1x}^*\hat{b}_x^\dagger + \sigma_{1y}^*\hat{b}_y^\dagger) \exp\left(-\frac{i}{2}\hat{R}\alpha_1\hat{R}\right). \quad (5.1)$$

The vector  $\hat{B}^\dagger$  of real raising operators  $\hat{b}_x^\dagger$  and  $\hat{b}_y^\dagger$  is obtained by taking the Hermitian conjugate of Eq. (4.52). It is convenient to define a dimensionless transverse coordinate vector  $R' = (x', y')$ , such that

$$R' = \frac{1}{\gamma}R. \quad (5.2)$$

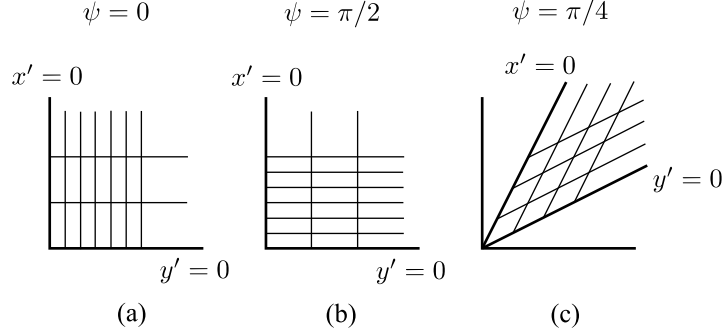


**Figure 5.1:** Graphical representation of the dimensionless basis discussed in the text. Lines of constant  $x'$  and  $y'$  are depicted for different orientations of the ellipses of constant intensity of the fundamental mode, where the ellipticity is fixed. The eigenvalues of  $\gamma$ , which determine the ellipticity, are  $\gamma_x = 3\gamma_y$ . The angle  $\psi$  of the orientation of  $\gamma$  determines the angle between  $x$  axis and the long axes of the ellipses. In (a) and (b) we have  $\psi = 0$  and  $\psi = \pi/2$ , respectively, which gives rise to orthogonal coordinates with different units. In (c) we have  $\psi = \pi/4$  and the coordinates are non-orthogonal.

Then we have

$$\hat{B}^\dagger = \frac{1}{\sqrt{2}} (\hat{R}' - i\hat{P}') , \quad (5.3)$$

where in the coordinate representation  $\hat{P}' = -i\partial/\partial R'$ .

The new dimensionless basis (5.2) of transverse coordinates depends on  $\gamma$  and is not orthogonal in general. The matrix  $\gamma$  determines the orientation and ellipticity of the ellipses of constant intensity of the fundamental mode profile. In Fig. 5.1 lines of constant  $x'$  and  $y'$  are depicted for different orientations of the ellipses of constant intensity of the fundamental mode, where the ellipticity is fixed. The angle  $\psi$  is the angle between the  $x$  axis and the long axes of the ellipses. For  $\psi = 0$  and  $\psi = \pi/2$ , the ellipses are oriented along the  $x$  and  $y$  axes, and the dimensionless coordinates  $x'$  and  $y'$  are orthogonal, but with different units. For  $\psi = \pi/4$  the dimensionless coordinates are non-orthogonal.

The state of the light beam is given by

$$|u_{n0}\rangle = \frac{1}{\sqrt{n!}} (\hat{a}_1^\dagger)^n |u_{00}\rangle , \quad (5.4)$$

which follows from (4.25) with  $m = 0$ . By using the mode profile  $u_{00}(R)$  in Eq. (4.1) it follows that the higher-order mode profiles are given by

$$u_{n0}(R) = \frac{1}{\sqrt{n! \pi 2^n \det \gamma}} \exp\left(-\frac{1}{2} R \alpha R\right) \times \sum_{k=0}^n \frac{n!}{k!(n-k)!} (\sigma_{1x}^*)^k (\sigma_{1y}^*)^{n-k} H_k(x') H_{n-k}(y') , \quad (5.5)$$

### 5. Vortices in Gaussian light beams

where  $H_n(x)$  are the Hermite polynomials defined in Eq. (4.61), and where the dimensionless coordinates  $x'$  and  $y'$  are given by (5.2). The matrix elements  $\sigma_{1x}$  and  $\sigma_{1y}$  of the matrix  $\sigma$  are expressed in terms of the spherical angles  $\theta$  and  $\phi$  of the point on the Hermite-Laguerre sphere. We write

$$\begin{aligned}\sigma_{1x} &= \frac{1}{\sqrt{2}} [\exp(i\phi/2) \cos(\theta/2) + \exp(-i\phi/2) \sin(\theta/2)] , \\ \sigma_{1y} &= \frac{1}{i\sqrt{2}} [\exp(i\phi/2) \cos(\theta/2) - \exp(-i\phi/2) \sin(\theta/2)] .\end{aligned}\quad (5.6)$$

It can be checked that the expressions in Eq. (5.6) satisfy Eq. (4.59). The expression for the higher-order mode profiles can be written in terms of a single Hermite polynomial by using a special case of the summation theorem for Hermite polynomials, which reads [43]

$$\sum_{k=0}^n \frac{n!}{k!(n-k)!} (d_x)^k (d_y)^{n-k} H_k(x) H_{n-k}(y) = (d_x^2 + d_y^2)^{n/2} H_n \left( \frac{d_x x + d_y y}{\sqrt{d_x^2 + d_y^2}} \right) , \quad (5.7)$$

where  $d_x$  and  $d_y$  are (complex) numbers. Using this relation we find that

$$u_{n0}(R) = \frac{(\sin \theta)^{n/2}}{\sqrt{n! \pi 2^n \det \gamma}} H_n \left( \frac{1}{\sqrt{2 \sin \theta}} f(x', y') \right) \exp \left( -\frac{1}{2} R \alpha R \right) , \quad (5.8)$$

where

$$f(x', y') = \exp(-i\phi/2) \cos(\theta/2) (x' + iy') + \exp(i\phi/2) \sin(\theta/2) (x' - iy') . \quad (5.9)$$

Astigmatic Hermite-Gaussian (HG) modes are characterised by a point on the equator of the Hermite-Laguerre sphere, for which we have  $\theta = \pi/2$ . The mode profiles are then given by

$$u_{n0}(R) = \frac{1}{\sqrt{n! \pi 2^n \det \gamma}} H_n (x' \cos(\phi/2) + y' \sin(\phi/2)) \exp \left( -\frac{1}{2} R \alpha R \right) , \quad (5.10)$$

which is a rotated version of the astigmatic HG modes in Eq. (4.60) with  $m = 0$ . The astigmatic Laguerre-Gaussian (LG) modes are characterised by a point on the north or south pole of the Hermite-Laguerre sphere, for which we have  $\theta = 0$  and  $\theta = \pi$ , respectively. When approaching one of the poles, only the highest-order term of the Hermite polynomial in the expression (5.8) for the mode profiles survives. By using that  $\lim_{x \rightarrow \infty} x^{-n} H_n(x) = 2^n$ , we find that the mode profiles are given by

$$u_{n0}(R) = \frac{1}{\sqrt{n! \pi \det \gamma}} \exp(\mp i n \phi / 2) (x' \pm iy')^n \exp \left( -\frac{1}{2} R \alpha R \right) , \quad (5.11)$$

where the plus and minus signs apply to the north and south pole, respectively. The phase factor  $\exp(\mp i n \phi / 2)$ , which expresses from which longitude on the sphere the pole is approached, is a geometric, or Berry phase [44]. When  $\gamma$  is isotropic, Eq. (5.11) is identical to the profiles of the familiar non-astigmatic LG modes with mode numbers  $l = \pm n$  and  $p = 0$  [26].

### 5.2.2 Position of the vortices

The centres of the vortices, or phase singularities, are located at positions in the transverse plane at which both the real and imaginary parts of the complex mode profile vanish. The mode profile in Eq. (5.8) can only vanish when the Hermite polynomial vanishes. The Hermite polynomial  $H_n$  has  $n$  zeroes, which occur at the  $n$  real values  $c_j$ . It follows that the mode profile vanishes at the positions determined by

$$f(x', y') = c_j \sqrt{2 \sin \theta}, \quad j = 1, 2, \dots, n, \quad (5.12)$$

where  $f(x', y')$  is given in Eq. (5.9). The real part of (5.12) defines the  $n$  lines

$$x' \cos(\phi/2) + y' \sin(\phi/2) = c_j \sqrt{\frac{2 \sin \theta}{1 + \sin \theta}} \quad j = 1, 2, \dots, n, \quad (5.13)$$

where we used that  $\cos(\theta/2) + \sin(\theta/2) = \sqrt{1 + \sin \theta}$ . On the equator of the Hermite-Laguerre sphere ( $\theta = \pi/2$ ) the function  $f(x', y')$  is real and the  $n$  lines in Eq. (5.13) are edge dislocation lines [45]. This also follows immediately from Eq. (5.10). Off the equator the imaginary part of  $f(x', y')$  vanishes at the line

$$y' \cos(\phi/2) = x' \sin(\phi/2), \quad (5.14)$$

which is a line through the centre of the beam. On this line there are  $n$  vortex centres, which are located at the  $n$  crossings with the lines in Eq. (5.13). The orientation of this line is determined by the azimuthal angle  $\phi$  of the point on the Hermite-Laguerre sphere and by the orientation and ellipticity of the intensity distribution, as determined by  $\gamma$ . The transverse coordinate vectors  $R_j$  of the centres of the vortices are given by

$$R_j = c_j \sqrt{\frac{2 \sin \theta}{1 + \sin \theta}} \gamma \begin{pmatrix} \cos(\phi/2) \\ \sin(\phi/2) \end{pmatrix}, \quad j = 1, 2, \dots, n, \quad (5.15)$$

where we used (5.2). In case that  $\theta = 0$ , all the vortex centres coincide on the optical axis, which is expected for astigmatic LG modes, and can be seen immediately from Eq. (5.11).

When the beam propagates through free space the positions of the vortex centres change. In each transverse plane  $z$  the positions of the vortex centres are given by Eq. (5.15) where for  $\theta$ ,  $\phi$  and  $\gamma$  the values in the plane  $z$  must be taken. In general the vortex centres follow a complicated trajectory upon propagation. The expression for the positions of the vortex centres in Eq. (5.15) is a generalisation of a result by Bekshaev *et al.* [41] to general astigmatic modes. For non-astigmatic modes the point on the Hermite-Laguerre sphere is independent of  $z$ . As a consequence, the vortex centres lie on a fixed line through the centre of the beam, and the distance to the centre scales with the spot size  $\gamma$  of the beam. The angle of this line with the  $x$  axis is then simply half the azimuthal angle of the point on the Hermite-Laguerre sphere.

### 5.2.3 Charge and morphology

Besides the position of the centre, other properties of a vortex are its charge and morphology. For a vortex with topological charge  $q$ , the phase change around the vortex centre in the

anti-clockwise direction is given by  $2\pi q$ . The morphology expresses how the phase changes around the vortex centre. When the increase of the phase around the vortex centre is constant, the vortex is called canonical. For a canonical vortex of charge  $\pm 1$  located on the optical axis, the beam profile in the vicinity of the vortex is  $\propto x \pm iy = \sqrt{x^2 + y^2} \exp(\pm i\phi)$ , where  $\phi$  is the azimuthal angle. When the lowest-order term in the expansion of the mode profile around the vortex centre is a linear term, the vortex has a unit charge. This linear term can be written as

$$\xi(x + iy - x_0 - iy_0) + \zeta(x - iy - x_0 + iy_0), \quad (5.16)$$

where  $\xi$  and  $\zeta$  are the parameters which determine the morphology. The morphology of the vortex can then be represented by a point on a sphere, the morphology sphere [42], in the same way as the nature of the higher-order modes is represented by a point on the Hermite-Laguerre sphere. The spherical angles of the point on the sphere are defined by

$$\begin{aligned} \cos(\theta_m) &= \frac{|\xi|^2 - |\zeta|^2}{|\xi|^2 + |\zeta|^2}, \\ \exp(i\phi_m) &= \frac{\xi^* \zeta}{|\xi| |\zeta|}. \end{aligned} \quad (5.17)$$

On the northern hemisphere  $|\xi| > |\zeta|$ , and the term  $x + iy$  dominates so that the charge is  $+1$ , while on the southern hemisphere the term  $x - iy$  dominates and the charge is  $-1$ . On the equator the terms balance, and there is an edge dislocation line. The north pole and south pole, for which  $\theta_m = 0$  and  $\theta_m = \pi$ , respectively, represent the cases for which the vortex is canonical, because then only one of both terms is present.

Since the zeroes of the Hermite polynomials are all different, the lowest-order term in the expansion around a zero is always a linear term. Since the function  $f(x', y')$  in (5.9) is first order in  $x'$  and  $y'$ , the vortices in the modes  $u_{n0}(R)$  in Eq. (5.8) have a charge  $\pm 1$ , where the sign depends on which hemisphere the point on the morphology sphere is. The function  $f(x', y')$  determines the morphology and it follows that the morphology of all the vortices is the same. We determine the morphology for the special case that the modes are non-astigmatic. In that case the dimensionless coordinates in (5.2) are simply given by  $x' = x/\gamma$  and  $y' = y/\gamma$ , where  $\gamma$  is the spot size. By using (5.9) and (5.17) we find that

$$\theta_m = \theta, \quad \phi_m = \phi. \quad (5.18)$$

Thus for non-astigmatic modes the point on the Hermite-Laguerre sphere has the same location as the point on the morphology sphere, which characterises the morphology of the vortices in the modes.

## 5.3 Vortices imposed on Gaussian beams

### 5.3.1 Position of the vortex

We consider the evolution of a vortex that is imposed on an astigmatic Gaussian beam propagating through free space. A vortex of unit charge of which the centre is located at  $R_0 = (x_0, y_0)$  is imposed by multiplying the beam profile with the function  $E_0(R - R_0)$ , where

$R$  is the transverse coordinate vector, and  $E_0$  is a row vector, which determines the morphology of the vortex [33]. For a canonical vortex with charge  $\pm 1$  we have  $E_0 = (1, \pm i)$ . In operator form the vortex is imposed by application of the operator  $E_0(\hat{R} - R_0)$ . When the vortex is imposed in the plane  $z = 0$ , the resulting (un-normalised) state is given by

$$|u(0)\rangle = E_0(\hat{R} - R_0)|u_{00}(0)\rangle. \quad (5.19)$$

The state in the transverse plane  $z$  is found by applying the propagation operator  $\hat{U}(z)$  in Eq. (4.8) to the state  $|u(0)\rangle$ . This gives

$$|u(z)\rangle = E_0(\hat{U}(z)\hat{R}\hat{U}^\dagger(z) - R_0)|u_{00}(z)\rangle = E_0\left(\hat{R} - \frac{z}{k}\hat{P} - R_0\right)|u_{00}(z)\rangle. \quad (5.20)$$

The mode profile in the coordinate representation is found by using that the operator  $\hat{P} = -i\partial/\partial R$  gives  $i\alpha(z)R$  when acting on the mode function (4.37). Since the  $z$  dependence of  $\alpha(z)$  is complicated, it is more convenient to use an expression in terms of  $\mu(z)$  in Eq. (4.39). By using that  $\alpha = \mu^{-1}$  we find that

$$u(R, z) = E_0(\mu^{-1}(z)\mu(0)R - R_0)u_{00}(R, z). \quad (5.21)$$

The position of the vortex centre is found by the requirement that  $u(R, z)$  vanishes, which is satisfied when

$$E_0\mu^{-1}(z)\mu(0)R = E_0R_0. \quad (5.22)$$

We consider the case of a canonical vortex of charge  $+1$  that is imposed on a non-astigmatic Gaussian beam, with the plane  $z = 0$  as the focal plane. Then  $\mu(z)$  is a complex number  $(b + iz)/k$  times the unit matrix, with  $b$  the Rayleigh range. It follows from Eq. (5.22) that the position of the vortex centre in the plane  $z$  is given by

$$x + iy = \frac{b + iz}{b}(x_0 + iy_0). \quad (5.23)$$

We find that the position of the vortex centre is given by

$$x = x_0 - \frac{z}{b}y_0, \quad y = y_0 + \frac{z}{b}x_0. \quad (5.24)$$

It follows that the vortex remains canonical, and moves on a straight line [33]. It traces a path in the transverse plane that is directed normal to the position  $R_0$  in the focal plane, where the distance from the optical axis is smallest. The variation of the azimuthal angle of the vortex position is identical to the variation of the Gouy phase. When going from focus to infinity, this azimuthal angle varies over  $\pi/2$ .

When a vortex is imposed on an astigmatic Gaussian beam, the trajectory of the vortex centre is no longer a straight line, and the morphology of the vortex changes, except for a special case. When  $E_0$  is an eigenvector of  $\mu(0)$ , it is also an eigenvector of  $\mu(z)$ , since  $\mu(z) = \mu(0) + iz/k$ . Then the matrices  $\mu(z)$  and  $\mu(0)$  in Eq. (5.22) can be replaced by their eigenvalues, which gives rise to a vortex with a constant morphology of which the centre moves on a straight line. This is remarkable since the intensity distribution of the astigmatic Gaussian beam tumbles upon propagation.

### 5.3.2 Change of the vortex charge

We want to demonstrate that in the case of astigmatism, the charge of the vortex can change sign during propagation. For large values of  $z$ , for which  $\mu(z) \rightarrow iz/k$ , it follows from Eq. (5.21) that the mode profile is given by

$$u(R, z) = \frac{k}{iz} E_0 \left( \mu(0)R - \frac{iz}{k} R_0 \right) u_{00}(R, z). \quad (5.25)$$

We consider the case that a canonical vortex of charge  $+1$  is imposed on a simple astigmatic Gaussian beam in the plane  $z = 0$ . We have  $E = (1, i)$ , and for  $\mu(0) = \mu_0 + i\mu_1$  we use the expressions

$$\mu_0 = \begin{pmatrix} m_{0x} & 0 \\ 0 & m_{0y} \end{pmatrix}, \quad \mu_1 = \begin{pmatrix} -z_0/k & 0 \\ 0 & -z_1/k \end{pmatrix}, \quad (5.26)$$

so that the planes  $z = z_0$  and  $z = z_1$  are the focal planes of the beam. By using these expressions it follows from Eq. (5.16) that for large values of  $z$  the morphology parameters are given by

$$\xi = \frac{1}{2}(m_{0x} + m_{0y}) - \frac{i(z_0 + z_1)}{2k}, \quad \zeta = \frac{1}{2}(m_{0x} - m_{0y}) - \frac{i(z_0 - z_1)}{2k}. \quad (5.27)$$

We see that the vortex is not canonical anymore for large values of  $z$ . When  $|\xi| > |\zeta|$ , the charge of the vortex is  $+1$ , while for  $|\xi| < |\zeta|$ , the charge of the vortex is  $-1$  for large values of  $z$ . Since at  $z = 0$  the charge of the imposed vortex is  $+1$ , it follows that in the latter case the charge of the vortex changes sign upon propagation. In the plane where the sign of the charge of the vortex changes, the vortex vanishes, giving rise to an edge dislocation. It follows from the expressions for  $\xi$  and  $\zeta$  in Eq. (5.27), that the charge of the imposed vortex changes sign upon propagation when

$$m_{0x}m_{0y} + \frac{z_0z_1}{k^2} < 0. \quad (5.28)$$

Since  $\det \mu_0 = m_{0x}m_{0y} > 0$ , it follows that this requirement can only be satisfied when  $z_0z_1 < 0$ . Therefore, for a simple astigmatic beam the vortex charge can only change sign when the vortex is imposed in between the focal planes of the beam.

### 5.3.3 Interaction between vortices

We study the interaction between vortices by imposing two vortices on an astigmatic Gaussian beam. Similar to Eq. (5.20) we write

$$|u(z)\rangle = E_1 \left( \hat{R} - \frac{z}{k} \hat{P} - R_1 \right) E_0 \left( \hat{R} - \frac{z}{k} \hat{P} - R_0 \right) |u_{00}(z)\rangle, \quad (5.29)$$

where  $R_0$  and  $R_1$  are the positions of the vortex centres in the plane  $z = 0$  and where  $E_0$  and  $E_1$  determine the morphologies of the vortices. The difference with the case of the single vortex is that the operator  $\hat{P}$  of the second vortex, which is a differentiation in the coordinate

representation, does not only operate on the profile  $\langle R|u_{00}\rangle$ , but also on the first vortex. As a consequence, there is interaction between the vortices in general. We find that

$$u(R, z) = [E_1 (\mu^{-1}(z)\mu(0)R - R_1)E_0 (\mu^{-1}(z)\mu(0)R - R_0) + \frac{iz}{k}E_0\mu^{-1}(z)\mu(0)E_1^T]u_{00}(R, z). \quad (5.30)$$

The last term between the square brackets is the interaction term, which vanishes for special cases.

In case that the Gaussian beam on which the two vortices are imposed is non-astigmatic,  $\mu(z)$  is a complex number times the unity matrix. Then the interaction term is proportional to the inner product  $E_0E_1^T$ . We express  $E_0$  and  $E_1$  in terms of the morphology parameters  $\xi_{m0}$  and  $\zeta_{m0}$ , and  $\xi_{m1}$  and  $\zeta_{m1}$ , respectively. The interaction term is then proportional to  $\xi_{m0}\zeta_{m1} + \zeta_{m0}\xi_{m1}$ . It follows from Eq. (5.17) that the interaction vanishes when the vortices are represented by points on the morphology sphere which have the same latitude, but for which the azimuthal angles differ by  $\pi$ . When both vortices are canonical with the same sign of the charge, this condition is satisfied, since then both vortices are represented by points on the north or the south pole of the morphology sphere. Without interaction the two vortex centres follow a straight line and their morphologies are constant, just like for a single vortex.

When two canonical vortices of the same charge are imposed on an astigmatic Gaussian beam, the interaction term vanishes only for specific choices of  $\mu(0)$ . Since for canonical vortices of the same charge  $E_0E_1^T = 0$ , it follows that the interaction term vanishes in the plane  $z = 0$  when  $\mu(0)$  has  $E_0 = E_1 = (1, \pm i)$  as an eigenvector. If  $z = z_0$  and  $z = z_1$  are the focal planes of the astigmatic Gaussian beam, the matrix  $\mu(0)$  has  $(1, \pm i)$  as an eigenvector when

$$\mu(0) = \begin{pmatrix} m_0 - iz_0/k & \pm(z_0 - z_1)/2k \\ \pm(z_0 - z_1)/2k & m_0 - iz_1/k \end{pmatrix}, \quad (5.31)$$

with real  $m_0 > |z_0 - z_1|/2k$ . This corresponds to the case of maximal astigmatism. Since  $\mu(z) = \mu(0) + iz/k$ , it follows that  $(1, \pm i)$  is also an eigenvector of  $\mu(z)$ . The matrices  $\mu(z)$  and  $\mu(0)$  in Eq. (5.30) can then be replaced by their eigenvalues. As a consequence, the interaction vanishes for all values of  $z$ . Then the two vortices remain canonical and their centres move on a straight line.

When more than two vortices are imposed on a non-astigmatic Gaussian beam, the interaction terms all vanish when  $E_iE_j^T = 0$  for all the combinations of two vortices. This can only occur when all the imposed vortices are canonical of the same charge, as represented by a point on the north or the south pole of the morphology sphere. The vortices are then independent and move on a straight line. When more than one vortex is imposed on a single position, a vortex of higher charge is formed, which is stable and follows a straight line as well, because the vortices that constitute it follow the same straight line. When more than two canonical vortices of the same charge  $\pm 1$  are imposed on the maximal astigmatic beam described by (5.31), all the interaction terms vanish as well. Then the vortices remain canonical and their centres move on a straight line.

## 5.4 Dark rays

### 5.4.1 Propagation through lens guide

We consider the propagation of a non-astigmatic Gaussian beam with imposed canonical vortices through a lens guide of non-astigmatic lenses. The waist of the beam is in the input plane of the lens guide and the beam is located on axis. In the input plane multiple canonical vortices of charge +1 are imposed on the beam. A canonical vortex of charge +1 is imposed at the position  $(x_0, y_0)$  by operating with the operator  $\hat{x} + i\hat{y} - x_0 - iy_0$  on the state of the fundamental mode. In terms of the circular ladder operators defined in Eq. (3.32) we can write

$$\hat{x} + i\hat{y} = \gamma \left( \hat{a}_- + \hat{a}_+^\dagger \right), \quad (5.32)$$

where  $\gamma$  is the spot size of the Gaussian beam at the waist. It follows that the (un-normalised) state  $|u\rangle$  with  $N$  vortices at the positions  $(x_m, y_m)$  is given by

$$|u\rangle = \left\{ \prod_{m=0}^{N-1} \left[ \gamma \left( \hat{a}_- + \hat{a}_+^\dagger \right) - x_m - iy_m \right] \right\} |u_{00}\rangle. \quad (5.33)$$

At the waist of the beam the state  $|u_{00}\rangle$  is identical to the ground state of the two-dimensional isotropic harmonic oscillator. Therefore, the state  $|u\rangle$  is a linear combination of the states  $|u_{n_+n_-}\rangle$  with  $n_- = 0$ , since operation with the lowering operator  $\hat{a}_-$  on  $|u_{00}\rangle$  gives zero.

The state at the output plane of the lens guide is found by applying the Iwasawa decomposition (3.14) for the unitary operator  $\hat{U}$  of the lens guide to the state at the input plane. The parameters  $\theta$ ,  $\xi$  and  $\alpha$  of the Iwasawa decomposition are expressed in terms of the elements of the ABCD matrix of the lens guide in Eq. (3.16). We use the Iwasawa decomposition for both transverse dimensions. The exponential term in the Iwasawa decomposition containing the harmonic oscillator Hamiltonian is written in terms of the circular ladder operators as

$$\exp \left[ -i \frac{\theta}{2} (\hat{n}_+ + \hat{n}_- + 1) \right], \quad (5.34)$$

as is done in Eq. (3.33). Since the state  $|u\rangle$  in the input plane is a linear combination of states with  $n_- = 0$ , it follows that the operation with (5.34) is, within a phase factor, identical to the operation with  $\exp(-i\theta \hat{l}_z/2)$ , where  $\hat{l}_z = \hat{n}_+ - \hat{n}_-$  is the angular-momentum operator defined in Eq. (3.31). As a consequence, operation with (5.34) gives rise to a rotation of the beam profile about the  $z$  axis over an angle  $\theta/2$  in the counter-clockwise direction. The exponential term in the Iwasawa decomposition containing  $\hat{T}_1$  scales the beam profile with the factor  $\exp(\xi/2)$  in both transverse dimensions. The exponential term that introduces the curved wave fronts is not important for the study of the vortices.

It follows that the coordinate vectors of the vortex centres are rotated over the angle  $\theta/2$ , after which they are multiplied with the factor  $\exp(\xi/2)$ . Then the vortex located at the transverse coordinates  $(x_0, y_0)$  in the input plane of the lens guide, is located in the output

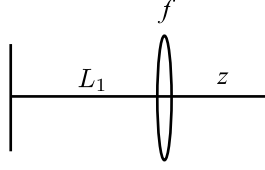


**Figure 5.2:** Lens guide where a lens with focal distance  $f$  is located at a distance  $L_1$  from the input plane, and a distance  $z$  from the output plane.

plane at the transverse coordinates

$$\begin{aligned} x &= \exp\left(\frac{\xi}{2}\right) \left[ x_0 \cos\left(\frac{\theta}{2}\right) - y_0 \sin\left(\frac{\theta}{2}\right) \right] = Ax_0 - \frac{B}{b}y_0, \\ y &= \exp\left(\frac{\xi}{2}\right) \left[ y_0 \cos\left(\frac{\theta}{2}\right) + x_0 \sin\left(\frac{\theta}{2}\right) \right] = Ay_0 + \frac{B}{b}x_0, \end{aligned} \quad (5.35)$$

where we used Eq. (3.16) to express  $\theta$  and  $\xi$  in terms of the elements  $A$  and  $B$  of the ABCD matrix of the lens guide. It is also clear that the vortices move independently. For a canonical vortex with charge  $-1$  the same results hold, but the angle  $\theta$  must be replaced by  $-\theta$ .

### 5.4.2 Change in the propagation direction of the vortex

We consider a canonical vortex of charge  $+1$  that is imposed on a non-astigmatic Gaussian beam at the position  $(x_0, y_0)$  at the waist of the beam. After propagation through free space over a distance  $z$ , the position of the vortex centre is given by Eq. (5.35), where  $A$  and  $B$  are the matrix elements in the first row of the ABCD matrix for free space propagation over a distance  $z$ . From (3.8) we obtain  $A = 1$  and  $B = z$ , and by substitution in (5.35) we recover Eq. (5.24), which describes a straight line. It follows that the trajectory of the vortex centre in the transverse plane is described by the line  $x_0x + y_0y = x_0^2 + y_0^2$ . The vector  $(x_0, y_0)$ , which is perpendicular to this line, is the coordinate vector of the vortex centre at the waist of the beam. The action of a lens does not change the position of the vortex centre, since the beam profile is multiplied with a parabolic phase factor, but the direction of propagation of the vortex centre is changed due to the lens.

In order to calculate the change of the transverse propagation direction of the vortex centre due to the lens we consider the lens guide in Fig 5.2. A lens with focal distance  $f$  is located at a distance  $L_1$  from the input plane of the lens guide. The distance from the lens to the output plane of the lens guide is  $z$ . The ABCD matrix  $M$  for the lens guide is given by

$$M = M_f(z)M_l(f)M_f(L_1) = \begin{pmatrix} 1 - \frac{z}{f} & L_1 + z\left(1 - \frac{L_1}{f}\right) \\ -\frac{1}{f} & 1 - \frac{L_1}{f} \end{pmatrix}, \quad (5.36)$$

where  $M_f(z)$  and  $M_l(f)$  are given in Eqs. (3.8) and (3.9), respectively. In the input plane of the lens guide at the waist of the beam the vortex is imposed at the position  $(x_0, y_0)$ . The expressions for  $A$  and  $B$ , which are the matrix elements in the first row of  $M$ , are substituted

in (5.35), describing the position of the vortex in the output plane of the lens guide as a function of  $z$ . By eliminating  $z$  we find that behind the lens the trajectory of the vortex centre is described by the line

$$\left[ \left( 1 - \frac{L_1}{f} \right) x_0 - \frac{b}{f} y_0 \right] x + \left[ \left( 1 - \frac{L_1}{f} \right) y_0 + \frac{b}{f} x_0 \right] y = x_0^2 + y_0^2. \quad (5.37)$$

The vector perpendicular to this line can be read off immediately. Before the lens the vector perpendicular to the line of propagation of the vortex centre in the transverse plane is  $(x_0, y_0)$ . It follows that the angle between the lines before and after the lens is given by

$$\cos \alpha_v = \frac{f - L_1}{\sqrt{(f - L_1)^2 + b^2}}. \quad (5.38)$$

Due to the lens the direction in the transverse plane in which the vortex centre moves, rotates over an angle  $\alpha_v$  in the counter-clockwise direction. Notice that  $\alpha_v$  depends on the distance between the lens and the waist of the beam, but that it is independent of the initial position of the vortex centre. We conclude that inside the lens guide the trajectory of the vortex centre is described by straight lines, which change direction at the lenses. Since the intensity of the light beam vanishes at the vortex centre, the trajectory can be considered a dark ray.

### 5.4.3 Vortex modes of a resonator at degeneracy

We consider the symmetric two-mirror resonator in Fig. 3.1. The Rayleigh range of the Gaussian fundamental mode is given by Eq. (3.25). We follow the centre of a canonical vortex of charge  $+1$  that is imposed on the Gaussian fundamental mode of the resonator. At the mirror the transverse direction of propagation of the vortex centre rotates over the angle  $\alpha_v$ . With the values  $f = R/2$  and  $z = L_1 = L/2$  the lens guide in Fig. 5.2 is the lens guide for half a round trip inside the resonator. With these values and the Rayleigh range given by (3.25) we find that  $\cos \alpha_v = g$ . We see that  $\alpha_v$  is the Gouy phase of the fundamental mode of the resonator for half a round trip.

When  $2N\alpha_v = 2\pi K$ , where  $N$  and  $K$  are integer numbers with no common divisor, the vortex returns to its initial position after  $N$  full round trips in the resonator. This corresponds to the case of an  $N$ -fold degenerate resonator (see Section 2.4). We now construct a vortex mode by imposing  $N$  canonical vortices of charge  $+1$  on the Gaussian fundamental mode of the  $N$ -fold degenerate resonator. When the vortex centres are spread evenly over a circle, it immediately follows that the beam with the vortices is a mode, since the vortices exchange positions after a round trip. The coordinates  $(x_m, y_m)$  of the initial positions of the vortex centres are expressed as

$$x_m + iy_m = \exp\left(-\frac{2\pi im}{N}\right) (x_0 + iy_0) \quad m = 0, 1, \dots, N-1, \quad (5.39)$$

where  $(x_0, y_0)$  are the initial coordinates of one of the vortex centres, which can be chosen freely. With these coordinates of the vortex centres, the vortex state in the plane in the middle of the resonator is given by Eq. (5.33), where the Gaussian mode profile  $u_{00}(R)$  has a

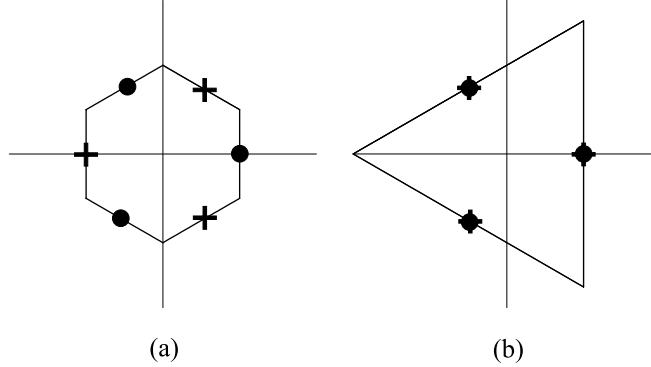


**Figure 5.3:** The trajectory of the vortex centres in the vortex mode for the two cases of three-fold degeneracy. In between the mirrors the trajectories are straight lines, while at the mirrors the vortex centres change their directions of propagation. The circles and the pluses indicate the positions of the vortex centres at the waist of the beam in the middle of the resonator for the wave that propagates to the right and to the left, respectively. In (a) we have  $g = 1/2$  and the trajectory is a regular hexagon, while in (b)  $g = -1/2$  and the trajectory is an equilateral triangle, which is traversed twice after three round trips.

Rayleigh range given by Eq. (3.25). We find that the (un-normalised) vortex state is given by

$$|u\rangle = \frac{\gamma^N}{\sqrt{N!}} |u_{N0}\rangle - (x_0 + iy_0)^N |u_{00}\rangle. \quad (5.40)$$

The vortex mode is simply a linear combination of the fundamental mode and the LG eigenmode of the resonator with mode numbers  $l = N$  and  $p = 0$ . These modes have the same round trip Gouy phase in case of  $N$ -fold degeneracy. The vortex modes are special cases of the geometric modes discussed in Chapter 2.

In Fig. 5.3 the trajectory in the transverse plane of the vortex centres in the vortex mode is given for the resonator configurations with  $g = \pm 1/2$ . In both cases we have three-fold degeneracy, but for  $g = 1/2$  the direction of propagation of the vortex centres rotates over the angle  $\pi/3$  after reflection by a mirror, while for  $g = -1/2$ , the angle is  $2\pi/3$ . In the former case the trajectory of the vortex centres is a regular hexahedron, while in the latter case it is an equilateral triangle, which is traversed twice after three round trips.

When a vortex centre in the vortex mode is followed during propagation, it follows a closed trajectory. Since the trajectory of a vortex centre is a black ray, the vortex mode contains a black ray that retraces itself after  $N$  round trips. This is similar to a displaced Gaussian beam, of which the centre retraces itself after  $N$  round trips (see Section 2.5). A difference is that the vortex mode is on axis. Also, the reflection of a light ray by a mirror only depends on the position and slope of the light ray, while for a dark ray it depends on the properties of the Gaussian mode on which it is imposed.

We assumed that the waist of the mode is in the centre of the resonator, which is not necessary in case of degeneracy. A more general vortex mode is obtained by unfolding the

resonator into an  $N$ -fold lens guide (see Section 2.5). As an input we use a Gaussian beam with an arbitrary spot size, which does not have to have a waist in this plane, on which a canonical vortex of charge  $+1$  is imposed. When the lens guide is folded back into a resonator, automatically we obtain a mode. It contains a black ray which retraces itself after  $N$  round trips. The trajectory of the vortex centre is again a polyhedron, which is in general not regular as in Fig. 5.3.

## 5.5 Conclusions

We derived an expression for the positions of the vortex centres in the higher-order astigmatic modes with mode numbers  $n$  and  $m$ , where  $m = 0$ , which is a generalisation of the result by Bekshaev *et al.* [41] to general astigmatism. These modes contain  $n$  vortices of the same charge and morphology which are located on a line through the centre of the beam. When the point on the Hermite-Laguerre sphere characterising the higher-order modes is on the equator the vortices vanish, giving rise to  $n$  edge dislocation lines. The morphology of the vortices is represented by a point on the morphology sphere. For non-astigmatic beams the point on the Hermite-Laguerre sphere that characterises the higher-order modes is the same as the point on the morphology sphere representing the morphology of the vortices in the mode.

By imposing mathematical vortices on astigmatic Gaussian beams, the propagation properties and interaction of vortices were studied. When a vortex is imposed on an astigmatic Gaussian beam which propagates through free space, the sign of the vortex charge can change upon propagation. When several canonical vortices with the same sign of the charge are imposed on a non-astigmatic Gaussian beam, the vortex trajectories are straight lines and there is no interaction between the vortices, which is also the case when the vortices are imposed on a maximal astigmatic beam under certain conditions. We conclude that in general when several vortices are imposed on a Gaussian beam and the vortex centres move on a straight line, there is no interaction between the vortices.

When a canonical vortex is imposed on a non-astigmatic Gaussian beam that propagates through a lens guide, the vortex centre moves on a straight line between the lenses, while changing direction at the lenses. The intensity of the light beam at the vortex centre vanishes, and therefore the trajectory of the vortex centre represents a dark ray. In a degenerate resonator a dark ray forms a closed trajectory, similar to a light ray of a geometric mode. We derived an expression for the beam profile of such a vortex mode. When the waist of the vortex mode is in the middle of the resonator, the trajectory of the dark ray in the transverse plane is a regular polyhedron. At the mirrors the transverse direction of propagation rotates over an angle which is equal to half the round trip Gouy phase of the Gaussian fundamental mode of the resonator.

## CHAPTER 6

---

### Using paraxial quantum operators

---

*In many optical experiments the light fields propagate in well-defined directions. The transverse profiles of these light beams satisfy the paraxial wave equation. For a description in the single-photon regime we define paraxial creation and annihilation operators and write the expression for the electric-field operator in terms of these operators. Then we apply the paraxial approximation and generalise the description to include the propagation through an arbitrary optical system. The paraxial creation operator creates a photon in a paraxial mode that is localised in one point in a specific transverse plane. This allows for a very simple description of the two-photon state created by the process of spontaneous parametric down-conversion, where the photons of a twin are created at the same location in the crystal. As an application we study quantitatively a quantum-eraser scheme by Zeilinger.*

## 6.1 Introduction

In a general optical experiment a light field is created by a source, after which the field propagates through an optical system towards a detector, which detects the intensity of the field. Inside the optical system the field propagates in well-defined directions, along the axis of the optical system. Then it is allowed to apply the paraxial approximation to the description of the field, which becomes much simpler than a general description in terms of solutions of the Maxwell equations. For experiments in the single-photon regime, such as experiments with twin photons, a quantum description is used where the electric field is quantised in terms of plane waves. Since in these experiments the paraxial approximation is usually also valid, it is useful to apply the paraxial approximation to the quantum description as well. Deutsch and Garrison [46] restrict the Hilbert space to states where the photons propagate in a well-defined direction. In this Chapter we define paraxial creation and annihilation operators, and write the expression for the electric-field operator in terms of these operators. Then we apply the paraxial approximation and generalise the description to include the propagation through a general optical system.

The paraxial creation operator creates a photon in a paraxial mode that is localised in one point in a specific transverse plane. It is not evident that such modes can exist, because Maxwell's equations require that in vacuum the divergence of the electric field vanishes. In order for the divergence of the electric field to vanish, the transverse profile of a light beam must be constant, like for a plane wave. Clearly, a mode of which the profile is localised in one point in a specific transverse plane, does not satisfy this requirement. Lax *et al.* [2] showed that in the paraxial approximation the transverse profile is allowed to vary and that the divergence of the electric field vanishes when corrections to the paraxial solution are taken into account.

As an application we use the paraxial creation and annihilation operators for a description of the creation and detection of twin photons. Twin photons are created by the process of spontaneous parametric down-conversion (SPDC) in a non-linear crystal [47]. Since the photons of a twin are created at the same location inside the crystal, it is advantageous to write the two-photon state in terms of paraxial creation operators that create photons in modes that are localised in one point in the plane of the crystal. After propagation through an optical system, the photons of a twin are detected in coincidence by two point detectors. The detection is described by the application of annihilation operators that annihilate photons in modes that are localised in one point in the detector plane. By using the transfer functions of the optical systems these annihilation operators are then expressed in terms of annihilation operators of photons in modes localised in one point in the crystal plane. This gives rise to a very simple description of twin-photon experiments.

In Section 6.2 we define the paraxial creation and annihilation operators, express the electric-field operator in terms of these operators and apply the paraxial approximation. In Section 6.3 we write the two-photon state created by SPDC in terms of paraxial creation operators, and describe the detection of the twin photons by using paraxial annihilation operators. In Section 6.4 we consider, as an example of a twin-photon experiment, a scheme that is reminiscent of the eraser scheme of Zeilinger [48], and determine the coincidence detection rate.

## 6.2 Paraxial operators

### 6.2.1 Electric-field operator

The positive-frequency part of the electric-field operator in the Heisenberg picture is given by

$$\hat{E}^+(\vec{r}, t) = i \int d\vec{k} \sqrt{\frac{\hbar\omega(k)}{2\epsilon_0(2\pi)^3}} \exp[i\vec{k} \cdot \vec{r} - i\omega(k)t] \sum_{\lambda} \vec{\epsilon}_{\lambda}(\vec{k}) \hat{a}_{\lambda}(\vec{k}), \quad (6.1)$$

where  $\hat{a}_{\lambda}(\vec{k})$  creates a photon with wave vector  $\vec{k}$  and polarisation vector  $\vec{\epsilon}_{\lambda}(\vec{k})$  at time  $t = 0$ . The dispersion relation in vacuum is given by  $\omega(k) = ck$ . The annihilation operator  $\hat{a}_{\lambda}(\vec{k})$  satisfies the commutation rules

$$[\hat{a}_{\lambda}(\vec{k}), \hat{a}_{\lambda'}^{\dagger}(\vec{k}')] = \delta_{\lambda\lambda'} \delta(\vec{k} - \vec{k}'). \quad (6.2)$$

For later convenience, we separate the wave vector as  $\vec{k} = \vec{\kappa} + k_z \vec{e}_z$ , with  $\vec{\kappa}$  in the  $xy$  plane, normal to  $\vec{e}_z$ . In the spirit of the description of narrow light beams, we wish to replace the variable  $k_z$  specifying the wave vector by the frequency  $\omega$ . For each value of  $\vec{\kappa}$  and  $\omega$ , there are still two values  $k_z = \pm \sqrt{\omega^2/c^2 - \kappa^2}$ , corresponding to a beam propagating to the right ( $r$ ) or to the left ( $l$ ). We look for annihilation operators  $\hat{a}_{\lambda s}(\vec{\kappa}, \omega)$ , with  $s = r, l$ , obeying the modified commutation rules

$$[\hat{a}_{\lambda s}(\vec{\kappa}, \omega), \hat{a}_{\lambda' s'}^{\dagger}(\vec{\kappa}', \omega')] = \delta_{\lambda\lambda'} \delta_{ss'} \delta(\vec{\kappa} - \vec{\kappa}') \delta(\omega - \omega'). \quad (6.3)$$

Since

$$\delta(\vec{k} - \vec{k}') = \delta(\vec{\kappa} - \vec{\kappa}') \delta(\omega - \omega') |dk_z/d\omega|, \quad (6.4)$$

the commutation rules (6.3) require the identification

$$\hat{a}_{\lambda}(\vec{k}) = \hat{a}_{\lambda s}(\vec{\kappa}, \omega) \sqrt{|d\omega/dk_z|}, \quad (6.5)$$

where  $s = r$  and  $s = l$ , for  $k_z > 0$  and  $k_z < 0$ , respectively. We have

$$|d\omega/dk_z| = c \sqrt{\omega^2 - c^2 \kappa^2} / \omega = c |\cos \theta|, \quad (6.6)$$

where  $\theta$  is the angle between  $\vec{k}$  and  $\vec{e}_z$ . The positive-frequency part of the electric-field operator in Eq. (6.1) can then be written as

$$\begin{aligned} \hat{E}^+(\vec{r}, t) = & i \int d\vec{\kappa} \int_{c\kappa}^{\infty} d\omega \sqrt{\frac{\hbar\omega}{2\epsilon_0 c (2\pi)^3 |\cos \theta|}} \exp(i\vec{\kappa} \cdot \vec{\rho} - i\omega t) \\ & \times \exp\left(i \frac{\omega z}{c} \cos \theta\right) \sum_{\lambda} \vec{\epsilon}_{\lambda r}(\vec{\kappa}, \omega) \hat{a}_{\lambda r}(\vec{\kappa}, \omega) + (\text{to the left}), \end{aligned} \quad (6.7)$$

where 'to the left' is the left-propagating part, which is found by replacing  $r$  by  $l$  and  $\cos \theta$  by  $-\cos \theta$ .

## 6. Using paraxial quantum operators

We define the two-dimensional Fourier transform of  $\hat{a}_{\lambda_s}(\vec{k}, \omega)$  as

$$\hat{a}_{\lambda_s}(\vec{k}, \omega) = \frac{1}{2\pi} \int d\vec{\rho} \exp(-i\vec{k} \cdot \vec{\rho}) \hat{a}_{\lambda_s}(\vec{\rho}, \omega), \quad (6.8)$$

where  $\vec{\rho}$  lies in the  $xy$  plane. We will call  $\hat{a}_{\lambda_s}(\vec{\rho}, \omega)$  the paraxial annihilation operator. The commutation rules follow from Eq. (6.3):

$$[\hat{a}_{\lambda_s}(\vec{\rho}, \omega), \hat{a}_{\lambda'_s}^\dagger(\vec{\rho}', \omega')] = \delta_{\lambda\lambda'} \delta_{ss'} \delta(\vec{\rho} - \vec{\rho}') \delta(\omega - \omega'). \quad (6.9)$$

Now the paraxial approximation is applied to the expression for the electric-field operator in Eq. (6.7). Instead of applying the approximation to the operators, Deutsch and Garrison [46] put a restriction on the Hilbert space. We define  $\vec{e}_z$  as the direction of propagation. The  $\vec{k}$  space is restricted to a cone around the direction of  $\vec{e}_z$  with a small opening angle. In the expression for the positive-frequency part of the electric-field operator in Eq. (6.7) the left-propagating part is left out. To simplify the notation the label  $r$  is dropped. In the restricted  $\vec{k}$  space we have

$$\cos \theta = \sqrt{1 - \frac{c^2 \kappa^2}{\omega^2}} \approx 1 - \frac{c^2 \kappa^2}{2\omega^2}. \quad (6.10)$$

Since  $\cos \theta$  varies slowly with  $\vec{k}$  and  $\omega$ , the  $\cos \theta$  inside the square root in (6.7) is approximated by 1. In the integration over  $\omega$ , the lower bound  $c\kappa$  is replaced by 0. In the restricted  $\vec{k}$  space it is justified to choose a basis for the polarisation that is independent of  $\vec{k}$  and  $\omega$ , and therefore  $\vec{e}_\lambda(\vec{k}, \omega)$  is replaced by  $\vec{e}_\lambda$ , which lies in the  $xy$  plane. In the paraxial approximation the positive-frequency part of the electric-field operator in Eq. (6.7) is then given by

$$\begin{aligned} \hat{E}^+(\vec{r}, t) = i \int_0^\infty d\omega \sqrt{\frac{\hbar\omega}{4\pi\epsilon_0 c}} \int d\vec{\rho}' h_f(\vec{\rho}, \vec{\rho}'; z, \omega) \\ \times \exp[-i\omega(t - z/c)] \sum_\lambda \vec{e}_\lambda \hat{a}_\lambda(\vec{\rho}', \omega), \end{aligned} \quad (6.11)$$

where

$$h_f(\vec{\rho}, \vec{\rho}'; z, \omega) = \frac{1}{(2\pi)^2} \int d\vec{k} \exp[i\vec{k} \cdot (\vec{\rho} - \vec{\rho}')] \exp\left(-\frac{icz\kappa^2}{2\omega}\right). \quad (6.12)$$

The function (6.12) is the transfer function for free-space propagation, which describes the field in the plane  $z$  due to a point source with frequency  $\omega$  that is located in the plane  $z = 0$  at the transverse coordinate  $\vec{\rho}'$ , within the paraxial approximation. The functions  $h_f(\vec{\rho}, \vec{\rho}'; z, \omega)$  form for each value of  $z$  and  $\omega$  a complete set of paraxial modes. The coordinate  $\vec{\rho}'$  designates the label of the modes while  $\vec{\rho}$  is the transverse coordinate in space. In each transverse plane  $z$  the modes form an orthogonal basis:

$$\int d\vec{\rho} h_f(\vec{\rho}, \vec{\rho}'; z, \omega) h_f^*(\vec{\rho}, \vec{\rho}''; z, \omega) = \delta(\vec{\rho}' - \vec{\rho}''). \quad (6.13)$$

From Eq. (6.12) it follows immediately that in the plane  $z = 0$  we have

$$h_f(\vec{\rho}, \vec{\rho}'; 0, \omega) = \delta(\vec{\rho} - \vec{\rho}'), \quad (6.14)$$

and we see that in this plane the modes are localised in one point, with transverse coordinates  $\vec{\rho}'$ . Equation (6.11) has the standard structure as an integration over an annihilation operator  $\hat{a}_\lambda(\vec{\rho}', \omega)$  multiplied by the corresponding mode function.

## 6.2.2 Interpretation of the paraxial creation operator

In the expression for the electric-field operator in Eq. (6.1) the annihilation operator  $\hat{a}_\lambda(\vec{k})$  appears in conjunction with the plane-wave mode  $\exp(i\vec{k} \cdot \vec{r})$ . The corresponding creation operator  $\hat{a}_\lambda^\dagger(\vec{k})$  creates at  $t = 0$  a photon in the polarisation state  $\lambda$  in this plane-wave mode. Similarly, by considering Eq. (6.11), we conclude that the paraxial creation operator  $\hat{a}_\lambda^\dagger(\vec{\rho}', \omega)$  creates a photon in the mode  $\exp(i\omega z/c)h_f(\vec{\rho}, \vec{\rho}'; z, \omega)$ , where  $\vec{\rho}'$  and  $\omega$  are the labels of the mode, and  $(\vec{\rho}, z)$  are the coordinates in space. According to Eq. (6.14), the mode function is a  $\delta$ -function in the plane  $z = 0$ , which means that in this plane the mode is localised in one point, with transverse coordinates  $\vec{\rho}'$ . It is also possible to define creation operators  $\hat{a}_{nm}^\dagger(\omega)$  that create photons in the transverse modes  $u_{nm}(\vec{\rho}, z)$  which form other complete sets of solutions of the paraxial wave equation, like Hermite-Gaussian or Laguerre-Gaussian modes. The numbers  $n$  and  $m$  are then the mode labels. The operators  $\hat{a}_{nm}(\omega)$  are expressed in terms of  $\hat{a}(\vec{\rho}, \omega)$ , and vice versa, as

$$\begin{aligned}\hat{a}_{nm}(\omega) &= \int d\vec{\rho} u_{nm}^*(\vec{\rho}, 0) \hat{a}(\vec{\rho}, \omega), \\ \hat{a}(\vec{\rho}, \omega) &= \sum_{nm} u_{nm}(\vec{\rho}, 0) \hat{a}_{nm}(\omega).\end{aligned}\tag{6.15}$$

So far we have only considered propagation in vacuum, but it is also possible that the light beam propagates through an optical system that contains lenses, apertures and other optical elements. In the paraxial approximation, when the profile of a light beam in the input plane of the optical system is given, the profile at the output plane, or in any other transverse plane is completely determined. Therefore it is always possible to define paraxial creation operators  $\hat{a}_\lambda^\dagger(\vec{\rho}', \omega, \text{in})$  which create photons with polarisation  $\lambda$  in modes that are  $\delta$ -functions in the input plane, for which we take  $z = 0$ . The mode function with the labels  $\vec{\rho}'$  and  $\omega$  is then the field due to a point source with frequency  $\omega$  at the transverse location  $\vec{\rho}'$  in the input plane. The mode function at the transverse coordinate  $\vec{\rho}$  in the output plane  $z$  of the optical system is simply given by the transfer function of the optical system  $h_{\lambda\lambda'}(\vec{\rho}, \vec{\rho}'; \omega)$ , which is allowed to depend on the polarisation  $\lambda$ . In the same way we define paraxial creation operators which create photons in modes that are  $\delta$ -functions in the output plane of the optical system. Similar to Eq. (6.15), the output operators  $\hat{a}_\lambda^\dagger(\vec{\rho}, \omega, \text{out})$  are expressed in terms of the input operators  $\hat{a}_\lambda^\dagger(\vec{\rho}, \omega, \text{in})$  as

$$\hat{a}_\lambda(\vec{\rho}, \omega, \text{out}) = \exp(i\omega z/c) \int d\vec{\rho}' \sum_{\lambda'} h_{\lambda\lambda'}(\vec{\rho}, \vec{\rho}'; \omega) \hat{a}_{\lambda'}(\vec{\rho}', \omega, \text{in}) + \hat{f}_\lambda(\vec{\rho}, \omega),\tag{6.16}$$

where  $\hat{f}$  is a noise source, which appears when the optical system is not lossless [49]. In case that there is scattering in the optical system, the noise operator  $\hat{f}$  arises from coupling to the outside world. The presence of the noise term is needed in order to conserve the commutation rules in Eq. (6.3). As we will see, the noise term is unimportant for the paraxial photon detection rates. In the next Section we use the paraxial creation operators for a description of twin photons created by the process of SPDC.

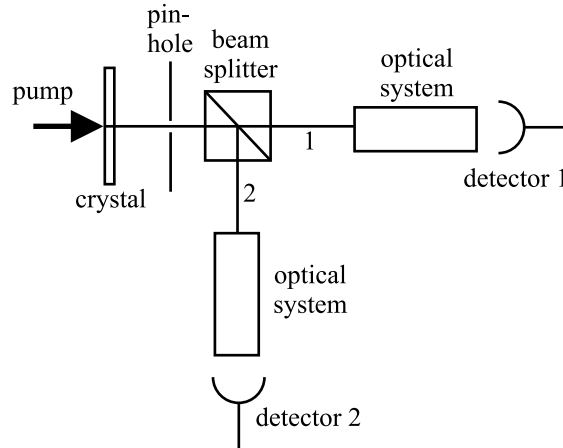


**Figure 6.1:** A monochromatic pump beam creates collinear twin photons in a non-linear crystal. After creation the twin photons pass a beam splitter. In the two output channels of the beam splitter are optical systems at the end of which coincidences are detected.

## 6.3 Spontaneous parametric down-conversion

### 6.3.1 Two-photon state

In the experiments with twin photons created by the process of SPDC in a non-linear crystal, the photons that are to be detected propagate along the lines connecting the crystal and the detectors. Since then the propagation directions are well-defined, it is advantageous to use a description of the two-photon state in terms of paraxial creation operators. A paraxial creation operator creates a photon in a mode that is localised in a single point in the output plane of the crystal, which simplifies the description greatly, because the photons are created at the same location in the crystal. We derive an expression for the two-photon state created by SPDC in terms of paraxial creation operators and obtain an expression for the coincidence detection amplitude.

We consider the scheme in Fig. 6.1. A pump beam creates collinear twin photons in a non-linear crystal, which is cut such that there is type-I phase matching for collinearly propagating twin photons. After creation the twin photons fall on a 50% : 50% beam splitter. In the output channels of the beam splitter are optical systems, at the end of which the photons are detected. The optical lines between the output plane of the crystal and the detection planes of detector 1 and 2 are referred to as the detection channels 1 and 2, respectively. Only coincidence detection counts are considered for which one photon of a twin is detected in each channel.

In order to arrive at a simple expression for the two-photon state, we apply the paraxial approximation to the electric-field operator that appears in the Hamiltonian for SPDC. In the

interaction picture the Hamiltonian is given by [47]

$$\hat{H}_I(t) = \int_C d\vec{r} E_p^+(\vec{r}, t) \hat{E}^-(\vec{r}, t) \hat{E}^-(\vec{r}, t), \quad (6.17)$$

where  $E_p^+$  is a component of the positive-frequency part of the classical electric field of the pump beam, and where  $\hat{E}^-$  is a component of the negative-frequency part of the electric-field operator. The integration domain ranges over the space  $C$  that is occupied by the crystal. In Chapter 8 polarisation aspects of SPDC are discussed. With the vacuum state  $|0\rangle$  as the initial state and the evolution governed by the Hamiltonian for SPDC in Eq. (6.17), the state at time  $t$  is, up to first order, the two-photon state

$$|\Psi(t)\rangle \propto \int_{-\infty}^t dt' H_I(t') |0\rangle. \quad (6.18)$$

The Hamiltonian (6.17) contains the positive-frequency part of the electric field of the pump beam, and the negative-frequency part of the electric-field operator. We apply the paraxial approximation to these fields, and take  $\vec{e}_z$  as the direction of propagation of the twin photons and the pump beam. The output plane of the crystal is located at the plane  $z = 0$ . We consider cases for which the pump beam is monochromatic with frequency  $\omega_p$ , while the photons of a twin are detected in a narrow frequency band centred around  $\omega_p/2$ . We assume that the crystal is thin so that the transverse profile of the pump field is constant inside the crystal. Then the Rayleigh range of the pump beam must be larger than the thickness of the crystal. For the pump field inside the crystal at the transverse coordinate  $\vec{\rho}$  in the plane  $z$  we write

$$E_p^+(\vec{r}, t) = G(\vec{\rho}) \exp[-i\omega_p(t - n_p z/c)], \quad (6.19)$$

where  $n_p$  is the refractive index, which is determined by the frequency  $\omega_p$  and the polarisation of the pump beam. The negative-frequency part of the electric-field operator in the paraxial approximation is given by the Hermitian conjugate of Eq. (6.11). Since the photons of a twin are detected around the frequency  $\omega_p/2$ , we replace  $\omega$  in the square-root term inside the integral over  $\omega$  by  $\omega_p/2$ , and take it out of the integral. The transverse profile is assumed to be constant inside the crystal, so we insert  $z = 0$  into  $h_f(\vec{\rho}, \vec{\rho}'; z, \omega)$  and use Eq. (6.14). We drop the polarisation labeling, which is justified since the photons of the twin have identical polarisations and the optical systems are insensitive to polarisation. Instead, we introduce a label that refers to the detection channel. The negative-frequency part of the electric-field operator inside the crystal is then written as

$$\hat{E}^-(\vec{r}, t) \propto \int_0^\infty d\omega \exp[i\omega(t - n_t z/c)] \left[ \hat{a}_1^\dagger(\vec{\rho}, \omega) + \hat{a}_2^\dagger(\vec{\rho}, \omega) \right], \quad (6.20)$$

where  $n_t$  is the refractive index for the twin photons, which is determined by the frequency  $\omega_p/2$  and the polarisation. In this expression the paraxial creation operator  $\hat{a}_i^\dagger(\vec{\rho}, \omega)$  creates a photon in detection channel  $i = 1, 2$ .

We insert Eqs. (6.19) and (6.20) into Eq. (6.18). The integration over the space occupied by the crystal gives rise to the phase-matching condition. The integration over the longitudinal coordinate  $z$  yields the longitudinal phase-matching condition, which is satisfied in our case for collinear twin photons with the frequency  $\omega_p/2$ . The integration over  $t'$  gives rise

to the frequency-matching condition, allowing only states where the frequencies of the photons of the twin add up to the pump frequency. Since the pump beam is monochromatic, the two-photon state is in principle independent of time, and we can replace in Eq. (6.18) the upper limit of the integration over  $t'$  by  $\infty$ . The two-photon state is then a superposition of all the states where the frequencies of the photons of the twin add up to  $\omega_p$ . Since the twin photons are detected with frequency  $\omega_p/2$  we only retain the part of the superposition where both photons of the twin have this frequency. Since we consider only coincidence detections, the part of the state where both photons exit the beam splitter in the same output channel is dropped. Under these assumptions the two-photon state can be written as

$$|\Psi\rangle \propto \int d\vec{\rho} G(\vec{\rho}) \hat{a}_1^\dagger(\vec{\rho}, \text{in}) \hat{a}_2^\dagger(\vec{\rho}, \text{in}) |0\rangle, \quad (6.21)$$

where  $\hat{a}_i^\dagger(\vec{\rho}, \text{in})$  creates a photon with frequency  $\omega_p/2$  in detection channel  $i = 1, 2$  in the mode that is a  $\delta$ -function at the location  $\vec{\rho}$  in the output plane  $z = 0$  of the crystal. By writing the two-photon state (6.21) in this form, it becomes clear that the photons of a twin are created at the same transverse location, but that this location itself is uncertain within the pump spot, which means that the twin photons are spatially entangled (see Chapter 7).

### 6.3.2 Coincidence detection rate

After creation the photons of a twin propagate through the detection channels. The amplitude for the detection of a photon at position  $\vec{\rho}_1$  in the plane of detector 1, in coincidence with the detection of a photon at position  $\vec{\rho}_2$  in the plane of detector 2, is given by

$$A(\vec{\rho}_1, \vec{\rho}_2) = \langle 0 | \hat{a}_1(\vec{\rho}_1, \text{out}) \hat{a}_2(\vec{\rho}_2, \text{out}) | \Psi \rangle. \quad (6.22)$$

where  $\hat{a}_i(\vec{\rho}, \text{out})$  annihilates a photon with frequency  $\omega_p/2$  in a mode that is a  $\delta$ -function at the location  $\vec{\rho}$  in the plane of detector  $i = 1, 2$ . As in Eq. (6.16) the 'out' operators are expressed in terms of the 'in' operators by

$$\hat{a}_i(\vec{\rho}, \text{out}) = \int d\vec{\rho}' h_i(\vec{\rho}, \vec{\rho}') \hat{a}_i(\vec{\rho}', \text{in}) + \hat{f}_i(\vec{\rho}), \quad (6.23)$$

where  $h_i(\vec{\rho}, \vec{\rho}')$  is the transfer function of detection channel  $i = 1, 2$  for a light field with frequency  $\omega_p/2$ . Inserting Eq. (6.23) into Eq. (6.22) gives rise to four terms, three of which contain a noise source. The noise operator annihilates a photon in a mode of the outside world. As a consequence, only the term that does not contain a noise source contributes to the coincidence detection amplitude. Accordingly, for coincidence detection the noise sources are irrelevant. It follows that

$$A(\vec{\rho}_1, \vec{\rho}_2) \propto \int d\vec{\rho} G(\vec{\rho}) h_1(\vec{\rho}_1, \vec{\rho}) h_2(\vec{\rho}_2, \vec{\rho}). \quad (6.24)$$

This result was also obtained and employed elsewhere [50–52]. The coincidence detection rate is given by

$$I(\vec{\rho}_1, \vec{\rho}_2) = |A(\vec{\rho}_1, \vec{\rho}_2)|^2. \quad (6.25)$$

## 6.4 Quantum erasing

### 6.4.1 Scheme

The results of the previous Section are used for a quantitative description of the quantum eraser which is discussed qualitatively by Zeilinger [48]. In Fig. 6.2(a) the scheme for the quantum eraser is depicted. One of the photons of a twin created by SPDC passes through a double slit, while the other photon is detected at various distances  $z$  behind a lens. When the latter photon is detected in the plane where the lens makes an image of the double slit ( $z = 2f$ ), the location at which the photon is detected reveals through which slit the other photon went, because the photons of a twin are created at the same location in the crystal. This which-path information destroys the interference and no double-slit interference pattern is observed behind the double slit. When the photon is detected in the focal plane of the lens ( $z = f$ ), information about the transverse momentum of the photon is obtained, but the information about the location at which the photon was created, is destroyed. Therefore, detecting the photon in the focal plane erases the which-path information and a familiar double-slit interference pattern is observed. Recently, this eraser setup has been used in an experiment by Gatti *et al.* [53].

We consider a similar scheme and show the mechanism of the quantum eraser by a calculation of the coincidence detection rate. The scheme is given in Fig. 6.2(b). Before the monochromatic pump beam enters the non-linear crystal it propagates through a mask, of which the transmission function is described by two Gaussian functions that are translated with respect to each other. In detection channel 1 the detector is located at a distance  $f$  from the output plane of the crystal. In detection channel 2 a lens with focal distance  $f$  is located at a distance  $2f$  from the output plane of the crystal. The detector is at a variable distance  $z$  from the lens. In front of both detectors are narrow-band frequency filters which have a centre frequency that is half the pump frequency. The difference with the eraser scheme of Zeilinger is that the double slit, which is part of detection channel 1 in the scheme of Zeilinger, is replaced by the mask in front of the non-linear crystal. In the picture by Belinskii and Klyshko [54] the schemes are virtually identical. In this picture the coincidence detection amplitude is the field in the plane of detector 1 as produced by a point source in the plane of detector 2. The field of this point source propagates through detection channel 2, is then multiplied by the pump profile in the crystal, after which it propagates through detection channel 1 to detector 1.

We will calculate the coincidence detection rate for this scheme for the case that detector 2 is in the plane where the lens makes an image of the mask ( $z = 2f$ ), and for the case where detector 2 is in the focal plane of the lens ( $z = f$ ). Since our setup in Fig. 6.2(b) has in fact only one transverse dimension, we simply write  $x$  for  $\vec{\rho}$ . The expression for the coincidence detection amplitude in Eq. (6.24) is written as

$$A(x_1, x_2) \propto \int dx G(x) h_1(x_1, x) h_2(x_2, x), \quad (6.26)$$

while, similar to Eq. (6.25), the coincidence detection rate is

$$I(x_1, x_2) = |A(x_1, x_2)|^2. \quad (6.27)$$

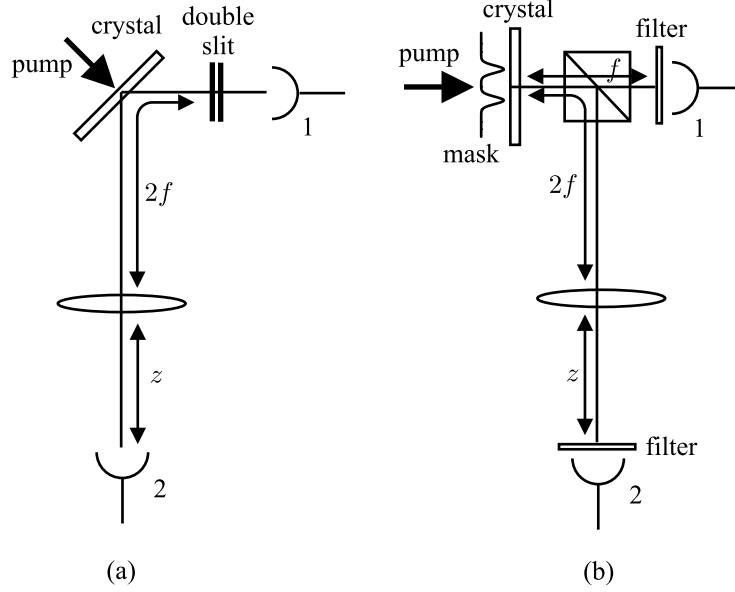


**Figure 6.2:** Similar schemes of the quantum eraser. The scheme (a) is discussed by Zeilinger. The scheme (b) is used to show the mechanism of the quantum eraser by a calculation of the coincidence detection amplitude. In (b) the pump beam propagates through a transmission mask before entering the crystal. In the crystal the pump beam creates twin photons, after which the photons of a twin are detected in coincidence by detectors 1 and 2.

### 6.4.2 Transfer functions

In order to calculate the coincidence detection amplitude the transfer functions of the optical systems must be determined. The transfer function for the propagation through free space over a distance  $z$  of a light field with frequency  $\omega_p/2$  is given by

$$h_f(x, x'; z) = \sqrt{\frac{\omega_p}{4\pi icz}} \exp\left[\frac{i\omega_p}{4cz}(x - x')^2\right], \quad (6.28)$$

which is the one-dimensional variant of (6.12). When a light beam with frequency  $\omega_p/2$  propagates through a lens with focal distance  $f$ , the beam profile is multiplied with the phase factor

$$h_l(x) = \exp\left(-\frac{i\omega_p x^2}{4cf}\right). \quad (6.29)$$

In detection channel 2 the propagation over a distance  $2f$  is followed by the passage through a lens and the propagation over a distance  $z$ . The corresponding transfer function is given by

$$h_2(x_2, x; z) = \int dx' h_f(x_2, x'; z) h_l(x') h_f(x', x; 2f). \quad (6.30)$$

The transfer function for the cases that  $z = f$  and  $z = 2f$  are calculated. We find that

$$\begin{aligned} h_2(x_2, x; f) &\propto \exp\left(-\frac{i\omega_p x_2 x}{2cf}\right), \\ h_2(x_2, x; 2f) &\propto \delta(x_2 + x), \end{aligned} \quad (6.31)$$

where the proportionality constants are phase factor independent of  $x$ , which drop out when the absolute value of the coincidence detection amplitude is taken. For both cases the transfer function for detection channel 1 is given by the transfer function for the propagation over a distance  $f$ , that is,

$$h_1(x_1, x) = h_f(x_1, x; f). \quad (6.32)$$

The pump profile behind the mask  $G(x)$ , which resembles the transmission function of a double slit, is given by

$$G(x) \propto \exp\left[-\frac{(x-d/2)^2}{2w^2}\right] + \exp\left[-\frac{(x+d/2)^2}{2w^2}\right], \quad (6.33)$$

where  $w$  is the width of the Gaussian function (or slit width), and  $d \gg w$  is the spacing between the Gaussian functions (or the spacing between the slits). With this pump profile the twins are created either in the first 'slit' or in the second. The coincidence detection rate is obtained by inserting the pump profile (6.33), the transfer function (6.32) for detection channel 1 and the transfer function (6.31) for detection channel 2, either for  $z = 2f$  or  $z = f$ , into the expression for the coincidence detection amplitude in Eq. (6.26), and then Eq. (6.27) is used to obtain the coincidence detection rate.

### 6.4.3 The two cases

In the case that  $z = 2f$  we find that the coincidence detection rate is given by

$$I(x_1, x_2) \propto \left\{ \exp\left[-\frac{(x_2-d/2)^2}{2w^2}\right] + \exp\left[-\frac{(x_2+d/2)^2}{2w^2}\right] \right\}^2. \quad (6.34)$$

The location at which detector 2 detects the photon completely determines the location at which the twin was created, since it is detected in the plane in which the lens creates an image of the crystal. Therefore, detector 1 measures the field from a point source in the crystal plane, which explains why the intensity  $I(x_1, x_2)$  is independent of  $x_1$ . The detection of the photon in the image plane  $z = 2f$  by detector 2 provides information in which 'slit' the twin was created. Therefore, no interference pattern is measured by detector 1. On the other hand, detection of the photon by detector 1 does not reveal any information about the location at which the twin was created. The pattern registered by detector 2 is then simply the image of the intensity distribution of the pump beam.

In the case that  $z = f$  we find that the coincidence detection rate is given by

$$\begin{aligned} I(x_1, x_2) &\propto \exp\left[-\frac{b^2}{b^2+f^2}\left(\frac{x_1+x_2}{w}\right)^2\right] \\ &\times \left\{ \cosh\left[\frac{b^2}{b^2+f^2}\frac{d(x_1+x_2)}{w^2}\right] + \cos\left[\frac{bf}{b^2+f^2}\frac{d(x_1+x_2)}{w^2}\right] \right\}, \end{aligned} \quad (6.35)$$

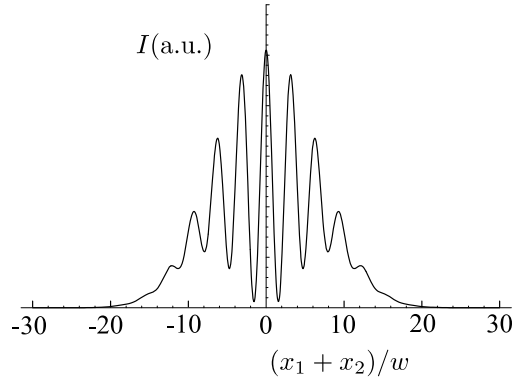


**Figure 6.3:** Coincidence detection rate as a function of  $(x_1 + x_2)/w$  for the case that  $z = f$ .

where

$$b = \frac{\omega_p w^2}{2c} \quad (6.36)$$

is the Rayleigh range corresponding to the Gaussian function in the pump beam profile. We see that the arguments of the cosh and the cos function differ by a factor  $b/f$ . As a consequence, a high visibility of the fringes can be expected when  $b \ll f$ . Physically this means that the width of the 'slits' must be much smaller than the distance  $f$  to detector 1, so that an interference pattern can develop.

In Fig. 6.3 the coincidence detection rate is given as a function of  $(x_1 + x_2)/w$  for the case that  $b/f = 0.1$  and  $w/d = 0.1$ . It is similar to the double-slit interference pattern observed in Zeilinger's scheme. When detector 2 detects the photon in the focal plane of the lens, information about the transverse momentum is obtained, which does not reveal information about the location in the crystal at which the twin was created. This erases the information in which 'slit' the twin was created, giving rise to the double-slit-like interference pattern measured by detector 1.

## 6.5 Conclusions

The paraxial wave equation describes the propagation of monochromatic light beams in free space and can simply be expanded to describe the propagation inside a general optical system. To obtain a description in the single-photon regime we defined paraxial creation operators which create photons with a specific frequency  $\omega$  at the transverse position  $\vec{\rho}$  in a transverse plane. The positive-frequency part of the electric-field operator is expressed in terms of the paraxial annihilation operators in Eq. (6.7). After application of the paraxial approximation, we arrived at Eq. (6.11). In this expression the paraxial annihilation operator appears together with the corresponding paraxial mode function, which is simply the transfer function for the propagation through free space for a light field with frequency  $\omega$ . The description was

generalised to include the propagation through a general optical system, by using the transfer function of the optical system as the mode function.

The paraxial creation operator creates a photon in a mode that is localised in a point in a specific transverse plane. The transfer function is then simply the paraxial field due to a point source at this location. The paraxial annihilation operator of a photon at a point in the output plane of an arbitrary optical system is expressed in terms of the paraxial annihilation operator of a photon at a point in the input plane by Eq. (6.16). By the transformation in Eq. (6.15) paraxial creation operators are defined that create a photon in other paraxial modes, such as Hermite-Gaussian or Laguerre-Gaussian modes.

As an application the two-photon state created by the process of SPDC is expressed in terms of paraxial creation operators of a photon in the plane of the non-linear crystal, which is the input plane of the optical lines to the detectors. The coincidence detection amplitude is expressed in terms of paraxial annihilation operators of a photon in a point in the planes of the detectors, which are the output planes of the optical lines. The 'out' and 'in' operators are then simply related by Eq. (6.16). This gives rise to a very simple and elegant description of the creation and detection of twin photons. The results are used to obtain a quantitative description of the quantum eraser discussed by Zeilinger.

6. Using paraxial quantum operators

## CHAPTER 7

---

### Interference between entangled photon states in space and time

---

*An interference scheme is proposed for studying the spatial entanglement of twin photons. By Fourier transformation, phase and frequency matching takes the form of spatial and temporal entanglement, respectively. We use a description in space and time to show the analogy between the spatial and temporal entanglement of twin photons.*

*J. Visser and G. Nienhuis, Eur. Phys. J. D 29, 301 (2004).*

## 7.1 Introduction

Entanglement of two separate parts of a quantum system implies that a measurement on one subsystem affects the state vector of the other one. Twin photons are often used for the study of entanglement. They are mostly created by the process of spontaneous parametric down-conversion (SPDC), by a pump pulse in a non-linear crystal. Polarisation entanglement of the photons of a twin has been studied thoroughly. In many experiments with twin photons it was found that the Bell inequalities are violated, showing that the photons of the twins are entangled [55]. It has recently been demonstrated that this entanglement is still present after the two photons have been transmitted by a metal screen with a periodic pattern of perforations, where the photons have been converted into surface plasmons [56]. In the case of polarisation entanglement, the two subsystems have a two-dimensional state space. The entanglement of two particles with eigenspaces larger than the two-dimensional polarisation space has been studied only recently. *Vaziri et al.* have demonstrated the entanglement of orbital angular momentum in an experiment with twin photons [57].

Twin photons can also be entangled in continuous degrees of freedom, such as frequency or transverse wave vector. Frequency entanglement takes the form of time entanglement after Fourier transformation to the time domain. Most theoretical descriptions of SPDC involve summations over plane-wave modes, characterised by frequency and wave vector. However, in many situations a description in terms of field operators that depend on time and transverse space more closely follows the actual life of the two photons from their creation to their detection. This can make the description more transparent. An example is the experiment by *Hong et al.* [58], where it is shown that the two photons of a twin arriving one in each input channel of a beam splitter at the same instant exit in the same output channel. This shows up as a destructive interference in the coincidence rate. This experiment is described in terms of integrals over wave vectors and frequencies of the emitted photons. The condition for interference that the two photons must arrive simultaneously at the beam splitter is brought out more clearly by a formulation in the domain of space and time [59]. An equivalent experiment, with two independent photons from two separate emitters, has been studied recently [60]. *Franson* [61] proposed an experiment where the photons of a twin can both take a short and a long path to the detector. As a consequence of temporal entanglement, there is interference between the two amplitudes where both take the long, or both take the short path. This cannot be understood as interference between single photons, only as an interference between two different histories of the photon pair. The proposed experiment has been realised by *Tittel et al.* [62]. The same argument holds for the experiment of *Pittman et al.* [63], who show that for interference to occur it is not necessary that the photons of a twin arrive at the beam splitter at the same instant. In this experiment the two photons are created with orthogonal polarisation, and a polarisation-dependent delay is imposed, so that the photons do not arrive at the beam splitter simultaneously. As a consequence of the polarisation-dependent delay, the arrival times of the photons at the detectors generally contain information on the polarisation. The temporal entanglement of the twin photons is then exploited to erase this information, so that interference with 100% visibility is recovered. Viewed in the time domain, these experiments rely on the fact that the photons of a twin are created at the same instant of time, but where the exact time of creation of the twin is undetermined.

We point out that, apart from temporal entanglement, the photons of a twin can also be

spatially entangled. After Fourier transformation to the transverse space, entanglement of the transverse wave vector takes the form of spatial entanglement. Due to the local nature of the non-linear interaction in the crystal, the photons of a twin are created at the same instant of time and at the same position. The two-photon state is a linear superposition of states corresponding to different times of creation, which are undetermined within the duration of the pump pulse. The same holds for the location in the crystal. The photons of a twin are created at the same location in the crystal, but this location is undetermined within the pump spot on the crystal.

In Section 7.2 we give a general expression for the two-photon state created by SPDC. In Section 7.3 we propose an experiment for studying the spatial entanglement of twin photons. This experiment is the spatial equivalent of an experiment by Pittman *et al.* [63], which we discuss in Section 7.4. For both experiments we calculate the two-photon state and the coincidence detection rates. We use a description in the space and time domain, which more closely follows the life of the photons in the experiment. Another advantage is that then the analogy between temporal and spatial entanglement is much more evident.

## 7.2 Two-photon state

In the process of SPDC twin photons are created by a pump beam in a non-linear crystal at one point and one time instant. The amplitude for the creation of a twin at time  $t$  and position  $\vec{r}$  in the crystal is proportional to the positive-frequency part of the electric field of the classical pump beam  $E_p(\vec{r}, t)$ . We assume that the pump beam and the photons of the twin have a common direction of propagation, which we call the  $z$  direction. In the  $xy$  plane, or transverse plane, the crystal is much larger than the pump spot. The output plane of the crystal is located at  $z = 0$  and we write

$$E_p(\vec{r}, t)|_{z=0} = g(t)G(\vec{\rho}), \quad (7.1)$$

where  $g(t)$  is the pulse shape, and  $G(\vec{\rho})$  the transverse profile of the pump beam. The two-dimensional vector  $\vec{\rho} = (x, y)$  is the transverse coordinate.

For the basis of polarisation we take the eigenvectors  $\{\vec{\epsilon}_H, \vec{\epsilon}_V\}$  as determined by the crystal birefringence and the propagation direction of the pump beam. By using a pinhole twins are selected that propagate collinearly with the pump beam. The orientation of the crystal with respect to the propagation direction of the pump beam and polarisation of the pump beam are chosen such that the amplitude for the photons of the twin to have orthogonal polarisations is much larger than the amplitude for identical polarisations: we have type-II phase matching. Because the crystal is birefringent, the speed and direction of propagation of a photon inside the crystal is polarisation dependent. The resulting walk-offs can be compensated by using compensating crystals [55]. After compensation the two-photon state in the interaction picture can be written as

$$|\Psi(t)\rangle \propto \int_{-\infty}^t dt' g(t') \int d\vec{\rho} G(\vec{\rho}) \hat{a}_H^\dagger(\vec{\rho}, t') \hat{a}_V^\dagger(\vec{\rho}, t') |0\rangle, \quad (7.2)$$

where  $\hat{a}_H^\dagger(\vec{\rho}, t)$  and  $\hat{a}_V^\dagger(\vec{\rho}, t)$  create an  $H$ -polarised and a  $V$ -polarised photon, respectively, at time  $t$ , and transverse coordinate  $\vec{\rho}$ . The state  $|0\rangle$  is the vacuum state. The expression for the

two-photon state is only valid when the dispersion in the crystal can be neglected. This is the case when the spectrum of the pulse shape  $g(t)$  is narrow band, and the photons of the twins are detected with a well-determined frequency, which is at the cost of the brightness of the parametric down-conversion. When these conditions are relaxed, the brightness increases, but the visibility in an interference experiment is reduced because of dispersion in the crystal [64, 65]. Since we study the entanglement of the twin photons using two-photon interference, a large visibility is favoured over a large brightness. The operators  $\hat{a}_i^\dagger(\vec{\rho}, t)$  with  $i = H, V$  can be assumed to satisfy the commutation relations

$$[a_i(\vec{\rho}, t), a_j^\dagger(\vec{\rho}', t')] = \delta_{ij} \delta(\vec{\rho} - \vec{\rho}') \delta(t - t'), \quad (7.3)$$

where  $i, j = H, V$  [66]. Note that we describe the process in the domain of time  $t$  and transverse position  $\vec{\rho}$ , rather than the more common picture of frequency  $\omega$  and transverse wave vector  $\vec{k}$ . These pictures are related by Fourier transformations as

$$\hat{a}_i(\vec{\rho}, t) = \frac{1}{(2\pi)^{3/2}} \int d\omega \int d\vec{k} \hat{a}_i(\vec{k}, \omega) \exp(i\vec{k} \cdot \vec{\rho} - i\omega t), \quad (7.4)$$

where the momentum-frequency field operators  $\hat{a}_i(\vec{k}, \omega)$  obey the commutation relations

$$[\hat{a}_i(\vec{k}, \omega), \hat{a}_j^\dagger(\vec{k}', \omega')] = \delta_{ij} \delta(\vec{k} - \vec{k}') \delta(\omega - \omega'). \quad (7.5)$$

Notice that the photon state can be perfectly localised in the transverse plane [46]. With the definitions

$$\tilde{G}(\vec{k}) = \frac{1}{(2\pi)^2} \int d\vec{\rho} G(\vec{\rho}) \exp(-i\vec{k} \cdot \vec{\rho}), \quad \tilde{g}(\omega, t) = \frac{1}{2\pi} \int_{-\infty}^t dt' g(t') \exp(i\omega t'), \quad (7.6)$$

the two-photon state in Eq. (7.2) can be written as

$$|\Psi(t)\rangle \propto \int d\vec{k} \int d\vec{k}' \tilde{G}(\vec{k} + \vec{k}') \int d\omega \int d\omega' \tilde{g}(\omega + \omega', t) \hat{a}_H^\dagger(\vec{k}, \omega) \hat{a}_V^\dagger(\vec{k}', \omega') |0\rangle. \quad (7.7)$$

In this expression we recognise the conservation of energy and transverse momentum, which is equivalent to the fact that the two photons are created at the same location and the same instant of time.

After propagation through an optical system, which might contain several optical elements, the photons of the twins are detected in coincidence by two detectors  $a$  and  $b$ . These detectors detect photons behind linear polarisers, and integrate over time and over the transverse location in the detector plane. A component of the positive-frequency part of the electric-field operator at the transverse coordinate  $\vec{\rho}_a$  in the detection plane of detector  $a$  at time  $t_a$  is written as  $\hat{E}_a^+(\vec{\rho}_a, t_a)$ . For detector  $b$  we write  $\hat{E}_b^+(\vec{\rho}_b, t_b)$ . These operators can be expressed in terms of the annihilation operators  $\hat{a}_i(\vec{\rho}, t)$ , where  $i = H, V$ . These expressions depend on the transfer functions of the optical systems. The transverse part of the transfer function describes the evolution of the transverse profile of a light field when it propagates from the crystal plane to the detector plane. It is frequency dependent, but since a narrow-band filter is used, it is justified to fix this frequency at the centre frequency of the filter. As a consequence, the transfer function factorises in a transverse and a longitudinal, or temporal part.

The amplitude where detector  $a$  detects a photon at time  $t_a$  and position  $\vec{\rho}_a$ , and detector  $b$  detects a photon at time  $t_b$  and position  $\vec{\rho}_b$ , is given by

$$A = \langle 0 | \hat{E}_b^+(\vec{\rho}_b, t_b) \hat{E}_a^+(\vec{\rho}_a, t_a) | \Psi(t_a) \rangle, \quad (7.8)$$

where  $t_b > t_a$ . We shall now consider separately cases where either the spatial entanglement or the temporal entanglement is responsible for interference.

## 7.3 Spatial entanglement

### 7.3.1 Spatial interferometer

We use the interference scheme in Fig. 7.1 to study spatial entanglement. A pump beam creates twin photons in a non-linear crystal by the process of SPDC. The orientation of the crystal with respect to the propagation direction of the pump beam and the polarisation of the pump beam are such, that the twin photons that propagate collinearly have orthogonal polarisation. The walk-offs that result from the birefringence of the crystal, are compensated by compensating crystals. For simplicity they are not shown in the picture. A pinhole is used to select collinear twins. The crystal birefringence together with the direction of propagation defines a unique basis for the polarisation, consisting of the unit vectors  $\vec{e}_H$  and  $\vec{e}_V$ . A translation  $\Delta\vec{s}_V$  in the transverse direction is imposed on  $V$ -polarised photons. This is done by propagation of the beam through a tilted birefringent crystal. Then also a time difference between  $H$ - and  $V$ -polarised photons results, introducing polarisation information in the arrival time of the photons at the detectors. This polarisation information can be erased by propagation through a compensating crystal with the appropriate thickness. The collinear twins fall on a 50% : 50% beam splitter. In one of the output channels a translation  $\Delta\vec{s}_H$  is imposed in the transverse direction on  $H$ -polarised photons. Coincidences are detected by the detectors  $a$  and  $b$  in the output channels. In front of both detectors are narrow-band filters and linear polarisers set to transmit when the polarisation is at an angle of  $45^\circ$  with respect to both  $\vec{e}_H$  and  $\vec{e}_V$ . The narrow-band filters have a centre frequency of half the frequency of the pump beam. The detectors are bucket detectors that integrate both over the time and the transverse space. In front of detector  $b$  is also a circular aperture with radius  $d$ . For this setup the coincidence detection rate is considered as a function of the translation  $\Delta\vec{s}_H$  for fixed value of  $\Delta\vec{s}_V$ . Now two amplitudes are relevant. The first is the amplitude that the  $H$ -polarised photon is detected by detector  $a$  and the  $V$ -polarised photon is detected by detector  $b$ . For the second amplitude it is the other way around. It is necessary that the polarisers are both at  $45^\circ$ , because then the information about the polarisation is completely erased, and these amplitudes can interfere.

### 7.3.2 The coincidence detection rate

In section 7.2 we argued that the transfer functions that describe the propagation from the crystal to the detector, factorise in transverse and temporal parts. In the interferometer in Fig. 7.1 there are no optical elements that introduce any polarisation dependence in the temporal properties. As a consequence, the temporal part of the problem drops out, and we can write

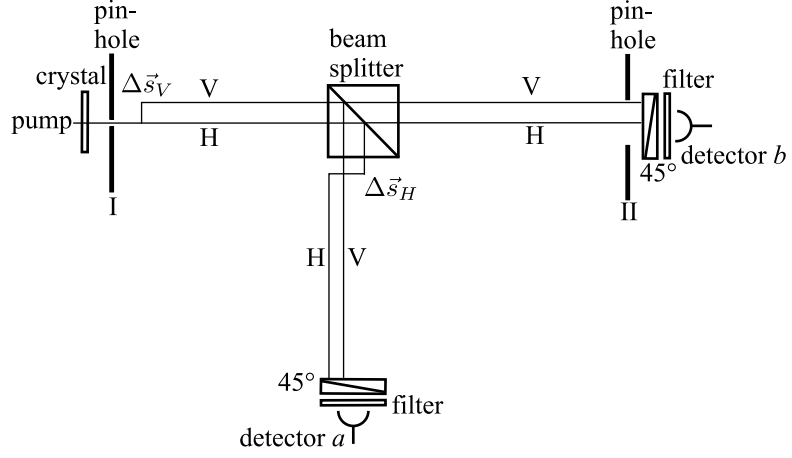


**Figure 7.1:** Scheme of the spatial interferometer. The pump beam creates twin photons in a non-linear crystal. Collinear twins with orthogonal polarisations are selected with a pinhole. On V-polarised photons a transverse translation  $\Delta\vec{s}_V$  is imposed. Then the beam falls on a beam splitter. In one of the output channels a transverse translation  $\Delta\vec{s}_H$  is imposed on H-polarised photons. The detectors a and b detect coincidences in the two output channels. In front of both detectors is a narrow-band filter and a linear polariser at  $45^\circ$ . There is a pinhole in front of detector b.

the two-photon state in Eq. (7.2) as

$$|\Psi\rangle \propto \int d\vec{\rho} G(\vec{\rho}) \hat{a}_H^\dagger(\vec{\rho}) \hat{a}_V^\dagger(\vec{\rho}) |0\rangle, \quad (7.9)$$

where  $\hat{a}_H^\dagger(\vec{\rho})$  and  $\hat{a}_V^\dagger(\vec{\rho})$  create a photon at the transverse position  $\vec{\rho}$  in the crystal plane, with H and V polarisation, respectively. For simplicity the translation  $\Delta\vec{s}_V$  is imposed at the output plane of the crystal, and the translation  $\Delta\vec{s}_H$  is imposed immediately behind the output plane of the beam splitter. The detectors are both at a distance  $z$  from the crystal along the optical lines. The transfer function for free space propagation over a distance  $z$  is given by

$$h_f(\vec{\rho}, \vec{\rho}'; z) = \frac{k}{2\pi iz} \exp\left[\frac{ik}{2z} (\vec{\rho} - \vec{\rho}')^2\right], \quad (7.10)$$

where  $k$  is the wavenumber of the light. We consider as an example the transfer function for the propagation from the output plane of the crystal to the detection plane of detector a for a beam with H polarisation. We split up the optical line in two parts with lengths  $z_1$  and  $z_2$ , where the first part stretches from the crystal plane to the output plane of the beam splitter, and the second from the latter plane to the detector plane. The vectors  $\vec{\rho}$ ,  $\vec{\rho}'$ , and  $\vec{\rho}_a$  refer to a point in the plane of the crystal, beam splitter, and detector, respectively. Then the transfer function for the propagation from the crystal to detector a for an H-polarised beam is given by

$$\int d\vec{\rho}' h_f(\vec{\rho}_a, \vec{\rho}' + \Delta\vec{s}_H; z_2) h_f(\vec{\rho}', \vec{\rho}; z_1) = h_f(\vec{\rho}_a, \vec{\rho} + \Delta\vec{s}_H; z), \quad (7.11)$$

where  $z = z_1 + z_2$ . We have ignored that the beam splitter changes the handedness of the basis of the transverse space. We see that for the transfer function it is not relevant in which plane the translation  $\Delta\vec{s}_H$  is imposed. Now we can express the positive-frequency parts of the electric-field operators in the detector planes in terms of the annihilation operators  $\hat{a}_H(\vec{\rho})$  and  $\hat{a}_V(\vec{\rho})$ , that annihilate a photon at the location  $\vec{\rho}$  in the detector plane with  $H$  and  $V$  polarisation, respectively. Because the polarisers in front of the detectors are at  $45^\circ$ , only photons with polarisation vector  $(\vec{e}_H + \vec{e}_V)/\sqrt{2}$  are detected. Therefore we only consider the component of the electric-field operator in the  $45^\circ$  direction. We have

$$\begin{aligned}\hat{E}_a^+(\vec{\rho}_a) &= \int d\vec{\rho} [h_f(\vec{\rho}_a, \vec{\rho} + \Delta\vec{s}_H; z)\hat{a}_H(\vec{\rho}) + h_f(\vec{\rho}_a, \vec{\rho} + \Delta\vec{s}_V; z)\hat{a}_V(\vec{\rho})] , \\ \hat{E}_b^+(\vec{\rho}_b) &= \int d\vec{\rho} [h_f(\vec{\rho}_b, \vec{\rho}; z)\hat{a}_H(\vec{\rho}) + h_f(\vec{\rho}_b, \vec{\rho} + \Delta\vec{s}_V; z)\hat{a}_V(\vec{\rho})] .\end{aligned}\quad (7.12)$$

By using Eq. (7.9) and the commutation rules in Eq. (7.3) we find that the coincidence detection amplitude in Eq. (7.8) is given by

$$\begin{aligned}A(\vec{\rho}_a, \vec{\rho}_b) &= \langle 0 | \hat{E}_a^+(\vec{\rho}_a) \hat{E}_b^+(\vec{\rho}_b) | \Psi \rangle \\ &= \int d\vec{\rho} G(\vec{\rho}) [h_f(\vec{\rho}_a, \vec{\rho} + \Delta\vec{s}_H; z)h_f(\vec{\rho}_b, \vec{\rho} + \Delta\vec{s}_V; z) \\ &\quad + h_f(\vec{\rho}_a, \vec{\rho} + \Delta\vec{s}_V; z)h_f(\vec{\rho}_b, \vec{\rho}; z)] ,\end{aligned}\quad (7.13)$$

where only the cross products  $\propto \hat{a}_H \hat{a}_V$  from  $\hat{E}_a^+ \hat{E}_b^+$  contribute. The coincidence detection rate is given by

$$R = \int d\vec{\rho}_a \int_{\text{II}} d\vec{\rho}_b |A(\vec{\rho}_a, \vec{\rho}_b)|^2 , \quad (7.14)$$

where II indicates that the integration domain is over the opening of pinhole II. We perform the integration over  $\vec{\rho}_a$  and use that the transfer function for free space propagation is unitary:

$$\int d\vec{\rho} h_f(\vec{\rho}_2, \vec{\rho}; z) h_f^*(\vec{\rho}, \vec{\rho}_1; z) = \delta(\vec{\rho}_2 - \vec{\rho}_1) . \quad (7.15)$$

We then find that

$$\begin{aligned}R &= \frac{k^2 d^2}{2\pi z^2} \int d\vec{\rho} |G(\vec{\rho})|^2 + 2\text{Re} \int d\vec{\rho} G(\vec{\rho}) G^*(\vec{\rho} + \Delta\vec{s}_V - \Delta\vec{s}_H) \\ &\quad \times \int_{\text{II}} d\vec{\rho}_b h_f(\vec{\rho}_b, \vec{\rho}; z) h_f^*(\vec{\rho}_b, \vec{\rho} + 2\Delta\vec{s}_V - \Delta\vec{s}_H; z) .\end{aligned}\quad (7.16)$$

For the integration over  $\vec{\rho}_b$  we use the property

$$\begin{aligned}\int_{\text{II}} d\vec{\rho}' h_f(\vec{\rho}', \vec{\rho} + \Delta\vec{s}/2; z) h_f^*(\vec{\rho}', \vec{\rho} - \Delta\vec{s}/2; z) = \\ \frac{kd}{2\pi z \|\Delta\vec{s}\|} J_1(kd \|\Delta\vec{s}\|/z) \exp[ik\vec{\rho} \cdot \Delta\vec{s}/z] ,\end{aligned}\quad (7.17)$$

where

$$J_n(x) = \frac{1}{2\pi i^n} \int_0^{2\pi} d\phi \exp(ix \cos \phi + in\phi) \quad n = 0, 1, 2, \dots \quad (7.18)$$

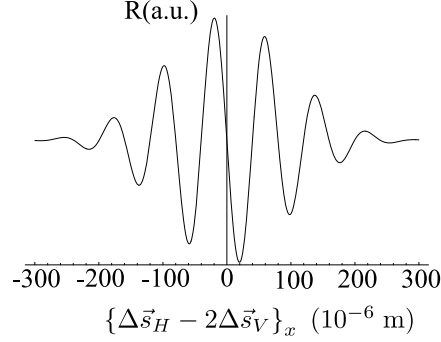


**Figure 7.2:** The coincidence detection rate  $R$  as a function of the  $x$  component of  $\Delta\vec{s}_H - 2\Delta\vec{s}_V$  for a Gaussian pump beam tilted at  $0.6^\circ$ . The intensity of the pump beam drops off to  $1/e$  at a distance of 3 mm from the beam axis. The wavelength of the pump beam is 400 nm. The distance from the crystal to the detectors is 2 m. For the radius of the pinhole in front of detector  $b$  we have  $d = 3$  mm. The value of the  $x$  component of  $\Delta\vec{s}_V$  is fixed at 0.1 mm.

are the Bessel functions of the first kind. By using this property we find that

$$R \propto \frac{1}{2} \int d\vec{\rho} |G(\vec{\rho})|^2 + \frac{z}{kd\|\Delta\vec{s}\|} J_1(kd\|\Delta\vec{s}\|/z) \times \text{Re} \int d\vec{\rho} \exp(ik\vec{\rho} \cdot \Delta\vec{s}/z) G(\vec{\rho} + \Delta\vec{s}/2) G^*(\vec{\rho} - \Delta\vec{s}_H/2), \quad (7.19)$$

where  $\Delta\vec{s} = \Delta\vec{s}_H - 2\Delta\vec{s}_V$ . To see interference fringes, the exponential factor inside the integral must oscillate at least once over the range of the pump spot, which puts a lower bound on  $\|\Delta\vec{s}\|$ . The visibility of the fringes is determined by the factor in front of the integral, which puts an upper bound on the radius  $d$  of pinhole II. As a consequence, to see interference fringes the spot size must in general not be smaller than the size of pinhole II.

As an example we use a Gaussian function for the pump beam profile  $G(\vec{\rho})$ . In order to obtain interference fringes, we assume that the pump beam is slightly tilted, such that the propagation direction is in the  $xz$  plane. Then the profile of the pump beam has a phase pattern. The translations  $\Delta\vec{s}_H$  and  $\Delta\vec{s}_V$  are imposed in the  $x$  direction. In Fig. 7.2 the coincidence detection rate is given for this case as a function of the  $x$  component of  $\Delta\vec{s}_H$  for fixed value of  $\Delta\vec{s}_V$ . We see in Fig. 7.2 that for  $\Delta\vec{s}_H = 2\Delta\vec{s}_V$  the visibility is 100%. The reason for this can be understood by considering again the two relevant amplitudes that we discussed at the end of Section 7.3.1. We first consider the amplitude  $A(H \rightarrow a; V \rightarrow b)$  where the  $H$ -polarised photon is detected by detector  $a$ , and the  $V$ -polarised photon by detector  $b$ . These photons are translated by  $\Delta\vec{s}_H - \Delta\vec{s}_V$  with respect to each other. For the amplitude  $A(H \rightarrow b; V \rightarrow a)$  where the  $H$ - and the  $V$ -polarised photon are detected by detector  $b$  and  $a$ , respectively, the photons are translated by  $\Delta\vec{s}_V$  with respect to each other. Since in front of the detector there is a linear polariser at  $45^\circ$ , the information about the polarisation is erased. As a consequence, these two amplitudes are indistinguishable when the polarisation is concerned. For interference with maximum visibility, the two amplitudes must also be indistinguishable concerning

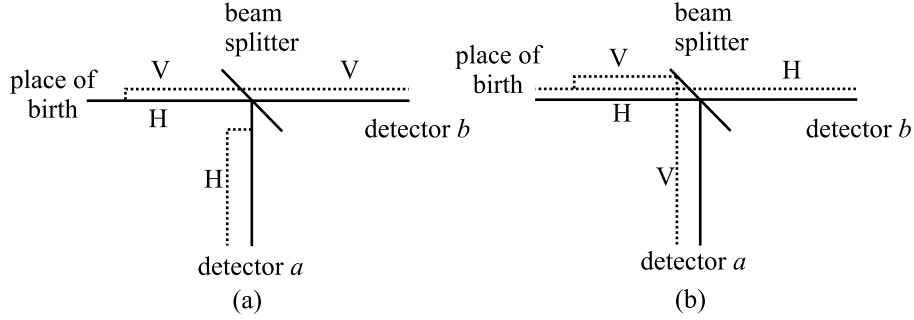


**Figure 7.3:** The two relevant amplitudes for the case that  $\Delta\vec{s}_H = 2\Delta\vec{s}_V$ , where the location of birth of the twin photons for the amplitude  $A(H \rightarrow a; V \rightarrow b)$  in (a) differs by  $\Delta\vec{s}_V$  with respect to the location of birth for the amplitude  $A(H \rightarrow b; V \rightarrow a)$  in (b). The thick lines are the optical axes of the system and the paths of the photons are dashed. We see that for both amplitudes the location at detector  $a$  at which a photon arrives, is the same, but that the polarisation of the photon is different. The same holds for the photon arriving at detector  $b$ . Nevertheless, the two amplitudes are indistinguishable since the polarisers in front of both detectors erase the information about the polarisation.

their spatial properties. This is the case when, for the two amplitudes, the vectors over which the  $H$ - and  $V$ -polarised photon are translated with respect to each other, are identical. That is, when  $\Delta\vec{s}_H = 2\Delta\vec{s}_V$ , indeed. Under this condition there might still be another spatial property that distinguishes the two amplitudes. For the amplitude  $A(H \rightarrow a; V \rightarrow b)$  one photon is translated by  $\Delta\vec{s}_V$ , and the other by  $2\Delta\vec{s}_V$ , while for the amplitude  $A(H \rightarrow b; V \rightarrow a)$  the translations are 0 and  $\Delta\vec{s}_V$ . The relative translation is the same for both, but the absolute translations are different. The reason that the visibility is 100% anyway, is because of the spatial entanglement: the photons of the twins are created at the same location in the crystal, but this location itself is undetermined within the spot size of the pump beam on the crystal. Therefore, when  $\Delta\vec{s}_V$  is small with respect to the spot size, the two amplitudes cannot be distinguished by a difference in the absolute translation mentioned above. This can be seen in Fig. 7.3, where the location of birth of the twin photons for the amplitude  $A(H \rightarrow a; V \rightarrow b)$  differs by  $\Delta\vec{s}_V$  with respect to the location of birth for the amplitude  $A(H \rightarrow b; V \rightarrow a)$ . Then the two amplitudes cannot be distinguished. The width of the envelope in Fig. 7.2 depends on the radius of the pinhole in front of detector  $b$ . A smaller pinhole radius decreases the spatial distinguishability of the detector. Because the detector is then less able to obtain spatial information, the width of the envelope becomes larger.

By imposing the translation  $\Delta\vec{s}_H$  on  $H$ -polarised photons the spatial information introduced by the translation  $\Delta\vec{s}_V$  on the  $V$  polarisation can be erased. In Fig. 7.1 we see that the erasing is done in one of the output channels of the beam splitter. The condition for erasing is then that there must be spatial entanglement. The information can also be erased by imposing a translation  $\Delta\vec{s}_H = \Delta\vec{s}_V$  on  $H$ -polarised photons before the beam splitter. Then spatial entanglement is not necessary, because before the beam splitter the collinear twins are not polarisation entangled. Erasing behind the beam splitter without using spatial entanglement

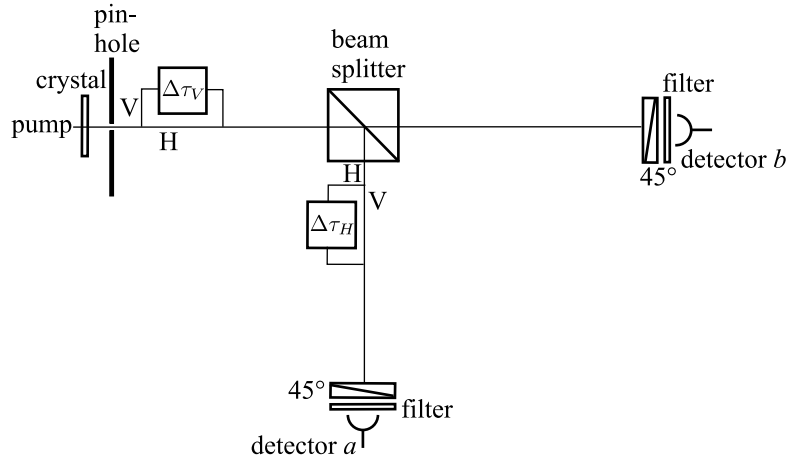


**Figure 7.4:** Scheme of the temporal interferometer. The pump beam creates twin photons in a non-linear crystal. A pinhole selects collinear twins with orthogonal polarisation. On V-polarised photons a delay  $\Delta\tau_V$  is imposed. Then the beam falls on a beam splitter. In one of the output channels a delay  $\Delta\tau_H$  is imposed on H-polarised photons. Coincidences are detected by the detectors *a* and *b* in the two output channels. In front of both detectors is a narrow-band filter and a linear polariser at  $45^\circ$ .

can be done by imposing the translation  $\Delta\vec{s}_H = \Delta\vec{s}_V$  on H-polarised photons in both output channels of the beam splitter.

## 7.4 Temporal entanglement

The interference scheme that we discussed in Section 7.3 is the spatial analogue of the interference scheme in an experiment of Pittman *et al.* [63] where delays instead of transverse translations are imposed. For the spatial interferometer the spatial entanglement of the twin photons is necessary, while for the temporal interferometer it is the temporal entanglement of the twin photons. We show that the temporal interferometer of Pittman *et al.* is similar to the spatial interferometer. For this we calculate the coincidence detection rate as a function of the delays that are imposed. A simplified version of the experiment of Pittman *et al.* is given in Fig. 7.4, which is almost exactly the same as Fig. 7.1, except that the translations are replaced by delays. Twins photons are created with a plane wave pump by the process of SPDC in a non-linear crystal. A pinhole selects collinear twins with orthogonal polarisation. By using a birefringent crystal a delay  $\Delta\tau_V$  is imposed on V-polarised photons. The collinear twins fall on a 50% : 50% beam splitter. In one of the output channels of the beam splitter a delay  $\Delta\tau_H$  is imposed on H-polarised photons. Coincidences are detected by the detectors *a* and *b* in the output channels. The detectors integrate over space and time. In front of both detectors are narrow-band frequency filters and polarisers at an angle of  $45^\circ$  with respect to both  $\vec{e}_H$  and  $\vec{e}_V$ . Since the basic idea of the experiment is relying on the time dependence

of the field, we ignore the transverse-field distribution. This is justified under the assumption that the transverse parts of the transfer functions are independent of the polarisation. As a consequence, the transverse profile does not contain polarisation information. Then the transverse part of the problem does not affect the interference, and introduces only an overall factor in the coincidence detection rate. Therefore we simply write the two-photon state in Eq. (7.2) as

$$|\Psi(t)\rangle \propto \int_{-\infty}^t dt' g(t') \hat{a}_H^\dagger(t') \hat{a}_V^\dagger(t') |0\rangle, \quad (7.20)$$

where  $\hat{a}_H^\dagger(t)$  and  $\hat{a}_V^\dagger(t)$  create at time  $t$  an  $H$ -polarised and a  $V$ -polarised photon, respectively. The coincidence detection amplitude in Eq. (7.8) is then given by

$$A = \langle 0 | \hat{E}_b^+(t_b) \hat{E}_a^+(t_a) | \Psi(t_a) \rangle, \quad (7.21)$$

where  $t_b > t_a$ .

To find the coincidence detection amplitude we express the positive-frequency part of the electric-field operator at the locations of the detectors  $a$  and  $b$  in terms of the annihilation operators  $\hat{a}_H(t)$  and  $\hat{a}_V(t)$ . For the positive-frequency part of the electric-field operator at the location of detector  $a$  at time  $t_a$ , and detector  $b$  at time  $t_b$ , we write in the Heisenberg picture  $\hat{E}_a^+(t_a)$  and  $\hat{E}_b^+(t_b)$ , respectively. With free propagation in one dimension, the operator  $\hat{a}(z, t)$ , which annihilates a photon at time  $t$  at the position  $z$ , differs from the operator  $\hat{a}(0, t) \equiv \hat{a}(t)$  by a delay in time. This follows from

$$\begin{aligned} \hat{a}(z, t) &= \frac{1}{\sqrt{2\pi}} \int d\omega \hat{a}(\omega) \exp[-i\omega t + ik(\omega)z] \\ &= \frac{1}{\sqrt{2\pi}} \int d\omega \hat{a}(\omega) \exp[-i\omega(t - z/c)] \\ &= \hat{a}(0, t - z/c), \end{aligned} \quad (7.22)$$

where  $\hat{a}(\omega)$  is the annihilation operator for a photon with frequency  $\omega$  in the output plane of the crystal, and where we used the dispersion relation  $k(\omega) = \omega/c$ . Because the polarisers in front of the detectors are at  $45^\circ$ , both detectors detect photons with the polarisation vector  $\vec{E} = (\vec{e}_H + \vec{e}_V)/\sqrt{2}$ . Therefore we only consider the component of the electric-field operator in the  $45^\circ$  direction. The distance between the detectors and the crystal along both optical paths is  $z$ . Apart from the delay  $\Delta\tau$ , the time for a photon to travel from the crystal to a detector is  $z/c$ . Before being detected, the photon passes through the narrow-band filter. The amplitude for the photon to reside in the filter for a duration  $\tau$  is proportional to  $f(\tau)$ , the memory function of the filter. We have

$$\begin{aligned} \hat{E}_a^+(t_a) &= \int_0^\infty d\tau f(\tau) [\hat{a}_H(t_a - z/c - \Delta\tau_H - \tau) + \hat{a}_V(t_a - z/c - \Delta\tau_V - \tau)], \\ \hat{E}_b^+(t_b) &= \int_0^\infty d\tau f(\tau) [\hat{a}_H(t_b - z/c - \tau) + \hat{a}_V(t_b - z/c - \Delta\tau_V - \tau)]. \end{aligned} \quad (7.23)$$

These expressions are similar to the expressions in Eq. (7.12) that we used for the spatial interferometer. Then the expression for the coincidence detection amplitude is proportional

to

$$A(t_a, t_b) = \int_{-\infty}^{\infty} dt g(t) [f(t_b - z/c - t)f(t_a - z/c - \Delta\tau_V - t) + f(t_b - z/c - \Delta\tau_V - t)f(t_a - z/c - \Delta\tau_H - t)] . \quad (7.24)$$

The upper limit of the integration in Eq. (7.24) should be the lower one of  $t_a$  and  $t_b$ . The time arguments of the filter functions in Eq. (7.24) indicate the time delay of the photons in the filters.

We consider the case that the pump beam is monochromatic with frequency  $\omega_p$ , and we write

$$g(t) = \exp(-i\omega_p t) . \quad (7.25)$$

Then we can neglect the dispersion in the crystal and use the expression in Eq. (7.20) for the two-photon state. The frequency filters are modeled by a Lorentzian with a bandwidth  $\alpha$ , and a centre frequency that is equal to half the pump frequency  $\omega_p$ , so that

$$f(\tau) = \exp(-\alpha\tau - i\omega_p\tau/2)\Theta(\tau) . \quad (7.26)$$

The step function  $\Theta(\tau)$  makes the memory function disappear for negative  $\tau$ , which reflects causality [67]. Inserting the expressions for the pump profile and the memory function of the filters into Eq. (7.24) gives the explicit expression

$$A(t_a, t_b) = \frac{1}{2\alpha} \exp[-i\omega_p(t_a + t_b - 2z/c - \Delta\tau_V)/2] \times [\exp(-\alpha|t_a - t_b - \Delta\tau_V|) + \exp(i\omega_p\Delta\tau_H/2) \exp(-\alpha|t_a - t_b + \Delta\tau_V - \Delta\tau_H|)] . \quad (7.27)$$

The first term in Eq. (7.24) or Eq. (7.27) represents the amplitude that detector  $a$  sees the  $V$ -polarised photon, and the  $H$ -polarised photon goes to detector  $b$ . This term is maximal when  $t_a - t_b = \Delta\tau_V$ . The inverse situation that detector  $a$  sees the  $H$ -polarised photon and  $b$  the  $V$ -polarised one is expressed by the second term. This term is maximal when  $t_a - t_b = \Delta\tau_H - \Delta\tau_V$ . We assume that the detection window is large compared with the inverse bandwidth  $1/\alpha$  of the filters, so that the net coincidence rate  $R$  is proportional to  $\int_{-\infty}^{\infty} dt_b |A(t_a, t_b)|^2$ , which gives the result

$$R \propto 1 + (1 + \alpha|\Delta\tau_H - 2\Delta\tau_V|) \cos(\omega_p\Delta\tau_H/2) \exp(-\alpha|\Delta\tau_H - 2\Delta\tau_V|) . \quad (7.28)$$

In Fig. 7.5 the envelope of the coincidence detection rate  $R$  is given as a function of the dimensionless parameter  $\alpha(\Delta\tau_H - 2\Delta\tau_V)$ . Here the value of  $\Delta\tau_V$  is fixed, and the value of  $\Delta\tau_H$  is varied. The envelope is filled with interference fringes with frequency  $\omega_p/2$ . With this experiment Pittman *et al.* show that it is not necessary for the two photons of a twin to arrive at the beam splitter at the same instant of time for interference to occur. Again two amplitudes are of importance. The first is the amplitude  $A(H \rightarrow a; V \rightarrow b)$  where detector  $a$  detects the  $H$ -polarised photon, and detector  $b$  detects the  $V$ -polarised photon. For the second amplitude  $A(H \rightarrow b; V \rightarrow a)$  it is the other way around. The polarisers at  $45^\circ$  in front of the detectors erase the information about the polarisation of the detected photon,

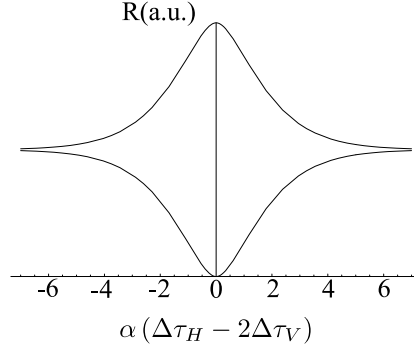


**Figure 7.5:** Envelope of the coincidence detection rate  $R$  as a function of the dimensionless parameter  $\alpha(\Delta\tau_H - 2\Delta\tau_V)$  for the temporal interferometer.

so that interference between these amplitudes can occur. Polarisation information is also contained in the difference in time between the two detection events, because the photons of a twin are created at the same instant of time. For interference with 100% visibility to occur it is then necessary that the difference in arrival time at the filters is the same for both amplitudes. When  $\Delta\tau_H = 2\Delta\tau_V$  this requirement is fulfilled, so that there is interference with 100% visibility, as can be seen in Fig. 7.5. On the other hand, we see that then there is a difference of  $\Delta\tau_V = \Delta\tau_H/2$  in the total travel time of the photons from the crystal to the filter for the two amplitudes. This does not destroy the interference because these amplitudes cannot be distinguished. The reason for this is, that, although the photons of a twin are created at identical times, the absolute time at which a twin is created, is undetermined, because the pump beam is monochromatic: there is temporal entanglement. We also notice that for one of the amplitudes the  $H$ -polarised photon arrives at the filter before the  $V$ -polarised photon, while it is the other way around for the other amplitude. Again the polarisers erase this difference. The interference fringes are a consequence of the fact that the pump beam changes phase under translation in time. The filters erase the information about the creation time of a photon from the observed detection time. The bandwidth  $\alpha$  determines the width of the envelope in the coincidence detection rate when measured as a function of  $\Delta\tau_H$ . For the spatial interferometer the interference fringes arise because the pump beam changes phase under a translation in the transverse space, which is a consequence of the fact that the pump beam is slightly tilted. The width of the envelope in the coincidence detection rate for the spatial interferometer depends on the radius of the pinhole in front of detector  $b$ .

There is one striking difference between the description of the temporal and the spatial entanglement. The detectors integrate both over time and transverse space, but in the temporal case the ordering of the detection times of the photons is relevant, which is not the case for the spatial variant. The coincidence detection amplitude for  $t_b > t_a$  is different from the one where  $t_b < t_a$ , as can be seen from Eq. (7.24), because the detection of a photon puts an end to the evolution of the two-photon state. On the other hand, this does not occur in the spatial case, as we see in Eq. (7.13). There is no such ordering problem with the locations of detection  $\vec{p}_a$  and  $\vec{p}_b$ . In order to clarify the analogy between spatial and temporal entanglement we have

focused on either the spatial or the temporal aspect of the interferometer under consideration. By using the general expression for the two-photon state in Eq. (7.2) also more general experiments can be described, where both the spatial and temporal entanglement is relevant.

## 7.5 Conclusions

We have proposed an interference scheme for studying the spatial entanglement of twin photons. The spatial entanglement arises from the fact that the photons of a twin are created at the same location in the crystal, while this location itself is undetermined within the spot size of the pump beam. Expressed in transverse momentum, this spatial entanglement takes the form of transverse phase matching. The photons of the twin are created with opposite polarisation and the coincidence detection signal of the two photons arises from a coherent superposition of two amplitudes. An interference structure in the coincidence detection rate occurs as a function of a polarisation-dependent translation in the transverse direction. It is necessary that the photons of a twin are spatially entangled for this interference to occur.

The proposed interference scheme is the spatial analogue of the interference scheme in an experiment by Pittman *et al.* [63] which relies on the temporal entanglement of the twin photons. Besides that the photons of a twin are created at the same location in the crystal, they are also created at the same instant of time. The exact creation time of the twin itself is undetermined within the duration of the pump pulse. This implies that the two-photon state is entangled in time, or, equivalently, in longitudinal position along the propagation direction. In the experiment of Pittman *et al.* the interference occurs as a function of a polarisation-dependent time delay.

We give a description of the proposed interference scheme in a form where the analogy and the difference with its temporal counterpart is best visible. We believe that this comparison elucidates the role of both types of entanglement.

## CHAPTER 8

---

### Polarisation entanglement in a crystal with three-fold symmetry

---

*Polarisation entanglement of twin photons created in the process of parametric down-conversion is fully determined by the pump polarisation when the pump, signal and idler beams are collinear with the symmetry axis of the non-linear crystal. We point out that in this situation a three-fold rotational symmetry is needed for the process to occur. We describe the polarisation entanglement of the twin photons in terms of correlations on the Poincaré sphere. The inherent non-conservation of the intrinsic angular momentum of light in this process is discussed.*

*J. Visser, E. R. Eliel, and G. Nienhuis, Phys. Rev. A **66**, 033814 (2002).*

## 8.1 Introduction

Polarisation entanglement between pairs of photons is commonly created in the process of spontaneous parametric down-conversion (SPDC), where one photon absorbed from a pump beam in a non-linear crystal leads to the creation of two photons, which are called signal and idler photons. The crystal must have a non-vanishing second-order non-linear susceptibility, and polarisation-entangled pairs are selected by appropriate filtering of the down-converted light.

In general, the orbital and intrinsic angular momenta of the light field are not conserved in the SPDC process [68, 69]. In the special case that pump, signal and idler beams have a common axis, the *orbital* angular momentum along this axis is conserved at the single-photon level [70–72]. This follows basically from the overlap integral of the pump field and the product of the signal and idler fields, which involves the integral  $\int d\phi \exp[i\phi(l_p - l_s - l_i)]$ , with  $\phi$  the azimuthal angle in the transverse plane, and  $l$  the azimuthal mode index, which determines the orbital angular momentum  $l\hbar$  per photon [73–76].

In the present paper we analyse the polarisation entanglement of twin photons and the corresponding *intrinsic* angular momentum in a spherical basis using the Poincaré sphere. As an example we discuss the case of a crystal with  $C_{3v}$  symmetry, where the propagation directions are chosen to coincide with the symmetry axis of the crystal. As pointed out by Bloembergen [77] in the context of second-harmonic generation, for this case a circularly-polarised fundamental mode is converted into a harmonic with the opposite circular polarisation. In a similar fashion, during SPDC, a circularly-polarised pump photon creates a signal-idler photon pair with the opposite circular polarisation. For a pump photon with an arbitrary polarisation, a polarisation entangled photon pair is created. Obviously, the intrinsic angular momentum is in general not conserved during this process. The change in angular momentum of the light field is compensated by that of the crystal medium.

In Section 8.2 we discuss a representation of the two-photon polarisation state on the Poincaré sphere and we consider the intrinsic angular momentum associated with the polarisation. We will show that, for the process of SPDC, the polarisation entanglement of the photon pair is determined by the polarisation of the pump and by the non-linear susceptibility of the crystal. In Section 8.3 we derive properties of the susceptibility tensor  $\chi^{(2)}$  from symmetry arguments. We do this in the basis of spherical unit vectors, which is unusual, but powerful and elegant. In Section 8.4 we use the results from previous Sections to study the polarisation entanglement and the associated intrinsic angular momentum of twins created in a crystal with  $C_{3v}$  symmetry. We end with conclusions in Section 8.5.

## 8.2 Representation of the two-photon polarisation state on the Poincaré sphere

### 8.2.1 Single-photon polarisation states

The polarisation vector of a light beam with a given propagation direction can always be expressed as a linear combination of the circular polarisation vectors  $\vec{u}_{\pm 1}$ . We take the propagation direction parallel to the  $z$  axis, in which case the circular polarisation vectors are given

by

$$\vec{u}_{+1} = -\frac{1}{\sqrt{2}}(\vec{x} + i\vec{y}), \quad \vec{u}_{-1} = \frac{1}{\sqrt{2}}(\vec{x} - i\vec{y}), \quad (8.1)$$

where  $\vec{x}$  and  $\vec{y}$  are Cartesian unit vectors. For one photon, these polarisation states are denoted as  $|\pm\rangle$ . When the states  $|+\rangle$  and  $|-\rangle$  are mapped onto the states up and down of a spin 1/2, each polarisation state is equivalent to a specific spin state. A pure state of a spin 1/2 is uniquely determined by the expectation value  $\langle \vec{S} \rangle$  of the spin vector, which always has a length of 1/2. Therefore, such a state can be represented in a unique way as a point on a sphere, commonly called the Bloch sphere. Because of the aforementioned mapping, a pure polarisation state is also represented by a point on a sphere; the latter is named after Poincaré. The spherical coordinates  $\theta$  and  $\phi$  of this point fully determine the polarisation state. The poles of the Poincaré sphere correspond to opposite circular polarisations, and points on the equator represent states of linear polarisation. The ellipticity of the polarisation is determined by the polar angle  $\theta$ , such that the cross product  $\vec{e} \times (\vec{e})^*$  of the polarisation vector and its complex conjugate has the strength  $\cos \theta$ . The angle between the long axis of the ellipse and the  $x$  axis is equal to  $(\pi + \phi)/2$ , where  $\phi$  is the azimuthal angle. The absolute value of the overlap  $|\vec{e}_1^* \cdot \vec{e}_2|$  of two polarisation states is given by  $\cos(\alpha/2)$ , where  $\alpha$  is the angular distance between the corresponding points on the Poincaré sphere. Consequently, opposite points on the Poincaré sphere always correspond to orthogonal polarisations. The polarisation of a photon that corresponds to the point on the Poincaré sphere with polar angle  $\theta$  and azimuthal angle  $\phi$  is then given by (see Fig. 8.1)

$$|\theta, \phi\rangle = \cos(\theta/2) \exp(-i\phi/2)|+\rangle + \sin(\theta/2) \exp(+i\phi/2)|-\rangle. \quad (8.2)$$

## 8.2.2 Two-photon polarisation states

Now we use the Poincaré representation for the description of the entangled polarisation state  $|\Psi\rangle\rangle$  of twin photons, where the double ket is used to indicate that it is a two-photon state. When one photon is detected in a selected polarisation state  $|\psi^{(1)}\rangle = |\theta_1, \phi_1\rangle$ , the state of the remaining photon collapses into the state  $|\psi^{(2)}\rangle = |\theta_2, \phi_2\rangle$ , which, apart from a normalisation factor, is given by  $\langle \psi^{(1)} | \Psi \rangle\rangle$ . The two-photon polarisation state is then represented by the two points on the Poincaré sphere that correspond to the states  $|\psi^{(1)}\rangle$  and  $|\psi^{(2)}\rangle$ .

As an example we discuss the singlet and triplet Bell states, which are given by

$$|\Psi_S\rangle\rangle = \frac{1}{\sqrt{2}}(|x\rangle|y\rangle - |y\rangle|x\rangle) = \frac{1}{i\sqrt{2}}(|+\rangle|-\rangle - |-\rangle|+\rangle), \quad (8.3)$$

$$|\Psi_T\rangle\rangle = \frac{1}{\sqrt{2}}(|x\rangle|y\rangle + |y\rangle|x\rangle) = \frac{1}{\sqrt{2}}(|-\rangle|-\rangle - |+\rangle|+\rangle), \quad (8.4)$$

where  $|x\rangle$  and  $|y\rangle$  form the basis of linear polarisation. In Fig. 8.2, the singlet and triplet Bell states are represented on the Poincaré sphere. For the singlet state (8.3), if we detect one photon in a specific polarisation state, the other photon is projected in a state that is orthogonal to it. As a consequence, the detected and projected states are antipodes on the Poincaré sphere, that is

$$\theta_1 + \theta_2 = \pi, \quad \phi_1 - \phi_2 = \pi \bmod(2\pi). \quad (8.5)$$

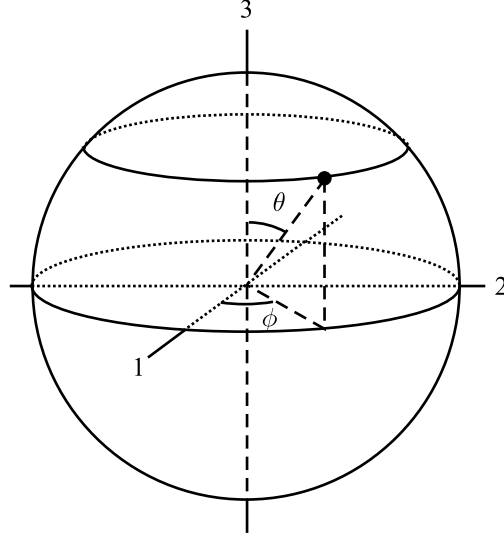


**Figure 8.1:** Representation of the one-photon polarisation state on the Poincaré sphere. If  $\theta = \pi/2$ , we have linear polarisation in the y direction for  $\phi = 0$  and in the x direction for  $\phi = \pi$ . For  $\theta = 0$  and  $\theta = \pi$ , we have right- and left-handed circular polarisations, respectively.

For the triplet state (8.4), we find

$$\theta_1 - \theta_2 = 0, \quad \phi_1 + \phi_2 = \pi \text{ mod}(2\pi), \quad (8.6)$$

and we see that the detected and projected states have the same latitude. Note that these relations are invariant if we interchange the detected and projected states.

The states  $|\psi^{(1)}\rangle$  and  $|\psi^{(2)}\rangle$  cannot be interchanged in general. For a state  $|\Psi\rangle$  of the combined system, interchangeability of the detected and projected states holds, if, for each pair of states  $|\psi^{(1)}\rangle$  and  $|\psi^{(2)}\rangle$  that are related by  $|\psi^{(2)}\rangle \propto \langle\psi^{(1)}|\Psi\rangle$ , the opposite relation  $|\psi^{(1)}\rangle \propto \langle\psi^{(2)}|\Psi\rangle$  is also satisfied. In the Appendix we prove that these conditions do not hold unless the state  $|\Psi\rangle$  is maximally entangled. The singlet and triplet Bell states discussed above are maximally entangled states, and thus satisfy interchangeability. In general, the two-photon polarisation state is not maximally entangled, thus the order of detected and projected states is important.

### 8.2.3 Intrinsic angular momentum associated with polarisation

As basis vectors for polarisation we have taken the circular polarisation vectors of Eq. (8.1). Then the expectation value of the intrinsic angular momentum is in the z direction. For the total intrinsic angular momentum operator in the propagation direction  $\Sigma_3$ , we have

$$\Sigma_3 = \sum_i \sigma_3^i, \quad (8.7)$$

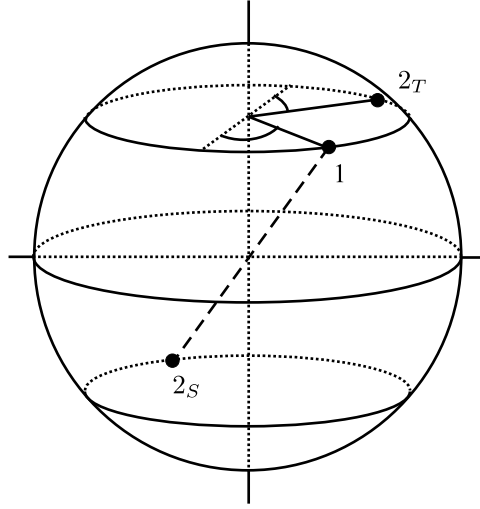


**Figure 8.2:** Representation of the singlet and triplet Bell states on the Poincaré sphere. The first photon is detected in the state with label 1. Then the second photon is projected in the state labeled with  $2_S$  and  $2_T$  for the singlet and triplet Bell states, respectively.

where the summation runs over the photons and where  $\sigma_3^i$  is the third Pauli matrix for photon  $i$ . For the third Pauli matrix we can write  $\sigma_3 = |+\rangle\langle+| - |-\rangle\langle-|$ .

The expectation value of the intrinsic angular momentum, in units of  $\hbar$ , for the one-photon polarisation state (8.2) is given by  $\cos \theta$ , where  $\theta$  is the polar angle on the Poincaré sphere. The expectation value for both the singlet and triplet Bell states vanishes. After detection of one photon in the state  $|\psi^{(1)}\rangle = |\theta_1, \phi_1\rangle$  the two-photon polarisation state  $|\Psi\rangle$  collapses to the product state  $|\psi^{(1)}\rangle|\psi^{(2)}\rangle$ , with  $|\psi^{(2)}\rangle \propto \langle\psi^{(1)}|\Psi\rangle$ . For the singlet Bell state, the detected and projected states are on opposite sides of the Poincaré sphere, so the expectation value of the intrinsic angular momentum after the detection vanishes as well. On the other hand, for the triplet Bell state the detected and projected states have the same latitude, so that after detection the expectation value of the intrinsic angular momentum is  $2 \cos \theta_1$ . We see that the intrinsic angular momentum is not conserved. We will come back to this point in Section 8.4.3.

## 8.3 Symmetry properties of the susceptibility tensor

### 8.3.1 Invariances of the susceptibility

The most common way to create a two-photon polarisation state is by the process of SPDC. The basic process of SPDC is the annihilation of one pump photon, and the creation of two photons, into the signal and the idler mode. The interaction Hamiltonian arises from the non-linear polarisation of the medium coupled to the pump field, and corresponds to three-wave

mixing. The polarisation dependence of the interaction Hamiltonian is described by

$$H_I = \int d\vec{r} \chi^{(2)} : \vec{E} \vec{E}^\dagger \vec{E}^\dagger + \text{H.c.} , \quad (8.8)$$

where  $\vec{E}$  is the positive-frequency part of the electric-field operator, and the integration extends over the volume of the medium. The three dots symbolise an inner product of the second-order susceptibility tensor  $\chi^{(2)}$  with the electric-field vectors. The first part of the Hamiltonian describes down-conversion, its Hermitian conjugate describes up-conversion. The Hamiltonian can be written in the elegant form in Eq. (8.8) because we consider operation in the optical regime where  $\chi^{(2)}$  is virtually frequency independent [78].

The tensor  $\chi^{(2)}$  has rank 3, and therefore it has 27 components. For all materials with some spatial symmetry, not all of these components are independent and non-zero. The material transforms onto itself under the application of a covering operation of its symmetry group. Since the tensor  $\chi^{(2)}$  is a property of the crystal material, it must be invariant under any one of these covering operations. This is known as Von Neumann's principle [78]. These operations form the symmetry group of the crystal, and each covering operation  $R$  is represented by a Cartesian matrix  $\mathbf{O}(R)$ . The susceptibility tensor must be identical to its transformation for each covering operation  $R$ . This gives

$$\chi_{ijk}^{(2)} = \sum_{lmn} \chi_{lmn}^{(2)} O(R)_{li} O(R)_{mj} O(R)_{nk} . \quad (8.9)$$

All indicated indices attain the values  $x, y, z$ . In this sense, the symmetry properties of the susceptibility reflect the symmetry of the crystal. The identities in Eq. (8.9) introduce relations between the different components of  $\chi^{(2)}$ , thereby reducing the number of independent components.

The number of independent components of  $\chi^{(2)}$  can be found by applying group theory [79–81]. The independent components themselves and their relations with the other components can be obtained by using the method of direct inspection [78, 82, 83]. The latter method can be illustrated by considering materials that are invariant under space inversion. The matrix elements of the transformation matrix of the inversion operation  $I$  are simply  $O(I)_{ij} = -\delta_{ij}$ . Hence, we find from Eq. (8.9) that  $\chi_{ijk}^{(2)} = (-1)^3 \chi_{ijk}^{(2)}$ . This shows that  $\chi^{(2)}$  vanishes for a material with inversion symmetry. Only the susceptibilities of an even rank (*i.e.*,  $\chi^{(1)}, \chi^{(3)}, \dots$ ) can be non-zero in a medium with inversion symmetry.

### 8.3.2 Rotations and spherical basis

Most crystalline materials that are of relevance for SPDC are invariant under a rotation over an angle  $2\pi/N$  about their symmetry axis, which we take to be the  $z$  axis. To describe the effect of a rotation, it is efficient to replace the basis of Cartesian unit vectors  $\vec{x}$ ,  $\vec{y}$ , and  $\vec{z}$  by the basis of spherical unit vectors

$$\vec{u}_{+1} = -\frac{1}{\sqrt{2}}(\vec{x} + i\vec{y}) , \quad \vec{u}_{-1} = \frac{1}{\sqrt{2}}(\vec{x} - i\vec{y}) , \quad \vec{u}_0 = \vec{z} . \quad (8.10)$$

Note that we encountered  $\vec{u}_{\pm 1}$  before in Eq. (8.1) as the basis vectors for circular polarisation. These unit vectors transform under rotations in the same way as the spherical harmonics  $Y_{lm}$  with  $l = 1$ . In particular, they are eigenvectors of the rotation matrix about the symmetry axis.

When  $\mathbf{O}(\phi)$  denotes the rotation matrix for a counter-clockwise rotation about the  $z$  axis over an angle  $\phi$ , the transformation reads

$$\mathbf{O}(\phi) \cdot \vec{u}_{\sigma} = \exp(-i\phi\sigma)\vec{u}_{\sigma}, \quad \sigma = -1, 0, +1. \quad (8.11)$$

This eigenvalue character makes the spherical unit vectors into the natural basis for analysing the components of the susceptibility tensor. In particular, on this basis, it is simple to identify the components that must vanish. The spherical components of the susceptibility are defined by the relations

$$\chi_{\rho\sigma\tau}^{(2)} = \chi^{(2)} : \vec{u}_{\rho}\vec{u}_{\sigma}\vec{u}_{\tau}, \quad \rho, \sigma, \tau = -1, 0, +1. \quad (8.12)$$

### 8.3.3 Non-vanishing spherical components of $\chi^{(2)}$

For a material with an  $N$ -fold rotation axis, we apply a counter-clockwise rotation about this axis over an angle  $2\pi/N$ . We will now determine the number of non-zero and independent components of  $\chi^{(2)}$  for all values of  $N$ . With the invariance requirement (8.9), Eq. (8.11) leads to the simple identity

$$\chi_{\rho\sigma\tau}^{(2)} = \exp[-(\rho + \sigma + \tau)2\pi i/N]\chi_{\rho\sigma\tau}^{(2)}, \quad \rho, \sigma, \tau = -1, 0, +1, \quad (8.13)$$

so that the component  $\chi_{\rho\sigma\tau}^{(2)}$  must vanish whenever the exponential factor differs from 1. It follows that the component  $\chi_{\rho\sigma\tau}^{(2)}$  can only be non-zero under the condition that

$$\rho + \sigma + \tau = kN, \quad (8.14)$$

with  $k$  being an integer. Obviously, the sum  $\rho + \sigma + \tau$  can acquire the values  $0, \pm 1, \pm 2, \pm 3$  for the possible values of  $\rho, \sigma$  and  $\tau$ .

- For each value of  $N$ , the condition (8.14) is satisfied when the sum of the indices is zero. This is true when all indices are zero, or when they are one of the six permutations of the three different values  $-1, 0, +1$ . The corresponding seven components can be non-zero for any value of  $N$ , and also when the system possesses full axial symmetry.
- For  $N = 4$  and higher, the condition (8.14) cannot be obeyed for any value of  $k$  other than zero, so that all components other than these seven must vanish.
- For  $N = 3$ , the two components  $\chi_{+1+1+1}^{(2)}$  and  $\chi_{-1-1-1}^{(2)}$  correspond to the condition (8.14) with  $k = \pm 1$ ; they can be non-zero in addition to the seven components mentioned above.
- For  $N = 2$ , the condition (8.14) with  $k = \pm 1$  is obeyed by the six components with  $\rho + \sigma + \tau = \pm 2$ ; here  $\rho, \sigma, \tau$  are permutations of  $+1, +1, 0$  or of  $-1, -1, 0$ . Only these six components can be non-zero for  $N = 2$ , in addition to the seven mentioned above.

- Finally, there are 12 components for which  $\rho + \sigma + \tau = \pm 1$ . These are the ones where  $\rho, \sigma, \tau$  are permutations of  $0, 0, \pm 1$  or of  $\mp 1, \pm 1 \pm 1$ . These components can only be non-zero in the trivial case that  $N = 1$ . In this case without any symmetry, no restriction is set for any one of the 27 components.

In general, materials have other symmetry operations besides an  $N$ -fold rotation axis. The requirement that  $\chi^{(2)}$  is invariant under the additional operations, introduces relations between the non-zero components found above, thereby further reducing the number of independent components.

### 8.3.4 Transverse part of $\chi^{(2)}$

In the case that pump, signal, and idler propagate parallel to each other and to the symmetry axis, the polarisation vectors lie in the  $xy$  plane. This we call the transverse configuration. The only relevant part of the susceptibility in this case is the transverse susceptibility  $\chi_T^{(2)}$ , defined as the projection of  $\chi^{(2)}$  on this plane. Hence,  $\chi_T^{(2)}$  contains the eight spherical components  $\chi_{\rho\sigma\tau}^{(2)}$  with  $\rho, \sigma, \tau = -1, +1$  only. For the components of  $\chi_T^{(2)}$ , the sum  $\rho + \sigma + \tau$  can only attain the values  $\pm 1, \pm 3$ .

For  $N = 2$  and  $N = 4$  and higher, it follows from Eq. (8.14) that all components of  $\chi_T^{(2)}$  vanish. Hence a non-vanishing transverse susceptibility  $\chi_T^{(2)}$  only occurs for materials without any symmetry, or for materials with a three-fold rotation axis. In the following Section we discuss the polarisation properties of twin photons created by SPDC in a crystal with three-fold rotational symmetry.

## 8.4 SPDC in a crystal with $C_{3v}$ symmetry

### 8.4.1 Hamiltonian

We consider a crystal with  $C_{3v}$  symmetry in the transverse configuration. It has six covering operations, which are generated by a rotation over  $2\pi/3$  and a reflection in a vertical plane that contains the  $z$  axis, for which we take the  $xz$  plane. The corresponding matrix  $\mathbf{O}(R_v)$  acting on the spherical unit vectors is represented by the transformation

$$\mathbf{O}(R_v) \cdot \vec{u}_{+1} = -\vec{u}_{-1}, \quad \mathbf{O}(R_v) \cdot \vec{u}_{-1} = -\vec{u}_{+1}. \quad (8.15)$$

For the transverse configuration we are only interested in  $\chi_T^{(2)}$ . As shown in Section 8.3.3, it follows from the three-fold rotation symmetry that  $\chi_{+1+1+1}^{(2)}$  and  $\chi_{-1-1-1}^{(2)}$  are the only non-zero components of  $\chi_T^{(2)}$ . According to Eq. (8.15), the invariance relation (8.9) applied to reflection about the  $xz$  plane yields the relation

$$\chi_{+1+1+1}^{(2)} = -\chi_{-1-1-1}^{(2)} \equiv G. \quad (8.16)$$

Hence, for  $C_{3v}$ , we find that  $\chi_T^{(2)}$  is determined by a single independent parameter  $G$ . This is in agreement with the result obtained using the procedure by Bhagavantam and Suryanarayana [79].

Now we obtain the Hamiltonian in the transverse configuration for a crystal with  $C_{3v}$  symmetry. For the positive-frequency part of the electric-field operator, we write

$$\vec{E}(\vec{r}, t) \propto \int d\vec{k} \sum_{\lambda} \sqrt{\omega_{\lambda}(\vec{k})} a_{\lambda}(\vec{k}) \vec{\epsilon}_{\lambda}(\vec{k}) \exp \left[ i\vec{k} \cdot \vec{r} - i\omega_{\lambda}(\vec{k})t \right], \quad (8.17)$$

where  $a_{\lambda}(\vec{k})$  annihilates a photon with wave vector  $\vec{k}$  and polarisation vector  $\vec{\epsilon}_{\lambda}(\vec{k})$  and where the summation over  $\lambda$  runs over the two basis states of polarisation. In the transverse configuration, the index of refraction of the crystal does not depend on the polarisation for the common direction of propagation. We then have  $\vec{\epsilon}_{\lambda}(\vec{k}) \rightarrow \vec{\epsilon}_{\lambda}$  and  $\omega_{\lambda}(\vec{k}) \rightarrow \omega(\vec{k})$ , and we find that

$$\vec{E}(\vec{r}, t) \propto \int d\vec{k} \sqrt{\omega(\vec{k})} \exp \left[ i\vec{k} \cdot \vec{r} - i\omega(\vec{k})t \right] \sum_{\lambda} a_{\lambda}(\vec{k}) \vec{\epsilon}_{\lambda}. \quad (8.18)$$

We see that the electric-field operator is split into a polarisation part and a part concerning the modes in  $k$  space. As a basis for polarisation we use the circular polarisation states  $|\pm\rangle$ . Since we are only interested in the polarisation part, we write

$$\vec{E} \propto a_+ \vec{u}_{+1} + a_- \vec{u}_{-1}. \quad (8.19)$$

Here  $a_+$  and  $a_-$  are the annihilation operators for a photon with right- and left-handed circular polarisations, respectively.

From Eq. (8.16) and the definition in Eq. (8.12), it follows that the transverse susceptibility can be expressed in terms of the spherical unit vectors  $\vec{u}_{\pm 1}$  as

$$\chi_T^{(2)} = G (\vec{u}_{+1}^* \vec{u}_{+1}^* \vec{u}_{+1}^* - \vec{u}_{-1}^* \vec{u}_{-1}^* \vec{u}_{-1}^*). \quad (8.20)$$

Using the fact that the spherical basis is unitary and that

$$(\vec{u}_{+1})^* = -\vec{u}_{-1}, \quad (8.21)$$

we find that

$$\vec{u}_{+1} \cdot \vec{u}_{+1} = \vec{u}_{-1} \cdot \vec{u}_{-1} = 0, \quad \vec{u}_{+1} \cdot \vec{u}_{-1} = -1. \quad (8.22)$$

We substitute the expressions that we obtained above in Eq. (8.8) and, apart from an irrelevant overall factor, the Hamiltonian in the transverse configuration is found as

$$H_I \propto G (a_{p+} a_{s-}^{\dagger} a_{i-}^{\dagger} - a_{p-} a_{s+}^{\dagger} a_{i+}^{\dagger}) + \text{H.c.}, \quad (8.23)$$

where the labels  $p$ ,  $s$ , and  $i$  refer to the modes in  $k$  space of the pump, signal, and idler photon, respectively. This shows that the absorption of a left-circularly-polarised pump photon is accompanied by the creation of a signal and an idler photon, which are both right-circularly polarised, and vice versa.

## 8.4.2 Representation on the Poincaré sphere

We now use the Poincaré representation for the description of the entangled state of the two SPDC photons for a given polarisation of the pump. We consider a pump photon in the state

$|\theta_p, \phi_p\rangle$ . The interaction Hamiltonian (8.23) in the transverse configuration applied to this initial state yields, to first order, the two-photon state

$$|\Psi\rangle\rangle = \cos(\theta_p/2) \exp(-i\phi_p/2) |-\rangle|-\rangle - \sin(\theta_p/2) \exp(+i\phi_p/2) |+\rangle|+\rangle. \quad (8.24)$$

This expression gives the two-photon state as a linear superposition of two-photon states that are pairwise orthogonal, so that this state is already in Schmidt-decomposed form. According to the definition by Abouraddy *et al.* [84] the degree of entanglement is  $\sin \theta_p$ . For linear polarisation ( $\theta_p = \pi/2$ ), the created two-photon state is maximally entangled. We find the triplet Bell state (8.4) in the case that the direction of the linear polarisation of the pump is parallel to the vertical reflection plane containing the  $x$  axis, so that  $\phi_p = 0$ . The singlet Bell state (8.3) cannot be obtained by choosing an appropriate pump polarisation since for the state  $|\Psi\rangle\rangle$  of Eq. (8.24), the overlap  $\langle\langle \Psi_S | \Psi \rangle\rangle$  with the singlet Bell state vanishes for all pump polarisations.

When one photon is detected in the selected polarisation state  $|\psi^{(1)}\rangle = |\theta_1, \phi_1\rangle$ , the state of the remaining photon collapses into the state  $|\psi^{(2)}\rangle = |\theta_2, \phi_2\rangle \propto \langle\psi^{(1)} | \Psi\rangle\rangle$ . The spherical angles  $\theta_2$  and  $\phi_2$  of  $|\psi^{(2)}\rangle$  are found to be given by the equalities

$$\frac{\tan(\theta_1/2)}{\tan(\theta_2/2)} = \tan(\theta_p/2), \quad \phi_1 + \phi_2 + \phi_p = \pi \bmod(2\pi). \quad (8.25)$$

Note that the states  $|\psi^{(1)}\rangle$  and  $|\psi^{(2)}\rangle$  cannot be interchanged, since in general the polarisation state of the two created photons is not maximally entangled, except for the case of a linearly-polarised pump. The relation between the two polarisation states  $|\psi^{(1)}\rangle$  and  $|\psi^{(2)}\rangle$  is illustrated in Figs. 8.3 and 8.4.

The relation between the azimuthal angles in Eq. (8.25) is invariant when all angles are increased by an amount of  $2\pi/3$ . This corresponds to a rotation in real space about the  $z$  axis, or symmetry axis, over half this angle, that is, over  $\pi/3$ , as can be seen from Eqs. (8.11) and (8.2). This is somewhat surprising, since the crystal is invariant only under a rotation over  $2\pi/3$ . To check consistency, we perform a rotation of the crystal over an angle  $\beta$  about the  $z$  axis. Using the transformation property under rotations in Eq. (8.11), we find that the relation between  $\chi_{+1+1+1}^{(2)}$  and  $\chi_{-1-1-1}^{(2)}$  in Eq. (8.16) changes to

$$\exp(-3i\beta) \chi_{+1+1+1}^{(2)} = -\exp(+3i\beta) \chi_{-1-1-1}^{(2)}. \quad (8.26)$$

Hence, a rotation over  $\pi/3$  produces a sign change for  $\chi_T^{(2)}$  as a whole, which does not change the polarisation properties of signal and idler. The same conclusion follows by noting that a polarisation state is basically unchanged by a rotation over  $\pm\pi$ . Therefore, a rotation of all polarisation vectors over  $\pi/3$  is equivalent to a rotation of the polarisation states over  $-2\pi/3$ , or, for that matter, a rotation of the crystal over  $2\pi/3$ .

The Hermitian conjugate of the interaction Hamiltonian in Eq. (8.23) represents the non-linear process of up-conversion. This process transforms the two-photon polarisation state  $|\psi^{(1)}\rangle|\psi^{(2)}\rangle$  into the one-photon state  $|\theta_p, \phi_p\rangle$ . The spherical angles  $\theta_p$  and  $\phi_p$  can then again be obtained from Eq. (8.25), but with the labels 1 and  $p$  interchanged.

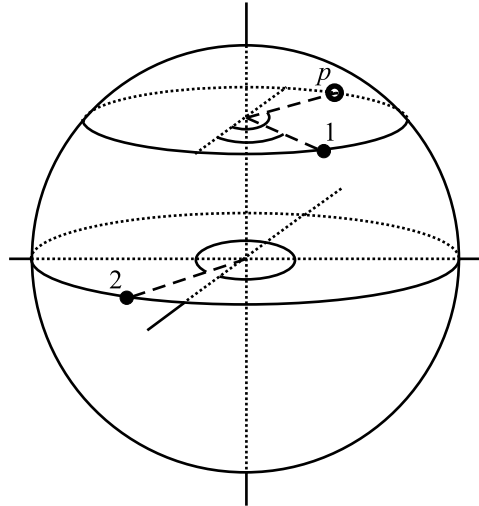


**Figure 8.3:** Representation of a two-photon state created by SPDC where the projected polarisation state 2 is found upon detection in state 1. The polarisation of the pump is represented by the open dot and labeled with  $p$ .

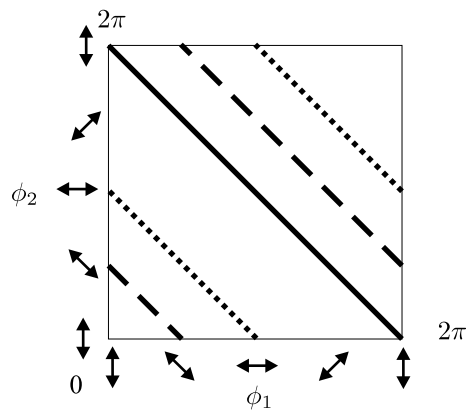


**Figure 8.4:** Representation of the two-photon state created by SPDC with a linearly-polarised pump. Then the polarisation states 1 and 2 have the same latitude on the Poincaré sphere. For  $\phi_p = 0$ , the relation between  $\phi_1$  and  $\phi_2$  is represented by the dotted lines, for  $\phi_p = \pi/2$  by the broken lines, and for  $\phi_p = \pi$  by the continuous line. The double arrow below and next to the axes represents the orientation of the long axis of the polarisation ellipse.

### 8.4.3 Intrinsic angular momentum

For a pump photon in the state  $|\theta_p, \phi_p\rangle$ , the expectation value of the intrinsic angular momentum, in units of  $\hbar$ , is given by  $\cos \theta_p$ , while for the two-photon state (8.24) created by SPDC in the crystal we find  $-2 \cos \theta_p$ . We see that the *intrinsic* angular momentum is not conserved in the process of SPDC, while, in the transverse configuration, the *orbital* angular momentum is conserved [70–72]. In order to satisfy conservation of total angular momentum, we conclude that there must be a transfer of angular momentum to the crystal [77]. The expectation value of the amount of transferred angular momentum to the crystal is then  $3 \cos \theta_p$ . Like we saw in Section 8.2.3 when discussing the triplet Bell state (8.4), the actual amount of transfer of angular momentum to the crystal will depend on the detected polarisation state  $|\psi^{(1)}\rangle$ , which shows the highly non-local nature of the transfer.

Conservation or non-conservation of angular momentum in SPDC depends on the transformation properties of the Hamiltonian under rotation. The orbital angular momentum depends on the position dependence of the complex field amplitude, and its conservation results from the fact that the Hamiltonian does not depend on position. On the other hand, the intrinsic angular momentum depends on the polarisation properties of the fields, which are determined by the tensor character of  $\chi^{(2)}$ . The effect of a rotation about the symmetry axis in the spherical basis is a complex phase change, since the spherical basis vectors are eigenvectors of rotation. For  $C_{3v}$  symmetry, the relevant elements  $\chi_{+1+1+1}^{(2)}$  and  $\chi_{-1-1-1}^{(2)}$  are only invariant under a rotation over an angle of  $2\pi/3$  and not under a rotation over an arbitrary angle. As a consequence, in case of a crystal with  $C_{3v}$  symmetry, the intrinsic angular momentum is not conserved.

## 8.5 Conclusions

We have discussed the use of a spherical basis for describing polarisation entanglement of twin photons as produced in the process of spontaneous parametric down conversion. This choice leads to a very transparent discussion regarding the conservation of intrinsic angular momentum in SPDC. We have used the Poincaré sphere to describe arbitrary polarisation states of pump, signal and idler. On this sphere, the singlet Bell state corresponds to a pair of antipodes, while in the triplet Bell state, the photons have equal latitude.

We have employed the spherical basis to analyse the polarisation entanglement of signal and idler as it arises in the process of SPDC in a crystal of  $C_{3v}$  symmetry when all optical beams are collinear with the symmetry axis of the crystal. We have shown that the three-fold crystalline symmetry is a prerequisite for SPDC in this geometry. For this crystal and geometry, we have derived simple relationships between the spherical coordinates of pump, signal and idler photons on the Poincaré sphere; these relationships provide direct insight into the issue of conservation of intrinsic angular momentum.

Twin photon generation in the chosen configuration cannot be phase matched; experimental realisation of SPDC in the proposed geometry will therefore be non-trivial. With a  $\beta$  barium borate (BBO) crystal ( $C_{3v}$  symmetry), cut for  $0^\circ$  phase matching, having a length equal to the coherence length ( $\approx 13 \mu\text{m}$  at  $\lambda = 800 \text{ nm}$  [85]), such an experiment should be feasible.

## 8.A Interchangeability of detected and projected states

When a quantum system consisting of two subsystems 1 and 2 with the same dimension  $d$  is in a state  $|\Psi\rangle$ , and system 1 is detected in the state  $|\psi^{(1)}\rangle$ , system 2 is projected into the state  $|\psi^{(2)}\rangle$  that is proportional to the partial inner product  $\langle\psi^{(1)}|\Psi\rangle$ . In general, the inverse statement is not true: detection of system 2 in  $|\psi^{(2)}\rangle$  projects system 1 in a state that is not necessarily equal to  $|\psi^{(1)}\rangle$ . In this appendix we prove that the roles of  $|\psi^{(1)}\rangle$  and  $|\psi^{(2)}\rangle$  can be interchanged for all choices of the detected state if and only if the state  $|\Psi\rangle$  is maximally entangled.

Consider a state  $|\Psi\rangle$  for which the detected state and the resulting projected state can be interchanged. For any normalised detected state  $|\psi^{(1)}\rangle$  of system 1, the resulting normalised projected state  $|\psi^{(2)}\rangle$  of system 2 obeys the identity

$$\langle\psi^{(1)}|\Psi\rangle = c|\psi^{(2)}\rangle, \quad (8.27)$$

and the normalisation constant is obviously  $c = \langle\psi^{(1)}|\langle\psi^{(2)}|\Psi\rangle$ . Because of the assumption of interchangeability, we can also write

$$\langle\psi^{(2)}|\Psi\rangle = c|\psi^{(1)}\rangle, \quad (8.28)$$

with the same normalisation constant.

We choose an orthonormal basis  $|\psi_n^{(1)}\rangle$  of system 1. Detection of system 1 in the state  $|\psi_n^{(1)}\rangle$  projects system 2 in the state  $|\psi_n^{(2)}\rangle$ , defined by

$$\langle\psi_n^{(1)}|\Psi\rangle = c_n|\psi_n^{(2)}\rangle. \quad (8.29)$$

This allows us to express the state  $|\Psi\rangle$  in the form

$$|\Psi\rangle = \sum_{n=1}^d c_n |\psi_n^{(1)}\rangle |\psi_n^{(2)}\rangle. \quad (8.30)$$

Now we use the interchangeability of the detected and projected states, which gives

$$\langle\psi_n^{(2)}|\Psi\rangle = c_n |\psi_n^{(1)}\rangle. \quad (8.31)$$

Substituting Eq. (8.30) into Eq. (8.31) shows that the states  $|\psi_n^{(2)}\rangle$  form an orthonormal basis of system 2.

Finally, we apply the assumption of interchangeability for an arbitrary state  $|\psi^{(1)}\rangle = \sum_{n=1}^d a_n |\psi_n^{(1)}\rangle$ . This gives for the projected state of system 2,

$$c|\psi^{(2)}\rangle = \sum_{n=1}^d a_n^* \langle\psi_n^{(1)}|\Psi\rangle = \sum_{n=1}^d a_n^* c_n |\psi_n^{(2)}\rangle, \quad (8.32)$$

where we used Eq. (8.29) in the last step. Conversely, when we first detect system 2 in the state  $|\psi^{(2)}\rangle$ , system 1 is projected into a state proportional to

$$\langle\psi^{(2)}|\Psi\rangle = \frac{1}{c^*} \sum_{n=1}^d a_n c_n^* \langle\psi_n^{(2)}|\Psi\rangle = \frac{1}{c^*} \sum_{n=1}^d a_n |c_n|^2 |\psi_n^{(1)}\rangle. \quad (8.33)$$

8. Polarisation entanglement in a crystal with three-fold symmetry

This is proportional to the original state  $|\psi_n^{(1)}\rangle$  only when all coefficients  $|c_n|^2$  are identical. Then Eq. (8.30) can be expressed as a bi-orthogonal expansion

$$|\Psi\rangle = \frac{1}{\sqrt{d}} \sum_{n=1}^d \exp(i\phi_n) |\psi_n^{(1)}\rangle |\psi_n^{(2)}\rangle, \quad (8.34)$$

in which each term has the same strength. This is a state with maximal entanglement.

On the other hand, when the state of the combined system can be expressed in the form (8.34), one easily checks that it satisfies interchangeability.

## CHAPTER 9

---

### Quantum-trajectory description of laser noise with pump depletion

---

*The intensity fluctuations of a three-level laser are known to drop below shot noise in the presence of depletion of the ground state. We study the fluctuations of the laser output as a function of the parameter  $\epsilon$ , defined as the fraction of atoms needed for the laser to operate. For a sufficiently small number of active atoms, the value of  $\epsilon$ , and thereby the ground-state depletion, can be appreciable even for modest pumping. This suggests that the intensity fluctuations in the laser output would decrease below shot noise as the number of active atoms is reduced. A microscopic approach that uses a quantum-trajectory method and a macroscopic approach using semi-classical rate equations both show, however, that rather than decreasing, the intensity fluctuations actually increase with  $\epsilon$ . We find that the fluctuations of the output are determined by the dependence of the cycle time of the atoms on the number of photons in the laser mode.*

*J. Visser, G. Nienhuis, S. M. Dutra, M. P. van Exter, and J. P. Woerdman,  
Phys. Rev. A **65**, 063809 (2002).*

## 9.1 Introduction

One of the most important characteristics of laser radiation is its noise [86]. In recent years, it has been recognised that noise properties change when the pumping is strong enough to cause depletion of the number of atoms participating in the laser transition. The special case of a three-level laser with pump depletion has been studied [87, 88]. Strong pumping leads to depletion of the ground state and the common assumption that the atoms in the ground state form an independent reservoir breaks down. It was found that for a laser with an incoherent pump, this depletion leads to an effective reduction of the pump noise, which in turn causes the intensity fluctuations of the laser output to drop below the shot-noise limit. However, the strong pumping needed for this mechanism to occur is far beyond experimental possibilities.

In this paper we consider a situation where depletion of the ground state is possible already with modest pumping. When the total number of atoms in the gain medium  $N$  is not much larger than the inversion  $N_{thr}$  at threshold, ground-state depletion occurs already just above threshold, and extremely strong pumping is not required. This also raises the question whether the depletion of the ground state that occurs for atom numbers  $N$  comparable to  $N_{thr}$  is also accompanied by intensity fluctuations below shot noise. If so, a Poissonian pumped laser with a sub-Poissonian output would be experimentally realisable.

As an example of a laser with a limited number of atoms, we analyse a three-level laser in a  $\Lambda$  configuration where  $N$  is allowed to be comparable to  $N_{thr}$ . To find the intensity fluctuations we use a semi-classical rate equation for the number of photons in the laser mode with a noise source added. To account for the gain medium of the laser, a term  $G_{at}$  is added. An expression for  $G_{at}$  is obtained by using both a microscopic and a macroscopic approach to the dynamics of the gain medium. The optical Bloch equations are the starting point for both approaches.

The microscopic approach consists of a quantum-trajectory method to study the dynamics of a single atom in the gain medium. This allows us to derive the statistical properties of the stimulated emission of photons in the laser mode by a single atom. The dynamics of single atoms in the gain medium has been studied before by Ritsch and Zoller [89], but in their paper the atomic density matrix is calculated. A study of the intensity fluctuations in the fluorescence that accompanies quantum jumps in a driven three-level atom has been done by Kim and Knight [90]. From the dynamics of a single atom we derive the statistical properties of the photons deposited in the laser mode by the entire gain medium.

On the other hand, the macroscopic approach consists of a calculation based on semi-classical rate equations for the number of atoms in each level with noise sources added. For both approaches an expression for  $G_{at}$  is found and the intensity fluctuations of the laser output are calculated from the rate equation for the photon number. The fluctuations depend on the parameter  $\varepsilon = N_{thr}/N$ , which represents the fraction of the number of atoms minimally needed for laser action.

In Section 9.2 we discuss the rate equation for the photon number, and the optical Bloch equations that describe the interaction between the laser mode and the gain medium. In Section 9.3 we discuss the microscopic approach that uses quantum trajectories to describe the evolution of a single atom in the gain medium. The macroscopic approach, for which semi-classical rate equations for the number of atoms in each level are derived, is discussed in Section 9.4. The conclusions are given in Section 9.5.

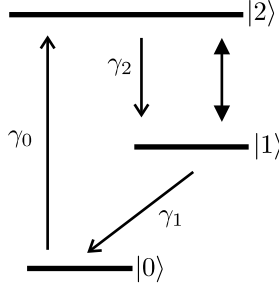


**Figure 9.1:** The three level scheme, where the 2-1 transition is the lasing transition.

## 9.2 Optical Bloch equations

### 9.2.1 Laser model

We model a laser by a laser mode in a cavity that is resonant with the lasing transition of the atoms in the gain medium. We use three-level atoms in the  $\Lambda$  configuration, as depicted in Fig. 9.1. The lasing transition 2-1 is coherently driven by the laser mode. Spontaneous emission occurs from state 2 to state 1, and from state 1 to state 0, and the corresponding rates are  $\gamma_2$  and  $\gamma_1$ . The lower state 0 is incoherently pumped to the upper level 2 at the rate  $\gamma_0$ . For the number of photons in the laser mode we use the following rate equation

$$\dot{n} = -2\kappa n + G_{at}(n) + f_n, \quad (9.1)$$

where  $\kappa$  is the cavity decay rate. The function  $G_{at}(n)$  models the effect the atoms in the gain medium have on the number of photons in the laser mode. It can be obtained from a detailed description of the interaction of the atoms in the gain medium with the photons in the laser mode. Because  $n$  is not a continuous but an integer number, the creation and annihilation of photons in the cavity introduces noise, which is accounted for by the noise source  $f_n$ .

The evolution of the density matrix of a three-level atom coherently coupled to the laser mode is described by the optical Bloch equations. We have

$$\begin{aligned} \frac{d}{dt}\rho_{22} &= -\gamma_2\rho_{22} + \gamma_0\rho_{00} + \frac{i}{2}\Omega(\rho_{12} - \rho_{21}), \\ \frac{d}{dt}\rho_{11} &= -\gamma_1\rho_{11} + \gamma_2\rho_{22} + \frac{i}{2}\Omega(\rho_{21} - \rho_{12}), \\ \frac{d}{dt}\rho_{21} &= -\gamma_{\perp}\rho_{21} + \frac{i}{2}\Omega(\rho_{11} - \rho_{22}) = \frac{d}{dt}\rho_{12}^*, \\ \frac{d}{dt}\rho_{00} &= -\frac{d}{dt}\rho_{22} - \frac{d}{dt}\rho_{11}. \end{aligned} \quad (9.2)$$

We neglect collisional dephasing, so that the optical coherence on the lasing transition decays at the transverse rate

$$\gamma_{\perp} = \frac{1}{2}(\gamma_1 + \gamma_2). \quad (9.3)$$

No optical coherence involving the state 0 is created. This scheme can be expected to give rise to laser action only when the lower state of the lasing transition decays much faster than the upper state, so that  $\gamma_1 \gg \gamma_2$ . The coupling of the lasing transition to the laser mode is modeled by an effective Rabi frequency  $\Omega$ . Adiabatic elimination of the optical coherence  $\rho_{21}$  shows that the effective rate of stimulated emission is

$$\gamma_{st} = \frac{\Omega^2}{2\gamma_\perp}. \quad (9.4)$$

This rate is related to the average photon number  $\bar{n}$  in the laser mode by the equality  $\gamma_{st} = \gamma_2\beta\bar{n}$ , with  $\beta$  being the fraction of spontaneously emitted photons on the laser transition that go into the laser mode. This connects the Rabi frequency to the properties of the laser cavity.

### 9.2.2 The fraction of atoms needed for lasing

In a laser the stimulated emission rate by the whole gain medium is equal to  $\gamma_2\beta n N_2$ , where  $N_2$  is the number of atoms in level 2. The absorption rate is  $\gamma_2\beta n N_1$ , where  $N_1$  is the number of atoms in level 1. The decay rate of photons from the cavity is  $2\kappa n$ . In the steady state above threshold we find

$$\gamma_2\beta\bar{n}(\bar{N}_2 - \bar{N}_1) = 2\kappa\bar{n}, \quad (9.5)$$

where the quantities with a bar refer to the steady-state values. For the inversion we find

$$\bar{D} = \bar{N}_2 - \bar{N}_1 = \frac{2\kappa}{\gamma_2\beta} = N_{thr}. \quad (9.6)$$

The number of atoms that is at least needed for the laser to operate is then equal to  $N_{thr}$ . We define  $\varepsilon$  as the fraction of the total number of atoms that is at least needed for the laser to operate, that is

$$\varepsilon = \frac{N_{thr}}{N}, \quad (9.7)$$

where  $N$  is the total number of atoms in the gain medium.

In the laser we distinguish a limited number of uncorrelated sources of noise in the photon number. We use  $f_{st}$  for stimulated emission,  $f_{abs}$  for absorption and  $f_{vac}$  for the fluctuations related to the emission of photons from the cavity. The relation between the noise term  $f_n$  in Eq. (9.1) and the uncorrelated noise terms is given by

$$f_n = f_{st} - f_{abs} - f_{vac}, \quad (9.8)$$

where the signs reflect the gain and loss nature of the noise process for the variable involved. We assume that the noise sources are Gaussian and  $\delta$ -correlated random variables with zero average. For the correlations between the noise sources we have

$$\langle f_i(t)f_j(t') \rangle = D_{ij}\delta(t-t'), \quad (9.9)$$

where  $D_{ij}$  are the diffusion coefficients. Since the noise sources are uncorrelated, the only non-zero diffusion coefficients are the diagonal ones, which we indicate as  $D_{st}$ ,  $D_{abs}$  and  $D_{vac}$ . According to Lax [91] these diffusion terms are equal to the corresponding rate, so that

$$D_{st} = \gamma_2\beta\bar{n}\bar{N}_2, \quad D_{abs} = \gamma_2\beta\bar{n}\bar{N}_1, \quad D_{vac} = 2\kappa\bar{n}. \quad (9.10)$$

### 9.2.3 Spectrum of intensity fluctuations

We are interested in the spectrum  $V(\omega)$  of the intensity fluctuations at the frequency  $\omega = 0$ . The spectrum  $V(\omega)$  is defined as follows

$$\langle \tilde{\Delta I}(\omega) \tilde{\Delta I}(\omega')^* \rangle = 2\kappa\bar{n}V(\omega)\delta(\omega - \omega') , \quad (9.11)$$

where

$$\tilde{\Delta I}(\omega) = \frac{1}{\sqrt{2\pi}} \int_{-\infty}^{\infty} dt \exp(-i\omega t) \Delta I(t) \quad (9.12)$$

is the Fourier transform of the fluctuations  $\Delta I(t)$  of the output intensity of the laser around the steady-state value  $\bar{I} = 2\kappa\bar{n}$ . To find  $\Delta I(t)$  we linearise Eq. (9.1) around the steady state by substituting  $n(t) = \bar{n} + \Delta n(t)$  and neglecting terms that are second order in  $\Delta n$  or higher. The next step is to relate the internal fluctuations in the photon number to the fluctuations in the output intensity. Therefore we use the input-output formalism of Gardiner and Collett [92]. In their paper they use the standard model of a system coupled to a heat bath. They derive a boundary condition that relates the input and the output to the internal modes of the system. In our case the input to the system is the vacuum state and the output is the intensity of the laser. We find

$$\Delta I(t) = 2\kappa\Delta n(t) + f_{vac}(t) . \quad (9.13)$$

We study the dependence of the intensity fluctuations on the parameter  $\varepsilon$  by using, respectively, a microscopic and a macroscopic approach to describe the effect of the gain medium on the number of photons in the laser mode. We determine the function  $G_{at}(n)$  that accounts for the gain medium in the rate equation for  $n$  Eq. (9.1) and use the approach given above to find an expression for the spectrum of the intensity fluctuations at frequency  $\omega = 0$  as a function of  $\varepsilon$ . In both cases the optical Bloch equations (9.2) are the starting point.

## 9.3 Quantum trajectories

### 9.3.1 Model description

In order to determine the function  $G_{at}(n)$  that accounts for the photon gain in the laser mode, we analyse in the present Section the statistical properties of the cycles performed by the internal state of the atoms of the gain medium. This is done by the technique of quantum trajectories, in which the density matrix of each atom is unraveled into an ensemble of pure states [93–95]. A trajectory description of lasers without inversion has been given before [96]. Spontaneous emission and pumping constitute the incoherent transitions in this model, which can be described by quantum jumps. The corresponding jump operators are  $S_2 = |1\rangle\langle 2|$ ,  $S_1 = |0\rangle\langle 1|$  and  $S_0 = |2\rangle\langle 0|$ . The optical Bloch equations (9.2) correspond to the master equation

$$\frac{d}{dt}\rho = -i(H\rho - \rho H^\dagger) + \gamma_2 S_2 \rho S_2^\dagger + \gamma_1 S_1 \rho S_1^\dagger + \gamma_0 S_0 \rho S_0^\dagger , \quad (9.14)$$

with  $H$  the effective non-Hermitian Hamiltonian

$$H = -\frac{1}{2} \left[ \Omega (S_2 + S_2^\dagger) + i\gamma_0 |0\rangle\langle 0| + i\gamma_1 |1\rangle\langle 1| + i\gamma_2 |2\rangle\langle 2| \right] . \quad (9.15)$$

Atoms are performing cycles  $0 \rightarrow 2 \rightarrow 1 \rightarrow 0$  along their internal states, thereby depositing photons into the laser mode when stimulated emission occurs. In order to describe the atomic contribution to the noise in the photon number, we consider the possible histories of an atom during a cycle. The atom undergoes coherent evolution periods, described by the effective Hamiltonian  $H$ . The coherent evolution is interrupted by instantaneous quantum jumps, described by the jump operators  $S_i$  with  $i = 0, 1, 2$ . Solutions of the master equation (9.14), or, equivalently, the optical Bloch equations (9.2) are faithfully reproduced after averaging these single histories over the instants of the jumps [93,94] with the proper probability distribution. We follow the atom during one cycle  $0 \rightarrow 2 \rightarrow 1 \rightarrow 0$ , which is the time period between two successive arrivals of the atom in state 0 by spontaneous emission from the state 1. After a lifetime of average duration  $\gamma_0^{-1}$  in 0, the atom is pumped to the upper state 2, as described by  $S_0$ , and the cycle ends with spontaneous decay from 1 to 0, expressed by  $S_1$ . In between these two jump instants, the atom undergoes coherent evolution within the two-state manifold 1 and 2, and any number  $k$  of spontaneous decays from 2 to 1, as described by the jump operator  $S_2$ .

### 9.3.2 Statistics of cycle trajectories

We denote a period of coherent evolution starting in state  $i$  and ending in state  $j$  as  $(i, j)$ . An atom starting a coherent period in state 0 can only remain in this state, and the only possible coherent period is  $(0, 0)$ . A coherent period starting in state 2 or in state 1 can end either in 2 or 1, with the corresponding periods  $(2, 2)$ ,  $(2, 1)$ ,  $(1, 2)$  or  $(1, 1)$ . Therefore, the probabilities  $P_{ij}$  that a coherent period starting in state  $i$  ends in state  $j$  obey the obvious sum rules

$$P_{00} = 1, \quad P_{11} + P_{12} = 1, \quad P_{21} + P_{22} = 1. \quad (9.16)$$

The average duration time of a coherent period  $(i, j)$  is indicated as  $T_{ij}$ .

In Fig. 9.2 the possible trajectories for cycles  $0 \rightarrow 2 \rightarrow 1 \rightarrow 0$  are depicted, where the number  $k$  indicates the number of spontaneous emissions during the cycle. Each spontaneous emission has a small probability  $\beta$  to return a photon to the laser mode. Stimulated emission into the laser mode takes place only during the coherent period  $(2, 1)$ . Such a period occurs only in the first trajectory in Fig. 9.2 with  $k = 0$ . This trajectory is termed the gain trajectory, and we will demonstrate that it becomes dominant above threshold. For non-zero values of the number  $k$  of spontaneous decays on the laser transition, the trajectory contains  $k - 1$  absorptions of a photon from the laser mode, each one corresponding to a coherent period  $(1, 2)$ . The passage through the manifold of lasing states starts with a coherent period  $(2, 2)$ , and ends with a coherent period  $(1, 1)$ .

The probability distribution  $p_k$  over trajectories with  $k$  spontaneous emissions on the lasing transition can be read off from Fig. 9.2, with the result

$$p_0 = P_{21}, \quad p_k = P_{22}P_{12}^{k-1}P_{11} \quad \text{for } k \geq 1. \quad (9.17)$$

By using the sum rules (9.16) it is easy to check that the probabilities add up to 1. Using these probabilities the average value of interesting physical quantities, such as the average duration of a cycle, can be calculated. The average duration  $T_k$  of a trajectory with  $k$  spontaneous emissions is simply the sum over the average durations of the coherent periods, so that

$$T_0 = T_{00} + T_{21}, \quad T_k = T_{00} + T_{22} + (k-1)T_{12} + T_{11} \quad \text{for } k \geq 1. \quad (9.18)$$

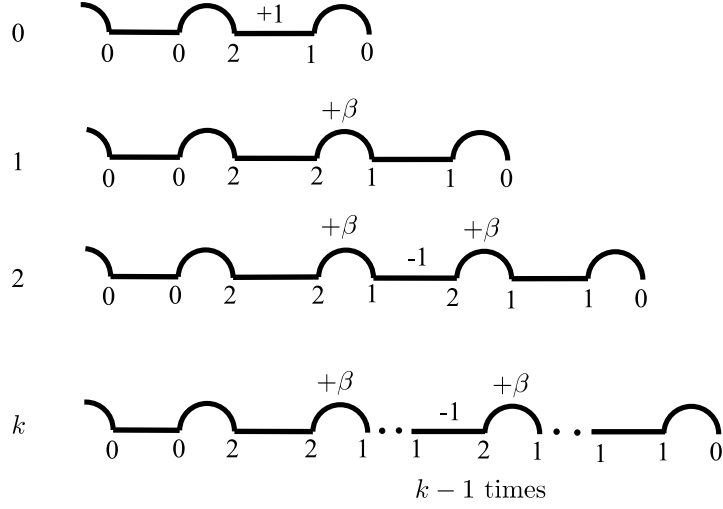


**Figure 9.2:** The different trajectories an atom can follow during one cycle, starting in the ground state level 0. The trajectories are labeled on the left. An arc represents a quantum jump and a straight line a coherent period. The state of the atom is given at the beginning and the end of each coherent period. The net effect of a coherent period or a quantum jump on the photon number is also given.

By using the sum rules (9.16), and the expressions (9.17) and (9.18) for  $p_k$  and  $T_k$ , the average duration of a cycle  $T_{cycle} = \sum_k p_k T_k$  can be simplified to the form

$$T_{cycle} = T_{00} + P_{21}T_{21} + P_{22}(T_{11} + T_{22}) + \frac{P_{22}}{P_{11}}P_{12}T_{12}. \quad (9.19)$$

In order to evaluate the probabilities  $P_{ij}$  and the average durations  $T_{ij}$ , we notice that for a given initial density matrix  $\rho_0$ , the time-dependent density matrix

$$\tilde{\rho}(\tau) = \exp(-iH\tau)\rho_0\exp(iH^\dagger\tau) \quad (9.20)$$

constitutes the partial density matrix for the situation that no quantum jump occurred during the time interval  $[0, \tau]$ . Its trace  $\text{Tr} \tilde{\rho}$  represents the corresponding probability that no quantum jump occurred in  $[0, \tau]$ . We introduce the decaying transition amplitudes

$$c_{ij}(\tau) = \langle j | \exp(-iH\tau) | i \rangle, \quad (9.21)$$

such that the quantity  $\gamma_j |c_{ij}(\tau)|^2$  is the probability density that a coherent period that started in the state  $i$  ends after a time duration  $\tau$  with a jump from the state  $j$ . This leads to the expression

$$P_{ij} = \gamma_j \int_0^\infty d\tau |c_{ij}(\tau)|^2 \quad (9.22)$$

for the probability of a coherent period  $(i, j)$  under the condition that it started in state  $i$ . We define  $L_{ij}(\tau)$  as the normalised probability density that a coherent period  $(i, j)$  ends after a

time duration  $\tau$  and find

$$L_{ij}(\tau) = \gamma_j |c_{ij}(\tau)|^2 / P_{ij}. \quad (9.23)$$

For the average duration time of a coherent period  $(i, j)$  we find

$$T_{ij} = \int_0^\infty d\tau L_{ij}(\tau) \tau. \quad (9.24)$$

Obviously, for the coherent period  $(0,0)$  in the lower state we recover that  $P_{00} = 1$ , and  $T_{00} = \gamma_0^{-1}$ . For the transition amplitudes within the manifold of the laser states, we obtain the results

$$\begin{aligned} c_{22}(\tau) &= \exp\left[-\frac{1}{4}(\gamma_1 + \gamma_2)\tau\right] \left(\cosh(\Gamma\tau) + \frac{\gamma_1 - \gamma_2}{4\Gamma} \sinh(\Gamma\tau)\right), \\ c_{11}(\tau) &= \exp\left[-\frac{1}{4}(\gamma_1 + \gamma_2)\tau\right] \left(\cosh(\Gamma\tau) - \frac{\gamma_1 - \gamma_2}{4\Gamma} \sinh(\Gamma\tau)\right), \\ c_{21}(\tau) &= c_{12}(\tau) = i \frac{\Omega}{2\Gamma} \exp\left[-\frac{1}{4}(\gamma_1 + \gamma_2)\tau\right] \sinh(\Gamma\tau), \end{aligned} \quad (9.25)$$

where

$$\Gamma = \frac{1}{4} \sqrt{(\gamma_1 - \gamma_2)^2 - 4\Omega^2}. \quad (9.26)$$

These expressions (9.25) are generally valid for the coherent evolution of the states coupled by the lasing transition. The Rabi frequency  $\Omega$  is related to the photon number by

$$\frac{\Omega^2}{2\gamma_\perp} = \gamma_2 \beta n, \quad (9.27)$$

as argued below Eq. (9.4).

### 9.3.3 Cycle time of the gain trajectory

As argued above, the only trajectory leading to stimulated emission is the first one in Fig. 9.2 (with  $k = 0$ ). Using the results of the previous subsection, we calculate the probability  $p_0$  of this first trajectory and find

$$p_0 = P_{21} = \frac{\gamma_1 \gamma_2 \beta n}{\gamma_1 \gamma_2 + (\gamma_1 + \gamma_2) \gamma_2 \beta n}. \quad (9.28)$$

Far above the threshold it is known that  $\beta n \gg 1$ , and since  $\gamma_1 \gg \gamma_2$  we see that the probability of the gain trajectory  $p_0$  is close to 1. Therefore we assume that far above the threshold, atoms in the gain medium of the laser follow only the gain trajectory.

During a coherent period the photon number is not known, because of the entanglement with the states of the atom. Therefore we cannot describe the gain of the photon in the gain trajectory as an event that takes place at a specific time  $t$ . For simplicity we assume that the actual gain of the photon takes place at the end of the coherent period  $(2, 1)$ . Far above the threshold, the atom follows the gain trajectory and we can view the atom as a source

that emits photons in the laser mode with varying time intervals between two consecutive emissions. We define  $w_1(\tau)$  as the normalised waiting-time distribution for the creation of the next photon. Since between the emissions of two consecutive photons the atom evolves through the coherent periods  $(0, 0)$  and  $(2, 1)$ , we have

$$w_1(\tau) = \int_0^\tau dt L_{21}(\tau-t)L_{00}(t), \quad (9.29)$$

where the  $L_{ij}(\tau)$  are the normalised probability densities defined in (9.23). Because directly after the emission of a photon it takes time for the atom to get excited again, the emission of a single atom in the gain medium is anti-bunched as can be seen from (9.29).

We define  $f_1(\tau_1)d\tau_1$  as the probability that there is an emission of a photon in the time interval  $(\tau_1, \tau_1 + d\tau_1)$ , regardless of how many photons have been emitted outside this time interval [97]. The expectation value of the number  $m$  of emitted photons in the time interval  $(0, T)$  is given by

$$\langle m \rangle_T = \int_0^T d\tau_1 f_1(\tau_1). \quad (9.30)$$

If we divide  $\langle m \rangle_T$  by the time  $T$ , we have the average intensity. In the limit of  $T \rightarrow \infty$  we have

$$\lim_{T \rightarrow \infty} \frac{\langle m \rangle_T}{T} = f_1(\infty), \quad (9.31)$$

which is the steady-state emission rate. The Laplace transform  $\hat{f}$  of a function  $f$  is defined as

$$\hat{f}(s) = \int_0^\infty d\tau \exp(-s\tau)f(\tau). \quad (9.32)$$

Using (9.32) and (9.31) we derive that

$$f_1(\infty) = \lim_{s \rightarrow 0} s\hat{f}_1(s). \quad (9.33)$$

Since a photon emitted at time  $\tau_1$  can be the first, the second and so on after time 0, the relation between the emission rate  $f_1(\tau_1)$  and the waiting-time distribution  $w_1(\tau_1)$  in Laplace-transform language takes the form [98]

$$\hat{f}_1(s) = \hat{w}_1(s) + [\hat{w}_1(s)]^2 + \dots = \frac{\hat{w}_1(s)}{1 - \hat{w}_1(s)}. \quad (9.34)$$

From (9.29) we find that

$$\hat{w}_1(s) = \hat{L}_{21}(s)\hat{L}_{00}(s). \quad (9.35)$$

Using (9.34) we find

$$\frac{1}{f_1(\infty)} = -\lim_{s \rightarrow 0} \frac{d}{ds} \hat{w}_1(s) = \int_0^\infty d\tau w_1(\tau)\tau, \quad (9.36)$$

which is equal to the average time between the emissions of two consecutive photons as expected. Since the atoms follow only the gain trajectory, we may write  $f_1(\infty) = 1/T_0$ . Using (9.35) we find

$$\frac{1}{f_1(\infty)} = T_0 = -\lim_{s \rightarrow 0} \frac{d}{ds} \hat{w}_1(s) = -\lim_{s \rightarrow 0} \frac{d}{ds} [\hat{L}_{21}(s)\hat{L}_{00}(s)] = T_{00} + T_{21}, \quad (9.37)$$

as expected from Fig. 9.2. Using (9.37) together with the expression (9.24) for  $T_{ij}$  we find for  $f_1(\infty)$  the following expression

$$\frac{1}{f_1(\infty)} = \frac{1}{\gamma_0} + \frac{2}{\gamma_1 + \gamma_2} + \frac{\gamma_1 + \gamma_2}{\gamma_1 \gamma_2 + (\gamma_1 + \gamma_2) \gamma_2 \beta n} . \quad (9.38)$$

### 9.3.4 Dynamics of a laser

In the steady state the number of photons created per second by the gain medium of  $N$  atoms is equal to the number of photons annihilated per second by cavity decay. Far above threshold we have

$$Nf_1(\infty) = 2\kappa\bar{n} , \quad (9.39)$$

where  $\bar{n}$  is the steady-state number of photons. We make the following assumptions

$$\beta n \gg 1 , \quad \gamma_2 \beta n \ll \gamma_1 , \quad (9.40)$$

which define a range of pump rates far above the threshold for which the number of photons in the laser mode is proportional to the pump rate  $\gamma_0$ . Under these assumptions we have

$$\frac{1}{f_1(\infty)} = T_0 = \frac{1}{\gamma_0} + \frac{1}{\gamma_2 \beta n} . \quad (9.41)$$

We solve for  $\bar{n}$  in (9.39) and find

$$\bar{n} = \frac{\gamma_0}{\gamma_2 \beta} \frac{1 - \varepsilon}{\varepsilon} , \quad (9.42)$$

where  $\varepsilon$ , defined in (9.7), is the fraction of atoms that is at least needed for the laser to operate. From (9.42) we find that in general the assumptions (9.40) are satisfied for the range of pump rates for which we have  $\gamma_2 \ll \gamma_0/\varepsilon \ll \gamma_1$ .

We calculate the average cycle time of an atom far above the threshold, which is equal to the average duration time of the gain trajectory  $T_0$  given in (9.37). Under the present assumptions and using the steady-state value (9.42) for  $n$ , we find

$$T_0 = \frac{1}{\gamma_0(1 - \varepsilon)} . \quad (9.43)$$

We see that the cycle time increases when  $\varepsilon$  is increased. This is because for a fixed pump rate the number of photons in the laser mode decreases if  $\varepsilon$  increases. Then the Rabi frequency becomes smaller and it takes more time for the atoms to make the 2-1 transition. Each cycle results in the gain of one photon in the laser mode. Thus if  $\varepsilon$  increases and thereby the cycle time, the atoms become less productive in creating photons.

### 9.3.5 Intensity fluctuations

The number of atoms in the gain medium is a macroscopically large number. If we assume that there is no correlation between the atoms, the creation of photons in the laser mode by the gain medium as a whole, is a random process. The emission rate at time  $t$  is then given

by  $Nf_1(\infty)$  which is time dependent because it is a function of  $n(t)$  as we see in (9.41). So in the rate equation (9.1) for  $n$  we substitute  $G_{at}(n) = Nf_1(\infty)$  and we obtain

$$\dot{n} = -2\kappa n + N \left( \frac{1}{\gamma_0} + \frac{1}{\gamma_2 \beta n} \right)^{-1} + f_n . \quad (9.44)$$

As discussed in Section 9.2 we linearise around the steady state. From (9.41) we find

$$f_1(\infty) = \left( \frac{1}{\gamma_0} + \frac{1}{\gamma_2 \beta \bar{n}} \right)^{-1} + \frac{2\kappa \varepsilon}{N} \Delta n + \mathcal{O}(\Delta n^2) , \quad (9.45)$$

and Eq. (9.44) gives for the fluctuations  $\Delta n(t)$  in the photon number

$$\Delta \dot{n} = -2\kappa(1 - \varepsilon) \Delta n + f_n , \quad (9.46)$$

with the solution

$$\Delta n(t) = \int_{-\infty}^t dt' \exp[-2\kappa(1 - \varepsilon)(t - t')] f_n(t') . \quad (9.47)$$

According to (9.13) we have  $\Delta I(t) = 2\kappa \Delta n(t) + f_{vac}(t)$ . The noise source  $f_n$  is related to the uncorrelated noise sources in (9.8). The corresponding diffusion coefficients are given in (9.10). Because of the assumptions (9.40), the decay rate  $\gamma_1$  of the lower lasing level is much larger than the other rates in the model. For the evaluation of the diffusion coefficients it is, therefore, justified to neglect the number of atoms in level 1, and so that  $\bar{N}_1 = 0$  and  $\bar{N}_2 = \bar{D} = N_{thr}$ . We use the Wiener-Khintchine theorem [99], that is

$$\langle \tilde{\Delta I}(\omega) \tilde{\Delta I}(\omega')^* \rangle = \delta(\omega - \omega') \lim_{T \rightarrow \infty} \int_{-\infty}^{\infty} d\tau \exp(-i\omega\tau) \langle \Delta I(T + \tau) \Delta I(T) \rangle , \quad (9.48)$$

and obtain the following expression for the spectrum of intensity fluctuations as defined in (9.11):

$$V(\omega) = 1 + \frac{8\kappa^2 \varepsilon}{4\kappa^2(1 - \varepsilon)^2 + \omega^2} . \quad (9.49)$$

For the spectrum at frequency  $\omega = 0$  we have

$$V(0) = 1 + \frac{2\varepsilon}{(1 - \varepsilon)^2} . \quad (9.50)$$

The value  $V(0) = 1$  corresponds to shot noise in our definition (9.11). We see that for  $\varepsilon = 0$ , which is the case of no depletion of the ground state at all, we have shot noise. If  $\varepsilon$  is increased, the fluctuations rise above shot noise.

We can see this also from a qualitative argument. The average cycle time of the atom is  $T_0 = 1/f_1(\infty)$ . If we calculate the average fraction of the total cycle time that the atom spends in the ground state we find, using (9.43),

$$\frac{T_{00}}{T_0} = \frac{1}{\gamma_0 T_0} = 1 - \varepsilon . \quad (9.51)$$

We see that for small  $\varepsilon$  the atom is in the ground state for most of the time. In that case the cycle time is not sensitive to fluctuations in the photon number. If  $\varepsilon$  is increased, the atom spends less time in the ground state and a fluctuation in the photon number will cause more fluctuations in the cycle time.

In the Appendix the Mandel  $Q$  parameter [100] is calculated for the emission of a single atom in the gain medium that follows only the gain trajectory. It is defined by  $Q + 1 = \Delta m^2 / \langle m \rangle$ , where  $m$  is the number of photon emissions. We have  $Q = 0$  for a Poisson process. Under the assumptions (9.40) and using (9.42) it is found that

$$Q = -2\varepsilon(1 - \varepsilon). \quad (9.52)$$

We see that for  $\varepsilon = 0$  we have  $Q = 0$  and the emission of a single atom is Poissonian. This is expected from the fact that for  $\varepsilon = 0$  the atom spends (almost) all its time in the ground state and thus the statistics of its emission are determined by the statistics of the pump, which are Poissonian. For  $\varepsilon = 0$  the output fluctuations are at the shot-noise level. If  $\varepsilon$  is increased, the value of  $Q$  decreases until a minimum value of  $-\frac{1}{2}$  is reached for  $\varepsilon = \frac{1}{2}$ . We can understand this from the fact that for  $\varepsilon = \frac{1}{2}$  we have  $T_{00} = T_{21}$ , so that the cycle contains two coherent periods with the same average duration. According to Ritsch and Zoller [89] this regular recycling of the atom is accompanied by anti-bunching and sub-Poissonian emission. It is surprising that for non-zero  $\varepsilon$  the emission of a single atom is sub-Poissonian, while the output fluctuations are above shot noise.

## 9.4 Semi-classical rate equations

### 9.4.1 Steady state

In this Section we study the steady-state and noise properties of the three-level laser from a macroscopic point of view using semi-classical rate equations. We assume that the total number of active atoms in the gain medium is constant and given by  $N$ , a macroscopically large number. Classical Langevin rate equations for the number of atoms in the different levels  $N_2$ ,  $N_1$ ,  $N_0$  follow from the optical Bloch equations (9.2) where we adiabatically eliminate the atomic coherences of the lasing transition. We identify  $N\rho_{ii}$  as the number of atoms  $N_i$  in level  $i$ , which is justified for macroscopic  $N$ , and add Langevin noise terms. We find

$$\begin{aligned} \dot{N}_2 &= -\gamma_2 N_2 - \gamma_2 \beta n (N_2 - N_1) + \gamma_0 N_0 + f_2, \\ \dot{N}_1 &= -\gamma_1 N_1 + \gamma_2 \beta n (N_2 - N_1) + \gamma_2 N_2 + f_1, \\ \dot{N}_0 &= -\gamma_0 N_0 + \gamma_1 N_1 + f_0, \end{aligned} \quad (9.53)$$

with  $n$  the number of photons in the laser mode and  $\beta$  the fraction of spontaneously emitted photons on the laser transition that go into the laser mode, as mentioned in Section 9.2. The fraction  $\beta$  is an independent parameter in this configuration. The terms  $\gamma_2 N_2$  and  $\gamma_1 N_1$  describe spontaneous emission from levels 2 and 1, respectively, and the terms  $\gamma_2 \beta n N_2$  and  $\gamma_2 \beta n N_1$  represent stimulated emission and absorption. From this we derive the rate equation for the number of photons in the laser mode. We assume operation in the good-cavity regime,

by which we mean that the cavity decay rate  $2\kappa$  is much smaller than the transverse relaxation rate  $\gamma_{\perp}$  as given in (9.3). Under this assumption we find

$$\dot{n} = -2\kappa n + \gamma_2\beta [N_2(n+1) - N_1n] + f_n. \quad (9.54)$$

If we compare this expression with (9.1) we can identify  $G_{at}(n)$  as the second term on the right. The noise sources  $f_i$  with  $i = n, 0, 1, 2$  are Gaussian  $\delta$ -correlated random variables with zero average. They appear in the rate equations because the quantities that are involved are not continuous numbers, but refer to an integer number such as the number of atoms for example. In (9.54) the factor  $n+1$  instead of  $n$  accounts for spontaneous emission in the laser mode. The rate equations (9.53) and (9.54) can also be derived directly from phenomenological considerations of the dynamics of a laser. The constraint on the total number of atoms is given by

$$N_0(t) + N_1(t) + N_2(t) = N. \quad (9.55)$$

The steady-state photon number  $\bar{n}$  and inversion  $\bar{D} = \bar{N}_2 - \bar{N}_1$  can be found from (9.53) and (9.54) by setting the time derivatives to zero and omitting the noise sources. If we assume that  $\beta \ll 1$  we find

$$\begin{aligned} \bar{n} &= \frac{1}{2\beta} \left( M - 1 + \sqrt{(M-1)^2 + 4 \frac{\beta M}{1-\varepsilon} \frac{\gamma_1}{\gamma_1 - \gamma_2}} \right), \\ M &= \frac{1-\varepsilon}{\varepsilon} \frac{\gamma_0}{\gamma_2} \frac{\gamma_1 - \gamma_2}{\gamma_1 + 2\gamma_0}, \\ \bar{D} &= N\varepsilon \frac{\bar{n}(\gamma_1 - \gamma_2)}{\bar{n}(\gamma_1 - \gamma_2) + \gamma_1}, \end{aligned} \quad (9.56)$$

where the parameter  $\varepsilon$  defined in (9.7) again has the significance of the fraction of the total number of atoms that is at least needed for the laser to operate. Above threshold, where  $\bar{n} \gg 1$ , the inversion  $\bar{D}$  equals  $N_{thr}$ . The parameter  $M$  is the pump parameter that is normalised to 1 at the threshold. In all the figures below we use the values  $\beta = 10^{-6}$  and  $\gamma_2/\gamma_1 = 10^{-5}$ , which are characteristic for a typical Nd:YVO<sub>4</sub> laser.

In Fig. 9.3 the steady-state photon number  $\bar{n}$  as a function of the pump rate is given for different values of  $\varepsilon$ . We see that when  $\varepsilon$  is increased, the threshold moves to a higher pump rate. This is because just above the threshold the population in the ground state is  $1 - \varepsilon$ . An increase in  $\varepsilon$  is thus an increase in the depletion of the ground state, which must be compensated by a higher pump rate. The photon number stops increasing when the pump rate becomes of the same order of magnitude as the decay rate  $\gamma_1$  of level 1. Then the 1-0 transition starts to act as a bottleneck, with the consequence that a further increase in the pump rate increases the population in level 1 and depletes the ground state.

If we multiply the steady-state photon number  $\bar{n}$  with the cavity decay rate  $2\kappa$  and divide by the total number of atoms  $N$ , we have the steady-state output intensity per atom. In Fig. 9.4 this quantity is given as a function of the pump rate for different values of  $\varepsilon$ . We see that the atoms become less productive when  $\varepsilon$  is increased. This is understood from the discussion below (9.43), where it was found that the cycle time of an atom increases if  $\varepsilon$  is increased.

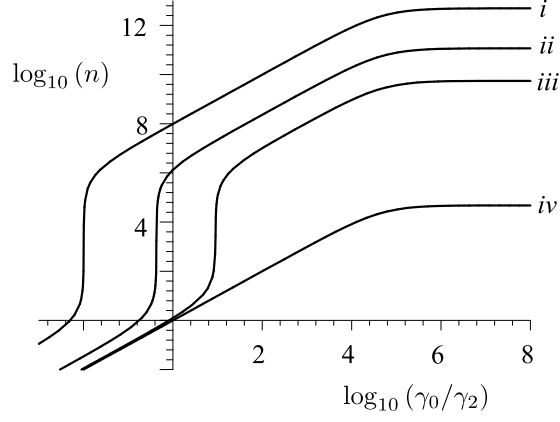


**Figure 9.3:** Steady-state photon number  $n$  as a function of the pump rate  $\gamma_0$  in units of  $\gamma_2$ . We have (i)  $\varepsilon = 0.01$ , (ii)  $\varepsilon = 0.3$ , (iii)  $\varepsilon = 0.9$ , (iv)  $\varepsilon = 1$ .

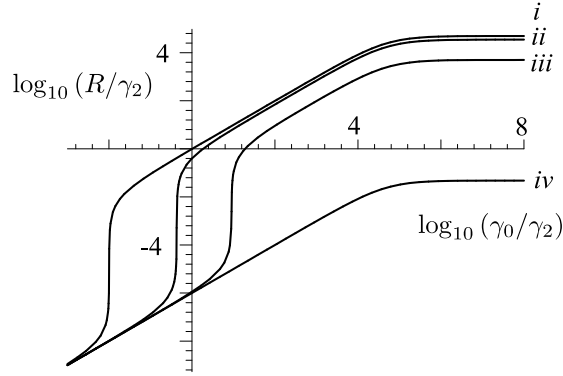


**Figure 9.4:** Steady-state output intensity per atom  $R = 2\kappa\bar{n}/N$  in units of  $\gamma_2$  as a function of the pump rate  $\gamma_0$  in units of  $\gamma_2$ . We have (i)  $\varepsilon = 0.01$ , (ii)  $\varepsilon = 0.3$ , (iii)  $\varepsilon = 0.9$ , (iv)  $\varepsilon = 1$ .

### 9.4.2 Intensity fluctuations

We are interested in the spectrum  $V(\omega)$  of the intensity fluctuations at the frequency  $\omega = 0$ , as defined in (9.11). To obtain this spectrum at  $\omega = 0$  we start from Eqs. (9.53)-(9.55). We neglect the spontaneous emission in the laser mode and eliminate the rate equation for  $N_0$  by using the assumption (9.55) that the total number of atoms is constant and is given by  $N$ . We linearise the remaining rate equations for  $n$ ,  $N_1$ , and  $N_2$  around the steady state by writing

$$n(t) = \bar{n} + \Delta n(t), \quad N_1(t) = \bar{N}_1 + \Delta N_1(t), \quad N_2(t) = \bar{N}_2 + \Delta N_2(t), \quad (9.57)$$

and neglecting terms that are quadratic in the fluctuations. We take the Fourier transform of the linearised equations and solve for  $\widetilde{\Delta n}(\omega)$ , the Fourier transform of the photon-number fluctuations  $\Delta n(t)$ . Because we are interested in the spectrum at zero frequency, we neglect the Fourier transforms of the time derivatives since they are proportional to  $\omega$ . We assume that  $\bar{n} \gg 1$  and find

$$2\kappa\widetilde{\Delta n}(\omega) = \left(1 + \frac{1}{\beta\bar{n}} + \frac{\gamma_0 A}{\gamma_2 \beta \bar{n}}\right) \tilde{f}_n(\omega) + (A-1)\tilde{f}_1(\omega) + A\tilde{f}_2(\omega), \quad (9.58)$$

where  $\tilde{f}_i(\omega)$  is the Fourier transform of  $f_i(t)$ , and where

$$A = \frac{\gamma_1 - \gamma_2}{\gamma_1 + 2\gamma_0}. \quad (9.59)$$

In Section 9.2 we introduced three uncorrelated noise sources in a laser,  $f_{st}$  for stimulated emission,  $f_{abs}$  for absorption, and  $f_{vac}$  for the fluctuations related to the emission of photons from the cavity. We distinguish three more noise sources,  $f_{sp}^1$  and  $f_{sp}^2$  for spontaneous emission in the 1-0 transition and 2-1 transition, respectively, and  $f_{pump}$  for the pump process. Their diffusion coefficients are given by [91]

$$D_{sp}^1 = \gamma_1 \bar{N}_1, \quad D_{sp}^2 = \gamma_2 \bar{N}_2, \quad D_{pump} = \gamma_0 \bar{N}_0. \quad (9.60)$$

The relation between the noise source  $f_n$  and the uncorrelated noise sources has already been given in (9.8). For the noise sources  $f_i$  with  $i = 0, 1, 2$  we have

$$f_0 = f_{sp}^1 - f_{pump}, \quad f_1 = f_{st} - f_{abs} - f_{sp}^1 + f_{sp}^2, \quad f_2 = -f_{st} + f_{abs} - f_{sp}^2 + f_{pump}. \quad (9.61)$$

From (9.9) it directly follows that

$$\langle \tilde{f}_i(\omega) \tilde{f}_j(\omega')^* \rangle = D_{ij} \delta(\omega - \omega'). \quad (9.62)$$

By using (9.58) and the relation between the fluctuations in the photon number and the output intensity (9.13) we find for the spectrum defined in (9.11) at  $\omega = 0$  the following expression:

$$V(0) = \frac{\gamma_1}{\gamma_1 - \gamma_2} \frac{1 + \beta\bar{n}}{\beta\bar{n}} \left(1 + \frac{\gamma_2}{\gamma_1} - 2A + 2A^2\right) + \frac{1}{\beta\bar{n}} \left[1 - A + A \left(\frac{\gamma_0 A}{\gamma_2} \frac{1 - \varepsilon}{\varepsilon} - \beta\bar{n}\right)\right] + \frac{2}{\beta^2 \bar{n}^2} \left(\frac{\gamma_1 + \gamma_2 \beta \bar{n}}{\gamma_1 - \gamma_2}\right) \left(1 + \frac{\gamma_0 A}{\gamma_2}\right)^2, \quad (9.63)$$

where  $A$  is defined in (9.59).

With  $\bar{n}$  given in (9.56) this quantity is displayed in Fig. 9.5 as a function of the pump rate for different values of  $\varepsilon$ . With our definition (9.11) the value  $V(0) = 1$  corresponds to shot noise. We see that for  $\varepsilon \rightarrow 0$  and  $\gamma_0$  fixed, which corresponds to the limit of the steady-state photon number  $\bar{n}$  to infinity, the intensity fluctuations drop below shot noise if the pump rate becomes of the same order of magnitude as the decay rate  $\gamma_1$  of level 1. This result has been obtained before [87, 89]. Hart and Kennedy [87] relate this reduction in noise to the accompanying depletion of the ground state, which reduces the pump noise. Ritsch and

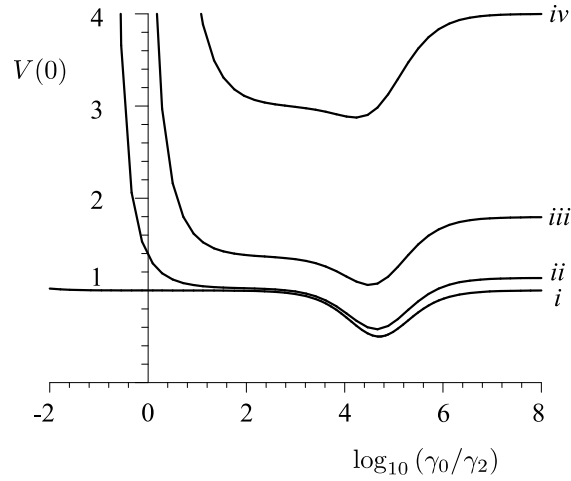


**Figure 9.5:** Spectrum of intensity fluctuations at zero frequency  $V(0)$  as a function of the pump rate  $\gamma_0$  in units of  $\gamma_2$ . We have (i)  $\varepsilon = 0$ , (ii)  $\varepsilon = 0.1$ , (iii)  $\varepsilon = 0.3$ , (iv)  $\varepsilon = 0.5$ .

Zoller [89] focus on the regular recycling of the atoms in the pumping process, which leads to anti-bunching of the emission of the individual atoms and therefore to a reduction in the intensity noise. If  $\varepsilon$  is increased we see that the divergence in noise that accompanies the threshold moves to higher pump rates. The noise increases for all pump rates and rises above shot noise, also in the range of pump rates where for  $\varepsilon = 0$  the intensity fluctuations are below shot noise.

Finally, applying the assumptions to the expression (9.56) for the steady-state number of photons in the laser mode, we find the same result as in Section 9.3, Eq. (9.42). For the spectrum of intensity fluctuations at the frequency  $\omega = 0$  we find that the result from the semi-classical rate equations is

$$V(0) = 1 + \frac{2\varepsilon^2}{(1-\varepsilon)^2} . \quad (9.64)$$

From the quantum-trajectory approach discussed in Section 9.3 we have Eq. (9.50)

$$V(0) = 1 + \frac{2\varepsilon}{(1-\varepsilon)^2} . \quad (9.65)$$

We notice that the quantum-trajectory approach predicts more noise than the semi-classical description. This may be due to our ignoring other trajectories than the gain trajectory (with  $k = 0$  in Fig. 9.2). The atom number used in (9.39) only refers to the number of atoms in the gain trajectory. This underestimates the actual number of atoms, and therefore overestimates the noise.

## 9.5 Conclusions

We have analysed a simple three-level model of a laser, where the number of active atoms  $N$  is a limiting factor for laser action. A crucial role is played by the parameter  $\varepsilon$ , defined as the fraction of the total number of atoms in the gain medium that is needed for the laser to operate. The microscopic approach in Section 9.3 focuses on the pumping cycle of an individual atom using a quantum-trajectory picture. It is the dependence of the emission rate  $f_1(\infty)$ , or, equivalently, the cycle time  $T_0$ , on the number of photons in the laser mode that determines the statistics of the output of the laser. We find that far above the threshold, for pump rates  $\gamma_0$  much smaller than the decay rate  $\gamma_1$  of the lower lasing level, the output fluctuations increase if  $\varepsilon$  is increased. We argue that the fraction of the total cycle time the atom spends in the ground state is  $1 - \varepsilon$ . This explains the increase in intensity fluctuations for increasing value of  $\varepsilon$ . From the calculation of the Mandel  $Q$  parameter we find that the emission of photons in the cavity mode by a single atom is anti-bunched and sub-Poissonian for  $\varepsilon > 0$ . We conclude that an anti-bunched and sub-Poissonian emission of single atoms in the gain medium does not guarantee that the statistics of the output of the laser are below shot noise or sub-Poissonian.

From the macroscopic approach in Section 9.4 we find that if  $\varepsilon$  increases, the threshold of the laser moves to higher pump rates and the cycle time of the individual atoms increases, which makes the atoms less productive in creating photons. In the case that  $\varepsilon = 0$ , the atoms on the ground state represent an infinite reservoir. In this limiting case, our results for the intensity fluctuations are in agreement with those of Hart and Kennedy [87] and Ritsch and Zoller [89]. For strong pumping, that is, for values of the pump rate  $\gamma_0$  of the same order of magnitude as the decay rate  $\gamma_1$  of the lower level 1 of the lasing transition, the intensity fluctuations are below shot noise. However, if the parameter  $\varepsilon$  is increased, the intensity fluctuations increase for all values of the pump rate  $\gamma_0$ . This is in agreement with the results from the microscopic approach. Hence, this scheme does not lead to an easy method to create sub-Poissonian laser radiation with a Poissonian pump of moderate strength.

## 9.A Mandel $Q$ parameter

Fluctuations in the number  $m$  of photon emissions are commonly expressed in terms of the Mandel  $Q$  parameter [100] defined by  $Q + 1 = \Delta m^2 / \langle m \rangle$ , so that  $Q = 0$  for a Poisson process. We define  $f_2(\tau_2, \tau_1) d\tau_1 d\tau_2$  as the probability that there is an emission of a photon in both time intervals  $(\tau_2, \tau_2 + d\tau_2)$  and  $(\tau_1, \tau_1 + d\tau_1)$ , regardless of how many photons have been emitted outside these time intervals. This function relates two events and can be interpreted as a correlation function. Since in our case the system is completely reset after each emission we can write

$$f_2(\tau_2, \tau_1) = f_1(\tau_2 - \tau_1) f_1(\tau_1) . \quad (9.66)$$

We have [97]

$$\frac{1}{2} \langle m(m-1) \rangle_T = \int_0^T d\tau_2 \int_0^{\tau_2} d\tau_1 f_2(\tau_2, \tau_1) . \quad (9.67)$$

The Mandel  $Q$  parameter in the steady state is then given by

$$Q = \lim_{T \rightarrow \infty} \frac{2 \int_0^T d\tau_2 \int_0^{\tau_2} d\tau_1 f_1(\tau_2 - \tau_1) f_1(\tau_1) - \int_0^T d\tau_2 \int_0^T d\tau_1 f_1(\tau_2) f_1(\tau_1)}{\int_0^T d\tau_1 f_1(\tau_1)}, \quad (9.68)$$

where we used (9.30), (9.66) and (9.67). From (9.30) we see that the integrals over  $f_1$  are divergent for  $T \rightarrow \infty$ . Therefore we introduce the deviation  $g_1(\tau_1)$  from the steady-state value as

$$g_1(\tau_1) = f_1(\tau_1) - f_1(\infty). \quad (9.69)$$

The integrals over  $g_1$  have an upper bound for  $T \rightarrow \infty$ . We can write the denominator in the expression (9.68) for  $Q$  as

$$\langle m \rangle_T = \int_0^T d\tau_1 f_1(\tau_1) = T f_1(\infty) + \int_0^T d\tau_1 g_1(\tau_1). \quad (9.70)$$

In the numerator the terms proportional to  $T^2$  drop out and, if we take the limit  $T \rightarrow \infty$ , we find [101]

$$Q = 2\hat{g}_1(0), \quad (9.71)$$

where  $\hat{g}_1(s)$  is the Laplace transform of  $g_1(\tau_1)$

$$\hat{g}_1(s) = \int_0^\infty d\tau_1 \exp(-s\tau_1) g_1(\tau_1). \quad (9.72)$$

Using results from Section 9.3 we calculate  $Q$ . We apply the assumptions (9.40) and the expression (9.42) to find

$$Q = -2\varepsilon(1 - \varepsilon). \quad (9.73)$$

---

## Bibliography

---

- [1] M. Born and E. Wolf, *Principles of Optics* (Cambridge University Press, Cambridge, UK, 1999), 7th edition.
- [2] M. Lax, W. H. Louisell, and W. B. McKnight, 'From Maxwell to paraxial wave optics', *Phys. Rev. A* **11**, 1365 (1975).
- [3] G. Nienhuis and L. Allen, 'Paraxial wave optics and harmonic oscillators', *Phys. Rev. A* **48**, 656 (1993).
- [4] M. Nazarathy and J. Shamir, 'Fourier optics described by operator algebra', *J. Opt. Soc. Am.* **70**, 150 (1980).
- [5] H. Bacry and M. Cadillac, 'Metaplectic group and Fourier optics', *Phys. Rev. A* **23**, 2533 (1981).
- [6] D. Stoler, 'Operator methods in physical optics', *J. Opt. Soc. Am.* **71**, 334 (1981).
- [7] A. E. Siegman, *Lasers* (Oxford University Press, Oxford, 1986).
- [8] J. Dingjan, M. P. van Exter, and J. P. Woerdman, 'Geometric modes in a single-frequency Nd:YVO<sub>4</sub> laser', *Opt. Commun.* **188**, 345 (2001).
- [9] H. Kogelnik, 'On the propagation of Gaussian beams of light through lens-like media including those with a loss or gain variation', *Appl. Opt.* **4**, 1562 (1965).
- [10] Y. F. Chen, C. H. Jiang, Y. P. Lan, and K. F. Huang, 'Wave representation of geometrical laser beam trajectories in a hemi-confocal cavity', *Phys. Rev. A* **69**, 053807 (2004).
- [11] S. Danakas and P. K. Aravind, 'Analogies between two optical systems (photon beam splitters and laser beams) and two quantum systems (the two-dimensional oscillator and the two-dimensional hydrogen atom)', *Phys. Rev. A* **45**, 1973 (1992).
- [12] E. E. Bergmann, 'Optical resonators with paraxial modes', *Appl. Opt.* **11**, 113 (1972).
- [13] R. Borghi, M. Santarsiero, and R. Simon, 'Shape invariance and a universal form for the Gouy phase', *J. Opt. Soc. Am. A* **21**, 572 (2004).
- [14] E. G. Abramochkin and V. G. Volostnikov, 'Generalised Gaussian beams', *J. Opt. A: Pure Appl. Opt.* **6**, S157 (2004).

Bibliography

- [15] M. A. Bandres and J. C. Gutiérrez-Vega, ‘Ince-Gaussian beams’, *Opt. Lett.* **29**, 144 (2004).
- [16] M. A. Bandres and J. C. Gutiérrez-Vega, ‘Ince-Gaussian modes of the paraxial wave equation and stable resonators’, *J. Opt. Soc. Am. A* **21**, 873 (2004).
- [17] J. A. Arnaud, ‘Degenerate optical cavities’, *Appl. Opt.* **8**, 189 (1969).
- [18] A. Messiah, *Quantum Mechanics* (North-Holland Publishing Company, Amsterdam, 1972).
- [19] V. N. Mahajan, *Optical Imaging and Aberrations* (SPIE Press, Bellingham, USA, 2001).
- [20] H. Laabs and A. T. Friberg, ‘Non-paraxial eigenmodes of stable resonators’, *IEEE J. Quantum Electron.* **35**, 198 (1999).
- [21] T. Klaassen, A. Hoogeboom, M. P. van Exter, and J. P. Woerdman, ‘Gouy phase of non-paraxial eigenmodes in a folded resonator’, *J. Opt. Soc. Am. A* **21**, 1689 (2004).
- [22] R. Simon and N. Mukunda, ‘Iwasawa decomposition in first-order optics: Universal treatment of shape-invariant propagation for coherent and partially coherent beams’, *J. Opt. Soc. Am. A* **15**, 2146 (1998).
- [23] D. R. Truax, ‘Baker-Campbell-Hausdorff relations and unitarity of SU(2) and SU(1,1) squeeze operators’, *Phys. Rev. D* **31**, 1988 (1985).
- [24] H. R. Lewis Jr. and W. B. Riesenfeld, ‘An exact quantum theory of the time-dependent harmonic oscillator and of a charged particle in a time-dependent electromagnetic field’, *J. Math. Phys.* **10**, 1458 (1969).
- [25] J. Wei and E. Norman, ‘Lie algebraic solution of linear differential equations’, *J. Math. Phys.* **4**, 575 (1963).
- [26] M. W. Beijersbergen, R. P. C. Coerwinkel, M. Kristensen, and J. P. Woerdman, ‘Helical-wavefront laser beams produced with a spiral phase plate’, *Opt. Commun.* **112**, 321 (1994).
- [27] S. S. R. Oemrawsingh, A. Aiello, E. R. Eliel, G. Nienhuis, and J. P. Woerdman, ‘How to observe high-dimensional two-photon entanglement with only two detectors’, *Phys. Rev. Lett.* **92**, 217901 (2004).
- [28] G. Molina-Terriza, A. Vaziri, J. Řeháček, Z. Hradil, and A. Zeilinger, ‘Triggered qutrits for quantum communication protocols’, *Phys. Rev. Lett.* **92**, 167903 (2004).
- [29] J. P. Torres, Y. Deyanova, L. Torner, and G. Molina-Terriza, ‘Preparation of engineered two-photon entangled states for multi-dimensional quantum information’, *Phys. Rev. A* **67**, 052313 (2003).
- [30] V. Y. Bazhenov, M. S. Soskin, and M. V. Vasnetsov, ‘Screw dislocations in light wavefronts’, *J. Mod. Opt.* **39**, 985 (1992).
- [31] S. S. R. Oemrawsingh, J. A. W. van Houwelingen, E. R. Eliel, J. P. Woerdman, E. J. K. Verstegen, J. G. Kloosterboer, and G. W. ’t Hooft, ‘Production and characterisation of spiral phase plates for optical wavelengths’, *Appl. Opt.* **43**, 688 (2004).
- [32] G. Molina-Terriza, J. Rekolons, J. P. Torres, L. Torner, and E. M. Wright, ‘Observation of the dynamical inversion of the topological charge of an optical vortex’, *Phys. Rev. Lett.* **87**, 023902 (2001).
- [33] G. Indebetouw, ‘Optical vortices and their propagation’, *J. Mod. Opt.* **40**, 73 (1993).

- [34] L. Allen, M. W. Beijersbergen, R. J. C. Spreeuw, and J. P. Woerdman, ‘Orbital angular momentum of light and the transformation of Laguerre-Gaussian laser modes’, *Phys. Rev. A* **45**, 8185 (1992).
- [35] S. J. van Enk and G. Nienhuis, ‘Eigenfunction description of laser beams and orbital angular momentum of light’, *Opt. Commun.* **94**, 147 (1992).
- [36] J. Courtial, K. Dholakia, L. Allen, and M. J. Padgett, ‘Gaussian beams with very high orbital angular momentum’, *Opt. Commun.* **144**, 210 (1997).
- [37] J. A. Arnaud and H. Kogelnik, ‘Gaussian light beams with general astigmatism’, *Appl. Opt.* **8**, 1687 (1969).
- [38] A. Y. Bekshaev, M. V. Vasnetsov, V. G. Denisenko, and M. S. Soskin, ‘Transformation of the orbital angular momentum of a beam with optical vortex in an astigmatic optical system’, *JETP Lett.* **75**, 127 (2002).
- [39] A. Y. Bekshaev, M. S. Soskin, and M. V. Vasnetsov, ‘Optical vortex symmetry breakdown and decomposition of the orbital angular momentum of light beams’, *J. Opt. Soc. Am. A* **20**, 1635 (2003).
- [40] A. Wünsche, ‘Generalised Gaussian beam solutions of paraxial optics and their connection to a hidden symmetry’, *J. Opt. Soc. Am. A* **6**, 1320 (1989).
- [41] A. Y. Bekshaev, M. S. Soskin, and M. V. Vasnetsov, ‘Transformation of higher-order optical vortices upon focusing by an astigmatic lens’, *Opt. Commun.* **241**, 237 (2004).
- [42] F. S. Roux, ‘Coupling of non-canonical optical vortices’, *J. Opt. Soc. Am. B* **21**, 664 (2004).
- [43] I. S. Gradshteyn and I. M. Ryzhik, *Table of Integrals, Series, and Products* (Academic Press, San Diego, 1994), 5th edition.
- [44] E. J. Galvez, P. R. Crawford, H. I. Sztul, M. J. Pysher, P. J. Haglin, and R. E. Williams, ‘Geometric phase associated with mode transformations of optical beams bearing orbital angular momentum’, *Phys. Rev. Lett.* **90**, 203901 (2003).
- [45] F. S. Roux, ‘Spatial evolution of the morphology of an optical vortex dipole’, *Opt. Commun.* **236**, 433 (2004).
- [46] I. H. Deutsch and J. C. Garrison, ‘Paraxial quantum propagation’, *Phys. Rev. A* **43**, 2498 (1991).
- [47] C. K. Hong and L. Mandel, ‘Theory of parametric frequency down-conversion of light’, *Phys. Rev. A* **31**, 2409 (1985).
- [48] A. Zeilinger, ‘Experiment and the foundations of quantum physics’, *Rev. Mod. Phys.* **71**, S288 (1999).
- [49] C. W. Gardiner and P. Zoller, *Quantum Noise* (Springer, Berlin, 2000), 2nd edition.
- [50] A. F. Abouraddy, B. E. A. Saleh, A. V. Sergienko, and M. C. Teich, ‘Role of entanglement in two-photon imaging’, *Phys. Rev. Lett.* **87**, 123602 (2001).
- [51] A. F. Abouraddy, M. B. Nasr, B. E. A. Saleh, A. V. Sergienko, and M. C. Teich, ‘Demonstration of the complementarity of one- and two-photon interference’, *Phys. Rev. A* **63**, 063803 (2001).
- [52] B. E. A. Saleh, A. F. Abouraddy, A. V. Sergienko, and M. C. Teich, ‘Duality between partial coherence and partial entanglement’, *Phys. Rev. A* **62**, 043816 (2000).
- [53] A. Gatti, E. Brambilla, and L. A. Lugiato, ‘Entangled imaging and wave-particle duality: From the microscopic to the macroscopic realm’, *Phys. Rev. Lett.* **90**, 133603 (2003).

Bibliography

- [54] A. V. Belinskii and D. N. Klyshko, 'Two-photon optics: Diffraction, holography and transformation of two-dimensional signals', *JETP Lett.* **78**, 259 (1994).
- [55] P. G. Kwiat, K. Mattle, H. Weinfurter, and A. Zeilinger, 'New high-intensity source of polarisation-entangled photon pairs', *Phys. Rev. Lett.* **75**, 4337 (1995).
- [56] E. Altewischer, M. P. van Exter, and J. P. Woerdman, 'Plasmon-assisted transmission of entangled photons', *Nature* **418**, 304 (2002).
- [57] A. Vaziri, G. Weihs, and A. Zeilinger, 'Experimental two-photon, three-dimensional entanglement for quantum communication', *Phys. Rev. Lett.* **89**, 240401 (2002).
- [58] C. K. Hong, Z. Y. Ou, and L. Mandel, 'Measurement of sub-picosecond time intervals between two photons by interference', *Phys. Rev. Lett.* **59**, 2044 (1987).
- [59] Y.-H. Kim and W. P. Grice, 'Generation of pulsed polarisation-entangled two-photon state via temporal and spectral engineering', *J. Mod. Opt.* **49**, 2309 (2002).
- [60] J. Bylander, I. Robert-Philip, and I. Abram, 'Interference and correlation of two independent photons', *Eur. Phys. J. D* **22**, 295 (2003).
- [61] J. D. Franson, 'Bell inequality for position and time', *Phys. Rev. Lett.* **62**, 2205 (1989).
- [62] W. Tittel, J. Brendel, B. Gisin, T. Herzog, H. Zbinden, and N. Gisin, 'Experimental demonstration of quantum correlations over more than 10 km', *Phys. Rev. A* **57**, 3229 (1998).
- [63] T. B. Pittman, D. V. Strekalov, A. Migdall, M. H. Rubin, A. V. Sergienko, and Y. H. Shih, 'Can two-photon interference be considered interference of two photons?', *Phys. Rev. Lett.* **77**, 1917 (1996).
- [64] W. P. Grice and I. A. Walmsley, 'Spectral information and distinguishability in type-II down-conversion with a broad-band pump', *Phys. Rev. A* **56**, 1627 (1997).
- [65] J. Peřina Jr., A. V. Sergienko, B. M. Jost, B. E. A. Saleh, and M. C. Teich, 'Dispersion in femtosecond entangled two-photon interference', *Phys. Rev. A* **59**, 2359 (1999).
- [66] R. Loudon, *The Quantum Theory of Light* (Oxford Science Publications, Oxford, UK, 2000), 3rd edition.
- [67] J. H. Eberly and K. Wódkiewicz, 'The time-dependent physical spectrum of light', *J. Opt. Soc. Am.* **67**, 1252 (1977).
- [68] H. H. Arnaut and G. A. Barbosa, 'Orbital and intrinsic angular momentum of single photons and entangled pairs of photons generated by parametric down-conversion', *Phys. Rev. Lett.* **85**, 286 (2000).
- [69] G. A. Barbosa and H. H. Arnaut, 'Twin photons with angular-momentum entanglement: Phase matching', *Phys. Rev. A* **65**, 053801 (2002).
- [70] S. Franke-Arnold, S. M. Barnett, M. J. Padgett, and L. Allen, 'Two-photon entanglement of orbital angular momentum states', *Phys. Rev. A* **65**, 033823 (2002).
- [71] A. Mair, A. Vaziri, G. Weihs, and A. Zeilinger, 'Entanglement of the orbital angular momentum states of photons', *Nature* **412**, 313 (2001).
- [72] E. R. Eliel, S. M. Dutra, G. Nienhuis, and J. P. Woerdman, 'Comment on 'Orbital and intrinsic angular momentum of single photons and entangled pairs of photons generated by parametric down-conversion'', *Phys. Rev. Lett.* **86**, 5208 (2001).
- [73] J. Leach, M. J. Padgett, S. M. Barnett, S. Franke-Arnold, and J. Courtial, 'Measuring the orbital angular momentum of a single photon', *Phys. Rev. Lett.* **88**, 257901 (2002).
- [74] A. T. O'Neil, I. MacVicar, L. Allen, and M. J. Padgett, 'Intrinsic and extrinsic nature of the orbital angular momentum of a light beam', *Phys. Rev. Lett.* **88**, 053601 (2002).

- [75] G. Molina-Terriza, J. P. Torres, and L. Torner, ‘Management of the angular momentum of light: Preparation of photons in multi-dimensional vector states of angular momentum’, *Phys. Rev. Lett.* **88**, 013601 (2002).
- [76] L. Allen, ‘Introduction to the atoms and angular momentum of light special issue’, *J. Opt. B: Quantum Semiclass. Opt.* **4**, S1 (2002).
- [77] N. Bloembergen, ‘Conservation laws in non-linear optics’, *J. Opt. Soc. Am.* **70**, 1429 (1980).
- [78] P. N. Butcher and D. Cotter, *The Elements of Non-Linear Optics* (Cambridge University Press, Cambridge, UK, 1990).
- [79] S. Bhagavantam and D. Suryanarayana, ‘Crystal symmetry and physical properties: Application of group theory’, *Acta Cryst.* **2**, 21 (1949).
- [80] J. S. Lomont, *Applications of Finite Groups* (Academic Press, New York, 1959).
- [81] P. Erdős, ‘The determination of the components of a tensor characterising a crystal’, *Helv. Phys. Acta* **37**, 493 (1964).
- [82] F. G. Fumi, ‘Physical properties of crystals: The direct-inspection method’, *Acta Cryst.* **5**, 44 (1952).
- [83] S. V. Popov, Y. P. Svirko, and N. I. Zheludev, *Susceptibility Tensors for Non-Linear Optics* (IOP Publishing, Bristol, UK, 1995).
- [84] A. F. Abouraddy, B. E. A. Saleh, A. V. Sergienko, and M. C. Teich, ‘Degree of entanglement for two qubits’, *Phys. Rev. A* **64**, 050101 (2001).
- [85] V. G. Dmitriev, G. G. Gurzadyan, and D. N. Nikogosyan, *Handbook of Non-Linear Optical Crystals* (Springer-Verlag, Berlin, 1999), 3rd edition.
- [86] M. O. Scully and M. S. Zubairy, *Quantum Optics* (Cambridge University Press, Cambridge, UK, 1997).
- [87] D. L. Hart and T. A. B. Kennedy, ‘Quantum noise properties of the laser: Depleted pump regime’, *Phys. Rev. A* **44**, 4572 (1991).
- [88] G. A. Koganov and R. Shuker, ‘Photon statistics of a ground-state-pumped laser’, *Phys. Rev. A* **63**, 015802 (2000).
- [89] H. Ritsch and P. Zoller, ‘Dynamic quantum-noise reduction in multi-level-laser systems’, *Phys. Rev. A* **45**, 1881 (1992).
- [90] M. S. Kim and P. L. Knight, ‘Quantum-jump telegraph noise and macroscopic intensity fluctuations’, *Phys. Rev. A* **36**, 5265 (1987).
- [91] M. Lax, ‘Quantum noise IV: Quantum theory of noise sources’, *Phys. Rev.* **145**, 110 (1966).
- [92] C. W. Gardiner and M. J. Collett, ‘Input and output in damped quantum systems: Quantum stochastic differential equations and the master equation’, *Phys. Rev. A* **31**, 3761 (1985).
- [93] J. Dalibard, Y. Castin, and K. Mølmer, ‘Wave-function approach to dissipative processes in quantum optics’, *Phys. Rev. Lett.* **68**, 580 (1992).
- [94] R. Dum, P. Zoller, and H. Ritsch, ‘Monte Carlo simulation of the atomic master equation for spontaneous emission’, *Phys. Rev. A* **45**, 4879 (1992).
- [95] H. J. Carmichael, *An Open System Approach to Quantum Optics* (Springer-Verlag, Berlin, 1993).

Bibliography

- [96] C. Cohen-Tannoudji, B. Zambon, and E. Arimondo, 'Quantum-jump approach to dissipative processes: Application to amplification without inversion', *J. Opt. Soc. Am. B* **10**, 2107 (1993).
- [97] N. G. van Kampen, *Stochastic Processes in Physics and Chemistry* (North-Holland, Amsterdam, 1981).
- [98] G. Nienhuis, 'Photon emission as a random event', *J. Stat. Phys.* **53**, 417 (1988).
- [99] H. Risken, *The Fokker-Planck Equation* (Springer-Verlag, Berlin, 1996).
- [100] L. Mandel, 'Sub-Poissonian photon statistics in resonance fluorescence', *Opt. Lett.* **4**, 205 (1979).
- [101] H. F. Arnoldus and G. Nienhuis, 'Conditions for sub-Poissonian photon statistics and squeezed states in resonance fluorescence', *Opt. Acta* **30**, 1573 (1983).

---

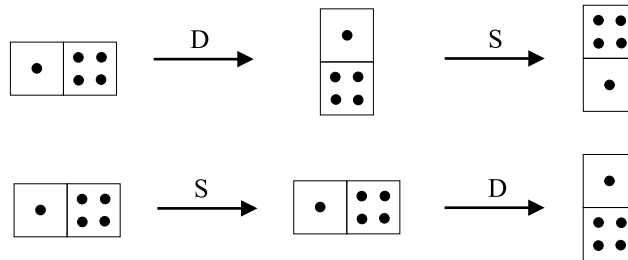
## Samenvatting

---

*In deze samenvatting worden een aantal begrippen uitgelegd die in dit proefschrift voorkomen. Aan bod komen onder meer: operator, paraxiaal, astigmatisme, baanimpulsmoment, vortex, mode, Gouy-fase, resonator, spectrum, aberratie, foton, quantum en verstrengeling.*

## Operator

Het eerste begrip in de titel van dit proefschrift is het wiskundige begrip **operator**. Een operator is iets wat je ergens op kunt laten werken. Een simpel voorbeeld van operatoren zijn de gewone getallen. Het ene getal op het andere getal laten werken, kan dan bijvoorbeeld het optellen van de getallen betekenen, of het vermenigvuldigen. Wanneer  $a$  en  $b$  getallen zijn en we laten  $a$  op  $b$  werken, dan geeft dat  $a + b$  in het geval van optellen, en  $a \times b$  in het geval van vermenigvuldigen. In het geval dat  $b$  op  $a$  werkt, vinden we  $b + a$  en  $b \times a$ , respectievelijk. We weten dat  $a + b = b + a$  en  $a \times b = b \times a$ . Dit geeft aan dat de volgorde er niet toe doet: het maakt niet uit of  $a$  op  $b$  werkt, of  $b$  op  $a$ . In het algemeen kan de volgorde van operatoren niet worden omgewisseld, zoals duidelijk wordt in het voorbeeld in figuur 1.

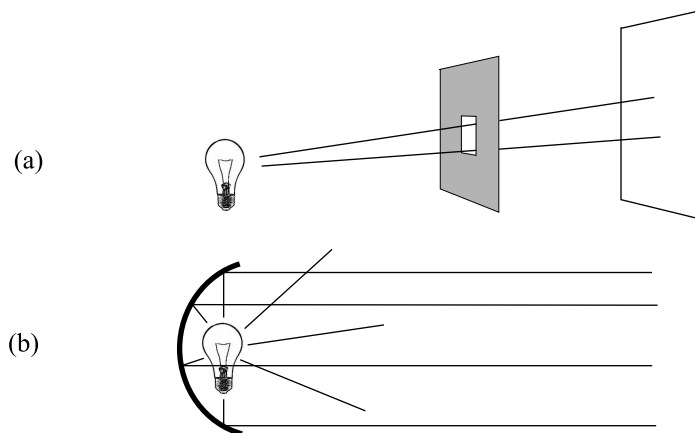


**Figuur 1:** Het maakt uit of een dominosteent eerst gedraaid wordt over een hoek van  $90^\circ$  met de wijzers van de klok mee (operatie D) en dan wordt gespiegeld in een horizontale lijn door het midden van de dominosteent (operatie S), of eerst wordt gespiegeld (S) en dan gedraaid (D).

Doordat de volgorde waarin operatoren worden toegepast van belang is, is het rekenen met operatoren in het algemeen lastiger dan het rekenen met gewone getallen. Het voordeel van operatoren is echter, dat we met operatoren kunnen rekenen zonder dat we hoeven te weten waarop ze werken. De resultaten die hiermee worden bereikt zijn algemeen en niet afhankelijk van waar de operatoren uiteindelijk op werken. Wanneer we besluiten de operatoren op iets anders te laten werken, dan hoeven we voor die nieuwe situatie de berekening niet opnieuw te doen.

## Lichtbundels

Een centrale rol in dit proefschrift spelen lichtbundels. Lichtbundels kunnen worden gemaakt door bijvoorbeeld het licht van een lichtbron door een klein gat in een stuk karton te laten schijnen, zoals weergegeven in figuur 2(a). Met behulp van een spiegel kan het licht van een lichtbron gebundeld worden, zoals in de koplamp van een auto; zie figuur 2(b). Het licht dat uit een laser komt is meestal ook in de vorm van een bundel. In feite bestaat een lichtbundel uit een groot aantal lichtstralen die min of meer dezelfde richting hebben, ofwel, een lichtbundel is **paraxiaal**. Wanneer in het proefschrift het begrip paraxiaal wordt gebruikt, dan betekent dat dus dat het over lichtbundels gaat.



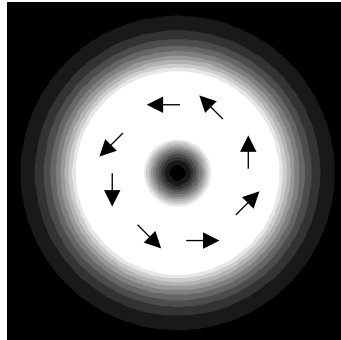
**Figuur 2:** Twee manieren om een lichtbundel te maken. In (a) schijnt het licht van een lichtbron door een klein gat in een stuk karton. Wanneer een stuk papier in de lichtbundel wordt gehouden, dan is het lichtpatroon van de lichtbundel te zien. In (b) wordt het licht van een lichtbron gebundeld door een gekromde spiegel.

Lichtbundels hebben verschillende eigenschappen waardoor ze gekarakteriseerd worden. De belangrijkste eigenschap is welke kleuren de lichtbundel bevat. De verzameling van alle kleuren die in de lichtbundel voorkomen wordt wel het **spectrum** van de lichtbundel genoemd. In dit proefschrift worden alleen lichtbundels van één kleur bestudeerd. Een andere eigenschap van een lichtbundel is het lichtpatroon. Dit lichtpatroon zien we wanneer we een stuk papier in een lichtbundel houden, loodrecht op de richting van de lichtbundel, zoals te zien in figuur 2(a). Dit lichtpatroon geeft de lichtsterkteverdeling van de lichtbundel weer. Voorbeelden van lichtpatronen zijn onder meer te zien in de figuren 4.3-4.6 van hoofdstuk 4. We zien dat de lichtpatronen in figuur 4.5(a) cirkelvormig zijn, terwijl de lichtpatronen in figuur 4.5(b) elliptisch zijn van vorm. Lichtbundels met een elliptisch lichtpatroon worden **astigmatisch** genoemd.

Wanneer we het stuk papier een klein stukje verderop in de lichtbundel houden, dan zien we dat het lichtpatroon iets is vervormd. De richting en sterkte van de vervorming wordt wel de fasegradiënt genoemd. De lichtbundel heeft dus in iedere positie in het vlak van het papier een lichtsterkte en een fasegradiënt. De fasegradiënt kan worden voorgesteld door een pijltje. Een voorbeeld hiervan is weergegeven in figuur 4.1. De gekantelde ellips geeft de vorm weer van het lichtpatroon, dat astigmatisch is in dit geval. Op vier posities is de fasegradiënt weergegeven door een pijltje, dat aangeeft in welke richting het lichtpatroon gaat vervormen. Door de pijltjes in beschouwing te nemen, zien we dat de ellips gaat draaien. In figuur 4.2 zien we hoe het lichtpatroon draait wanneer het stuk papier op verschillende plaatsen in de lichtbundel wordt gehouden. Een ander voorbeeld is weergegeven in figuur 3. Aan de richting van de pijltjes zien we dat het lichtpatroon om het middelpunt draait.

Net als een draaiend wiel, hebben draaiende lichtbundels **baanimpulsmoment** (in het Engels: **orbital angular momentum**). Het baanimpulsmoment van astigmatische lichtbun-

## Samenvatting



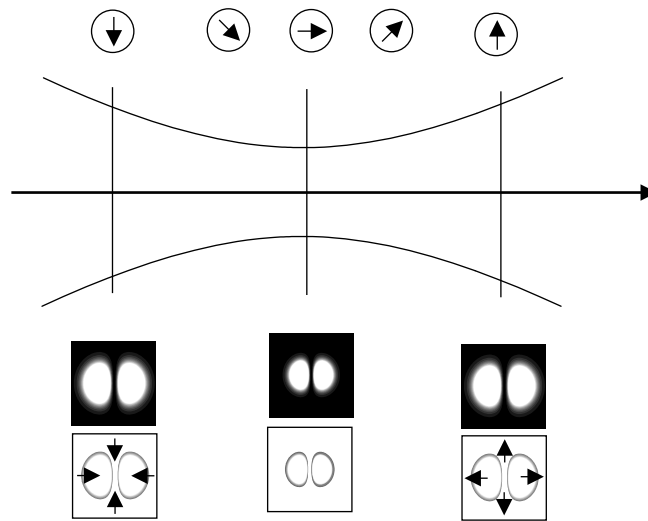
**Figuur 3:** Lichtpatroon en fasegradiënt van een lichtbundel. De fasegradiënt is weergegeven door de pijltjes. Het lichtpatroon verderop in de lichtbundel is gedraaid in de richting van de pijltjes, wat aangeeft dat het lichtpatroon draait. In het midden bevindt zich een vortex.

dels is het onderwerp van hoofdstuk 4. We zien dat we, wanneer we de pijltjes in figuur 3 volgen, om het middelpunt van de lichtbundel lopen. Dit betekent dat zich in het middelpunt van de bundel een **vortex** bevindt. Een lichtbundel met een vortex is te vergelijken met een draaikolk in water. Hoofdstuk 5 gaat over vortices in lichtbundels.

## Optische modes

Wanneer we het lichtpatroon bekijken op een stuk papier in een lichtbundel en we dat patroon vergelijken met het lichtpatroon op een andere plaats in de bundel, dan zal in het algemeen het lichtpatroon er anders uitzien. Voor sommige lichtbundels heeft het lichtpatroon echter precies dezelfde vorm, ongeacht de plaats in de bundel, maar is de schaal of grootte van het patroon wel anders. Zulke lichtbundels zullen we invariante **modes** noemen. In figuur 4 is het zijaanzicht van een invariante mode weergegeven die naar rechts beweegt. De kromme lijnen geven aan dat de bundel in het midden op z'n smalst is en links en rechts van het midden breder. Op drie plaatsen in de lichtbundel is een verticale lijn getekend. Onder iedere lijn staat het lichtpatroon en de fasegradiënt van de bundel op de plaats van de lijn weergegeven. We zien inderdaad dat het een invariante mode betreft, want de lichtpatronen hebben dezelfde vorm, hoewel het patroon in het midden kleiner is. De fasegradiënt is links in de bundel naar binnen gericht, hetgeen betekent dat het lichtpatroon naar rechts lopend inderdaad kleiner wordt. In het midden, waar de mode het kleinst is, is de fasegradiënt nul. Rechts van het midden is de fasegradiënt naar buiten toe gericht, zodat de mode naar rechts toe steeds groter wordt.

Behalve een constante vorm van het lichtpatroon hebben invariante modes een **Gouy-fase**. De snelheid waarmee de Gouy-fase verandert, zegt iets over de grootte van het lichtpatroon van de mode. De Gouy-fase is in figuur 4 weergegeven door middel van een pijltje boven de bundel. We zien dat het pijltje draait wanneer de mode naar rechts wordt gevolgd, wat aangeeft dat de Gouy-fase verandert. Als de mode klein is, verandert de Gouy-fase snel,



**Figuur 4:** Een invariante mode is een lichtbundel waarvan de vorm van het lichtpatroon op ieder plaats in de bundel hetzelfde is. In dit voorbeeld is het zijaanzicht weergegeven van een invariante mode die naar rechts beweegt. De kromme lijnen geven de grootte van de mode aan. Op drie plaatsen is het lichtpatroon en de fasegradiënt weergegeven. De pijltjes boven de mode geven de Gouy-fase van de lichtbundel weer.

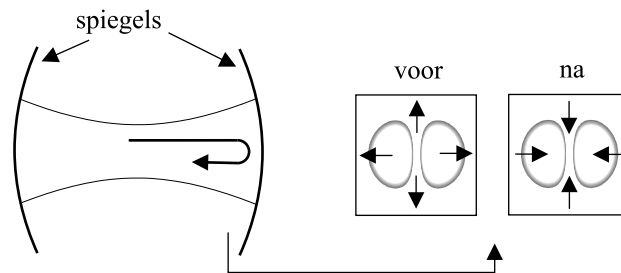
zoals te zien in de figuur. Is de mode groot, dan verandert de Gouy-fase langzamer.

## Resonator

Een **resonator** bestaat uit twee gekromde spiegels waartussen een lichtbundel kan worden opgesloten. In figuur 5 kaatst een lichtbundel heen en weer tussen de spiegels van een resonator. Rechts van de resonator staat de fasegradiënt van de lichtbundel weergegeven vlak voordat hij door de rechterspiegel wordt gereflecteerd en vlak erna. We zien dat vlak vóór de spiegel de fasegradiënt naar buiten is gericht, wat betekent dat de bundel steeds groter wordt. De spiegel zorgt ervoor dat de fasegradiënt na reflectie juist naar binnen is gericht, zodat de bundel weer kleiner wordt wanneer hij naar links beweegt. Op deze manier blijft de lichtbundel heen en weer lopen tussen de spiegels zonder dat hij steeds groter wordt en buiten de spiegels valt.

Niet alle lichtbundels passen in een resonator. Een voorwaarde is dat de lichtbundel na één rondgang precies hetzelfde is gebleven, zowel wat betreft het lichtpatroon als de fasegradiënt. In dat geval wordt de lichtbundel een eigenmode van de resonator genoemd. Hoofdstuk 2 gaat over resonatoren en hun eigenmodes. In het bijzonder wordt gekeken naar **geometrische modes**, die opgebouwd zijn uit meerdere, heen en weer kaatsende lichtbundels. In figuur 2.3 van hoofdstuk 2 is het zijaanzicht van twee geometrische modes te zien. In deze figuur bevinden de spiegels van de resonator zich links en rechts van de plaatjes.

## Samenvatting



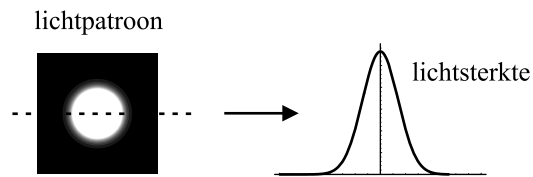
**Figuur 5:** Een resonator bestaat uit twee gekromde spiegels waartussen een lichtbundel kan worden opgesloten. Rechts van de resonator is de fasegradiënt weergegeven vlak vóór en vlak na reflectie door de rechterspiegel. De spiegels zorgen ervoor dat de fasegradiënt van de lichtbundel bij reflectie naar binnen gericht wordt, zodat de bundel bij het heen en weer kaatsen niet steeds groter wordt en ontsnapt.

Niet alle kleuren licht zijn toegestaan in een resonator. Iedere eigenmode heeft zijn eigen toegestane kleur licht. Wanneer het over het **spectrum** van een resonator gaat, dan betreft het de kleuren licht die zijn toegestaan in de resonator. In hoofdstuk 3 wordt het spectrum en de eigenmodes van een resonator onderzocht in het geval de spiegels **aberraties**, ofwel afwijkingen, hebben.

## **Foton**

De lichtsterkte van een lichtbundel kan worden verzwakt door in de bundel een glasplaatje te houden waar een laagje roet op zit. Wanneer steeds meer van die glasplaatjes met roet in de lichtbundel worden gehouden, wordt de lichtsterkte steeds geringer. Het licht in een zeer zwakke lichtbundel gedraagt zich alsof het uit pakketjes van energie bestaat. Deze pakketjes worden **fotonen** genoemd. We kunnen een lichtstraal wat dat betreft vergelijken met een straal zand. Wanneer we de straal zand steeds kleiner maken, zal de straal op een bepaald moment bestaan uit afzonderlijk vallende zandkorrels. In een typische laserbundel, zoals bijvoorbeeld gebruikt in een DVD-speler, komen er per seconde meer dan  $10^{15}$  fotonen langs. Fotonen planten zich voort met de snelheid van het licht (300.000 kilometer per seconde). Hoofdstuk 6 bestaat uit een theoretische beschrijving van de fotonen in een lichtbundel. Het woord **quantum** in de titel van dat hoofdstuk verwijst ernaar dat de lichtbundel in pakketjes, ofwel quanta, van licht is opgedeeld.

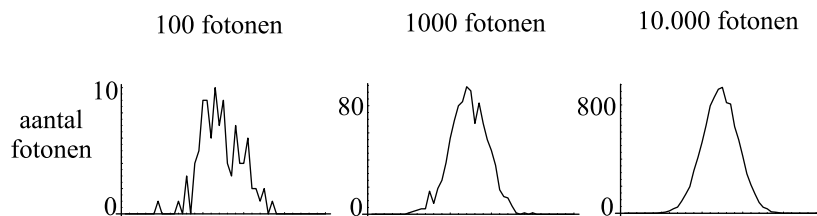
Wanneer de lichtbundel wordt verzwakt, wat gebeurt er dan met het lichtpatroon? Het lichtpatroon van een lichtbundel kan worden vastgelegd door een fotografische plaat (zwart-wit) een korte tijd in de lichtbundel te houden. De ontwikkelde plaat ziet er dan uit als het lichtpatroon links in figuur 6. De grafiek rechts in de figuur is een doorsnede van het lichtpatroon langs de stippellijn. Op de verticale as staat de lichtsterkte weergegeven. Wanneer de lichtbundel wordt verzwakt, dan blijft het lichtpatroon er hetzelfde uit zien, maar wordt de lichtsterkte van de ontwikkelde plaat steeds minder. Wanneer de lichtbundel zo zwak is dat er maar een paar fotonen op de plaat vallen tijdens het blootstellen van de plaat, dan is



**Figuur 6:** Lichtpatroon van de onverzwakte lichtbundel. De grafiek rechts is een doorsnede van het lichtpatroon langs de stippellijn. Op de verticale as van de grafiek staat de lichtsterkte.

het lichtpatroon helemaal verdwenen. In plaats daarvan zijn er hele kleine lichtvlekjes te zien op de ontwikkelde plaat. Ieder vlekje is veroorzaakt door een enkel foton. Wanneer de fotografische plaat langer wordt blootgesteld, worden er steeds meer fotonen waargenomen. De lichtvlekjes van al die fotonen samen vormen dan het lichtpatroon van de lichtbundel.

In figuur 7 is weergegeven hoe het lichtpatroon wordt opgebouwd uit de afzonderlijke fotonen van de lichtbundel. De doorsnede van de lichtbundel is opgedeeld in 50 hokjes van gelijke lengte. In ieder hokje wordt het aantal waargenomen fotonen geteld. De grafieken in figuur 7 geven weer hoeveel fotonen er per hokje zijn waargenomen, nadat er in totaal 100, 1000 en 10.000 fotonen zijn waargenomen. We zien dat de rechtergrafiek met in totaal 10.000 waargenomen fotonen bijna precies lijkt op de doorsnede van het lichtpatroon van de onverzwakte lichtbundel in figuur 6. Dit maakt duidelijk dat de lichtvlekjes van een groot aantal fotonen in een lichtbundel samen het lichtpatroon van de bundel vormen.



**Figuur 7:** Het lichtpatroon wordt opgebouwd uit de afzonderlijke fotonen. In de grafieken is op de verticale as het aantal waargenomen fotonen per hokje weergegeven, nadat in totaal 100, 1000 en 10.000 fotonen zijn waargenomen.

In de linkergrafiek van figuur 7 zijn er nogal veel pieken. Dit komt omdat het aantal getelde fotonen een geheel getal oplevert. De lijn in de grafiek moet dan steeds sprongen maken van 1,2,3,... om de meetpunten met elkaar te verbinden, waarden ertussen zijn niet mogelijk. Omdat het maximum aantal fotonen per hokje maar 10 is, zijn dat nogal grote sprongen, wat de oorzaak van de pieken is. In de middelste grafiek is het maximum aantal fotonen per hokje 80, waardoor de sprongen al veel minder opvallen. In de rechtergrafiek zijn de pieken vrijwel verdwenen. Een lichtbundel is dus opgebouwd uit pakketjes, fotonen, die alleen in zijn geheel kunnen worden waargenomen. Dat is de oorzaak van de piekjes, ofwel de ruis, in de grafieken. Dit verschijnsel wordt hagelruis genoemd, omdat de hagelkorrels in

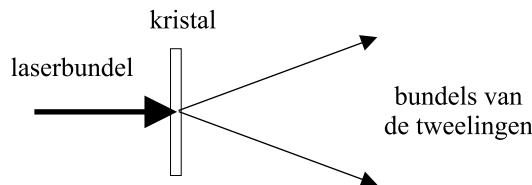
## Samenvatting

een hagelbui zijn te vergelijken met de fotonen in een lichtbundel. In hoofdstuk 9 wordt de hagelruis in een lichtbundel onderzocht.

We zien in de grafieken in figuur 7 ook dat er meer fotonen in het midden worden waargenomen dan naar de randen toe. Dit betekent dat de kans om een foton waar te nemen in het midden groter is dan naar de randen toe. De rechtergrafiek (groot aantal fotonen) geeft dan de kansverdeling weer om een foton waar te nemen. We hadden hierboven al gezien dat de rechtergrafiek (groot aantal fotonen) hetzelfde is als de doorsnede van het lichtpatroon in figuur 6. Dit betekent dat het lichtpatroon van een lichtbundel, behalve de lichtsterkte in de bundel, ook de kansverdeling weergeeft om fotonen uit de bundel waar te nemen.

## **Tweelingfotonen**

Wanneer een kristal in een lichtbundel wordt gehouden, dan wordt in het kristal af en toe een foton uit de lichtbundel opgesplitst in twee nieuwe fotonen. De nieuw ontstane fotonen worden tweelingfotonen genoemd. In figuur 8 is dit proces schematisch weergegeven.



**Figuur 8:** Een laserbundel valt op een kristal. Een fractie van de fotonen in de lichtbundel wordt in het kristal opgesplitst in twee nieuwe fotonen. De twee nieuwe fotonen planten zich voort in twee lichtbundels met een verschillende richting.

De fotonen van een tweeling zijn **verstrengeld** (in het Engels: **entangled**). Dit betekent dat de eigenschappen van de afzonderlijke fotonen van een tweeling niet vastliggen. Zodra echter de eigenschappen van één van de fotonen worden gemeten, liggen de eigenschappen van het andere foton ook gelijk vast. De fotonen van een tweeling worden bijvoorbeeld op hetzelfde moment in het kristal geboren (vandaar de naam), maar het moment waarop is onbepaald. Zodra we echter het tijdstip weten waarop één van de fotonen van een tweeling is geboren, weten we dus direct het tijdstip waarop het andere foton is geboren. Dit wordt tijdsverstrengeling genoemd. Een ander voorbeeld van verstrengeling is ruimtverstrengeling. De fotonen van een tweeling worden op dezelfde positie in het door de laserbundel belichte deel van het kristal geboren, maar waar dat gebeurt is onbepaald. De reden dat de geboorte-positie van een tweeling onbepaald is, is omdat een tweeling ontstaat uit één foton. We hebben hierboven gezien dat het lichtpatroon de kansverdeling voor het waarnemen van een foton weergeeft. De positie binnen het lichtpatroon waar het foton wordt waargenomen is dus onbepaald, net als de positie waarop een tweeling wordt geboren. Hoofdstuk 7 gaat over de overeenkomsten tussen tijd- en ruimtverstrengeling. Hoofdstuk 8 tenslotte gaat over weer een andere vorm van verstrengeling, namelijk polarisatieverstrengeling.

---

## List of publications

---

- *The spectrum of an optical resonator with spherical aberration*, J. Visser and G. Nienhuis, accepted for publication in J. Opt. Soc. Am. A..
- *Wave description of geometric modes of a resonator*, J. Visser, N. J. Zelders, and G. Nienhuis, accepted for publication in J. Opt. Soc. Am. A..
- *Vortices and angular momentum in general astigmatic modes*, J. Visser and G. Nienhuis, Proc. of SPIE **5736**, 126 (2005).
- *Orbital angular momentum of general astigmatic modes*, J. Visser and G. Nienhuis, Phys. Rev. A **70**, 013809 (2004).
- *Angular momentum and vortices in paraxial beams*, G. Nienhuis and J. Visser, J. Opt. A: Pure Appl. Opt. **6**, S248 (2004).
- *Interference between entangled photon states in space and time*, J. Visser and G. Nienhuis, Eur. Phys. J. D **29**, 301 (2004).
- *Polarization entanglement in a crystal with threefold symmetry*, J. Visser, E. R. Eliel, and G. Nienhuis, Phys. Rev. A **66**, 033814 (2002).
- *Quantum-trajectory description of laser noise with pump depletion*, J. Visser, G. Nienhuis, S. M. Dutra, M. P. van Exter, and J. P. Woerdman, Phys. Rev. A **65**, 063809 (2002).
- *Route toward the ideal thresholdless laser*, S. M. Dutra, J. P. Woerdman, J. Visser, and G. Nienhuis, Phys. Rev. A **65**, 033824 (2002).

List of publications

---

## Curriculum vitae

---

Jorrit Visser werd op 15 juni 1976 geboren te Haarlem. In 1994 behaalde hij het atheneum-diploma aan het Christelijk Lyceum te Alphen aan den Rijn. In datzelfde jaar begon hij de studie natuurkunde aan de Universiteit Leiden. Zijn afstudeerproject vond plaats in de groep Moleculen in Aangeslagen Toestand onder begeleiding van dr. E. J. J. Groenen. Het onderwerp van zijn afstudeerproject was de spin-spin-interactie in de laagste triplettoestand van  $C_{60}$  en  $C_{70}$ . In 2000 studeerde hij af.

In oktober 2000 trad hij als Onderzoeker in Opleiding in dienst van de Stichting voor Fundamenteel Onderzoek der Materie (FOM) om onderzoek te doen in de groep Quantumoptica aan de Universiteit Leiden. Het onderzoek werd verricht onder begeleiding van prof. dr. G. Nienhuis, en aanvankelijk ook van dr. S. M. Dutra. De resultaten van het onderzoek zijn verwerkt in dit proefschrift. Zijn onderwijstaak bestond uit het geven van de werkcolleges 'Speciale relativiteitstheorie' en 'Quantumfysica' aan natuur- en sterrenkundestudenten. In het schooljaar 2002-2003 was hij docent natuurkunde aan het Fioretti College te Lisse.

Curriculum vitae

---

## Nawoord

---

Op deze plaats in mijn proefschrift wil ik een aantal mensen bedanken die een belangrijke rol hebben gespeeld bij het tot stand komen van dit proefschrift.

Totdat ze door haar ziekte haar werk niet meer kon doen, was Anneke Aschoff de drijvende kracht achter de sociale activiteiten in de groep en zorgde ze voor de administratie, waarvoor ik haar erkentelijk ben. Ik wil ook Daniëlle van Raaij en Henriette van Leeuwen bedanken voor de administratieve ondersteuning. Dankzij Arno van Amersfoort, René Overgaww en Leendert Prevo functioneerden mijn computer en het netwerk optimaal, waardoor ik van alle gemakken voorzien mijn proefschrift kon schrijven.

Ik wil Sergio Dutra bedanken voor de begeleiding en samenwerking in het begin van mijn promotieonderzoek. Verder wil ik Niels Zelders bedanken voor de samenwerking in het onderzoek naar de geometrische modes. Dankzij Thijs Klaassen konden een aantal van mijn theoretische voorspellingen aan de werkelijkheid worden getoetst.

Mijn kamergenoot Javier Loaiza wil ik bedanken voor de discussies over ons onderzoek, voor zijn opgewektheid en voor al die gesprekken die we gevoerd hebben. Voor de gezelligheid in de groep wil ik bedanken: mijn collega oio's en aio's Alexander van der Lee, Marnix Willemsen, Steven van den Berg, Yngve Lien, Jos Dingjan, Sumant Oemrawsingh, Hayk Haroutyunyan, Javier Loaiza, Erwin Altewischer, Thijs Klaassen, Peter Lee, Nikolay Kuzmin, Graciana Puentes en Eduard Driessen; de post-docs Sergio Dutra, Andrea Aiello, Cyriaque Genet en Dirk Voigt, en ook alle studenten.

Zonder de mentale steun van mijn moeder en broer was dit proefschrift nooit voltooid. Lonneke wil ik tenslotte bedanken voor haar aanwezigheid en belangstelling.